Petrographic and Geochemical Constraints on Regionally Extensive Hydrothermal Dolomites in Jurassic Carbonates of Saudi Arabia

By

Mohammed A. Alqattan

B.S., University of Durham, 2008
M.S., University of Colorado, 2014

Submitted to the graduate degree program in the Department of Geology and the Graduate Faculty of the University of Kansas in partial fulfillment of the requirements for the degree of Doctor of Philosophy

Committee Members

_____
Dr. Robert Goldstein, Chair

_____
Dr. Andreas Möller

_____
Dr. Shahin Negahban

_____
Dr. Jennifer Roberts

_____
Dr. Marina Suarez

Date defended: 05/11/2022

The dissertation committee for Mohammed A. Alqattan certifies

that this is the approved version of the following dissertation:

Petrographic and Geochemical Constraints on Regionally Extensive Hydrothermal Dolomites in Jurassic Carbonates of Saudi Arabia

_____

Dr. Robert Goldstein, Chair

Date approved _____

Abstract

This research focuses on the petrographic, geochemical, and reservoir petrophysical aspects of Jurassic carbonates in the subsurface of northeast Saudi Arabia. Dolostones account for ~85% of the reservoir rocks and are composed of equant and baroque dolomites with the two commonly co-occurring. The two dolomite types record nearly identical stable isotopic and fluid inclusion values, characterized by negative $\delta^{18}O$ values (means: -7.5‰ and -7.4‰VPDB for equant and baroque dolomite, respectively) and high homogenization temperatures (means of 101.6ºC and 98.3ºC for equant and baroque dolomites, respectively). The $^{87}Sr/^{86}Sr$ in dolostones ranges from 0.70761 to 0.70787, which is higher than Late Jurassic seawater, indicating formation from marine-derived fluids of Paleogene age. Uranium–lead dating on dolomite yields ages of 58.0 ± 6.5 Ma to 11.9 ± 2.4 Ma. All data indicate that dolomites formed and recrystallized at high temperature after burial. Regional and burial studies show that the dolostones never experienced burial temperatures as high as those recorded by the fluid inclusions, indicating a hydrothermal origin. Integrating the data with previous structural and burial studies, we interpret the extensive dolomitization to have been facilitated by surface-breaching faults, which were active during part of the diagenetic history of the carbonates. The fault-damage zones served as conduits and allowed evaporated seawater to sink during the Paleogene. Sinking fluids charged a deeper aquifer and the bulk of dolomitization was from convective circulation of hot fluids within the fault and fracture network, with some seismic pumping possible. This process also altered some reservoir properties in the dolostones. Samples with porosities > 20% and permeabilities > 100 mD were only observed in the dolostone and not limestone. Petrographic and geochemical analyses revealed the presence of pore spaces exclusive to the dolostones. These pores are interpreted to have developed during the hydrothermal alteration, through mesogenetic dissolution events that are unrelated to and absent from the limestone. Combined petrographic and geochemical observations indicate dolomites precipitated and recrystallized in a hydrothermal setting. The recrystallization resulted from the pulsed nature of fluid flow, which either caused temperature fluctuations or introduced fluids of variable saturation state.

Dedication

This dissertation is dedicated to my mom and dad, my wife and son, and my entire family for their endless love, support, encouragement, and above all for their sacrifices through months, and years, of neglect and absence from my side.

Acknowledgments

I am grateful to have had the opportunity to work and learn from my advisor, Dr. Robert Goldstein. Thank you, Bob, for your guidance, patience, and more importantly for your unmatched willingness and enthusiasm to share your knowledge and experiences. I am thankful for all our discussions and meetings, those on Zoom or in the lab, where you have always provided constructive thoughts on many aspects of my project. I will miss our chats about geology, but I will also miss our chats about the state of the Kansas Jayhawks basketball team, RCJH. My committee members, Dr. Andreas Möller, Dr. Jennifer Roberts, Dr. Marina Suarez, and Dr. Shahin Negahban are thanked for helping with the proposal, and for their kindness to review this dissertation in a compressed time. Thanks also go to Dr. Gene Rankey, Dr. Steve Hasiotis, and Dr. Reza Barati for assisting me with some degree requirements. Dr. David Budd is thanked for providing advice and recommendations that helped before and during my study.

I would like to thank Tristan Betzner for helping with early drafts of this dissertation and for all interesting conversations we have had. Ibrahim Alkharadawi and Saeed Tofaif are thanked for their continuous encouragement and for lifting my spirit whenever I have been down.

My study at KU was fully sponsored by Saudi Aramco; I would like to thank the management in Aramco, especially Sa'id Alhajiri for making sure I had everything I needed to successfully complete the degree. I would like to thank Nassir Al-Naji for all the work he has done to ease any hardship I have faced and for his continuous guidance and encouragement. The management in my department are thanked for their support and for their approval of any data needed. Dr. Nassir Alghamdi is thanked wholeheartedly for his mentorship and for suggesting a good dataset for this study, he went above and beyond in making sure the project is in good shape.

Mahmood Katheri, Ali Alwaheed, Ahmed Alshawarb, and Thamer Alnasser assisted me greatly with data access while I was in Dhahran. The core lab staff in Aramco are recognized for accommodating my requests to look at cores and thin sections despite the short notice. Aramco Service Company in Houston, and particularly my advisor Jeffrey Brown, were always supportive and helped make my study at KU easier. Credit to them for providing world-class support during the midst of the COVID outbreak in mid-2020. They, and their parent department in Dhahran, managed to arrange for my safe travel back home, and my return to school, during the peak of the pandemic.

Finally, I take this opportunity to express my profound gratitude, deep regards, and love to my mom and dad, my wife and son, and my entire family. I could not have completed my degree without their continual blessing and support, which I needed on a daily basis.

Table of Contents

List of Figures

List of Tables

Chapter 1

Introduction

1.1 THE GEOLOGICAL PROBLEM

Despite decades of research on dolomites, there remain some gaps in our knowledge about how ancient carbonate platforms were dolomitized. Many studies have aimed at addressing the central questions of dolomite's origin, time of formation, and the likely mechanisms through which ancient platform dolomites formed (Zenger et al., 1980; Land, 1980; Mountjoy and Amthor, 1994; Morrow, 1998; Luczaj and Goldstein, 2000; Machel, 2004; Davies and Smith, 2006). Resolving dolomite's origin, time of formation, and the likely mechanisms through which it has formed, however, are not always easy tasks, especially when multiple dolomitization events have affected an area. This is particularly true when there is a large amount of high-temperature dolomite that now exhibits petrographic and geochemical properties unrelated to near-surface, seawater-driven diagenesis, as seawater is a good source for Mg-rich fluids for dolomitization.

One of the most daunting tasks when dealing with subsurface dolomite is to determine its origin and if there is a feasible geological mechanism capable of producing large volumes, and sometimes platform-wide, high-temperature dolomites at depth. Studies that have invoked major hydrothermal dolomitization via fault pumping (seismic pumping) to explain platform-wide burial dolomites (e.g., Davies and Smith, 2006) have failed to provide a convincing explanation for the source of dolomitizing fluids, and hence received criticism (Machel and Lonnee, 2002; Lonnee and Machel, 2006).

Part of the difficulty in interpreting the origin of high-temperature dolomites in ancient carbonate platforms is due to the possibility of a widespread recrystallization. Because dolomite recrystallization can cause a major alteration of the petrographic and geochemical attributes of original dolomites (Machel, 1997), there are always some ambiguities in interpreting these attributes. Do the geochemical signatures in recrystallized dolomite, for example, reflect the conditions of original formation? Or do they merely reflect the conditions of many subsequent recrystallization events? Failure to distinguish between 'pristine' and altered dolomite signatures leads to flawed interpretations of the origin and timing of dolomite. This is not trivial, as an accurate identification of dolomite origin is essential to understanding the controls on the lateral and temporal distributions of dolomite in an area. The latter is especially important when such dolomites have an economic importance.

Many ancient dolomitized platforms contain large proportions of the world's hydrocarbon reserves (Zenger et al., 1980; Sun, 1995; Warren, 2000), and understanding the mechanisms through which this dolomite formed, thus, is an essential first step to help with characterizing the reservoirs. After establishing the genesis of the dolomite, the characterization of dolostone reservoirs relies on establishing relationships between dolomite fabrics and reservoir petrophysical properties (Lucia and Major, 1994; Sun, 1995; Saller and Henderson, 1998; Lucia et al., 2001; Ehrenberg, 2004; Alqattan and Budd, 2017). How and if dolomite has any control on reservoir properties remains unclear. A complete quantification of the relative abundances of the different dolomite fabrics, their distribution, along with the implications for reservoir properties is often needed to evaluate dolomite impact on the reservoir and to better predict reservoir performance, and design exploration and development drilling plans.

This research integrates petrographic and geochemical results, which are constrained by a state-of-the-art application of uranium–lead (U–Pb) dating, to address fundamental questions pertaining to dolomites. The results obtained in this study are applicable to many regionally extensive, high-temperature dolomites. This study addresses the origin of regionally extensive high-temperature dolomites, provides evidence for a hydrothermal origin of the dolomite, provides a mechanism to produce the high-volumes of dolomites, explores the impact of dolomite recrystallization on interpreting the geochemical data, and addresses hydrothermal processes and their impact on dolomite reservoir properties.

1.2 REGIONAL BACKGROUND

This study utilizes datasets from the Upper Jurassic Arab Formation in northeast Saudi Arabia. The datasets include mostly thin and thick sections, and data generated from them that include stable isotope geochemistry, fluid inclusion microthermometry, strontium isotope ratios, and U–Pb dating analyses. Where applicable, knowledge of the published burial and structural history in the region is used to provide contextual guideline of the data generated herein.

The Arab Formation reservoirs in the Gulf region of the Middle East host some of the most prolific carbonate reservoirs of the world (Murris, 1980; Sharland et al., 2001; Cantrell et al., 2014). However, production from these reservoirs is not uniform across the entire region; as there are areas with superior productions, like in the Ghawar field, as well as with much inferior production potentials. The study area is away from the major producing fields and is characterized by an abundance of high-temperature dolomites. In the Ghawar field, dolostone accounts for ~15%

of reservoir rocks (Cantrell et al., 2001), whereas dolostone accounts for ~85% of reservoir rocks in the study area.

Much is already known about the region; however, most previous studies have focused on the Arab's sedimentology, biostratigraphy, and sequence stratigraphy; with most studies focusing on producing reservoir units or outcrops (Hughes, 2004; Lindsay et al., 2006; Al-Awwad and Collins, 2013; Eltom et al., 2014; Al-Mojel et al., 2020). Fewer studies deal with aspects of diagenesis in the Arab Formation (e.g., Cantrell et al., 2001, 2004; Swart et al., 2005, 2016; Lu and Cantrell, 2016; Rosales et al., 2018). In the vicinity of the study area, Broomhall and Allan (1987) provided a short summary of some aspects of dolomite petrography and geochemistry; this research is, thus, the first comprehensive petrographic and diagenetic study in the area.

1.3 OUTLINE OF THE DISSERTATION

This dissertation focuses on three main areas: (1) the origin and attributes of regionally extensive high-temperature dolomites; (2) the problem of dolomite recrystallization; and (3) dolomite implications on reservoir properties. Each of these areas is presented in a separate chapter. This dissertation has six chapters (including an appendices chapter); summaries of each chapter are provided below.

Chapter 1, titled ***Introduction***; and as presented herein, provides summaries of the geological problems and regional background of the study area, and presents the breakdowns of the chapters. A one-paragraph summary is provided below for each chapter.

Chapter 2, titled ***Fault-Controlled Hydrothermal Dolomite in a Jurassic Carbonate, Saudi Arabia***. This is the largest chapter in the dissertation and includes extensive datasets. The main purpose of this chapter is to provide regional, sedimentological, and diagenetic background of the area and address the nature of dolomite in the region as a whole. This chapter provides comprehensive petrographic and geochemical analyses on both limestone and dolostone but with emphasis on the latter. Petrographic and geochemical data are mostly presented using a well-by-well framework to allow for a better understanding of spatial trends in the area and to capture the lateral variability in the dolomite. Through the integration of data from this study, along with previously published regional and burial studies, this chapter provides a complete synthesis of the history of dolomitization in the region. The dolomite is interpreted to have formed through a fault-controlled mechanism, where surface-breaching faults allowed for the sinking of evaporated seawater during the Paleogene. The sinking fluids then charged a Triassic aquifer, and dolomitization commenced through the upward-expulsion of Mg-rich fluids. The bulk of dolomitization was accomplished and maintained through a geothermal convective cell that operated within the fault network. All dolomites are also interpreted to be hydrothermally formed and hydrothermally recrystallized. More focus on dolomite recrystallization is provided in chapter 3. The chapter will be submitted as a co-authored journal publication.

Chapter 3, titled ***Multiple Episodes of Dolomite Recrystallization in the Hydrothermal Realm: Jurassic Arab Formation, Saudi Arabia***. This chapter focuses on dolomite, the problem of dolomite recrystallization, and utilizes more focused datasets than those used in chapter 2. This chapter divides all dolomites into either equant or baroque types and provides a complete petrographic and geochemical analysis of both. The study relies on cathodoluminescence

petrography to separate heavily recrystallized dolomite (mottled CL) from less recrystallized to unrecrystallized dolomites (has dull CL) and uses that as a framework. The study reveals that equant and baroque, as well as, recrystallized vs. unrecrystallized dolomites exhibit nearly identical geochemical attributes. Uranium–lead (U–Pb) dating reveals a major temporal overlap between the formation of equant and baroque dolomites, as well as, a time overlap between dolomite formation and recrystallization; with all processes occurring in a hydrothermal realm from pulses of fluids with similar but varying temperature, salinity, and chemical composition. The chapter will be submitted as a co-authored journal publication.

Chapter 4, titled ***Impact of Mesogenetic Dissolution on Porosity and Permeability in a Heavily Dolomitized Jurassic Carbonate, Saudi Arabia***. This chapter provides important insights to the oil and gas industry regarding the nature of pore spaces in heavily dolomitized reservoirs. It starts by establishing the petrographic and geochemical aspects of both limestone and dolostone. Then it incorporates the petrophysical data (porosity and permeability) to demonstrate similarities and differences among the different limestone and dolostone facies and subfacies. Limestone and dolostone as a whole, have nearly identical median porosity and permeability values. At first glance, this might suggest that dolostone merely inherited its pores from the limestone. Petrographic and geochemical analyses on dolostone, however, reveal an abundance of pores in dolostones that are not related to and are absent from the limestone. Therefore, dolostone did not simply passively inherit its porosity from the precursor limestone. More importantly, the study concluded that mesogenetic (deep burial) dissolution contributed to large volumes of pores in dolostone. This process (mesogenetic dissolution) has been challenged in previous studies, with some authors describing it as an illusion. Here we provide a case for it, with relevant

quantifications, using comprehensive petrographic and geochemical analyses. The chapter will be submitted as a co-authored journal publication.

Chapter 5, titled ***Conclusions and recommendations.*** This chapter provides a summary of the main conclusions in this dissertation and provides recommendations for any future work. The recommendations include some pointers that are applicable to future regional studies in the area but also some recommendations to global studies that deal with extensive high-temperature dolomites, studies that may encounter extensive recrystallization, and studies that aim at understanding the controls on the petrophysics of dolomitized reservoirs. Chapter 6 is the appendices chapter.

1.4 REFERENCES

Al-Awwad, S. F., and L. B. Collins, 2013, Carbonate-platform scale correlation of stacked high frequency sequences in the Arab-D reservoir, Saudi Arabia: Sedimentary Geology, v. 294, p. 205–218.

Al-Mojel, A., Razin, and P., Dera, G., 2020, High-resolution sedimentology and sequence stratigraphy of the Oxfordian-Kimmeridgian, Hanifa, Jubaila and Arab outcrops along Jabal Tuwaiq, central Saudi Arabia: Journal of African Earth Science, v. 165, article 103803, https://doi.org/ 10.1016/j.jafrearsci.2020.103803.

Alqattan, M. A., and D. A. Budd, 2017, Dolomite and dolomitization of the Permian Khuff-C reservoir in Ghawar field, Saudi Arabia: AAPG Bulletin, v. 101, p. 1715–1745.

Broomhall, R. W., and J. R. Allen, 1987, Regional caprock-destroying dolomite on the Middle Jurassic to Early Cretaceous Arabian Shelf: Society of Petroleum Engineers Formation Evaluation, v. 2, p. 435–441.

Cantrell, D. L., P. G. Nicholson, G. W. Hughes, M. A. Miller, A. G. Bhullar, S. T. Abdelbagi, and A. K. Norton, 2014, Tethyan petroleum systems of Saudi Arabia, in L. Marlow, C. Kendall and L. Yose, eds., Petroleum systems of the Tethyan region: AAPG Memoir 106, p. 613–639.

Cantrell, D. L., P. K. Swart, R. C. Handford, C. G. Kendall, and H. Westphal, 2001, Geology and production significance of dolomite, Arab-D reservoir, Ghawar field, Saudi Arabia: GeoArabia, v. 6, p. 45–60.

Cantrell, D., P. K. Swart, and R. M. Hagerty, 2004, Genesis and characterization of dolomite, Arab-D reservoir, Ghawar field, Saudi Arabia: GeoArabia, v. 9, p. 1–26.

Davies, G. R., and L. B. Smith, 2006, Structurally controlled hydrothermal dolomite reservoir facies: An overview: AAPG Bulletin, v. 90, p. 1641–1690.

Ehrenberg, S. N., 2004, Porosity and permeability in Miocene carbonate platforms on the Marion Plateau, offshore NE Australia: Relationships to stratigraphy, facies and dolomitization, in C. J. R. Braithwaite, G. Rizzi, and G. Darke, eds., The geometry and petrogenesis of dolomite hydrocarbon reservoirs: Geological Society (London) Special Publication 235, p. 233–253.

Eltom, H., O. Abdullatif, M. Makkawi, and A. Abdulraziq, 2014, Characterizing and modeling the Upper Jurassic Arab-D reservoir using outcrop data from Central Saudi Arabia: GeoArabia, v. 19, p. 53–84.

Hughes, G. W., 2004, Middle to Upper Jurassic Saudi Arabian carbonate petroleum reservoirs: Biostratigraphy, micropalaeontology and palaeoenvironments: GeoArabia, v. 9, p. 79–114.

Land, L. S., 1980, The isotopic and trace element geochemistry of dolomite: the state of the art. In: Concepts and Models of Dolomitization (Eds D.L. Zenger, J.B. Dunham and R.L. Ethington): SEPM Special Publication 28, p. 87–110.

Lindsay, R. F., D. L. Cantrell, G. W. Hughes, T. H. Keith, H. W. Mueller III, and D. Russell, 2006, Ghawar Arab-D Reservoir: Widespread porosity in shoaling-upward carbonate cycles: AAPG Memoir, vol. 88, p. 97–138.

Lonnee, J., and H. G. Machel, 2006, Pervasive dolomitization with subsequent hydrothermal alteration in the Clarke Lake gas field, Middle Devonian Slave Point Formation, British Columbia, Canada: AAPG Bulletin, v. 90, p. 1739–1761.

Lu, P., and D. Cantrell, 2016, Reactive transport modelling of reflux dolomitization in the Arab-D reservoir, Ghawar Field, Saudi Arabia: Sedimentology, v. 63, p. 865–892, doi:10.1111/sed.12241.

Lucia, F. J., and R. P. Major, 1994, Porosity evolution through hypersaline reflux dolomitization, in B. Purser, M. Tucker, and D. Zenger, eds., Dolomites: International Association of Sedimentologists Special Publication 21, p. 325–341.

Lucia, F. J., J. W. Jennings, Jr., M. Rahnis, and F. O. Meyer, 2001, Permeability and rock fabric from wireline logs, Arab-D, reservoir, Ghawar field, Saudi Arabia: GeoArabia, v. 6, p. 619–645.

Luczaj, J. A., and R. H. Goldstein, 2000, Diagenesis of the Lower Permian Krider dolomite, southwest Kansas: fluid-inclusion, U-Pb, and fission-track evidence for reflux dolomitization during latest Permian time: Journal of Sedimentary Research, v. 70, p. 762–773.

Machel H. G., 1997, Recrystallization versus neomorphism, and the concept of “significant recrystallization” in dolomite research: Sedimentary Geology, v. 113, p. 161–168.

Machel, H. G., 2004, Concepts and models of dolomitization: A critical reappraisal, in C. J. R. Braithwaite, G. Rizzi, and G. Darke, eds., The geometry and petrogenesis of dolomite hydrocarbon reservoirs: Geological Society (London) Special Publication 235, p. 7–63.

Machel, H. G., and J. Lonnee, 2002, Hydrothermal dolomite— A product of poor definition and imagination: Sedimentary Geology, v. 152, p. 163–171.

Morrow, D. W., 1998, Regional subsurface dolomitization: Models and constraints: Geoscience Canada, v. 25, no. 2, p. 57–70.

Mountjoy, E. W., and J. E. Amthor, 1994, Has burial dolomitization come of age? Some answers from the Western Canada sedimentary basin, in B. Purser, M. Tucker, and D. Zenger, eds., Dolomites: International Association of Sedimentologists Special Publication 21, p. 203–229.

Murris, R. J., 1980, Middle East stratigraphic evolution and oil habitat: AAPG Bulletin, v. 64, p. 597–618.

Rosales, I., L. Pomar, and S. F. Al-Awwad, 2018, Microfacies, diagenesis and oil emplacement of the Upper Jurassic Arab-D carbonate reservoir in an oil field in central Saudi Arabia (Khurais Complex): Marine and Petroleum Geology, v. 96, p. 551–576, https://doi.org/10.1016/j.marpetgeo.2018.05.010.

Saller, A. H., and N. Henderson, 1998, Distribution of porosity and permeability in platform dolomites: Insight from the Permian of west Texas: AAPG Bulletin, v. 82, p. 1528–1550.

Sharland, P. R., R. Archer, D. M. Casey, R. B. Davies, S. H. Hall, A. P. Heward, A. D. Horbury and M. D. Simmons, 2001, Arabian Plate Sequence Stratigraphy: GeoArabia Special Publication v. 2, 371 p

Sun, S. Q., 1995, Dolomite reservoirs: porosity evolution and reservoir characteristics: AAPG Bulletin, v. 79, p. 186–204.

Swart, P. K., D. L. Cantrell, H. Westphal, C. R. Handford, and C. G. Kendall, 2005, Origin of dolomite in the Arab-D reservoir from the Ghawar field, Saudi Arabia: Evidence from petrographic and geochemical constraints: Journal of Sedimentary Research, v. 75, p. 476–491, https://doi.org/10.2110/jsr.2005.037.

Swart, P. K., D. L. Cantrell, M. M. Arienzo, and S. T. Murray, 2016, Evidence for high temperature and ^{18}O-enriched fluids in the Arab-D of the Ghawar field, Saudi Arabia: Sedimentology, v. 63, p. 1739–1752.

Warren J., 2000, Dolomite: Occurrence, evolution and economically important associations: Earth-Science Reviews, v. 52, p. 1–81.

Zenger, D. H., J. B. Dunham, and R. L. Ethington, eds., 1980, Concepts and models of dolomitization: SEPM Special Publication 28, 320 p.

Chapter 2

Fault-Controlled Hydrothermal Dolomite in an Upper Jurassic Carbonate Reservoir, Saudi Arabia

ABSTRACT

Upper Jurassic carbonates in the subsurface of northeast Saudi Arabia contain anomalously high volumes of high-temperature dolomites. These dolomites are composed of equant (~60%) and baroque (~40%) dolomite, with the two co-occurring in the same wells and commonly in the same thin sections. Stable isotopic values for equant and baroque dolomites are nearly identical. Equant dolomites have mean $\delta^{18}O$ and $\delta^{13}C$ values of -7.5 and 2.4‰VPDB, whereas baroque dolomites have mean $\delta^{18}O$ and $\delta^{13}C$ values of -7.4 and 2.2‰, respectively. Fluid inclusion microthermometry shows equant dolomites recording homogenization temperature (Th) and salinity means of 101.6ºC and 24.8 wt.% NaCl eq., compared to means of 98.3ºC and 23.4 wt.% NaCl eq. for the baroque dolomites. There is a spatial trend in the data, with dolostones located in the north, and closest to a known regional fault, recording less negative $\delta^{18}O$, less positive $\delta^{13}C$, and lower Th and salinity values than those to the south. The $^{87}Sr/^{86}Sr$ in the dolostones range from 0.70761 to 0.70787, which is noticeably higher than that of Late Jurassic seawater, indicating either a radiogenic input, or formation from late Paleogene-age marine-derived fluids. Uranium–lead dating on 44 dolomite textural domains yield ages of 58.0 ± 6.5 to 11.9 ± 2.4 Ma. Previous regional studies have indicated the reactivation of nearby deep-seated faults during the diagenetic history of Jurassic carbonates. We interpret the extensive dolomitization to have been facilitated by surface-breaching faults. The faults served as conduits and allowed evaporated seawater to sink during the Paleogene. Sinking fluids charged a deeper aquifer and dolomitization commenced via the upward flow of high-temperature, Mg-rich fluids through fault and fracture networks and continued through the convective circulation of hot fluids within the fault network. Most of the dolomite formed hydrothermally at depth, with subsequent recrystallization occurring shortly after initial dolomitization, and the two processes spatially overlapping.

2.1 INTRODUCTION

Despite decades of research on dolomites, there remain some gaps in our knowledge of how ancient carbonate platforms become dolomitized (Zenger et al., 1980; Land, 1980, 1985; Morrow, 1982, 1998; Machel and Mountjoy, 1986; Mountjoy and Amthor, 1994; Luczaj and Goldstein, 2000; Machel, 2004; Davies and Smith, 2006). Understanding the conditions that control and facilitate dolomitization is even more difficult when there is a large amount of dolomite that exhibits petrographic and geochemical properties unrelated to near-surface, seawater-driven diagenesis, as seawater is a good source for Mg-rich fluids for dolomitization. Studies that have invoked major hydrothermal dolomitization via fault-pumping (seismic-pumping) to explain platform-wide burial dolomites (e.g., Davies and Smith, 2006) have drawn criticism due to their failure to convincingly explain the source of dolomitizing fluids (Machel and Lonnee, 2002; Lonnee and Machel, 2006).

Commonly accepted dolomitization models have been successful in providing only a generalized understanding of how ancient dolomites may have formed (Morrow, 1982, 1998; Warren, 2000; Machel, 2004). Numerical modeling studies, including those utilizing reactive transport models, have now corroborated the feasibility of some traditional dolomitization models, although those models all require assumptions and simplifications (Whitaker et al., 2004; Jones and Xiao, 2005; Whitaker and Xiao, 2010; Garcia-Fresca et al., 2012; Al-Helal et al., 2012; Corbella et al., 2014; Gabellone et al., 2016; Lu and Cantrell, 2016; Consonni et al., 2018; Benjakul et al., 2020). Those numerical models have also highlighted some of the weaknesses in some of the accepted dolomitization models, especially those that lack mass–balance constraints and fail to explain the source of Mg-rich fluids responsible for dolomitization.

In recent studies on dolomite (Dewit et al., 2012; Corbella et al., 2014; Hollis et al., 2017; Hirani et al., 2018; Lukoczki et al., 2019; Koeshidayatullah et al., 2020; Stacey et al., 2021; Afify et al., 2022), the use of a new dolomitization model, termed 'fault-controlled dolomitization', that can explain the presence of massive burial dolomites has been proposed. This dolomitization model proposes that surface-breaching faults can provide effective fluid conduits that draw down surface seawater and evaporated fluids to charge a deep aquifer (Corbella et al., 2014; Hollis et al., 2017). Subsurface dolomitization then proceeds through the circulation of Mg-rich fluids through a series of local faults and joint systems, governed by a platform-wide geothermal convection cell that maintains fluid circulation (Corbella et al., 2014; Hollis et al., 2017). Reactive transport modelling has demonstrated that such a model, despite its simplicity, can fully account for the large volume of dolomitizing fluids required to dolomitize carbonates in some geological settings (Corbella et al., 2014; Benjakul et al., 2020). Rift basins, in particular, where the presence of large extensional (normal) and strike-slip faults are common, often include dolomite that could have been produced through a fault-controlled mechanism (Hirani et al., 2018; Lukoczki et al., 2019).

The Jurassic system in northeast Saudi Arabia contains regionally extensive, high-temperature dolomites that cover >30 km^2 laterally and extend to a stratigraphic thickness of >1 km in some locations (Broomhall and Allan, 1987; Lu et al., 2017). The area in which dolomite occurs is associated with known regional fault/fold networks that have been reactivated during the diagenetic history of the Jurassic formations (Faqira et al., 2009; Stewart, 2018). There remain some questions regarding the origin of the dolomite and through which mechanism(s) it has formed; a combination of early reflux and late hydrothermal dolomitization have previously been offered as potential origins for the dolomite (Lu et al., 2017). Petrographic and geochemical analyses (Broomhall and Allan, 1987), as well as the regional distribution of dolomite, preclude

substantial early dolomitization; thus, the exact mechanism through which dolomite formed remains unknown.

This study addresses questions about the mechanisms through which regional, high-temperature dolomites could have formed by utilizing and systematically analyzing an extensive dataset from the Upper Jurassic Formations in NE Saudi Arabia. The study employs an integrated analysis of petrographic, geochemical, U–Pb dating, and published knowledge of burial and structural history of the region. The results are applicable to the many global subsurface high-temperature dolomites. To achieve that, the study will focus on four main questions: (1) what are the petrographic and geochemical attributes of the dolomite in NE Saudi Arabia; (2) what is the absolute timing of the dolomitization; (3) is there a model that explains the dolomitization; and (4) is the dolomite hydrothermal, 'geothermal', or hydrothermally recrystallized, and what is the evidence for that?.

2.2 GEOLOGICAL SETTING

The Middle to Upper Jurassic formations in the Gulf region of the Middle East host some of the most prolific carbonate reservoirs in the world (Murris, 1980; Sharland et al., 2001; Cantrell et al., 2014). Carbonates and interbedded evaporites were deposited on a vast, shallow platform that extended for many hundreds of kilometers on the western end of the neo-Tethys (Figure 2.1; Murris, 1980; Al-Husseini, 1997; Ziegler, 2001). Due to differential intraplate subsidence, three isolated and slightly deeper intrashelf basins (Gotnia, Arabian, and Rub Al-Khali) formed on the platform, with regional highs (arches) separating them (Figure 2.1). The separation of the basins also led to variations in their depositional styles and diagenetic histories. Carbonates with exceptionally favorable reservoir qualities, typical of those in giant hydrocarbon fields, are mostly

located within the Arabian Basin. Elsewhere, including in the study area, good reservoir rocks are present but with much reduced areal continuity (McGuire et al., 1993; Mattner and Al-Husseini, 2002).

Two main long-term tectonic events govern the majority of Arabian Plate tectonism: (1) the development and subsequent reactivation of deep-seated basement faults that cross-cut strata up to the Triassic; and (2) more recent compressional deformation that occurred in at least two pulses during Late Cretaceous and Neogene times (Al-Husseini; 2000; Faqira et al., 2009; Stewart, 2018). Compressional deformation was a direct result of plate movements that also caused the closure of the Tethys, collision between the Arabian and micro-Iranian plates, and the subsequent formation of the Zagros Mountains during the Alpine Orogeny that spanned from the Late Mesozoic to recent times (Al-Husseini; 2000; Faqira et al., 2009). At the largest scale, these two long-term tectonic events jointly produced the majority of large SW–NE-trending fault/fold systems and structural traps in Saudi Arabia and adjacent countries (Figure 2.1; Al-Husseini; 2000; Ziegler, 2001; Faqira et al., 2009; Frizon de Lamotte et al., 2011). At a smaller scale, local areas with intense structural deformation, characterized by the presence of small-scale faults and joint systems, also formed in the region. Such areas often display structural elements consistent with the overall tectonic regime in the region but can also exhibit unique structural and diagenetic histories, unlike those observed near the major structural traps, such as the Ghawar area.

The study area is located on and around a paleogeographic high (the Rimthan Arch) that separated the Gotnia Salt Basin from the Arabian Basin (Figure 2.1), and is bounded by two known regional folds, the Khurais–Jauf–Burgan (KJB) and the El Nala–Safaniay folds (Figure 2.1; Al-Husseini, 2000; Ziegler, 2001; Frizon de Lamotte et al., 2011). These two folds are the younger structural expressions of the known SSW–NNE-trending (deep-seated) faults. Those faults have

been reactivated from Late Cretaceous to Neogene times and are proposed to impact the diagenetic history of the Jurassic formations (Faqira et al., 2009).

Despite the strong structural control on the majority of sedimentation on the Arabian Plate, sedimentation of the Upper Jurassic carbonates occurred during a tectonically quiescent time that favored the eustatically controlled deposition of thick carbonate and evaporite successions (Sharland et al., 2001; Al-Husseini, 2009). The carbonates and evaporites then underwent a rapid burial phase without any exposure or major uplifts (Abu-Ali and Littke, 2005). The amount of burial differed across the study area from the northwest to the southeast, and the Jurassic strata in the southeast wells have been buried to about twice the depth of the northeast wells. Stratigraphically, the Upper Jurassic series in Saudi Arabia consists of four formations; from oldest to youngest, these are the Hanifa (Oxfordian–early Kimmeridgian), the Jubaila (early Kimmeridgian), the Arab (middle–late Kimmeridgian), and the Hith (Tithonian) formations (Hughes, 2004; Al-Husseini, 2009; Figure 2.2). The Arab Formation, which is the subject of this study, is further subdivided into four upward-shoaling members (Arab-D at the base, Arab-C, Arab-B, and Arab-A at the top), with the Arab-D member typically containing the most productive reservoir unit (Lindsay et al., 2006; Al-Awwad and Collins, 2013). These four members represent couplets of carbonate–evaporite successions that are mappable across the majority of the countries bordering the Gulf (Sharland et al., 2001; Al-Husseini, 2009). Nevertheless, identifying the couplets is not always possible, especially in the study area, where much of the interbedded anhydrite is missing, leading to ambiguities in defining the boundaries between the different stratigraphic members (Figures 2.2 and 2.3). Limestone dominates all of the carbonates in the Arab Formation in most of the Arabian reservoirs; however, in the study area, dolostone is the main lithology and accounts for ~85% of all reservoir rocks (Figure 2.2).

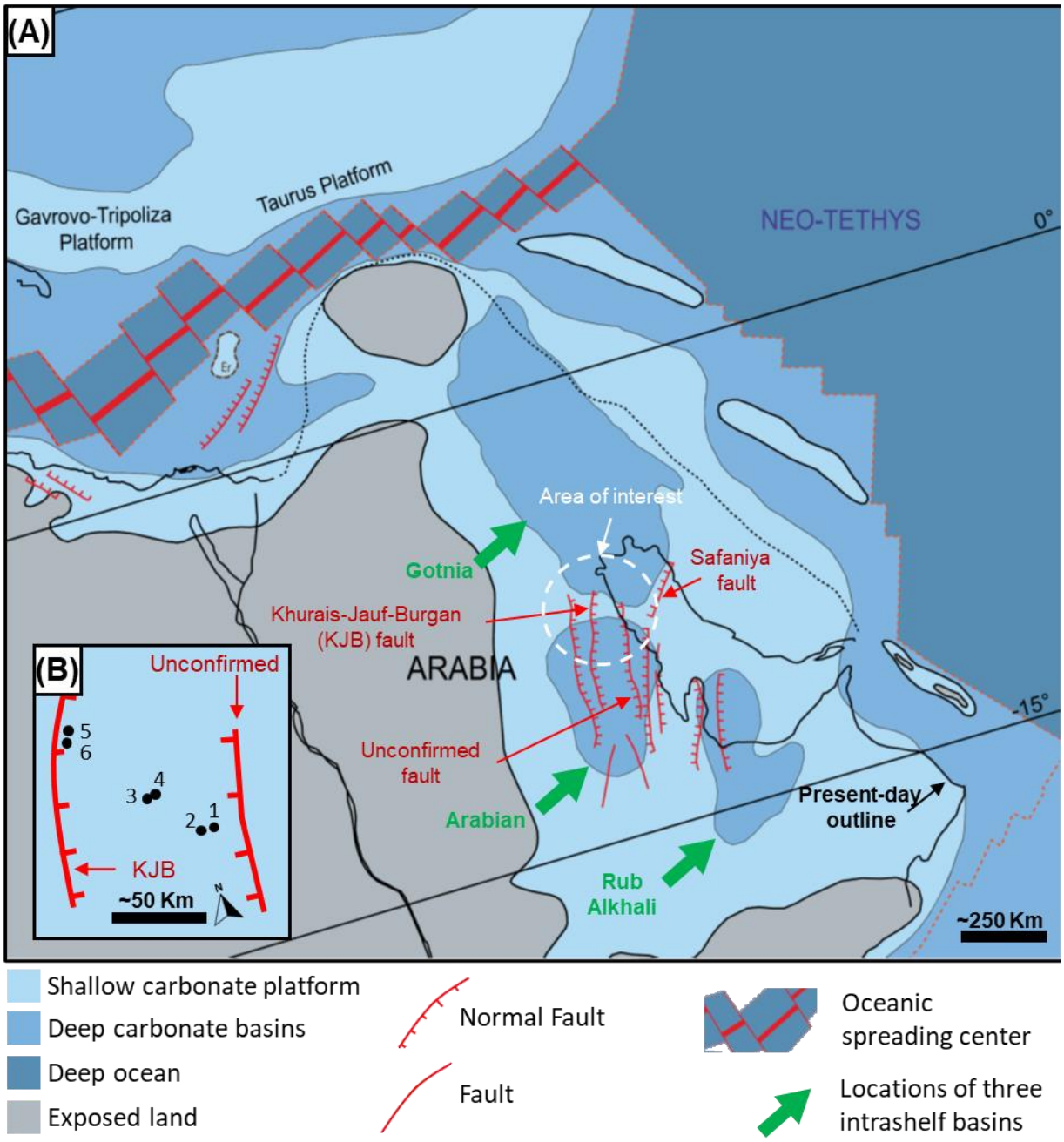

Figure 2.1. (A) A schematic paleogeographic map of the western end of Neo-Tethys region during Middle to Late Jurassic depicting the major structural elements in the region. Green arrows show the location of three intrashelf basins; from north to south are Gotnia, Arabian, and Rub Alkhali. Study area is situated on and around a paleogeographic high (Rimthan Arch; general interest area; white dashed circle). (B) Distribution of the six wells studied is shown in the magnified inset; due to the proprietary nature of the data, the exact locations of the wells cannot be provided. Figure is modified from Frizon de Lamotte et al. (2011) and based on multiple previous studies.

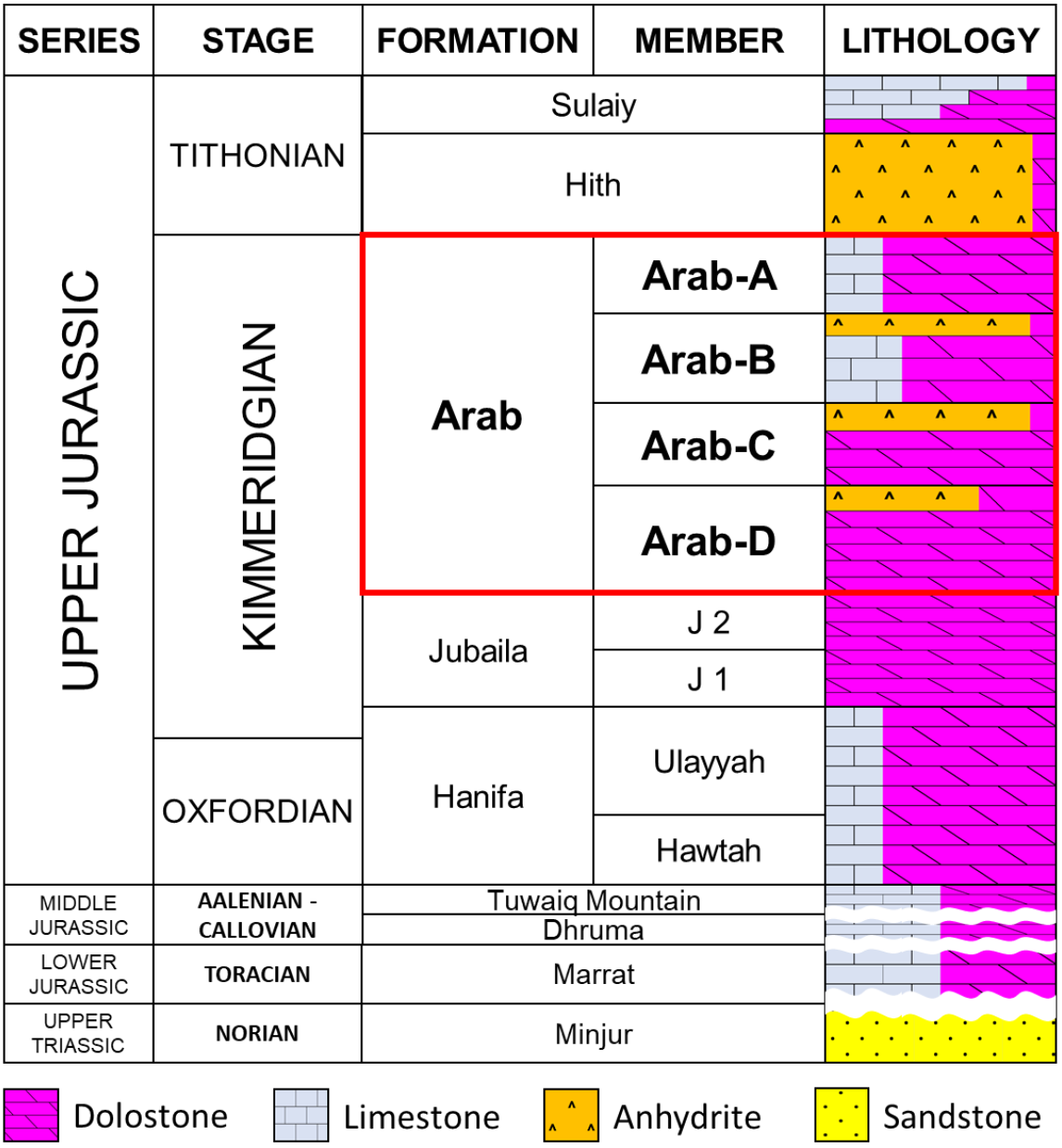

Figure 2.2. Lithostratigraphy of the Upper Triassic to Upper Jurassic units in Saudi Arabia. The Arab Formation (red box) consists of 4 members (A, B, C, and D). Note the carbonate-evaporite succession 'couplets' of the Arab members that can be mapped across the region. Anhydrites atop each Arab member are effective seals in most of the region but those anhydrites are commonly missing in northeastern Saudi Arabia. The thick regional seal (Tithonian Hith) is also commonly missing in the area.

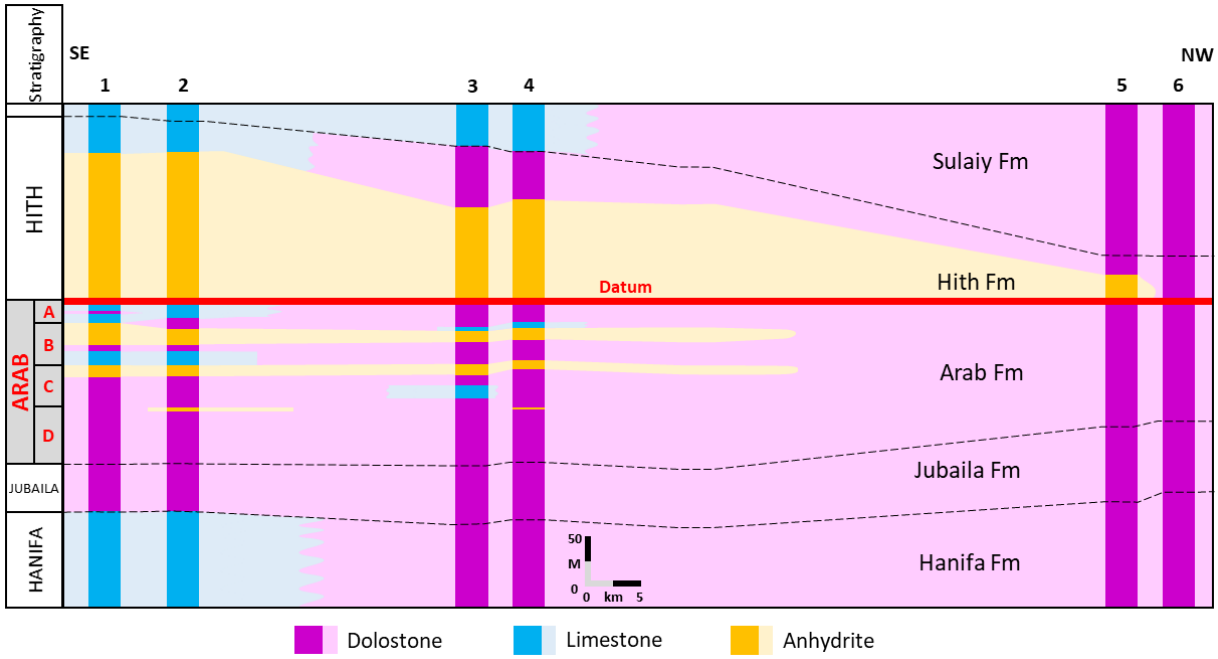

Figure 2.3. Southeast to northwest lithological correlation of the Upper Jurassic formations for the six studied wells. The Arab Formation is the subject of the study. Note the increase of dolostone towards well 6 and the absence of anhydrite in the proximity of this well. The anhydrites atop the different Arab members (see Figure 2.2) are also missing near well 6. All limestone samples used for the petrographic and geochemical analyses are from wells 1 and 2. See Figure 2.1 for key to locations.

2.3 METHODS

Six cored wells were made available for this study from which 315 thin sections (241 dolostone and 74 limestone) were used for petrographic analysis. All samples are either limestone (<0.2 dolomite–to–calcite ratio) or dolostone (>0.8 dolomite–to–calcite ratio). Some limestone samples contain minor dolomite cement (mostly <5%), but none have replacive dolomite. Each of the six wells sampled different intervals of the Arab Formation, but collectively all Arab members (A–D; Figure 2.2) were sampled. All thin sections were scanned using a DP74 camera attached to an Olympus System (Olympus Corp., Japan) capable of automatically scanning petrographic thin sections. The lithology, texture, grain, pore, and cement types, as well as detailed dolomite descriptions were determined for each thin section. Samples were stained with Alizarin Red S to

distinguish calcite from other minerals and with potassium ferricyanide to distinguish ferroan from non-ferroan carbonate minerals (Dickson, 1966).

Cathodoluminescence (CL) microscopy was performed on >40 polished thin and thick sections to decipher the CL attributes in limestone and dolostone. Analyses were conducted using an accelerating potential of 13.5–14.5 kV, a gun current of 350–400 mA, and an air chamber pressure of <0.05 torr. The analysis used a Leitz ORTHOLUX–POL microscope and a CITL mk5 CL imaging system (Cambridge Image Technology Ltd., UK).

Stable isotope analyses were conducted on microsamples (~50–100 μg) drilled directly from a total of 254 thin sections (220 dolostones, 29 limestones, and 5 dolomite cement samples in limestones). Microsampling targeted different depositional and diagenetic phases observed in the thin sections. After heating the microsamples to release organic compounds, they were reacted with 100% phosphoric acid at 70°C for 9 min. The liberated CO_2 gas was extracted with a Kiel IV carbonate device and isotopic ratios were measured using a dual inlet Finnigan MAT253 mass spectrometer (Thermo Fisher Scientific, USA) at the Keck Paleoenvironmental and Environmental Stable Isotope Lab at the University of Kansas. The calcite phosphoric acid fractionation was applied to all samples because of ambiguities with the dolomite fractionation (Land, 1980). The carbonate reference standards NBS-18 and NBS-19 were used during analysis and all values are reported in per mil (‰) and relative to Vienna Peedee belemnite (VPDB), with the reported standard deviation being <0.05‰ for both $\delta^{13}C$ and $\delta^{18}O$.

Fluid inclusion microthermometry analyses were performed on 41 polished thick sections (~100–150 μm), from four of the six wells, using a Linkam THMSG 600 stage (Linkam Scientific Instruments, Ltd., UK) and following the procedure of Goldstein and Reynolds (1994). In all analyses, homogenization temperatures were measured before freezing temperatures to ensure

measurements were taken prior to the alteration of inclusions after freezing. Tens of separate fluid inclusion assemblages (FIAs) were measured that, together, include 337 homogenization and 222 final melting temperature of ice measurements. No pressure correction was applied for homogenization temperatures; thus, all values represent minimum entrapment temperatures.

Strontium isotope ratios ($^{87}Sr/^{86}Sr$) were analyzed for 15 samples (10 dolostones, 3 limestones, and 2 anhydrites). Powdered samples (10–20 mg) were dissolved in 3.5-N nitric acid (HNO_3), followed by the separation of Sr using a Sr-spec-filled ion-exchange column and evaporated until dry. Analyses were conducted using a Sector 54 thermal ionization mass spectrometer at the University of Kansas, and the NIST 987 reference value of 0.71248 was used to normalize all $^{87}Sr/^{86}Sr$ data. All results retained 3 ppm or better external precision.

Uranium–lead analyses were conducted on 10 polished thick sections (9 dolostone and 1 limestone) using laser ablation inductively coupled plasma mass spectrometry (LA–ICP–MS) with an Element2 ICP–MS attached to a Photon Machines Analyte G2 193-nm ArF excimer laser ablation system (Thermo Fisher Scientific, USA), at the University of Kansas Isotope Geochemistry Laboratory. Approximately 80 circular spots (130 μm diameter) per sample were ablated at a fluency of 2.7 J cm^{-2} and a repetition rate of 10 Hz, resulting in 20 μm deep pits. The ablated material was carried to the ICP–MS in 1.1-l/min He gas and tied in with ~1.1-l/min Ar gas before entry into the plasma torch. Each analysis consisted of 3 pre-ablation shots to remove surface contamination, followed by 17 seconds of background acquisition, and 30 seconds of sample ablation. Corrections for isotopic and downhole fractionation, as well as drift calibration, were made by bracketing the measurements of the unknowns with the glass reference material (SRM NIST614) with a known Pb isotopic ratio (Woodhead and Hergt, 2001). This data-reduction step was performed in IOLITE v. 2.5 (Paton et al., 2010, 2011) using the U–Pb geochron3 data

reduction scheme. Uranium–lead elemental fractionation was corrected offline with an in-house Excel spreadsheet, using the calcite reference material DBTL (Hill et al., 2016) for age calibration, and WC1 (Roberts et al., 2017) for validation of the calibration. Analyses for separate analytical sessions yielded results within 99.1% of the published value for WC1. IsoplotR (Vermeesch, 2018) (http://isoplotr.geo.utexas.edu/) was used to create Tera–Wasserburg Concordia diagrams (Tera and Wasserburg, 1972) from the $^{238}U/^{206}Pb$ and $^{207}Pb/^{206}Pb$ values of individual dolomite and limestone phases and to calculate the intercept ages. All reported uncertainties in the text are internal uncertainties. Propagated uncertainties are provided in the accompanied tables and in Appendix C.

Finally, full suite wireline logs were available to aid with regional correlations and locating formation tops. The logs are not presented here but were used to constrain the stratigraphic and lateral distributions of the limestone, dolostone, and anhydrite in and around the study area.

2.4 RESULTS

2.4.1 Overall distribution of dolostone

Dolostone is the most abundant rock type in the Arab Formation in the study area, and it accounts for ~85% of all rocks (Figure 2.3). Limestone accounts for only ~15% of the reservoir rocks and was only encountered in the upper portion of the Arab Formation in wells 1 and 2, the southernmost wells in the study area (Figure 2.3). Wireline logs also reveal the presence of large volumes of dolomite in older Jurassic formations that spanned from the Lower Jurassic (Toarcian) Marrat Formation to the Upper Jurassic (Oxfordian) Hanifa Formation. Younger formations

overlying the Arab are also dolomitized and include the Upper Jurassic to Lower Cretaceous (Tithonian–Valanginian) Hith, Sulaiy, and younger formations (Figures 2.2 and 2.3).

In the Arab Formation, the amount of dolomite increases from the southeast to northwest, and dolomite distribution becomes stratigraphically discordant towards well 6 (Broomhall and Alan, 1987), which is the closest well to the Khurais–Jauf–Burgan (KJB) fold axis (Figures 2.1 and 2.3). Log and core analyses in this well show that dolostone exhibits fabrics characterized by brecciated 'chaotic' dolomites, multi-directional fractures, dissolution of bedded anhydrite, and multiple dissolution collapse horizons (Broomhall and Allan, 1987). The Tithonian Hith anhydrite, which is a regional reservoir seal of the Arab Formation across most of the region, is completely missing in and near well 6 as well as are the beds of anhydrite atop the Arab stratigraphic members (Figure 2.3). It is well established, however, that depositional bedded anhydrites occur in much larger quantities to the north (outside of the study area), in the proximity of Gotnia Basin, in present day Kuwait and Iraq, where the majority of the Jurassic System in those countries is composed of anhydrite (Sharland et al., 2001; Al-Husseini, 2009).

Despite the wide distribution of the dolomite in the study area, there are no transitional facies between dolostone and limestone (i.e., no dolomitic limestone or calcitic dolostone). All dolostone facies are almost entirely composed of dolomite, and the limestone facies are composed of calcite. A few limestone samples contain minor dolomite cement (mostly < 5%, but up to 18% in one sample) that is commonly associated with anhydrite cements but no replacive dolomite was observed in any limestone sample.

2.4.2 Depositional facies and their distribution

Due to the extensive dolomitization, dolostone facies are more abundant volumetrically than limestone facies, with the latter only sampled in the Arab-A and B members in wells 1 and 2 (the southernmost wells; Figure 2.3). The studied intervals include seven main facies (4 dolostone and 3 limestone facies; Table 2.1; Figure 2.4). The seven facies are: (1) peloidal-skeletal dolograinstone (D1; Figure 2.4A); (2) oolitic dolograinstone (D2; Figure 2.4B); (3) sponge dolorudstone (D3; Figure 2.4C); (4) fabric-destructive dolostone (D4; Figure 2.4D); (5) peloidal-skeletal grainstone (L1; the undolomitized equivalent of facies D1; Figure 2.4E); (6) bioclastic wackestone (L2; Figure 2.4F); and (7) intraclast floatstone (L3; Figure 2.4G).

The fabric-destructive dolostone (D4) is the most abundant facies (~37% of all samples; Figure 2.4H; Table 2.1); it was observed in all wells, all stratigraphic horizons, and intercalated with other facies. When grouped together, the peloidal-skeletal dolograinstone and grainstone (D1 and L1; Figure 2.4A, E) are the most common depositional facies (together account for ~39% of all samples; Figure 2.4H) and the only depositional facies with both limestone and dolostone examples, with D1 occurring in all wells (1 to 6) and in all stratigraphic members (Arab-D to Arab-A). The other facies are less abundant and do not occur in all members; for instance, the sponge dolorudstone was only observed in the Arab-D member (Table 2.1). Even less common limestone facies were also observed rarely and include foraminiferal wackestone and lime mudstone facies, a few cm thick, intercalated the more common facies.

Table 2.1. Facies Description and Distribution

	Facies Name	Facies Code	Lithology	# of Samples	Stratigraphic Distribution	Textures	Grains
1	Peloidal-Skeletal Dolograinstone	D1	Dolostone	63	All Members	Packstone to Grainstone	Green Algae, Foraminifera
2	Oolitic Dolograinstone	D2	Dolostone	43	All Members	Grainstone	Green Algae
3	Sponge Dolorudstone	D3	Dolostone	18	Arab-D	Rudstone	Stromatoporoids, Ooids, Green Algae
4	Fabric Destructive Dolostone	D4	Dolostone	117	All Members	n/a	n/a
5	Peloidal-Skeletal Grainstone	L1	Limestone	60	All Members	Wackestone to Grainstone	Pellets, Peloids, Foraminifera, Gastropods, Brachiopods, Green Algae
6	Bioclastic Wackestone	L2	Limestone	8	Arab-A, B	Wackestone	Brachiopods, skeletal debris
7	Intraclast Floatstone	L3	Limestone	6	Arab-A, B	Floatstone	Gastropods, skeletal debris

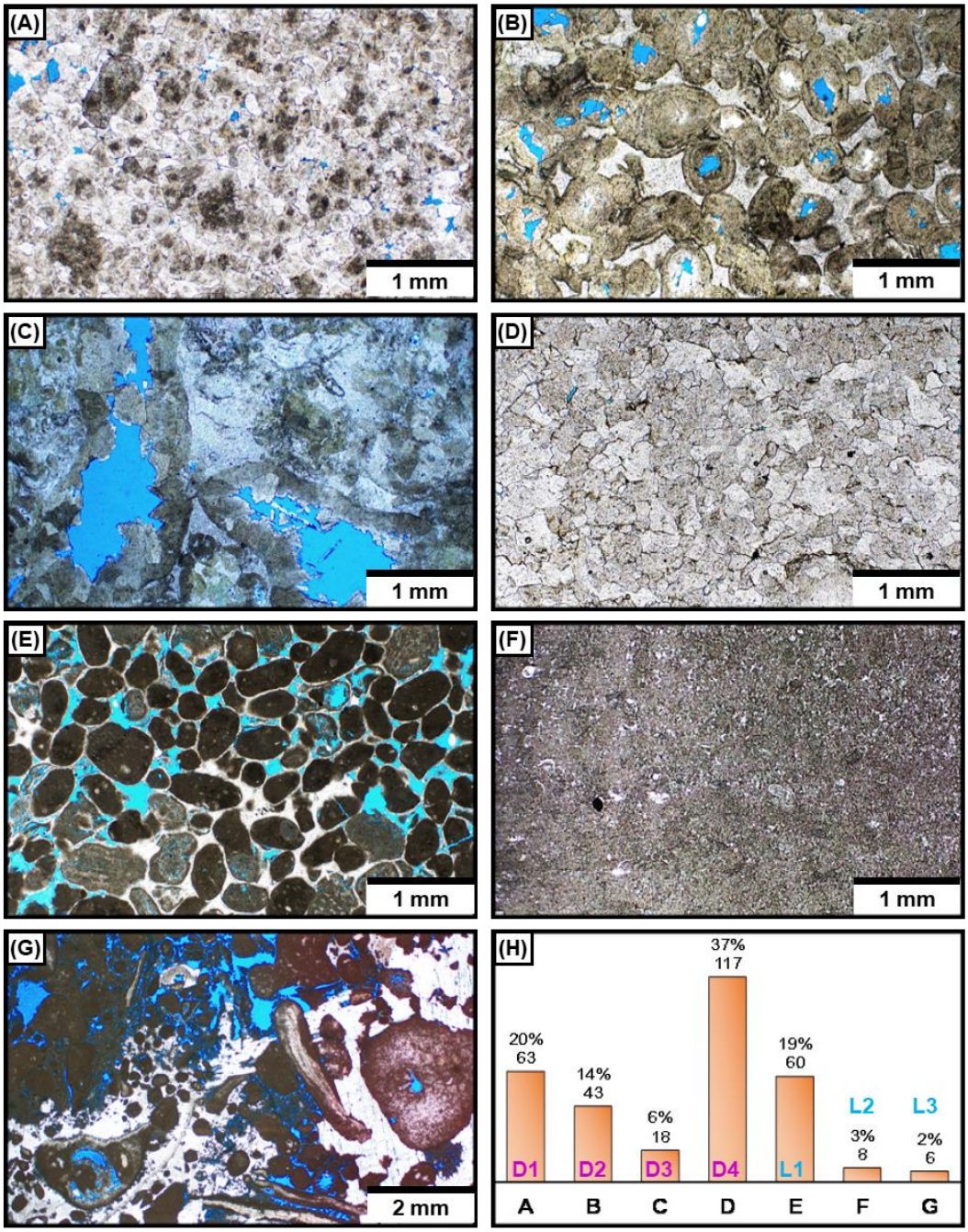

Figure 2.4. Photomicrographs of the four dolostone and three limestone facies encountered in the study. (A) Peloidal-skeletal dolograinstone (Facies D1). (B) Oolitic dolograinstone (D2); this sample is 100% dolomite. (C) Sponge dolorudstone (D3). Note the large molds inside the grain (possibly stromatoporoids); this sample is 100% dolomite. (D) Fabric destructive dolostone (D4). (E) Peloidal-skeletal grainstone (Facies L1; the undolomitized equivalent of facies D1 [A]). (F) Bioclastic wackestone (L2). (G) Intraclast floatstone (L3). (H) A histogram showing the relative abundance of the seven facies.

2.4.3 Dolomite petrography and cathodoluminescence

All dolomites encountered in this study can be classified as either equant (ED, ~60% of all dolomites) or baroque (BD, ~40% of all dolomites). Equant and baroque dolomites intercalate with each other stratigraphically, and regularly occur together in the same thin sections (Figure 2.5A). The two types of dolomites show no obvious relationship to well location, stratigraphic member, or original facies. Rather, ED and BD are in all wells (wells 1 to 6), all stratigraphic members (Arab-D to Arab-A), and in all dolostone facies (D1 to D4). Well 6 (Figures 2.1 and 2.3), the well closest to the KJB fold axis, contains the greatest relative amount of baroque dolomite (~90% of all dolomite is baroque), with baroque dolomite dominating in all samples. Equant dolomite is in some samples in the well, but is cross-cut, and partially replaced by the coarser baroque dolomite. In all wells, both ED and BD are either a replacement (EDR and BDR) or a cement phase (EDC and BDC). All dolomite phases are non-ferroan as they were not stained by potassium ferricyanide.

Replacive equant dolomite (EDR) exhibits mostly a fabric-preserving texture where the original grains and depositional textures are identifiable (Figure 2.5B). Fabric-destructive texture is less common. Medium to coarse (100 to 300 μm) nonplanar (anhedral) crystals dominate EDR. Crystals are interlocking, hydrocarbon-stained, mosaics of relatively uniform dolomite crystals (~200 μm in size; Figures 2.4D and 2.5A). EDR commonly retains the size and overall shape of the grain it has replaced and is typically fluid-inclusion poor, especially in the core of the crystal.

Equant dolomite cement (EDC) is either blocky interparticle/intercrystal cement (Figure 2.4B, C) that filled all or part of the pores or is a cement overgrowth (Figure 2.5C) where small dolomite crystals (~100 μm) overgrew on previously dolomitized grains. The blocky EDC is composed of microcrystalline crystals (<10 μm) and is observed in dolostone samples with well-

preserved original textures, such as the oolitic dolograinstone (Figure 2.4B). The overgrowth EDC is observed in large quantities in the peloidal-skeletal dolograinstone (Figure 2.5C).

Replacive baroque dolomite (BDR) is the most common type of baroque dolomite encountered in the study and it exhibits both fabric-preserving and fabric-destructive textures, with the latter dominating. Unlike the EDR, which replaced individual grains, BDR formed poikilotopic masses that replaced patches of grains and cement (Figure 2.5D, E); thus, the replacement has no relationship to the original fabrics, even though the replacement is fabric preserving. Consequently, the sizes of BDR crystals are much larger than the original grains (Figure 2.5D). BDR crystal sizes range from ~500 μm to over 2000 μm. Most replacive baroque dolomite crystals exhibit anhedral textures and lack the well-defined curved crystal faces, typical of baroque dolomite. The masses of replacive baroque dolomite show sweeping extinction (Figure 2.5E) and are fluid-inclusion rich, leading to a cloudy appearance in thin section.

Baroque dolomite cement (BDC) is a cement overgrowth (Figure 2.6A) and a void-filling cement phase composed of baroque (saddle) crystals (Figures 2.5A and 2.6B). The latter contains the most pristine examples of baroque dolomite, with very large (> 1000 μm), hydrocarbon-free, crystals, that display well-developed curved (saddle) crystal faces and cleavages (Figure 2.6B), and obvious sweeping extinction in cross polarization. This phase is easy to identify in cores, where dolomite crystals are large, milky white in color, and visibly cross-cut older dolomite, in some cases forming zebra fabric. Despite the conspicuous appearance of this dolomite phase, it is the least common phase of all dolomites. This phase is limited to thin (up to 10 cm thick) horizons that cross-cut the more common replacive equant and baroque dolomites.

All four dolomite types (EDR, EDC, BDR, and BDC) are typically unzoned under CL and show a dull luminescence with mottling (Figure 2.7). Despite the relatively prevalent mottling

observed in all dolomite phases, some samples, or areas within samples, display irregular patches of mottled luminescence characterized by areas within crystals and cement with brighter luminescence, commonly near the core of the crystals (Figure 2.7A to F). Partial dissolution was also observed near some bright luminescent areas. Five dolostone samples include a zonation, characterized by dull outer growth zones (or cement overgrowth), which coated some dolomite crystals (Figure 2.7E, F).

Cathodoluminescence petrography was also performed on the minor dolomite cement phase observed in some limestone samples (Figure 2.7G, H). This dolomite cement also shows an unzoned mottled appearance in CL, similar to that observed in the bulk of dolomite in dolostone.

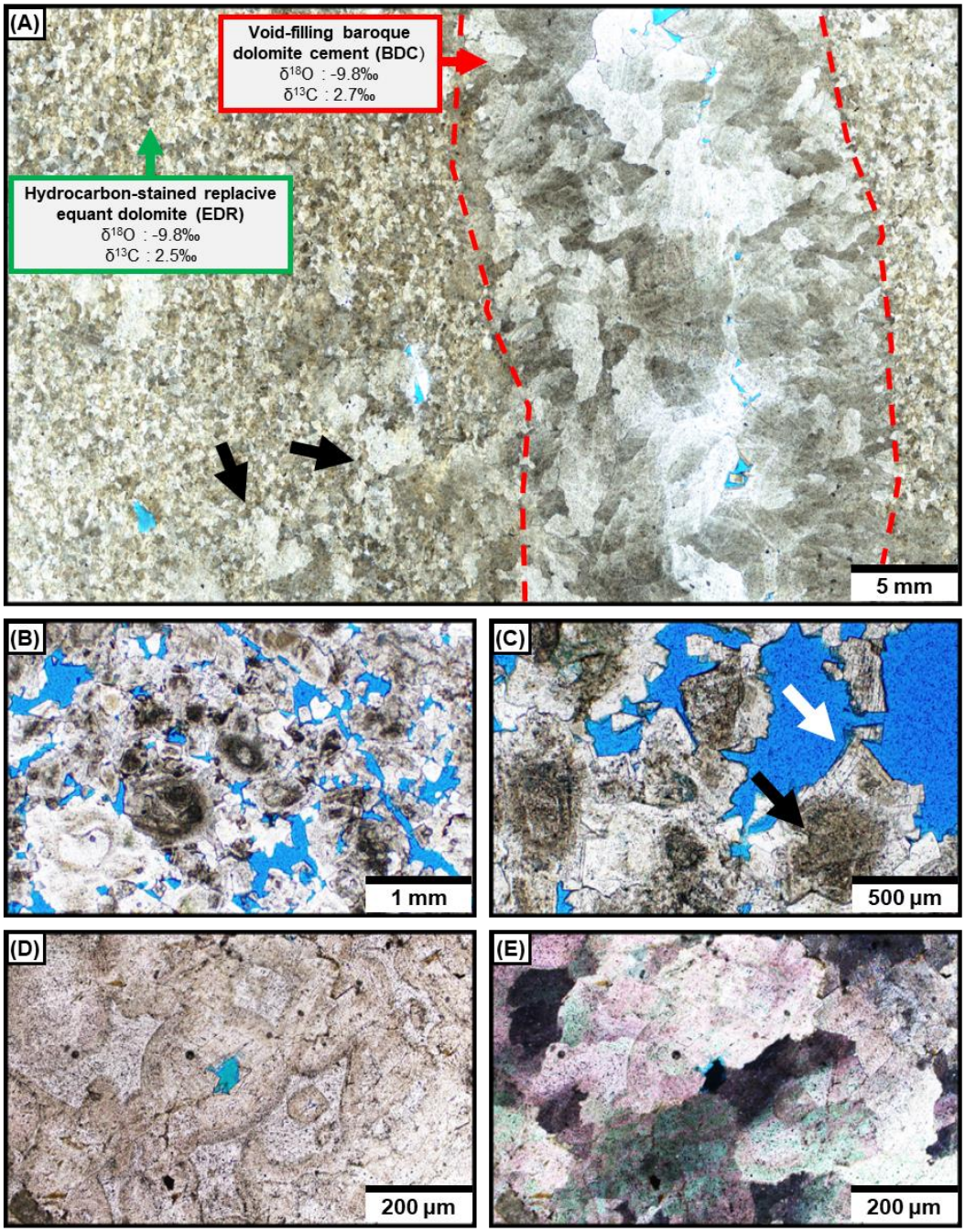

Figure 2.5. Photomicrographs of the different dolomite phases encountered in the study. (A) Full-thin section scan of a fabric-destructive dolostone that includes replacive baroque dolomite (BDR; black arrows), void-filling baroque dolomite cement (BDC; red arrow), and equant replacive dolomite (EDR; green arrow). Despite the cross-cutting relationship, the BDC and EDR phases record nearly identical isotopic values (refer to text and Figure 2.11 for details). (B) Equant replacive dolomite (EDR) in a fabric-preserving dolostone, where hints of peloids are visible. (C) A fabric-preserving dolostone with equant replacive dolomite (EDR; black arrow) and equant cement overgrowth (EDC; white arrow). (D, E) Plane and cross-polarized light images of baroque dolomite replacing patches of grains and cement.

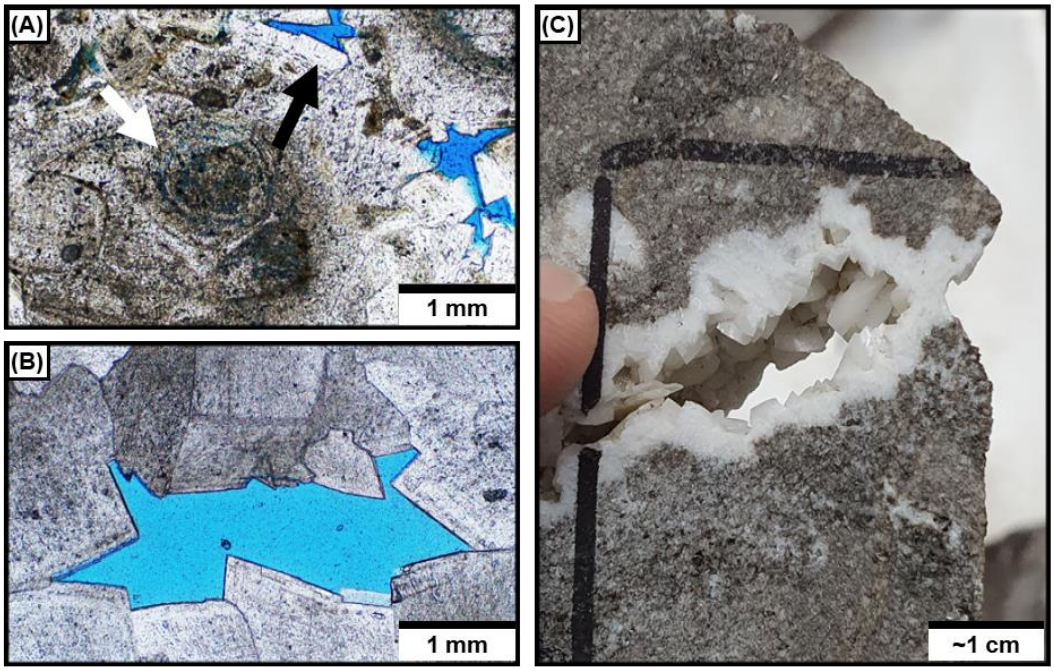

Figure 2.6. Photomicrographs of the different dolomite phases encountered in the study. (A) Replacive baroque dolomite (BDR; white arrow), and baroque dolomite overgrowth (BDC; black arrow). (B) A pristine example of void-filling baroque dolomite cement (BDC). (C) Hand specimen showing a pristine example of void-filling baroque dolomite cement (BDC). Zebra fabrics are also developed locally where BDC occurs.

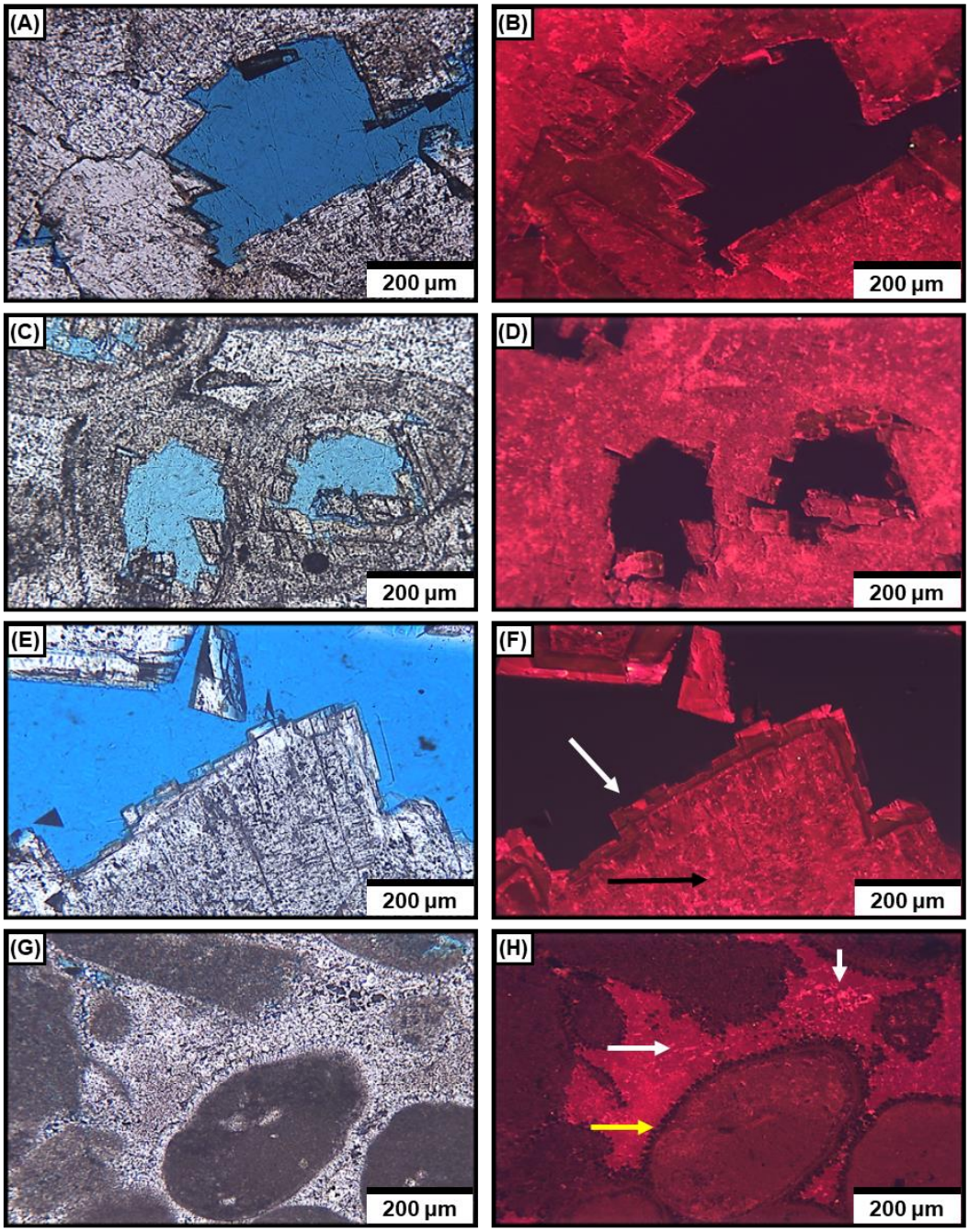

Figure 2.7. Paired plane-light (A, C, D, G) and cathodoluminescence (B, E, F, H) images of different dolomite phases in dolostone and limestone. All dolomite phases lack zonation and show mostly dull CL but with bright spots (mottling). (A, B) Corroded replacive Baroque dolomite with mottled luminescence. (C, D) Fabric-preserving dolostone with mottled luminescence observed in both the dolomitized grains and interparticle cement. (E, F) Baroque dolomite crystal with zonation (white arrow). Mottled luminescence also observed in the inner part of the crystal (black arrow). (G, H) Blocky dolomite cement in a limestone sample (white arrows) showing mottled luminescence. The rim cement is calcite and is showing non-luminescent CL (yellow arrow).

2.4.4 Main diagenetic events and products

Detailed paragenetic analysis that includes the description and interpretation of all diagenetic events observed in the limestones and dolostones is beyond the scope of this work because it focuses on dolomite. The main diagenetic events, however, are covered to help constrain the timing of the dolomite.

The diagenetic history of the carbonates in the area can be grouped into two stages: 1) a predolomitization stage preserved mostly in the limestone; and 2) a post onset of dolomitization stage. Predolomitization diagenesis likely affected all carbonates (limestones and dolostones) but only is retained in the limestone because of extensive dolomitization. Post onset of dolomitization diagenetic events had minimal impact on the undolomitized limestone.

2.4.4.1 *Predolomitization diagenesis*

Although dolomitization was intensive and represents the main diagenetic process that operated in the area, not all limestone has been dolomitized. The limited limestone, observed only in Arab-A and B in wells 1 and 2 (Figures 2.1 and 2.3), has been impacted predominantly by diagenetic processes that occurred prior to the bulk of dolomitization. Predolomitization diagenesis includes micritization of grains, isopachous rim calcite cement (Figure 2.8A), circumgranular rim calcite cement (Figure 2.8B), minor blocky dolomite cement (Figure 2.8C, D), anhydrite cement (Figure 2.8E), displacive anhydrite (Figure 2.8F), and grain dissolution (Figure 2.8G). All these events occurred prior to major compaction. Of these events, cementation by calcite, dolomite, and anhydrite, as well as dissolution are the most widespread events in limestone. Minor events in the

limestone include calcite recrystallization, fractures, stylolization, and replacive anhydrite. Only the main diagenetic events in limestone are addressed below.

Calcite cements occur as either a thick (~30 μm) isopachous cement (Figure 2.8A) or as a thin (5 to 20 μm) equant circumgranular rim cement (Figure 2.8B). The two cements are found together in most limestone thin sections and account for a mean of ~8% of all constituents in the limestone. The isopachous cement is composed mostly of microcrystalline crystals that fully enclosed peloids and pellets while the thinner circumgranular cement only partially enclosed grains. The latter was also observed inside some molds.

Blocky dolomite cement occurs in limestone partially filling some interparticle (Figure 2.8C) and moldic pores (Figure 2.8D). Dolomite cement accounts for ~5% of all constituents in the limestone and was mostly observed in the grainy facies. Anhydrite cement accounts for only ~2% of all constituents in the limestone. It partially fills some interparticle pores (Figure 2.8E), exhibits patchy distribution in thin section, and commonly co-occurs with replacive anhydrite. Displacive anhydrite is limited to muddy facies and occurs as rounded nodules of felted anhydrite crystals that appear to have displaced unlithified mud and sediments (Figure 2.8F).

Dissolution is common in the limestone and forms secondary porosity as molds in peloids and pellets; this was observed in all packstone and grainstone facies, with packstone, in general, containing greater proportions of moldic pores than grainstone (Figure 2.8E, G). Vugs are absent in the limestone, however, five grainstone samples contain small (~300 μm) dissolution-enhanced interparticle pores (Figure 2.8G). Some spalled rim cement crusts were also observed detached from the grains, occurring in most of the grainy limestone samples (Figure 2.8H).

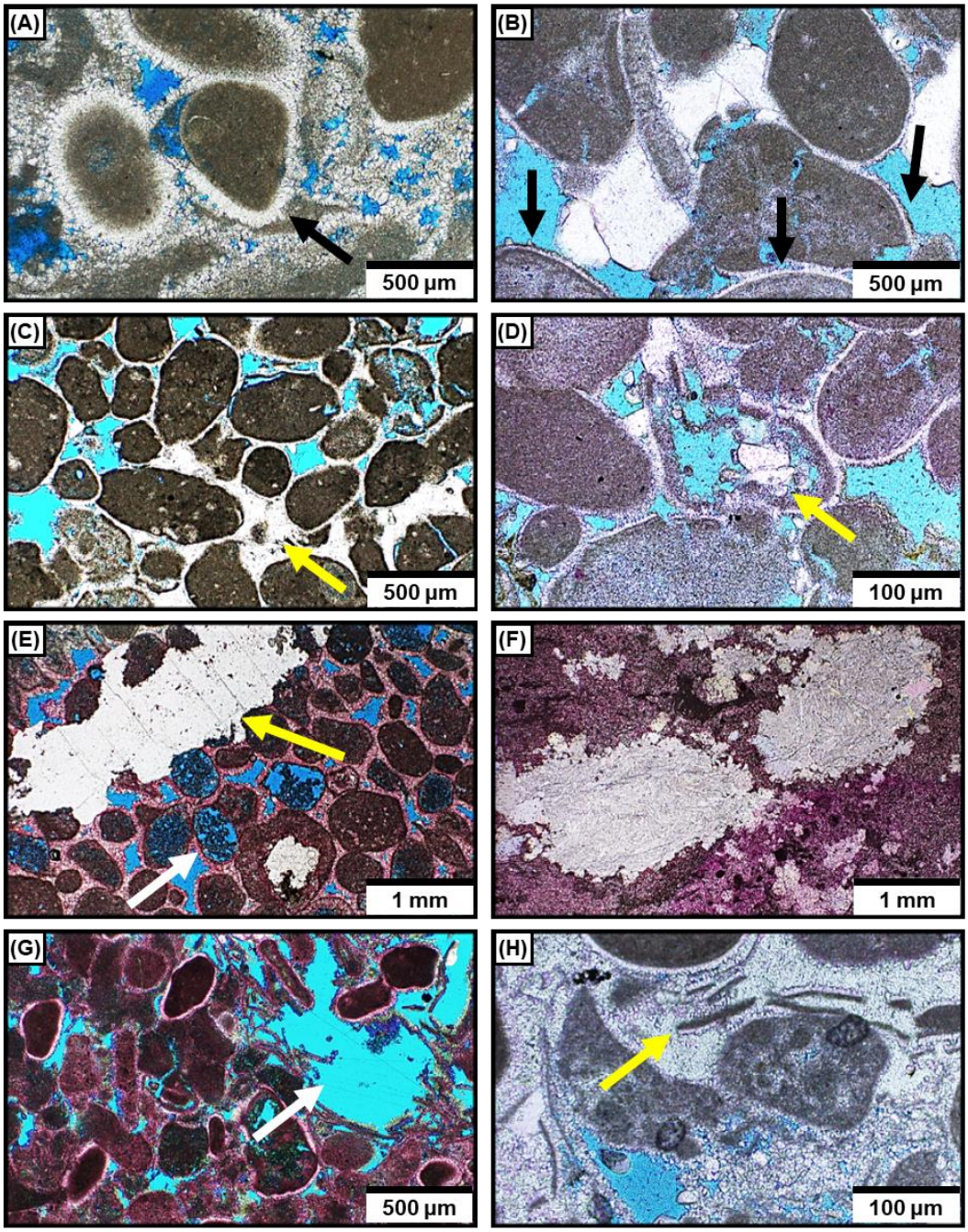

Figure 2.8. Main diagenetic alteration and products in limestone. (A) Thick isopachous rim cement surrounding peloids (arrow). (B) Thin circumgranular cement, composed of one or two calcite crystals (arrows). (C) Minor phase of interparticle dolomite cement (arrow) (see also Figure 2.7G, H for CL image of the same phase). (D) Dolomite cement inside some molds (arrow). (E) Anhydrite crystal (both replacive and cement) observed in a grainstone sample (yellow arrow). Note the molds (white arrow). (F) Large displacive anhydrite nodules composed of small felted anhydrite crystals observed in a wackestone. (G) Dissolution-enhanced interparticle pores observed in a peloidal grainstone sample (arrow). (H) Spalled cement crust (arrow) surrounded by dolomite cement in a limestone sample.

2.4.4.2 *Post onset of dolomitization diagenesis*

The main diagenetic processes and products in dolostones are the replacive equant and baroque dolomites (EDR and BDR) and the equant and baroque cements (EDC and BDC); these dolomite phases represent the bulk of all constituents in the dolostones. Additional diagenetic products and processes also occurred subsequent to the bulk of dolomitization. Dissolution of dolomite and anhydrite are the two main late diagenetic processes observed in the dolostones. Minor diagenetic events in the dolostones include replacive sphalerite, pyrobitumen, localized fractures, and stylolization. Collapse breccia fabric is minor in all wells, but dominant in well 6.

All dolostone samples include open pores that were created or enhanced by dissolution. Those pores range from small (few 10s of microns) isolated moldic pores found mostly within the masses of dolomite crystals and characterized by rounded shapes (Figure 2.9A), to large (up to 1 cm) vuggy pores (Figure 2.9B). The vuggy pores are only observed in the dolostone and not in the limestone. The dissolution-related pores are either fabric selective (e.g., moldic pores within dolomitized ooids; Figure 2.4B) or non-fabric selective (e.g., large vugs cross-cutting multiple dolomite phases; Figure 2.9B). Some moldic pores are formed in anhydrite (Figure 2.9C). Some vuggy pores cross-cut stylolites (Figure 2.9D), and are in close proximity to stylolite seams. The majority of baroque dolomite crystals also show some etching on the outermost surface (Figure 2.9E).

Anhydrite occurs as a cement and a replacement phase, with the former varying between 0 and 20% (mean: 2.9%) and occurring mostly as rounded or felted pore-filling masses. Replacive anhydrite that replaced older dolomite is also common and accounts for similar percentages to the cement; in most cases, both anhydrite phases co-occur in the same samples (Figure 2.9F). In many instances, it was difficult to conclusively determine the nature of the anhydrite as it appears

replacive when in contact with crystals but also to be pore-filling when near pore spaces (Figure 2.9F). The replacive anhydrite crystals cross-cut baroque dolomite crystals in some areas but also were themselves cross-cut by younger dolomite crystals; such relationships were observed in all dolostone facies.

Finally, collapse breccia fabrics are observed in all wells but are dominant in well 6. Most dolostone thin sections in this well contain multi-directional fracturing and capture some of these large-scale fabrics. Figure 2.9G, H shows examples of this fabric in well 6, the well nearest to the KJB fold.

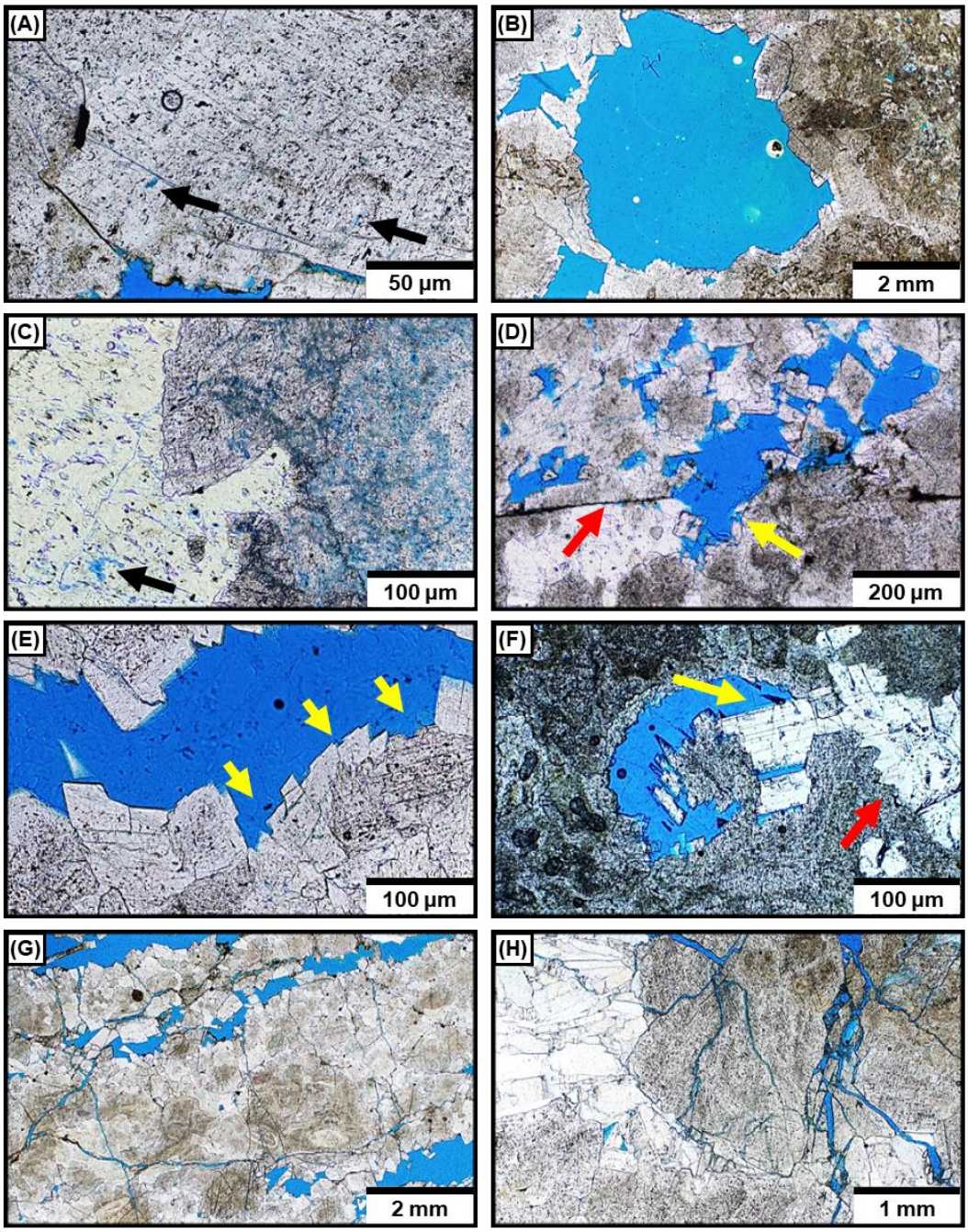

Figure 2.9. Main diagenetic alteration and products in dolostone. (A) Small moldic pores within baroque dolomite crystal (arrows). (B) Large vuggy pores observed in fabric-destructive dolostone sample. (C) Small moldic pores within a burial anhydrite phase observed in dolostone, these molds are a few microns to a few 10s of µm in size. (D) Vuggy pore (yellow arrow) cross-cutting stylolite seam (red arrow). (E) Corroded baroque dolomite crystals, indicating some etching of baroque dolomite (arrows). (F) Replacive (red arrow) and pore-filling anhydrites (yellow arrow) replacing some dolomite and filling secondary pores in an oolitic dolograinstone sample [Facies D2]. (G, H) Examples of collapse breccia from the dolostone in well 6.

2.4.5 Geochemical analysis

2.4.5.1 *Stable isotope analysis*

Oxygen ($\delta^{18}O$) and carbon ($\delta^{13}C$) isotope analyses were performed on 220 dolostone, 29 limestone, and 5 dolomite cement samples in limestone to elucidate the origin of the different lithologies and different dolomite phases (Table 2.2; Figure 2.10). Oxygen isotope ($\delta^{18}O$) values in limestone (n = 29) range from -6.3‰ to -3.5‰ (mean: -5.0‰) and carbon isotope ($\delta^{13}C$) values range from 0.1‰ to 2.8‰ (mean: 2.2‰; Figure 2.10A). The $\delta^{18}O$ values in dolostone samples (n = 220) have a wider range and more negative $\delta^{18}O$ values than the limestones, but a relatively similar $\delta^{13}C$ range. The $\delta^{18}O$ values in dolostone vary from -10.0‰ to -2.7‰ (mean: -7.4‰) and $\delta^{13}C$ values vary between 0.4‰ and 3.5‰ (mean: 2.3‰); the latter overlapped with the majority of the limestone $\delta^{13}C$ values. Despite the range in $\delta^{18}O$ values in limestones and dolostones, all values are more negative than those expected for Late Jurassic normal marine dolomites and calcites (Land, 1980; Veizer et al., 1999; Figure 2.10A). The five isotopic analyses on dolomite cement in limestone mostly overlapped those of the host limestone (Figure 2.10A), and are substantially less negative than the dolomite in the dolostones in the same well (well 2).

The ranges observed in the dolostone isotopic values varies as a function of well, with wells 1 and 2, the southernmost wells, recording the most negative $\delta^{18}O$ and most positive $\delta^{13}C$ values in all dolostones (Figure 2.10B; Table 2.2). On the other hand, wells 5 and 6, the northernmost wells, record the least negative $\delta^{18}O$ and least positive $\delta^{13}C$ values (Figure 2.10B; Table 2.2). The isotopic values also exhibit a spatially progressively decreasing range within each well, with well 6 showing the most widespread $\delta^{18}O$ values (minimum: -6.3‰, maximum: -3.0‰, a range of 3.3‰; Figure 2.10B; Table 2.2).

Equant and baroque dolomites record nearly identical isotopic values. Equant dolomite (n = 138) has mean $\delta^{18}O$ and $\delta^{13}C$ values of -7.5 and 2.4‰, respectively, while baroque dolomite (n = 82) has mean $\delta^{18}O$ and $\delta^{13}C$ values of -7.4 and 2.2‰, respectively (Table 2.2). The four dolomite phases (replacive equant and equant cement, and replacive baroque and baroque cement) record slightly different $\delta^{18}O$ isotopic ranges and means but relatively similar $\delta^{13}C$ ranges and means (Figure 2.10C; Table 2.2). The replacive equant and baroque dolomite phases (EDR and BDR), record slightly less negative $\delta^{18}O$ values (means: -7.2 and -7.1‰, respectively) than those in the cement phases (EDC and BDC, means: -8.4 and -8.8‰, respectively). On the other hand, the $\delta^{13}C$ values for all dolomite phases are essentially identical (means range from 2.2 to 2.6‰). Despite the narrow range, the overall isotopic compositions of the different dolomite phases overlap in the $\delta^{13}C$–$\delta^{18}O$ space, especially when normalized by well (Figure 2.10D). Plotting the isotopic data by well appears to be necessary as there appears to be a spatial control on isotopic values.

The most striking observation, however, is that in any one rock sample, the $\delta^{18}O$ and $\delta^{13}C$ values for all dolomite phases are almost identical, regardless of cross-cutting relationship. For example, in a dolostone sample from well 1, EDR was cross-cut by a later void-filling BDC phase (Figure 2.5A), yet, the two dolomite phases record almost identical isotopic values, despite the obvious morphological and relative time of formation differences. The same is also true for other dolomite phases, where EDR, BDR, EDC, and BDC, consistently record nearly identical isotopic values to each other in any one sample.

Table 2.2: Stable Isotope Statistics

		$\delta^{13}C$ (‰ VPDB)			$\delta^{18}O$ (‰ VPDB)		
Group	**Count**	**Min**	**Max**	**Mean**	**Min**	**Max**	**Mean**
All Dolostones	**220**	**0.4**	**3.5**	**2.3**	**-10.0**	**-2.7**	**-7.4**
Well 1	17	2.5	3.1	2.7	-10.0	-9.4	-9.8
Well 2	**61**	**2.5**	**3.5**	**2.8**	**-10.0**	**-8.0**	**-9.1**
2. EDR	*15*	*2.6*	*3.5*	*3.0*	*-10.0*	*-8.6*	*-9.3*
2. EDC	*19*	*2.5*	*2.9*	*2.7*	*-9.3*	*-8.6*	*-9.0*
2. BDR	*22*	*2.6*	*2.9*	*2.7*	*-9.8*	*-8.0*	*-9.0*
2. BDC	*5*	*2.6*	*3.1*	*2.9*	*-9.5*	*-9.0*	*-9.3*
Well 3	15	1.9	2.3	2.1	-7.3	-5.9	-6.7
Well 4	94	1.4	3.1	2.4	-8.0	-5.7	-7.1
Well 5	11	1.3	1.8	1.6	-4.5	-2.7	-3.7
Well 6	22	0.4	1.7	1.3	-6.3	-3.0	-5.1
All Equant Dolomite (ED)	**138**	**0.4**	**3.5**	**2.4**	**-10.0**	**-2.7**	**-7.5**
All Equant Replacive (EDR)	113	0.4	3.5	2.4	-10.0	-2.7	-7.2
All Equant Cement (EDC)	25	1.4	2.9	2.4	-9.3	-6.4	-8.4
All Baroque Dolomite (BD)	**82**	**0.6**	**3.1**	**2.2**	**-10.0**	**-2.7**	**-7.4**
All Baroque Replacive (BDR)	67	0.6	3.1	2.2	-9.9	-2.7	-7.1
All Baroque Cement (BDC)	15	1.7	3.1	2.6	-10.0	-5.8	-8.8
All Limestones	**29**	**0.1**	**2.8**	**2.2**	**-6.3**	**-3.5**	**-5.0**
Well 1	12	0.9	2.7	2.2	-6.2	-4.1	-5.1
Well 2	17	0.1	2.8	2.0	-6.3	-3.5	-4.9
Dolomite Cement in Limestone	5	2.5	2.7	2.6	-4.9	-3.8	-4.5

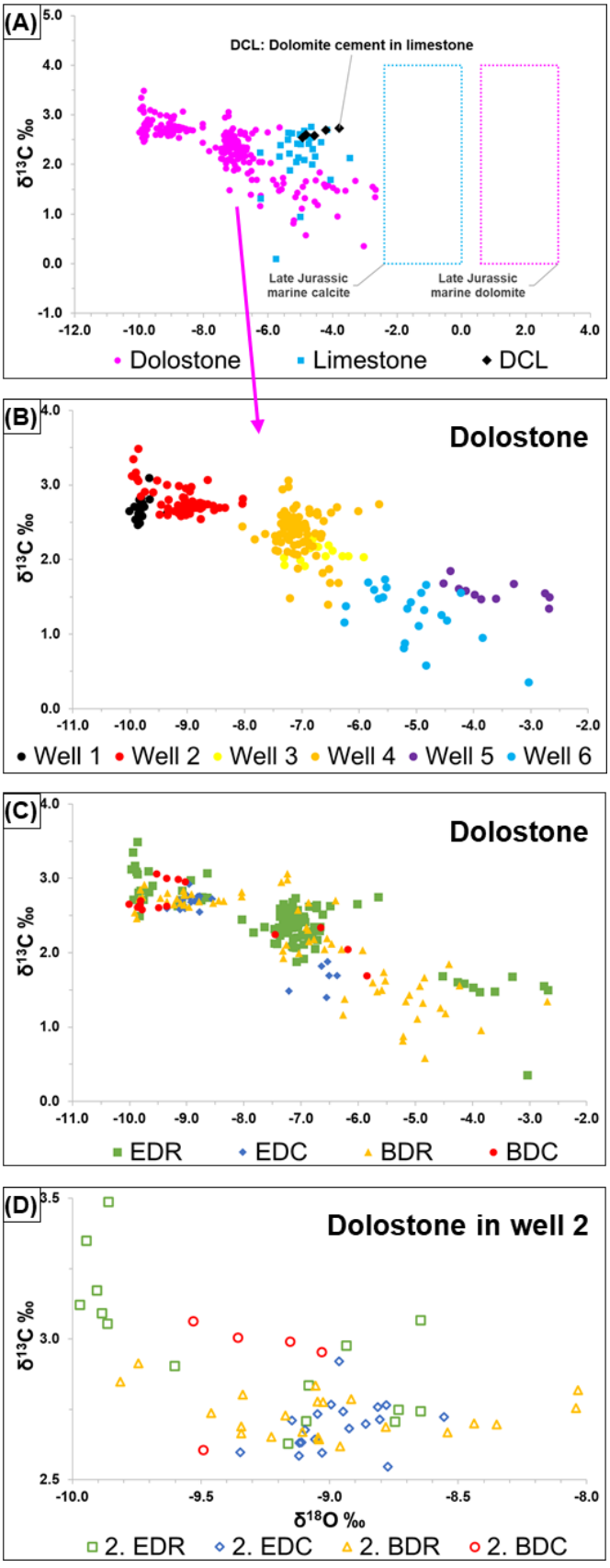

Figure 2.10. Carbon and oxygen stable isotope cross plots for dolostone and limestone and for the different dolomite phases. (A) Carbon isotope ($\delta^{13}C$) vs oxygen isotope ($\delta^{18}O$) cross plot of dolostone, limestone, and dolomite cement in limestone. Both lithologies plot outside the range expected for Late Jurassic marine calcite and dolomite (Veizer et al. 1999); the dolomite value is based on the fractionation value given by Land (1980). Note all limestone samples are from wells 1 and 2 (see Figure 2.3). (B) Dolostone data coded for wells. Note the trend from well 6 (least positive $\delta^{13}C$ and least negative $\delta^{18}O$ values) to wells 1 and 2 (most positive $\delta^{13}C$ and most negative $\delta^{18}O$ values). (C) Dolostone data coded for the four dolomite phases. Note the overlap and lack of separation between the isotopic values for the different dolomite phases. (D) Dolostone data coded for the four dolomite phases for one well (well 2). Similar to (C), the four dolomite phases overlap each other in the carbon vs oxygen stable isotope space.

EDR = Equant dolomite (replacive), EDC = Equant dolomite (cement), BDR = Baroque dolomite (replacive), and BDC = Baroque dolomite (cement).

2.4.5.2 *Fluid inclusion petrography and microthermometry*

Two-phase (aqueous-vapor) fluid inclusions were observed in all dolostone samples and in all dolomite phases. Two-phase fluid inclusions were also observed within the mostly dull luminescent CL and mottled luminescent with bright CL parts of the crystal. Within any one thin section, however, dolomite contains both fluid inclusion-rich and fluid inclusion-poor crystals. The majority of fluid inclusions are encountered in the outer growth zone of dolomite crystals. Zones with sparse fluid inclusions were also observed in the inner part of baroque dolomite crystals, in dolomite cements, and in replacive rhombic dolomite crystals. All fluid inclusions analyzed are primary inclusions, with their distribution constrained by growth zones (Figure 2.11A, B). Secondary and pseudosecondary fluid inclusions were not observed in the dolostones. Fluid inclusion sizes range from ~5 μm to ~30 μm (Figure 2.11A, B), with a consistent 1:10 bubble to inclusion ratio. Calcite cements in the limestone lack fluid inclusions; thus, microthermometry measurements were not possible. Thirty-seven fluid inclusion assemblages (FIAs) from four wells (1, 2, 4 and 6) represent all the data (Figure 2.11C, D). For every FIA defined here, >90% of the Th values are within 10–15ºC, fitting the requirements for a consistent FIA. These are typically regarded as FIAs that have not been altered by thermal re-equilibration (Goldstein and Reynolds, 1994). The FIAs show a range in both homogenization temperatures Th and melting temperatures of ice Tm, with FIAs in wells 1 and 2 recording the highest means of Th and Tm_{ice} (Figure 2.11C). There is also a wide range of Th and Tm_{ice} within individual FIAs. One FIA in a baroque dolomite crystal, for example, records a Th range from 83.5ºC to 114ºC, a range of ~30ºC. Another FIA in an equant dolomite records Th range from 92ºC to 117ºC, a range of ~25ºC. Such observations occur in all wells and all dolomite phases, and highlights that while mean Th and Tm_{ice} values

show minimal changes, individual FIAs capture a wide set of temperatures. These observations will be discussed in detail in Chapter 3 of this Dissertation.

As a whole, homogenization temperatures (Th) in dolostones (total n = 337 analysis) average 100.4ºC, with a range from 75.2ºC to 117.1ºC (Figure 2.12A; Table 2.3). Despite the range in Th, ~90% of all the measurements are between 90ºC and 110ºC, and the lowest homogenization temperatures (75.2ºC to 85.0ºC) are almost exclusively encountered in well 6, the northernmost well (also the well with the least negative $\delta^{18}O$ values; Figure 2.10B). Melting temperatures of ice (Tm_{ice}; n = 222 analysis) average -22.9ºC (equates to a salinity of 24.3 wt.% NaCl equivalent) (Bodnar, 1992) with a range from -27.9ºC to -17.5ºC (i.e., salinities from 27.4 to 20.6 wt.% NaCl eq.; ~6 to 8 times more saline than present-day normal marine seawater; Figure 2.12A). The Th and salinity ranges reported above are considered very narrow in comparison to many high-temperature carbonate systems, which often record wider ranges of temperatures (Davies and Smith, 2006).

Similar to the spatial trend observed in the stable isotope data, both homogenization temperatures and salinity vary as a function of well, with wells 1 and 2, the southernmost wells (Figures 2.1 and 2.3), recording the highest means of Th and salinity (Th means: 102.2ºC and 103.8ºC, and salinity means: 25.1 and 25.1 wt.% NaCl eq. for wells 1 and 2, respectively, Figure 2.12 A). Well 6, on the other hand, records the lowest Th and second lowest salinity values (means: 82.5ºC and 22.3 wt.% NaCl eq. for Th and salinity, respectively; Figure 2.12A; Table 2.3).

Equant and baroque dolomites, in general, record very similar fluid inclusion values. Equant dolomite (n = 212) has mean Th and salinity values of 101.6ºC and 24.8 wt.% NaCl eq., respectively, while baroque dolomite (n = 125) has mean Th and salinity values of 98.3ºC and 23.4 wt.% NaCl eq., respectively (Table 2.3). The four dolomite phases (EDR, EDC, BDR, BDC) also

only exhibit little variation, with the cement phases (EDC and BDC) recording higher homogenization temperatures (means: 104.1ºC and 100.8ºC, respectively; Figure 2.12B; Table 2.3) than the replacement phases (EDR and BDR, means: 98.6ºC and 97.0ºC, respectively). Salinity values are comparable for the EDR, EDC, and BDC (mean salinities ~25.0 wt.% NaCl eq.; Figure 2.12B; Table 2.3) but are slightly lower for the BDR phase (mean: ~23.0 wt.% NaCl eq.). The differences in Th and salinity means between the dolomite phases is not major, however. The variation in relative abundance of different dolomite phases within each well also contributes to the slight variation in Th and salinity observed. For example, well 6, contains only EDR and BDR, with no cement, and it records the lowest Th overall.

Because there appears to be a spatial control on both Th and Tm_{ice} in dolostones, such that the baselines of the microthermometry values vary as a function of wells, we plotted the different dolomite phases observed in one well separately. Figure 2.12C shows a great overlap in the Th and Tm_{ice} values for the different dolomite phases when shown for a single well. Meaning, the four dolomite phases (EDR, EDC, BDR, and BDC) record similar temperature of homogenization and melting temperature of ice within the same well (Table 2.3).

Table 2.3: Fluid Inclusion Statistics

	Th (ºc)				Tm_{ice} (ºc)				Salinity (%)		
Group	**Count**	**Min**	**Max**	**Mean**	**Count**	**Min**	**Max**	**Mean**	**Min**	**Max**	**Mean**
All Dolostones	**337**	**75.2**	**117.1**	**100.4**	**222**	**-27.9**	**-17.5**	**-22.9**	**20.6**	**27.4**	**24.3**
Well 1	37	97.5	111.5	102.2	20	-25.0	-23.7	-24.2	24.8	25.6	25.1
Well 2	**222**	**83.5**	**117.1**	**103.8**	**143**	**-27.9**	**-19.9**	**-24.2**	**22.3**	**27.4**	**25.1**
2. EDR	*40*	*95.1*	*112.3*	*103.2*	*33*	*-27.0*	*-20.5*	*-24.2*	*22.7*	*26.8*	*25.1*
2. EDC	*118*	*91.8*	*117.1*	*104.1*	*70*	*-27.9*	*-20.2*	*-24.3*	*22.5*	*27.4*	*25.1*
2. BDR	*33*	*93.3*	*117.0*	*103.4*	*19*	*-25.5*	*-19.9*	*-23.6*	*22.3*	*25.9*	*24.7*
2. BDC	*31*	*83.5*	*114.2*	*103.8*	*21*	*-26.5*	*-23.8*	*-24.8*	*24.8*	*26.5*	*25.4*
Well 4	48	90.0	99.9	94.5	37	-20.3	-17.5	-19.1	20.6	22.6	21.7
Well 6	30	75.2	90.8	82.5	22	-22.1	-18.0	-20.0	21.0	23.8	22.3
All Equant Dolomite (ED)	**212**	**77.5**	**117.1**	**101.6**	**135**	**-27.9**	**-17.5**	**-23.8**	**20.6**	**27.4**	**24.8**
All Equant Replacive (EDR)	94	77.5	112.3	98.6	65	-27.0	-17.5	-23.3	20.6	26.8	24.5
All Equant Cement (EDC)	118	91.8	117.1	104.1	70	-27.9	-20.2	-24.3	22.5	27.4	25.1
All Baroque Dolomite (BD)	**125**	**75.2**	**117.0**	**98.3**	**87**	**-26.5**	**-17.9**	**-21.6**	**20.9**	**26.5**	**23.4**
All Baroque Replacive (BDR)	83	75.2	117.0	97.0	61	-25.5	-17.9	-20.7	20.9	25.9	22.8
All Baroque Cement (BDC)	42	83.5	114.2	100.8	26	-26.5	-18.5	-23.7	21.3	26.5	24.7

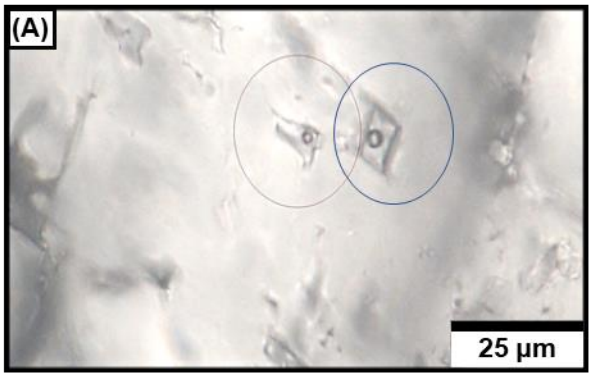

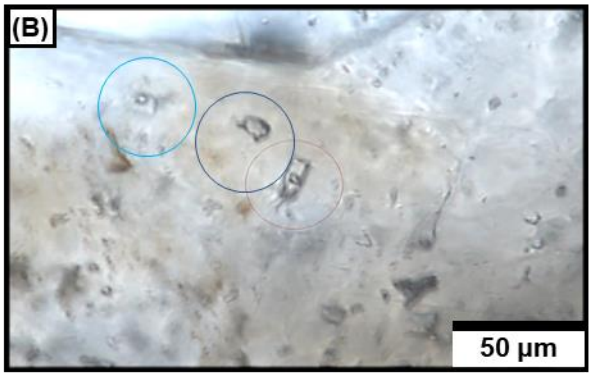

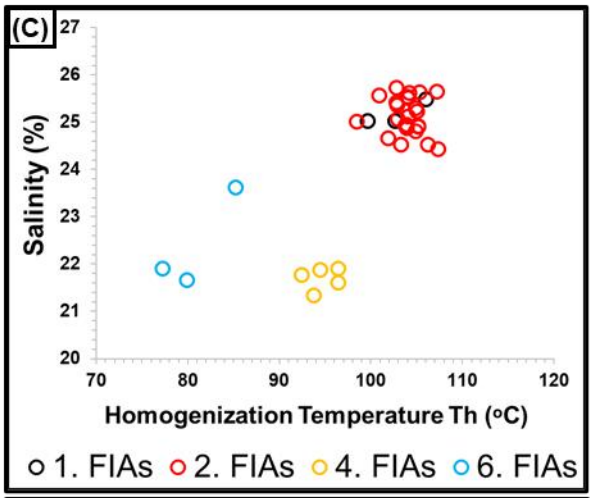

(D)

Well	1	2	4	6
No FIA	4	25	5	3
Min Th	99.6	98.5	92.4	77.2
Max Th	106	107.3	96.4	85.2
Min Salinity	25	24.4	21.3	21.7
Max Salinity	25.5	25.7	21.9	23.6

Figure 2.11. (A, B) Examples of two-phase fluid inclusions in primary growth zones in dolostone. (C) Salinity (wt. % NaCl eq.) vs homogenization temperature (Th) for fluid inclusion assemblages (FIAs) in dolostones from four wells. Each circle is a mean value for the FIA. Note how FIAs in wells 1 and 2 show higher temperatures and salinities than wells 4 and 6. (D) Summary table of the data in (C), showing the number of FIAs per well and the minimum and maximum values of Th and salinity per FIA.

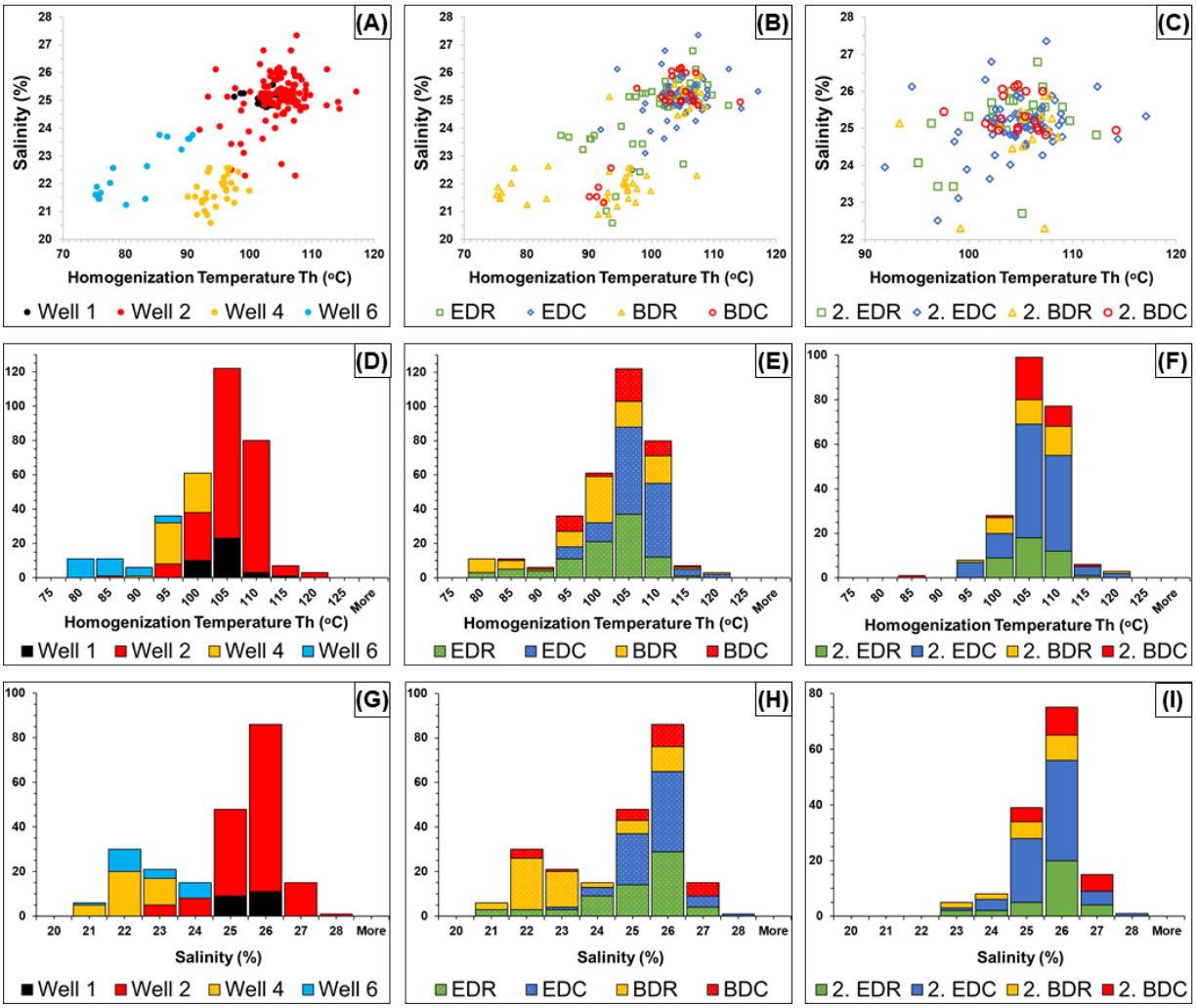

Figure 2.12. Fluid inclusion data for dolostone. (A, B, C) Salinity (wt. % NaCl eq.) vs homogenization temperature (Th) for dolostones, (A) coded for wells (B) coded for dolomite phases and (C) coded for dolomite phases in well 2. Note the spatial trend in salinity and Th observed in (A) where salinity and Th are highest in wells 1 and 2 (southernmost wells), and lowest in well 6 (northernmost well). (B, C) Salinity vs Th for the different dolomite phases as a whole in (C) and in well 2 (D). Note the overlap in salinity and Th for the different dolomite phases as a whole and for dolomite phases in well 2. (D, E, F) Homogenization temperature histograms for the same date as in (A, B, C). (G, H, I) Salinity (wt. % NaCl eq.) for the same data in (A, B, C).

EDR = Equant dolomite (replacive), EDC = Equant dolomite (cement), BDR = Baroque dolomite (replacive), and BDC = Baroque dolomite (cement).

2.4.5.3 *Strontium isotope ratio ($^{87}Sr/^{86}Sr$)*

Strontium isotope measurements of 15 whole-rock samples (10 dolostones, 3 limestones, and two anhydrite) were obtained to elucidate the origin of the dolostone, limestone, and anhydrite. Strontium isotope ratios ($^{87}Sr/^{86}Sr$) in dolostone range between 0.70761 and 0.70787, which are noticeably higher values than those of Late Jurassic seawater (McArthur et al., 2012; Figure 2.13). Limestone and anhydrite samples record values between 0.70701 and 0.70714, which are within the Late Jurassic seawater values (McArthur et al., 2012; Figure 2.13). Because the analysis required a large sample size, it was not possible to sample for individual dolomite phases and the 10 dolostone samples may have included multiple dolomite phases. The analysis was run on samples from multiple wells, however. The spatial trends observed in the isotopic and fluid inclusion data, where values vary as function of wells, are not evident with respect of $^{87}Sr/^{86}Sr$, as the different wells record comparable $^{87}Sr/^{86}Sr$ values (Figure 2.13).

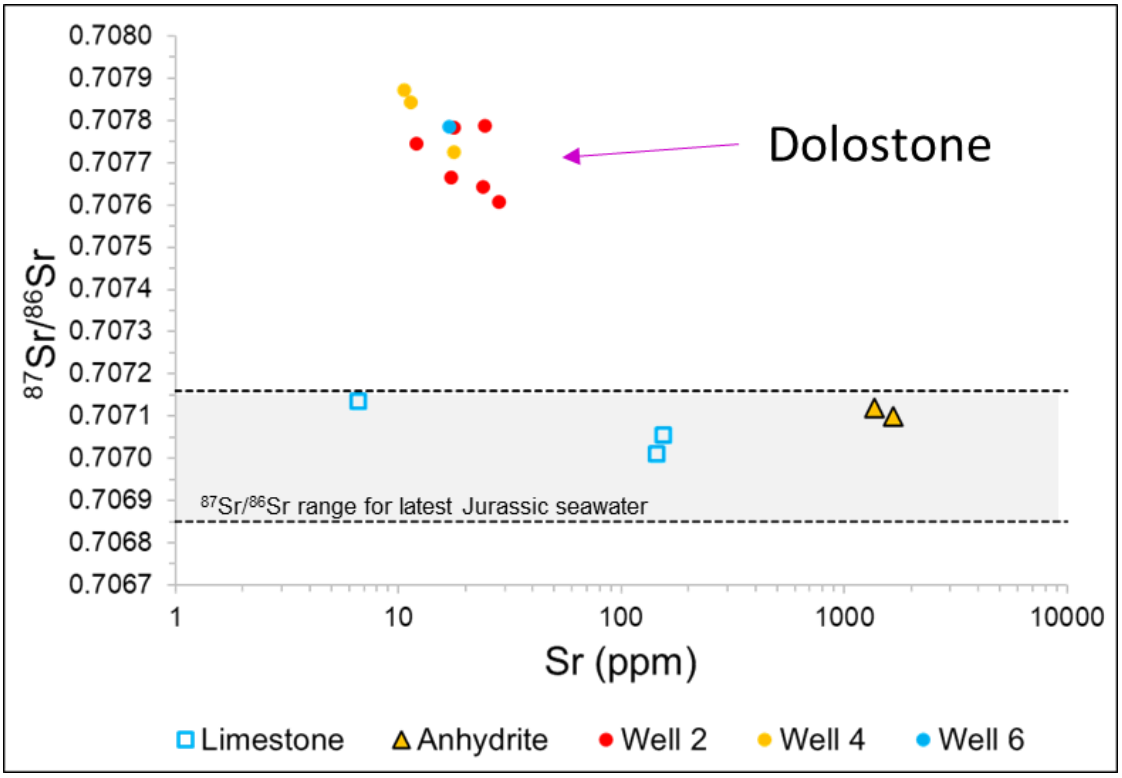

Figure 2.13. Strontium isotope ratio ($^{87}Sr/^{86}Sr$) vs Sr concentration (ppm) for ten dolostone, three limestone, and two anhydrite samples. Limestone and anhydrite samples fall within the range expected for Late Jurassic seawater (shaded area between two black dashed lines; McArthur et al., 2012). The dolostones record much higher $^{87}Sr/^{86}Sr$ values than those expected for Late Jurassic seawater, indicating either a radiogenic influence or formation from seawater-derived fluid of a younger age.

2.4.5.4 *Uranium–lead (U–Pb) dating*

Uranium–lead dating was performed on 10 (9 dolostones and 1 limestone) samples to constrain the timing of dolomitization/recrystallization in dolostone, as well as the timing of formation for different diagenetic phases in the limestone. For each sample, about 80 spots were selected for laser ablation and included multiple dolomite phases/crystals. Examples of a laser ablation run in a baroque dolomite crystal from a sample in well 6 is shown in Figure 2.14A, B. A Tera–Wasserburg Concordia diagram was plotted for an individual textural domain, which includes multiple laser spots and variable $^{238}U/^{206}Pb$ and $^{207}Pb/^{206}Pb$ values defining an array with

a lower Concordia intercept that can be interpreted as an age (Figure 2.14C). For the dolostones, a total of 55 dolomite phases/crystals were dated of which 44 (80% of the analyses) produced reliable ages (Figure 2.14D; Table 2.4). All dates obtained in the dolostones are shown in Figure 2.14D and are sorted by well, and by age, from youngest to oldest. As a whole, dolomite has a mean age of 36.0 ± 7.8 Ma, with a range from 58.0 ± 6.5 Ma to 11.9 ± 2.4 Ma to. The uncertainty (error) also varies in the measurements, with percentages of error ranging from 4.6% to 58.3%; the latter means a very wide range of possible ages. Obviously, the higher the degree of uncertainty of the calculated date, the less meaningful the age. An example of that is sample 520 in well 2, where the U–Pb age of a replacive baroque dolomite crystal yields an age of 47.2 ± 27.5 Ma (meaning a possible age range from 19.7 to 74.7 Ma). While this age is not necessarily invalid, the wide range means this dolomite phase could have formed anywhere from Late Cretaceous to early Miocene, rendering it a less meaningful datapoint when trying to constrain the dolomite timing. To ensure consistency, all values are reported in Table 2.4 along with their error percentage. For this study, we will rely on U–Pb dating measurements with an uncertainty of 25% or less; this will ensure the dates reflect usable ages that can be tied to geological events that might have happened in the region. The 25% cutoff value is subjective but seems a reasonable value considering the range in U–Pb dates obtained in this study.

Similar to both stable isotope and fluid inclusion data, the U–Pb ages show a relationship to well location. Well 6, contains a dolomite phase (EDR) that records the oldest age of all dolomite in all wells (age: 58.0 ± 6.5 Ma; Figure 2.14D; Table 2.4). Mean age for all dolomites in well 6 is also the oldest (mean: 47.5 ± 7.3 Ma). Recall, this well, the northernmost well, and the closest to the fold axis, also records the least negative $\delta^{18}O$ values, the least positive $\delta^{13}C$ values, and the lowest Th and salinities. The dolomite in wells 1 and 2 record mean ages of 29.4 ± 3.6 Ma and

30.6 ± 9.7 Ma, respectively. Well 1 also includes the youngest recorded dolomite in any well (age: 11.9 ± 2.4 Ma). Collectively, dolomite, on average, records older ages to the north, and younger ages to the south of the study area. This change in mean values, however, is mostly controlled by the younger dolomites. Essentially all wells record comparable upper limit of ages (ages from 58.0 ± 6.5 Ma to 52.8 ± 8.7 Ma). The main difference between wells is that wells 1 and 2 include multiple dolomite analyses with younger ages (ages < 30 Ma), whereas wells 4 and 6 do not include any dolomites with an age younger than 37.2 ± 6.8 Ma. Compared to fluid inclusion and stable isotope data, U–Pb dating displays a wide range of dolomite ages within any one sample (Table 2.4), which does not match stable isotope or fluid inclusion data, both of which record narrower, or even identical values, for different dolomite phases within the same sample.

The four dolomite phases also display variable ages, with the replacive phases (EDR and BDR) recording slightly older ages than the cement phases (EDC and BDC) (Table 2.4). The four dolomite phases also record slightly variable ages within the same sample. For instance, a baroque dolomite cement (BDC) phase in a dolostone sample from well 6 recorded an age of 37.2 ± 6.7 Ma, compared to an age of 46.6 ± 2.7 Ma for a replacive baroque dolomite (BDR) phase, in the same sample. Similarly, a rare BDC in a sample from well 1 recorded an age of 11.9 ± 2.4 Ma, while BDR, in the same sample, recorded an age of 52.8 ± 8.2 Ma, a range of ~41.0 million years between two dolomite phases in the same thin section (Table 2.4). These age variations, commonly occurring within the same rock sample, highlight the spread of U–Pb ages for the different dolomite phases.

The limestone sample also yielded reliable dates on all measurements (5/5 groups are interpretable). In the limestone sample, three phases were age-dated: (1) undolomitized peloids; (2) undolomitized mud lumps; and (3) patchy interparticle nonbaroque dolomite cement. The

undolomitized mud lump and peloids yielded ages of 139.6 ± 5.7 Ma to 111.1 ± 11.1 Ma, respectively, while the dolomite cement records ages from 128.9 ± 19.2 Ma to 112.1 ± 5.8 Ma.

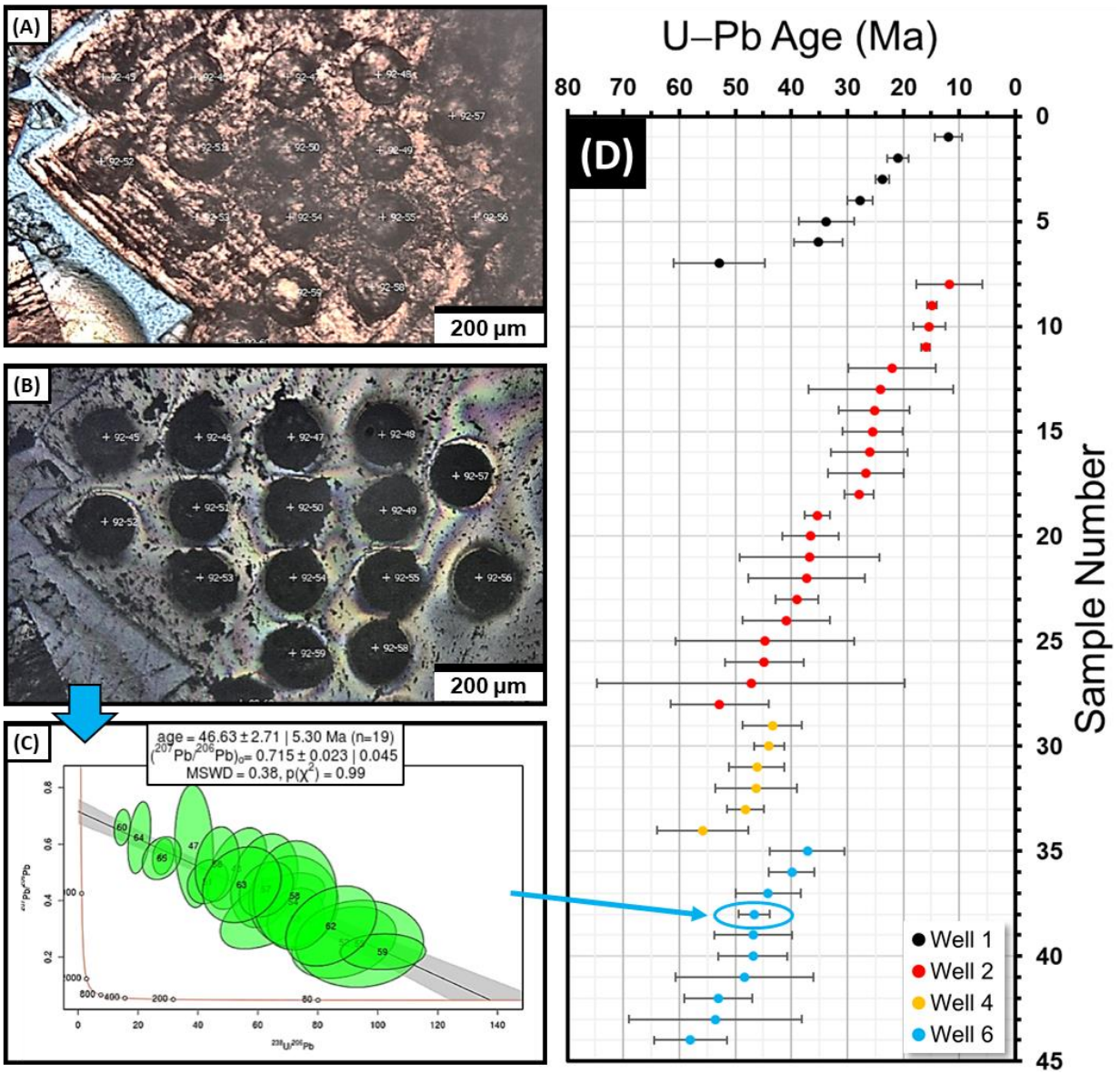

Figure 2.14. Uranium–lead (U–Pb) dating data for dolostone. (A) Photomicrograph of a baroque dolomite crystal that was dated using U–Pb. The circular spots (~130 µm diameter) are the locations of laser ablation. (B) Reflected image of the same baroque dolomite crystal. (C) Tera–Wasserburg Concordia diagram based on $^{238}U/^{206}Pb$ and $^{207}Pb/^{206}Pb$ values of 19 spots from the baroque crystal in Figure A and B. The dolomite crystal is from well 6 and yielded an age of 46.6 ± 2.7 Ma. Blue arrow shows the location of the sample in the dataset. (D) U–Pb dating results for 44 textural dolomite domains from 9 samples, color coded for wells and sorted from youngest to oldest for each well. Note how the ages become progressively older from wells 1 and 2 to well 6. Refer to Table 2.4 for the exact values of each analysis along with sample description.

Table 2.4: Uranium–Lead (U–Pb) Dating Data

Analysis #	Well #	Sample #	Dolomite Phase	U–Pb Date	Error (±)*	Error %*	Total Error (±)	Total Error %
1	1	364	BDC	11.9	2.4	20%	10.78	91%
2		364	BDR	21.0	1.9	9%	11.29	54%
3		364	BDR	23.7	1.2	5%	2.29	10%
4		364	EDR	27.8	2.3	8%	4.42	16%
5		364	BDR	33.7	5.0	15%	9.71	29%
6		364	BDR	35.2	4.4	12%	8.59	24%
7		364	BDR	52.8	8.2	15%	16.00	30%
8	2	439	BDR	11.8	5.9	50%	11.55	98%
9		540	EDR	14.9	0.8	5%	2.99	20%
10		560	EDR	15.3	2.8	18%	5.54	36%
11		540	EDR	16.0	0.7	5%	2.43	15%
12		540	EDR	22.0	7.9	36%	15.39	70%
13		520	EDR	24.0	12.9	54%	25.20	105%
14		520	EDC	25.2	6.3	25%	12.40	49%
15		520	EDC	25.5	5.3	21%	10.43	41%
16		520	EDR	26.1	6.9	26%	13.48	52%
17		480	BDC	26.7	6.8	25%	13.33	50%
18		560	EDR	28.0	2.6	9%	11.27	40%
19		439	BDR	35.3	2.3	6%	6.04	17%
20		520	EDR	36.6	5.0	14%	13.22	36%
21		560	EDR	36.7	12.5	34%	24.60	67%
22		480	BDC	37.3	10.4	28%	20.30	54%
23		480	EDR	39.0	3.9	10%	7.60	19%
24		439	BDR	40.9	7.8	19%	23.17	57%
25		540	EDR	44.7	16.0	36%	31.40	70%
26		439	BDR	44.8	7.0	16%	13.64	30%
27		540	BDR	47.2	27.5	58%	53.80	114%
28		560	EDR	52.8	8.7	16%	17.03	32%
29	4	338	EDR	43.4	5.4	12%	19.64	45%
30		231	BDC	44.0	2.8	6%	5.38	12%
31		231	BDR	46.2	5.0	11%	9.83	21%
32		338	EDC	46.3	7.3	16%	14.32	31%
33		231	EDR	48.1	3.3	7%	6.46	13%
34		338	EDC	55.8	8.2	15%	16.00	29%
35	6	92	BDC	37.2	6.7	18%	13.06	35%
36		92	BDC	39.9	4.1	10%	7.94	20%
37		92	EDR	44.1	5.8	13%	11.39	26%
38		92	BDR	46.6	2.7	6%	5.30	11%
39		92	BDR	46.8	6.9	15%	13.60	29%
40		92	EDR	46.9	6.1	13%	11.92	25%
41		92	BDR	48.4	12.3	25%	24.10	50%
42		92	EDR	53.1	6.1	11%	11.95	23%
43		92	BDR	53.6	15.4	29%	30.20	56%
44		92	EDR	58.0	6.5	11%	12.70	22%
1	2	414	Limestone Peloids (undolomitized)	111.0	11.1	10%	49.60	45%
2		414	Limestone Mud lump (undolomitized)	139.6	5.7	4%	11.16	8%
3		414	Dolomite cement in limestone	112.1	5.8	5%	11.44	10%
4		414	Dolomite cement in limestone	113.8	4.7	4%	9.27	8%
5		414	Dolomite cement in limestone	128.9	19.2	15%	37.60	29%

Uranium–lead dating for 44 dolostone textural domains and 5 limestone textural domains. Data are sorted by well (1, 2, 4, and 6) then by ages from youngest to oldest. See Figure 2.14D for a matching plot of dolostone data.
EDR= Equant dolomite (replacive), EDC = Equant dolomite (cement), BDR = Baroque dolomite (replacive), and BDC = Baroque dolomite (cement). * Denotes internal uncertainties (error) that are used in the text. Refer to Appendix C for discussion of the uncertainty.

2.5 DISCUSSION

2.5.1 Overall paragenesis

A 30-event paragenesis (Figure 2.15) is established for carbonates in the study area and incorporates both the major and minor diagenetic events. The paragenesis is constrained by cross-cutting relationships, $^{87}Sr/^{86}Sr$ analysis, U–Pb dating, and knowledge of the published burial and regional structural history (Ziegler, 2001; Abu-Ali and Littke, 2005; Faqira et al., 2009; Stewart, 2018).

All calcite in the limestone appears to have undergone some recrystallization events. This is supported by U–Pb absolute ages, where U–Pb analysis on calcitic peloids and mud lumps in a limestone sample yielded dates between 140 ± 6 Ma and 111 ± 11 Ma (Table 2.4). These ages are also consistent with stable isotope data, where $\delta^{18}O$ values of all limestones are more negative than those expected for Late Jurassic marine calcite (Figure 2.10A), attesting to lack of preservation of original isotopic signatures in the limestone. Despite the alteration of original stable isotopic values in the limestone, their $^{87}Sr/^{86}Sr$ values still fall within the Late Jurassic seawater range. The latter supports the idea that recrystallization does not always reset all geochemical properties in carbonates (aka concept of 'significant recrystallization'; Machel, 1997).

Regional studies, along with in-house seismic mapping, indicate the presence of active faulting during the diagenetic history of the Upper Jurassic Arab carbonates in the vicinity of the studied wells (Ziegler, 2001; Faqira et al., 2009; Stewart, 2018). Such faults could have breached the surface during the diagenetic history of the Arab carbonates. These structural events have operated at a scale much larger than thin sections and thus cannot be constrained by petrographic observations alone. Geographically, well 6 is the closest to the location of the Khurais–Jauf–Burgan (KJB) fold axis. The dolomite in this well also contains brecciated dolomites, multi-

directional fractures, dissolution of bedded anhydrite, and multiple solution collapse horizons (Figure 2.9 G, H), consistent with the idea of faulting. These features as well as microfractures are observed in other wells but with less intensity.

Successful U–Pb dating (Figure 2.14) on the different dolomite phases serves as a major time constraint on dolostone diagenesis (Figure 2.15). Because not all diagenetic products could be dated using U–Pb, traditional cross-cutting relationships have been used to establish dolostone paragenesis. Based on the petrographic, geochemical, and U–Pb data, the extensive dolomitization observed in the area (~85% of the rocks are dolostone; Figure 2.3) appears to be the result of multiple dolomitization or dolomite recrystallization events that have overlapped each other and have spatially overlapped with other diagenetic processes. Petrographic analysis on dolostone also shows the presence of mesogenetic (deep burial) porosity in dolostone (Figure 2.9), where moldic pore spaces were observed inside late dolomite and anhydrite crystals (Figure 2.9A, C), and some vugs were observed to cross-cut stylolite (Figure 2.9D). Appearing mostly as mottling in CL, petrographic and geochemical analyses also indicate occurrences of multiple dolomite recrystallization events (Figure 2.7). Because dolomite recrystallization is an important process that can complicate the interpretation of geochemical data, it is addressed briefly in this discussion, and explored more completely in a separate manuscript [Chapter 3 of this dissertation]. The majority of diagenetic processes and products in dolostones, thus, were alternating, and likely overlapping (Figure 2.15).

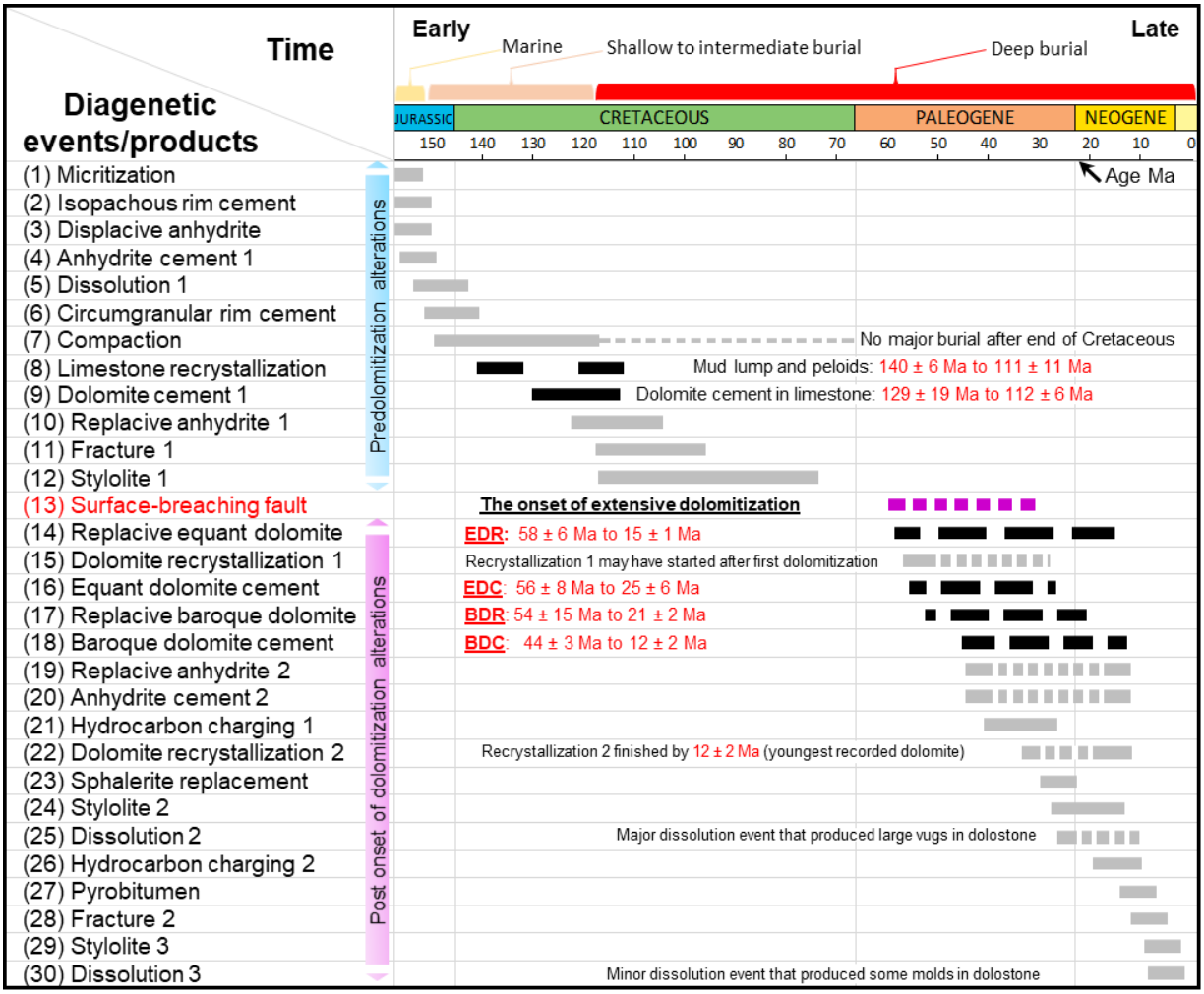

Figure 2.15. Paragenesis of the Upper Jurassic Arab Formation in northeast Saudi Arabia. The diagenetic history of the carbonates can be grouped generally into predolomitization and post onset of dolomitization events. The extensive dolomitization that produced the bulk of dolomite is the main diagenetic event. Bars in black are constrained by U–Pb dating with the ages provided by the red text. All other events are constrained by cross-cutting relationships, geochemical analyses, and knowledge of published structural and burial history of the region.

2.5.2 Spatial trends in stable isotope and fluid inclusion data

There is a conspicuous stable isotopic trend observed in the area, where both $\delta^{13}C$ and $\delta^{18}O$ vary progressively with the location of wells. Wells 5 and 6, the wells nearest to the known regional fold axis (the KJB fold; Figures 2.1 and 2.3), record the least positive and least negative $\delta^{13}C$ and $\delta^{18}O$ values in all wells (Figure 2.10B); whereas, wells 1 and 2, the farthest wells from the KJB

fold record the most positive and most negative $\delta^{13}C$ and $\delta^{18}O$ values (Figure 2.10B). One hypothesis for why such spatial trends exist, is the variation of depth from well to well, as the Arab carbonates in wells 1 and 2 are at much greater depth than those in wells 5 and 6. For reasons of confidentiality, the exact depth of the reservoirs is omitted in this study, however, the carbonates in wells 1 and 2 are almost twice as deep as those in wells 5 and 6; the greater the depth, the higher the ambient temperature. As $\delta^{18}O$ values fractionate as a function of temperature (Urey, 1947; Sharp, 2006), the expected changes of temperatures as a function of depth could be used to explain the more negative $\delta^{18}O$ values observed in wells 1 and 2 relative to wells 5 and 6 (Figure 2.10B), but that explanation is insufficient to fully explain the $\delta^{18}O$ values in dolostone. For example, the Arab carbonates in wells 3 and 4, are at slightly greater depths than those in wells 1 and 2, yet, the dolostones in wells 3 and 4 record less negative $\delta^{18}O$ values than those in wells 1 and 2. This shows that local temperatures at the site of dolomitization did not necessarily match those of country rocks.

Fluid inclusion data obtained in this study provide a better temperature constraint on dolomitization temperatures than do stable isotopes. Similar to stable isotopic trends, the fluid inclusion data exhibit a spatial trend, with dolostones in well 6 recording the lowest homogenization temperatures (Figures 2.11C, D and 2.12C, D; Table 2.3), with a mean Th of 82.5ºC and range of Th values in consistent FIAs from 77.2 to 85.2ºC (the dolostone in this well records the least negative $\delta^{18}O$ and is at the shallowest depth). Dolostones in wells 1 and 2 record the highest homogenization temperatures. Well 1 shows a mean Th of 102.2ºC and range of consistent FIAs means from 99.6 to 106.0ºC. Well 2 shows a mean Th of 103.8ºC and range of consistent FIAs from 98.5 to 107.3ºC (Figure 2.11C, D). Individual FIAs also record a wide range of Th (as much as ~30ºC). Similar to the discussion of the stable isotope data, the homogenization

temperatures cannot be attributed simply to ambient temperatures at depth. As an example, in well 4, dolostones record slightly lower temperatures at greater depths than the dolostones in wells 1 and 2. For well 6, present-day bottom-hole temperature is between 50 and 60ºC at the Arab Formation depths (Aramco internal data); the dolomite in this well records a range of homogenization temperatures from 75.2 to 90.2ºC, with a mean of 82.5ºC (Table 2.3; Figure 2.12A). For wells 1 and 2, the Arab Formation is at a greater depth (Figure 2.3) and bottom-hole temperature (at the Arab Formation depth) in those two wells is at ~85ºC (Aramco internal data). Dolomite homogenization temperatures range from 83.5–117.1ºC, with a mean of ~103.0ºC (Table 2.3; Figure 2.12A) for wells 1 and 2. These data show a mismatch between ambient burial temperature and temperature of formation of the dolomite, with the dolomite forming at higher temperatures. The up to 30ºC variability of homogenization temperatures in and among consistent FIAs in the same well, is also inconsistent with a simple burial heating at ambient conditions, which would not show such variability.

Based on mean oxygen isotope values and mean temperatures of homogenization for each well (Tables 2.2 and 2.3), estimates of the parent fluid's composition can be calculated. Using the expression of Kim and O'Neil (1997) and a $\Delta^{18}O$ of +4.9‰ for dolomite–calcite fractionation (Sheppard and Schwartz, 1970), the fluids that dolomitized the carbonates in wells 1 and 2 are calculated to have had mean $\delta^{18}O$ values of +0.2 and +1.1‰ [VSMOW], respectively. The calculated values get progressively more positive to the north, with calculated mean $\delta^{18}O$ values for the parent fluids that produced dolomite in wells 4 and 6 being +1.8 and +2.1‰ [VSMOW], respectively. Assuming a Paleocene–Eocene age normal marine seawater would likely have had a $\delta^{18}O_w$ of -1‰ [VSMOW] (Hollis et al., 2019), all calculations indicate a more positive $\delta^{18}O_w$ compared to normal marine seawater. This is evidence for evaporation of a seawater source, and

is consistent with the high salinities observed in fluid inclusions. The calculations also support some spatial variation in fluid composition from well to well.

The variation observed in dolostone's $\delta^{13}C$ (Figure 2.10A, B), could reflect either changes in the amount of water/rock buffering or slight differences in $\delta^{13}C$ composition of the dolomitizing/recrystallizing fluids (Lohmann, 1988; Sharp, 2007). The latter could result from temporal variation in the timing of dolomitization. What is clear from the $\delta^{13}C$ data is that there was a likely compositional variation of the dolomitizing fluids, albeit not major, during the dolomitization history of the Arab carbonates.

The variation in fluid inclusion salinity (Table 2.3), further supports the notion that the composition of the dolomitizing fluid was not uniform among wells. The dolomite in wells 1 and 2, record the most saline values (salinity mean: 25.1%), whereas the dolostone in well 6 (to the north) records lower salinity values (salinity mean: 22.3%; Figure 2.12; Table 2.3). The trend observed in both stable isotope and fluid inclusion data, thus, likely indicates some localized controls with progressive change from north (nearest to KJB fold) to south. The dolomitizing fluid was neither homogeneous in temperature nor in fluid composition.

2.5.3 Timing of dolomitization and recrystallization

Unlike stable isotopes and fluid inclusion data, U–Pb dating can provide absolute ages that constrain the timing of dolomitization or dolomite recrystallization in the area. Uranium–lead dates in dolostones range from 58.0 ± 6.5 Ma (recorded in a replacive equant dolomite phase in well 6) to 11.9 ± 2.4 Ma (recorded in a baroque dolomite cement phase in well 1; Table 2.4). Within any one well, and even within any one sample, dolomites also exhibit a range of ages (Figure 2.14D;

Table 2.4), likely attesting to either multiple times of dolomite formation and/or multiple recrystallization events at different times. The range of ages observed within individual samples is not consistent with stable isotope and fluid inclusion data, both of which show relatively homogenous values for individual dolostone samples regardless of the dolomite phase. Based on CL petrography (Figure 2.7B, D, F), dolomite experienced extensive recrystallization, evidenced by the prevalent mottled luminescence of inner cores of dolomite crystals in almost all dolomites.

While it is impossible to conclusively determine whether the U–Pb dates are recording the initial time of formation or the times of subsequent recrystallization, it is more likely than not, that the U–Pb data are recording both, as evidenced by the range in dates, and the generally low errors. For example, in sample number 364 from well 1 (Figure 2.14D; Table 2.4), five different replacive baroque dolomite crystals (BDR) were analyzed for U–Pb dating (Table 2.4). All of the baroque dolomite crystals have similar shapes, sizes, CL patterns with mottled luminescence, and without any cross-cutting relationships, yet, U–Pb dates yield ages from 52.8 ± 8.2 Ma to 21.0 ± 1.9 Ma for those five baroque dolomite crystals. Such a wide range in ages for the same dolomite phase within the same sample likely points toward multiple times of dolomite formation and recrystallization. An argument can also be made that the oldest age, the 52.8 ± 8.2 Ma, might represent either the initial formation or the oldest recrystallization event, but the younger ages likely indicate events of recrystallization.

The integration of $^{87}Sr/^{86}Sr$ and U–Pb dating provides the best approach to constrain the time of dolomitization and recrystallization. Dolomite replacement and cementation could have commenced around 58.0 ± 6.5 Ma with recrystallization likely beginning shortly after the initial dolomite formation (oldest recrystallization event could potentially have happened at 58.0 ± 6.5 Ma) and continuing up until the 12 ± 2 Ma age date. The $^{87}Sr/^{86}Sr$ values (Figure 2.16) are likely

a mixture among Sr from the dolomitizing fluid, recrystallizing fluid, and Jurassic host. As the Jurassic host has low $^{87}Sr/^{86}Sr$, it is a reasonable assumption that the highest dolomite value (0.70787) might record a fluid value. The other dolomite $^{87}Sr/^{86}Sr$ values cannot be easily interpreted. Using this 0.70787 as an end member, and assuming a derivation of the fluid from seawater, at least some of the dolomitizing or recrystallizing fluid would have been derived from evaporated seawater that formed on the surface ~32 Ma ago (McArthur et al., 2012), and then was heated. Regional geology shows that large volumes of evaporite, and hence evaporated waters, formed on the surface beginning in early Paleogene (~62 to 50 Ma years ago; Figure 2.17). This age is consistent with the oldest ages obtained from U–Pb dating (58 ± 6.5 Ma; Table 2.4). The ~32 Ma estimate of a seawater source is likewise consistent with the approximate cessation of a period of evaporite deposition (Figure 2.17). On the basis of the U–Pb dates younger than 32 Ma, and the ambiguity of the source of Sr in the dolomites, dolomitization and recrystallization certainly could have continued beyond 32 Ma.

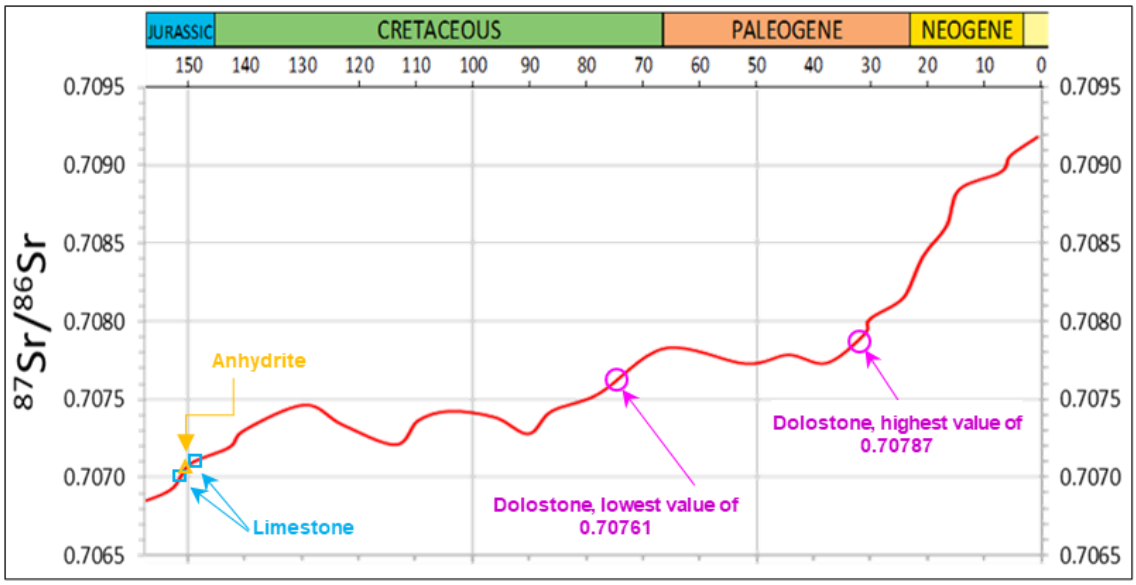

Figure 2.16. Strontium isotope ratio curve from the Late Jurassic to present showing the overall increase in $^{87}Sr/^{86}Sr$ values and data for limestone, anhydrite and highest and lowest dolomite value. Curve is from McArthur et al. (2012).

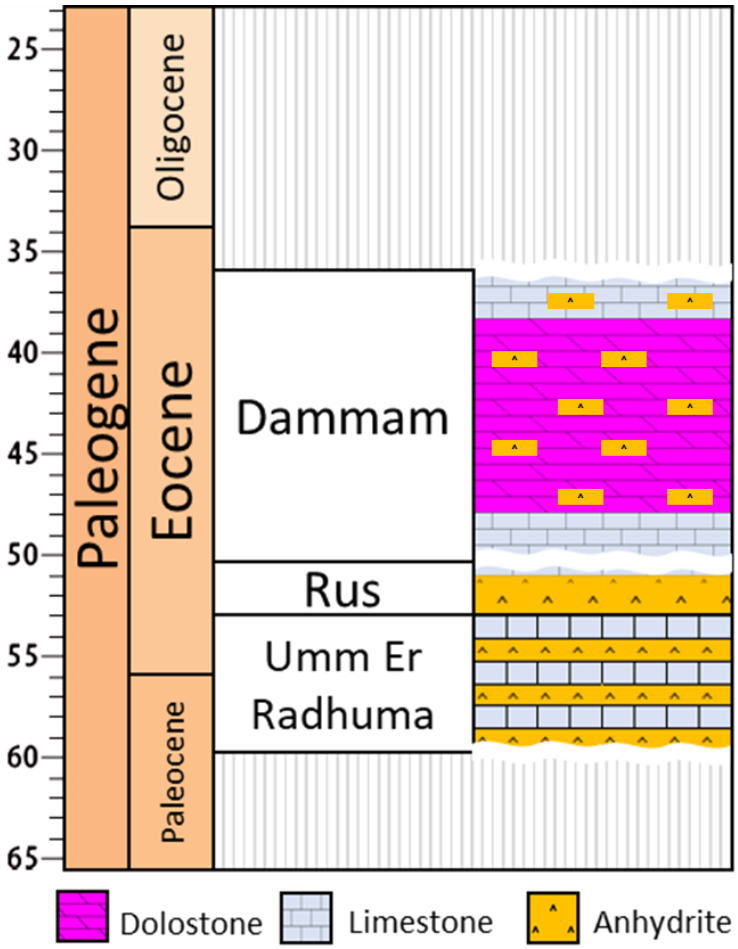

Figure 2.17. Paleogene stratigraphy in the area, showing the deposition of mostly evaporites and carbonates during the ~58 to ~ 35 Ma time span. Figure is based on established stratigraphy in the Eastern region of Saudi Arabia but also includes data from the study area (e.g., Stewart, 2018).

2.5.4 Fault-controlled dolomitization

Resolving the timing of dolomitization and recrystallization is an important step to understand the mechanism by which dolomite formed. All petrographic and geochemical data on dolostone indicate late formation/recrystallization of dolomite at high temperatures between 75.2 and 117.1ºC, with a mean of 100.4ºC (Table 2.3). Excluding the minor dolomite cement observed in the limestone, all dolomites in the dolostone are interpreted to have formed after burial. At the

interpreted time of dolomite formation (i.e., the ~58 to ~32 Ma or later), the Arab carbonates had already reached their present-day depth (Abu-Ali and Littke, 2005). The study area is in close proximity to KJB fold axis (Figure 2.1; Faqira et al., 2009; Stewart, 2018). Wells 5 and 6 are the nearest to this fold axis and these two wells, and particularly well 6, display fault-damage fabrics at a log, core, and thin section scale. This includes missing evaporite units, multiple evaporite solution collapse horizons of brecciated dolomite, and fractures and microfractures in all orientations. The amount of dolomite gradually decreases southward and away from well 6. For all the reasons above, we propose that at and near well 6 were some of the best conduits for fluids causing dolostone diagenesis.

The amount of dolomite in the region is laterally extensive, for example, Lu et al. (2017) estimated an area of more than 30,000 km to have been dolomitized. The dolomite also occurs in thick stratigraphic section (up to 1 km thick in some areas). A reactive transport modeling study concluded that fault-pumping dolomitization alone in this area could not account for all dolomites in the area (Lu et al., 2017). Rather, these authors, invoked a major early (i.e., Late Jurassic) reflux dolomitization as the main source of initial dolomite. This is a simple explanation to account for the large volumes of Mg-rich fluid needed to dolomitize the carbonates observed here. Based on petrography that shows a late timing, U–Pb dating, stable isotopes, fluid inclusion, and $^{87}Sr/^{86}Sr$ data, we can reject this interpretation. Barring the small amount of dolomite cement in some undolomitized limestone, there is currently no petrographic or geochemical evidence that points toward substantial early reflux dolomitization.

Previous studies on the Arab formation in Ghawar (Cantrell et al., 2004), and in Abu Dhabi (Morad et al., 2012) argued for the presence of some reflux dolomite, all of which experienced later recrystallization as evidenced by $\delta^{18}O$ more negative than Late Jurassic marine dolomites

(Figure 2.18). In both studies, however, dolomite only accounts for less than 15% of all reservoir rocks, and the interpreted reflux dolomite accounts for an even smaller fraction of the total dolomite. The basis for their reflux dolomite origin interpretation is based on petrographic evidence where dolomite was observed under anhydrite beds, the lack of two-phase fluid inclusions in some dolomites, and more importantly based on dolomite's $^{87}Sr/^{86}Sr$ values, which match those of Late Jurassic seawater in those two studies. Another study from Saudi Arabia (Rosales et al., 2018) interpreted all dolomites to have formed during burial diagenesis, based on the negative oxygen isotopic values, even though their dolomites' $^{87}Sr/^{86}Sr$ values match those of Late Jurassic seawater. In this study, all stable isotopic analyses, including the least negative $\delta^{18}O$ values, which were observed in wells 5 and 6 (Figure 2.10B), are well outside the range expected for marine dolomites (Figure 2.10A; Veizer et al., 1999). This indicates either a late formation of all dolomites in the presence of relatively high-temperature fluids, a 'wholesale' recrystallization of all dolomites, or a combination of late formation of some dolomites as well as recrystallization of earlier formed dolomite, albeit the early dolomite is not necessarily an early marine dolomite. This suggests the dolomitizing fluids that produced the younger void-filling baroque dolomite cements likely recrystallized the older dolomite phases as well. This also means that the stable isotopic values reflect the conditions of dolomitizing fluids that formed some dolomites, but also fluids that caused recrystallization. As such, recrystallization and dolomite precipitation events could very well have overlapped in the area during the paragenesis of the carbonates (Figure 2.15).

This minor dolomite cement in limestone could preserve some earlier signatures than the late dolomite. It plots well outside the range expected for low temperature marine dolomite (Figure 2.10A) but displays the least negative dolomite values in wells 2. The cement also overlaps with the host limestone's stable isotopic values (Figure 2.10A). This dolomite does not contain any

fluid inclusions and record U–Pb dates between 129 ± 19 Ma and 112 ± 6 Ma. It is thus the oldest dolomite recorded in the study area, much older than the oldest dolomite found in the dolostone (age = 58.0 ± 6.5 Ma).

The presence of faults and fault-damage zones could have provided the conduits between the surface and subsurface, that allowed brines generated at the surface, during Paleogene to sink because of their high density. This time span is consistent with the regional stratigraphy, with deposition of Paleogene Umm Er Raduhma, Rus, and Dammam carbonates and evaporites (Figure 2.17). All units contain anhydrite, and the Rus Formation contains halite (Stewart, 2018), we interpret that those sinking brines charged an underlying (Upper Triassic) clastic reservoir (the Minjur Formation; Figure 2.19A, B), because: (1) the depth of the Minjur below the Arab Formation is such that it would be hot enough to provide the Th values observed in the Arab dolomite; (2) the Minjur is a porous and permeable unit capable of storing large volumes of Mg-rich fluids; and (3) its pure quartz lithology would not result in contamination of the fluid with radiogenic Sr.

The fault that intersected the surface could very well be the KJB, but could also include other faults and fault-damage zones that were present in the area. Based on the integration of the U–Pb dating data, source of evaporitic fluids at the surface, and $^{87}Sr/^{86}Sr$, the sinking of fluids likely spanned a period from ~58 to ~32 Ma (Figure 2.19). At the same time fluids were sinking in one place and charging the underlying aquifer, they were likely rising in other places. Regional studies (Aramco internal reports) confirmed the presence of a dense network of faults and joints between well 6 (to the north) and wells 1 and 2 to the south. The upward flow of hot Mg-rich fluids through these fracture systems would explain dolomitization and dolomite recrystallization in the area. As the Th and stable isotope data show that individual wells have unique temperature

signatures, however, it is reasonable that fluid flow was not homogenized by a basin-wide geothermal convection cell (aka Corbella et al., 2014). The paleotemperature record in each well, instead, is tied to the temperature of the underlying Triassic aquifer immediately below. This unique record could be explained by seismic (fault) pumping of vertical faults, generated by multiple fault movements over a period of 40 million years. It could also be generated by localized geothermal convection, with the convective cells circulating within, rather than regionally between fault-damage zones. Moreover, the record of rise and fall in Th values among FIAs provides evidence for pulses of temperature rise and fall. This would indicate that repeated reactivation through fracturing or faulting was likely, rather than a simple convection.

Thus, the dolomitization was through a fault-controlled mechanism that (Figure 2.19) indicate that Mg-rich evaporated seawater sank, due to its high density, through a surface-breaching fault-damage zone to charge a deep clastic aquifer. This happened between ~58 Ma and ~32 Ma. The sinking itself could have caused some vertical fluid flow of hot fluids, or coincided with convection in fault damage zones. Once the aquifer was charged with brines, convection in fault damage zones, repeated fracturing events, or seismic pumping could have sporadically continued to cause dolomite and dolomite recrystallization. This injection of hot fluids progressively shut down, first in the NW at about 37 Ma and later in the SE at about 12 Ma. This progressive shut down is consistent with an active fault or fracture driver for fluid flow that is no longer active. The bulk of dolomite could have formed through highly localized geothermal convective cells that operated within and around individual fault damage zones. Understanding the details of fluid flow in such cells will require further work.

There are a vast number of studies that have invoked similar model (i.e., fault-controlled dolomitization) to explain the presence of large areas of burial dolomite in their respective study

areas (Dewit et al., 2012; Corbella et al., 2014; Hollis et al., 2017; Hirani et al., 2018; Lukoczki et al., 2019; Koeshidayatullah et al., 2020; Stacey et al., 2021; Afify et al., 2022). Many of those studies are rift basins (e.g., Hirani et al., 2018; Lukoczki et al., 2019; Afify et al., 2022) where there is an abundance of structures, mostly extensional and strike slip faults, to serve as fluid conduits. Reactive transport modeling of fault-controlled dolomitization (Corbella et al., 2014) demonstrated the effectiveness of such a model to produce large volumes of burial dolomite. Those authors concluded that Mg-rich fluids reach their maximum dolomitizing potential at ~100ºC, and a kilometer-long limestone body can be dolomitized in a time as short as a few millions of years. Interestingly, that ~100ºC is very consistent with the bulk of homogenization temperatures on dolomite in this study (Figure 2.12; Table 2.3).

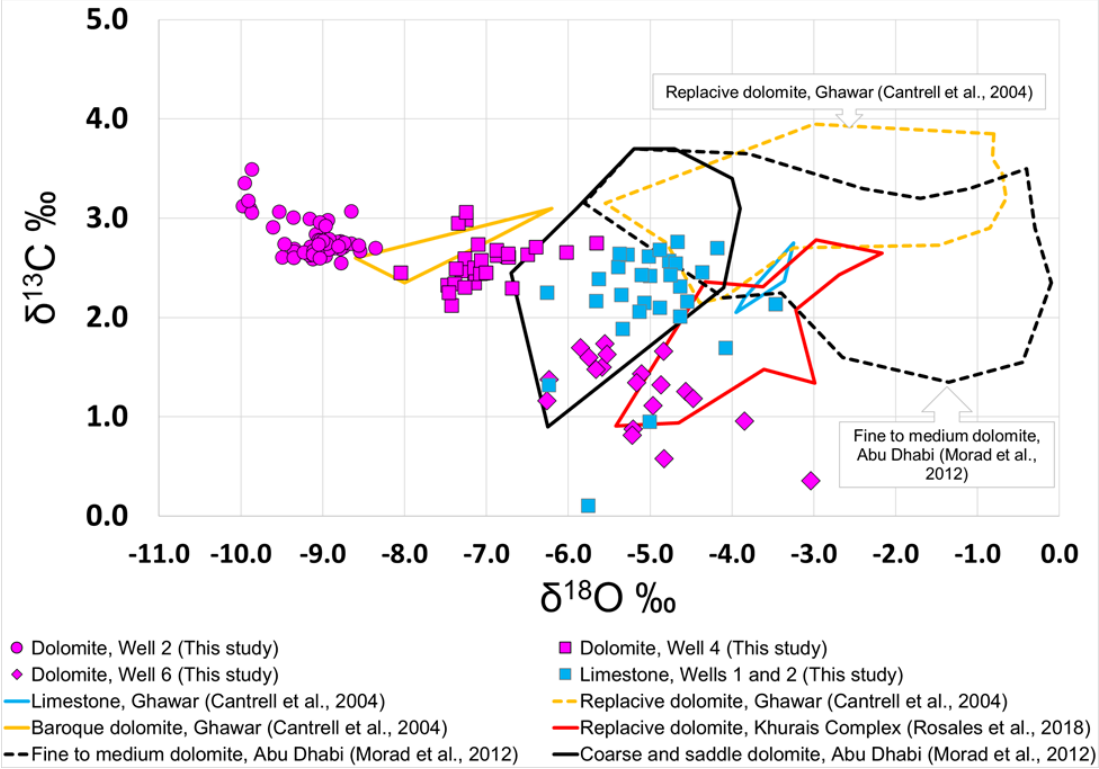

Figure 2.18. A comparison of stable isotope data from this study with previous studies in the region. Note essentially all dolomites in the region plot outside the fields of known Late Jurassic dolomites (see Figure 2.10A). Dolomites with the least negative $\delta^{18}O$ values in Ghawar and Abu Dhabi (labelled in the plot) were interpreted as early dolomites. All dolomites in Khurais (Rosales et al., 2018) were interpreted as burial dolomites. Refer to text for discussion.

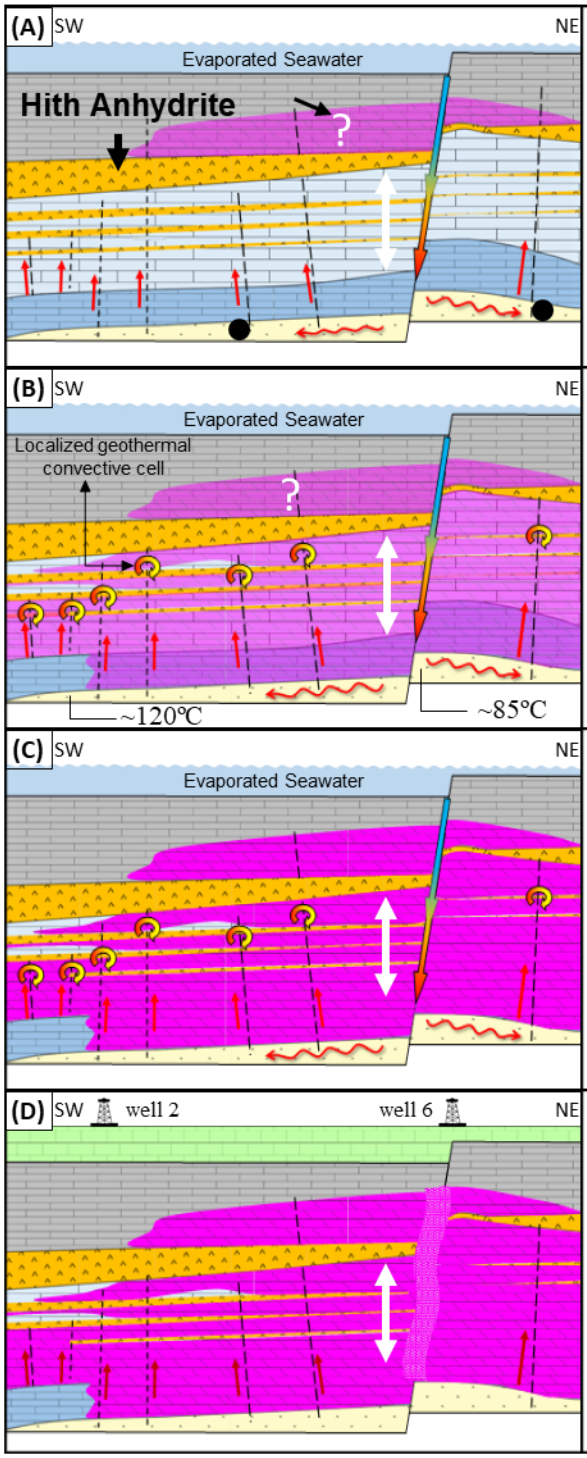

Time: ~58 Ma: Faults (either normal or strike-slip) breached the surface during the deposition of early Paleogene carbonates and evaporites (Figure 2.17). The faults produced conduits that allowed the sinking of evaporated water and charged the Upper Triassic Minjur sandstone aquifer (black dots). Initial 'reflux' dolomitization by evaporated water could have occurred during initial sinking of fluids as there is dolomite on top of the Hith anhydrite (black arrow) (Figure 2.3) No petrographic and geochemical data on this dolomite.

Time: ~58 to ~32 Ma: This period includes the charging of the aquifer at depth and is supported by U –Pb dating (Figures 2.14D and 2.15; Table 2.4) and $^{87}Sr/^{86}Sr$ ratios (Figures 2.13 and 2.16). Temperatures in the Minjur sandstone today are between ~85°C to the north and ~120°C to the south. Some dolomite could have been produced locally through 'fault-pumping' mechanism, however, the bulk of dolomite was produced after a likely localized geothermal convection cells developed near individual faults. Not clear if a basin-wide geothermal cell developed or not.

Time: ~58 to ~32 Ma: By ~32 Ma years ago the convection geothermal cells neared their end. Dolomitization beyond this date might have continued in the southern wells, which include younger dolomites (< 32 Ma) (Table 2.4). Dolomites with ages < 32 Ma could have been produced locally through a 'fault-pumping'. Alternatively, these ages may represent recrystallization events. Deposition of carbonates/evaporites at the surface ceased between 36 to 23 Ma (based on regional stratigraphy; Figure 2.17).

Time: ~32 to ~12 Ma: After sealing the fault, dolomitization and/or recrystallization continued in the southern area until ~12 Ma (youngest recorded age by U–Pb dating; Figures 2.14D and 2.15; and Table 2.4). Ages younger than 32 Ma are only recorded in wells 1 and 2. The area near well 6 is characterized by fault-damage fabrics and is missing anhydrite in all stratigraphic units (Figures 2.1 and 2.3). Some dissolutions in all dolostone happened beyond ~12 Ma (Figures 2.9 and 2.15). Locations of wells in the figure are approximate.

Figure 2.19. Schematic cross-sections (A–D) showing a summary of the dolomitization history in the study area. The ages are based on $^{87}Sr/^{86}Sr$ and U–Pb dating on dolostone. Dolomitization in the area commenced after a fault breached the surface around 58 Ma ago. Seawater-derived fluids sank down through the fault and charged the Upper Triassic Minjur sandstone. Some of the dolomitization may have been caused by fault pumping but the bulk of dolomitization is interpreted to have formed through localized convective geothermal cells that operated at a fault-damage zone scale. Area near present day well 6 (Figure D) is characterized by fault-damage fabrics, multiple solution collapse horizons and multidirectional core-scale fractures. Figure is not to scale (The Arab Formation, between white arrows, is enlarged for clarity). See Figure 2.3 for a lithological correlation.

2.5.5 Hydrothermal origin of dolomite

Despite the numerous dolomite studies that have invoked hydrothermal dolomitization as the main dolomitizing mechanism in their respective areas (e.g., Qing and Mountjoy, 1994; White and Al-Asam, 1997; Al-Asam, 2003; Lavoie et al., 2005; Luczaj, 2006; Davies and Smith, 2006; Smith, 2006), there remain some questions about the nature and capability of such a process to produce platform-wide dolomite (Machel and Lonnee, 2002; Lonnee and Machel, 2006; Friedman, 2007). There is currently no consensus on the definition of hydrothermal systems. Some workers recommended the use of a strict definition that necessitates a knowledge of ambient temperatures at the depth (and time) dolomite formed, and requires that dolomite formed from a fluid that is at least 5–10ºC warmer than ambient temperature (White, 1957; Machel and Lonnee, 2002). In practice, however, such a requirement is nearly impossible to attain because there will always be questions about the exact temperatures of country rocks at the time of dolomitization especially when the timing of dolomitization is unknown and the paleogeothermal gradients must be modeled or assumed. This led other workers to apply a more practical approach to determine whether or not certain dolomites are in fact hydrothermal in origin. The approach uses a robust knowledge of the dolomite system and requires a series of observations and data integration that include knowledge of dolomite's fluid inclusion homogenization temperatures, stable isotopes, a characterization of the dolomite's temperatures of formation, as well as knowledge of the depositional, structural, and burial history of the sedimentary system (Goldstein, 2012).

In this study, the integration of petrographic, geochemical, U–Pb dating, along with established knowledge of the burial history points toward a late origin for all dolomites in the dolostone. We interpret the dolomite to be a mixture of hydrothermally formed and hydrothermally recrystallized dolomites. The same fluids that hydrothermally precipitated some dolomite (e.g.,

pristine void-filling large baroque dolomite cement; Figure 2.5A), also recrystallized nearby dolomite, such as the equant replacive dolomite, leading to nearly identical stable isotopic and fluid inclusion values. This is also true for all dolomite phases including the equant dolomite cements and the baroque dolomites, where stable isotopes, fluid inclusions, CL, and U–Pb dating values, mimicked each other, and consistently exhibited values outside those expected for early, reflux, dolomite.

The carbonates in this study have undergone a history of constant burial since Early Cretaceous that continued until early Paleogene, with present-day burial depths being the maximum burial depths the Arab Formation has reached (Abu-Ali and Littke, 2005). The depth of the Arab Formation varies from one well to another, with the Arab Formation in wells 5 and 6, located at shallower depth than other wells. Multiple bottom-hole temperatures are available in all wells. For well 6, present-day bottom-hole temperature is between 50 and 60ºC at the Arab Formation depths (Aramco internal data); the dolomite in this well records a range of homogenization temperatures from 75.2 to 90.2ºC, with a mean of 82.5ºC (Table 2.3; Figure 2.12C). As reported above, the lowest homogenization temperature in well 6 is ~15ºC higher than the maximum burial temperature. For wells 1 and 2, typical homogenization temperatures are 18ºC above the maximum burial temperature. Almost all Th measurements in these three wells indicate a hydrothermal origin, with temperatures being well above the 5–10ºC requirements. Moreover, Th values in consistent FIAs show repeated rises and falls in temperature from ~10–30ºC. This is inconsistent with any known burial history, and therefore, is also interpreted as evidence for pulses of hydrothermal fluid flow.

In the vicinity of the study area, there are currently no reports of magmatic activity or any source of elevated heat flow during the diagenetic history of the Jurassic carbonates. Further away

from the study area, however, and closer to passive continental margins, some elevated heated flows were reported, and attributed to magmatic activity (Laws and Wilson, 1997). This elevated heat flow was reported in the Jurassic section in Lebanon (Nader et al., 2004), the Jurassic and Cretaceous sections in Turkey (Kırmacı et al., 2018) and the Cretaceous section in Iraq (Mansurbeg et al., 2021). All these studies, however, are much closer palaeogeographically to either the Zagros suture (Mansurbeg et al., 2021) or to the outer margin of the Arabian and Levant plates (Laws and Wilson, 1997; Nader et al., 2004; Kırmacı et al., 2018). These studies also reported substantial uplift and sometimes exposure of the Cretaceous and Jurassic sections, which is not observed in the vicinity of the study area here.

The Th values observed in all dolostones are, therefore, much higher than those of the surrounding country rocks and are interpreted as hydrothermal in origin. In the present day, these temperatures are reached in the underlying Upper Triassic Minjur Formation. The Minjur Formation is many 100s of meters deeper than the Jurassic Arab Formation and includes a coarse and porous sandstone unit in it. The present-day temperatures of the Minjur Formation are very close to its temperatures from ~58 to ~12 Ma (Abu-Ali and Littke, 2005), the time when all dolomitization and recrystallization took place. Bottom-hole temperatures in this unit are between ~85ºC in the northwest wells and ~120ºC in the southeast wells (Aramco internal data). This temperature range is a good match for the Th values observed immediately above in the dolostone (Table 2.3). It indicates the dolomite originated from vertical fluid flow out of the Minjur Formation and into the Arab Formation and above, once the Minjur had been charged with evaporated seawater at depth.

2.6 CONCLUSIONS

Integrated analyses of stable isotope, fluid inclusion, CL, $^{87}Sr/^{86}Sr$, and U–Pb dating on dolostone revealed important information about the genesis of regionally extensive burial dolomite in the Upper Jurassic carbonates in northeast Saudi Arabia:

1. Oxygen isotope data in all dolostones are more negative than those of Late Jurassic marine dolomite. No early marine or reflux isotopic signatures were observed in any sample, indicating either a late formation of all dolomites, or a recrystallization of any early dolomite that could have existed.
2. Primary homogenization temperatures (Th) in dolostones average 100.4ºC with a range from 75.2 to 117.1ºC and salinities average 24.3 wt. % NaCl equivalent, with a range from 20.6 to 27.4%. The mean Th as well as the range of Th are greater than the maximum burial temperatures the rocks were exposed to. The salinity indicates hypersaline fluids (~6 to 8 times more saline than seawater) were responsible for the bulk of dolomitization.
3. The dolomite is composed of a mixture of equant and baroque dolomite, both of which occurred as replacement or cement. All dolomite phases, within the same sample, exhibit nearly identical stable isotopic and fluid inclusion values, even when cross-cutting relationships are present. This indicates recrystallization of older dolomite by similar fluids to that which produced the younger dolomite.
4. There is a spatial trend in stable isotope and fluid inclusion data in dolostones. Dolostones located to the north in the study area, and closest to a known regional fault, record less negative $\delta^{18}O$, less positive $\delta^{13}C$, and lower Th and salinity values than

wells to the south. Likely indicating some localized control on dolomitizing fluid source.

5. The results from integrated $^{87}Sr/^{86}Sr$ and U–Pb data indicate that fluids charged a Triassic sandstone reservoir by sinking through faulted and fractured rocks. Those fluids were evaporated seawater that penetrated downward due to density contrast between ~58 Ma and ~32 Ma.
6. At the same time fluids were sinking and charging the Triassic aquifer with brine, they were rising upward from that reservoir as hydrothermal fluids that were injected into the Arab Formation and dolomitized it. The conduits for fluid flow were near vertical faults and fractures; and thus; the Th values of hydrothermal dolomite were the same as the burial temperatures of the more deeply buried Triassic sandstones, many 100s of meters below. This is easily explained as convective fluid flow, driven by temperature-controlled density differences. Fluids moved vertically and spread along tabular geobodies that were controlled by fault-damage zones. Part of the fluid movement may have been related to active faulting and fracturing, producing pulses of fluid flow and fluctuations in temperature. Between 40–30 Ma, these fault-damage zones closest to the KJB fold might have self-sealed or stopped deforming, whereas in other areas, these fault damage zones remained open to hydrothermal fluid flow up until 12 Ma.
7. All dolomites in the dolostone are either hydrothermally formed or hydrothermally recrystallized. Spatially, the processes of hydrothermal dolomite formation and hydrothermal dolomite recrystallization overlapped during the majority of the dolostone diagenesis. This is also true within individual locations, where petrographic and geochemical data reveal a relationship between the two processes.

2.7 REFERENCES

Abu-Ali, M., and R. Littke, 2005, Paleozoic petroleum systems of Saudi Arabia: A basin modeling approach: GeoArabia, v. 10, p. 131–168.

Afify, A. M., M. E. Sanz-Montero, and L. Gonzalez-Acebron, 2022, Dolomite–magnesite formation and polymetallic mineralization in a rift-sag basin on the western margin of the Red Sea: paleoenvironmental, hydrothermal, and tectonic implications: Journal of Sedimentary Research, V. 92, p. 144–165, DOI: 10.2110/jsr.2021.100.

Al-Aasm, I., 2003, Origin and characterization of hydrothermal dolomite in the Western Canada Sedimentary Basin: Journal of Geochemical Exploration, v. 78, p. 9–15, https://doi.org/10.1016/S0375-6742(03)00089-X.

Al-Awwad, S. F., and L. B. Collins, 2013, Arabian carbonate reservoirs: A depositional model of the Arab-D reservoir in Khurais field, Saudi Arabia: AAPG Bulletin, v. 97, n. 7, p. 1099–1119.

Al-Helal, A. B., F. F. Whitaker, and Y. Xiao, 2012, Reactive transport modeling of brine reflux dolomitization, anhydrite precipitation and porosity evolution: Journal of Sedimentary Research, v. 82, p. 196–215, doi:10.2110/jsr.2012.14.

Al-Husseini, M. I., 2000, Origin of the Arabian Plate structures: Amar Collision and Najd Rift: GeoArabia, v. 5, p. 527–542.

Al-Husseini, M., 1997, Jurassic sequence stratigraphy of the western and southern Arabian Gulf: GeoArabia, v. 2, p. 361–382.

Al-Husseini, M., 2009, Update to Late Triassic–Jurassic stratigraphy of Saudi Arabia for the Middle East geologic time scale: GeoArabia, v. 14, p. 145–186.

Benjakul, R., Hollis, C., Robertson, H.A., Sonnenthal, E.L., and Whitaker, F.F., 2020, Understanding controls on hydrothermal dolomitization: Insights from 3-D Reactive Transport Modelling of geothermal convection: Solid Earth Discussions, p. 1–35, https://doi.org/10.5194/se-2020-99.

Bodnar, R. J., 1992, Revised equation and table for freezing point depressions of H,O-salt fluid inclusions (Abstract): PACROFI IV, Fourth Biennial Pan-American Conference on Research on Fluid Inclusions, Program and Abstracts, Lake Arrowhead, CA, v. 14, p. 15.

Broomhall, R. W., and J. R. Allen, 1987, Regional caprock-destroying dolomite on the Middle Jurassic to Early Cretaceous Arabian Shelf: Society of Petroleum Engineers Formation Evaluation, v. 2, p. 435–441.

Cantrell, D. L., P. G. Nicholson, G. W. Hughes, M. A. Miller, A. G. Bhullar, S. T. Abdelbagi, and A. K. Norton, 2014, Tethyan petroleum systems of Saudi Arabia, in L. Marlow, C. Kendall and L. Yose, eds., Petroleum systems of the Tethyan region: AAPG Memoir 106, p. 613–639.

Cantrell, D., P. K. Swart, and R. M. Hagerty, 2004, Genesis and characterization of dolomite, Arab-D reservoir, Ghawar field, Saudi Arabia: GeoArabia, v. 9, p. 1–26.

Consonni, A., A. Frixa, and C. Maragliulo, 2018, Hydrothermal dolomitization: simulation by reaction transport modelling, In: Armitage, P.J., Butcher, A., Churchill, J., Csoma, A., Hollis, C., Lander, R.H., Omma, J., Worden, R.H. (Eds.), Reservoir Quality of Clastic and Carbonate Rocks: Analysis, Modelling and Prediction: Geological Society, London, Special Publication v. 435, p. 235–244.

Corbella, M., E. Gomez-Rivas, J.D. Martin-Martin, S.L. Stafford, A. Teixell, A. Griera, A. Trave, E. Cardellach, and R. Salas, 2014, Insights to controls on dolomitization by means of reactive transport models applied to the Benicàssim case study (Maestrat Basin, eastern Spain): Petroleum Geoscience, v. 20, p. 41–54.

Davies, G. R., and L. B. Smith, 2006, Structurally controlled hydrothermal dolomite reservoir facies: An overview: AAPG Bulletin, v. 90, p. 1641–1690.

Dewit, J., M. Huysmans, P. Muchez, D. W. Hunt, J. B. Thurmond, J. Verges, E. Saura, N. Fernandez, I. Romaire, P. Esestime, and R. Swennen, 2012, Reservoir characteristics of fault-controlled hydrothermal dolomite bodies: Ramales Platform case study, in J. Garland, J. E. Neilson, S. E. Laubach, and K. J. Whidden, eds., Advances in Carbonate Exploration and Reservoir Analysis: Geological Society, London, Special Publications, v. 370, p. 83–109, doi:10.1144/SP370.1.

Dickson, J. A. D., 1966, Carbonate identification and genesis as revealed by staining: Journal of Sedimentary Petrology, v. 36, p. 491–505.

Faqira, M., M. Rademakers, and A. M. Afifi, 2009, New insights into the Hercynian Orogeny, and their implications for the Paleozoic Hydrocarbon System in the Arabian Plate: GeoArabia, v. 14, p. 199–228.

Friedman, G. M., 2007, Structurally controlled hydrothermal dolomite reservoir facies: An overview: Discussion: AAPG Bulletin, v. 91, p. 1339–1341.

Frizon de Lamotte, D., C. Raulin, N. Mouchot, J.-C. Wrobel-Daveau, C. Blanpied, and J.-C. Ringenbach, 2011, The southernmost margin of the Tethys realm during the Mesozoic and Cenozoic: Initial geometry and timing of the inversion processes: Tectonics, v. 30, no. 3, doi:10.1029/2010TC002691.

Gabellone, T., F. Whitaker, D. Katz, G. Griffiths, and M. Sonnenfeld, 2016, Controls on reflux dolomitization of epeiric-scale ramps: insights from reactive transport simulations of the Mississippian Madison Formation (Montana and Wyoming): Sedimentary Geology v.345, p. 85–102. https://doi.org/10.1016/j.sedgeo.2016.09.003.

Garcia-Fresca, B., F. J. Lucia, J. M. Sharp Jr., and C. Kerans, 2012, Outcrop-constrained hydrogeological simulations of brine reflux and early dolomitization of the Permian San Andres Formation: AAPG Bulletin, v. 96, p. 1757–1781, doi:10.1306/02071210123.

Goldstein, R. H., 2012, Fluid inclusion geothermometry in sedimentary systems: From paleoclimate to hydrothermal, in Analyzing the thermal history of sedimentary basins: Methods and case studies: Tulsa, Oklahoma, SEPM Special Publication 103, p. 45–63.

Goldstein, R. H., and T. J. Reynolds, 1994, Systematics of fluid inclusions in diagenetic minerals: Tulsa, Oklahoma, SEPM Short Course 31, 199 p.

Hill, C.A., V. J. Polyak, Y. Asmerom, and P. Provencio, 2016, Constraints on a Late Cretaceous uplift, denudation, and incision of the Grand Canyon region, southwestern Colorado Plateau, USA, from U-Pb dating of lacustrine limestone: Tectonics, v. 35, p. 896–906.

Hirani, J., E. Bastesen, A. Boyce, H. Corlett, R. Gawthorpe, C. Hollis, and F. Whitaker, 2018, Controls on the formation of stratabound dolostone bodies, Hammam Faraun Fault block, Gulf of Suez: Sedimentology, v. 65, p. 1973–2002, https://doi.org/10.1111/ sed.12454.

Hollis, C., E. Bastesen, A. Boyce, H. Corlett, R. Gawthorpe, J. Hirani, and F. Whitaker, 2017, Fault-controlled dolomitization in a rift basin: Geology, v. 45, p. 219–222, https://doi.org/10.1130/G38s394.1.

Hollis, C.J., et al., 2019, The Deep MIP contribution to PMIP4: Methodologies for selection, compilation and analysis of latest Paleocene and early Eocene climate proxy data, incorporating version 0.1 of the Deep MIP database: Geoscience Model Development, Discussion, v. 12, p. 1–98, https://doi.org/10.5194/gmd-12-3149-2019.

Hughes, G. W., 2004, Middle to Upper Jurassic Saudi Arabian carbonate petroleum reservoirs: Biostratigraphy, micropalaeontology and palaeoenvironments: GeoArabia, v. 9, p. 79–114.

Jones, G. D., and Y. Xiao, 2005, Dolomitization, anhydrite cementation, and porosity evolution in a reflux system: Insights from reactive transport models: AAPG Bulletin, v. 89, p. 577–601, doi:10.1306/12010404078

Kim, S. T., and J. R. O'Neil, 1997, Equilibrium and nonequilibrium oxygen isotope effect in synthetic carbonates: Geochimica et Cosmochimica Acta, v. 61, p. 3461–3475, doi:10.1016/S0016-7037(97)00169-5.

Kırmacı, M.Z., M. Yıldız, R. Kandemir, and T. Eroˇglu-Gümrük, 2018, Multistage dolomitization in late Jurassic–early cretaceous platform carbonates (Berdiga formation), Başoba Yayla (Trabzon), NE Turkey: implications of the generation of magmatic arc on dolomitization. Marine and Petroleum Geology, v. 89, p. 515–529.

Koeshidayatullah, A., H. Corlett, J. Stacey, P.K. Swart, A. Boyce, H. Robertson, F. Whitaker, and C. Hollis, 2020, Evaluating new fault-controlled hydrothermal dolomitization models: Insights from the Cambrian Dolomite, Western Canadian Sedimentary Basin: Sedimentology, v. 67, p. 2945–2973, https://doi.org/10.1111/sed.12729.

Land, L. S., 1980, The isotopic and trace element geochemistry of dolomite: the state of the art. In: Concepts and Models of Dolomitization (Eds D.L. Zenger, J.B. Dunham and R.L. Ethington): SEPM Special Publication 28, p. 87–110.

Land, L. S., 1985, The origin of massive dolomite: Journal of Geological Education, v. 33, p. 112–125.

Lavoie, D., G. Chi, P. Brennan-Alpert, A. Desrochers, and R. Bertrand, 2005, Hydrothermal dolomitization in the Lower Ordovician Romaine Formation of the Anticosti Basin: Significance for hydrocarbon exploration: Canadian Society of Petroleum Geologists Bulletin, v. 53, p. 454–472.

Laws, D. M. and M. Wilson, 1997, Tectonics and magmatism associated with Mesozoic passive continental margin development in the Middle East: Journal of the Geological Society, v. 154, p. 459–464.

Lindsay, R. F., D. L. Cantrell, G. W. Hughes, T. H. Keith, H. W. Mueller III, and D. Russell, 2006, Ghawar Arab-D Reservoir: Widespread porosity in shoaling-upward carbonate cycles: AAPG Memoir 88, p. 97–138.

Lohmann, K. C., 1988, Geochemical patterns of meteoric diagenetic systems and their applications to studies of paleokarst. In: P.W. Choquette and N.P. James (Editors), Paleokarst. Springer, Berlin, p. 55–80.

Lonnee, J., and H. G. Machel, 2006, Pervasive dolomitization with subsequent hydrothermal alteration in the Clarke Lake gas field, Middle Devonian Slave Point Formation, British Columbia, Canada: AAPG Bulletin, v. 90, p. 1739– 1761.

Lu, P., and D. Cantrell, 2016, Reactive transport modelling of reflux dolomitization in the Arab-D reservoir, Ghawar Field, Saudi Arabia: Sedimentology, v. 63, p. 865–892, doi:10.1111/sed.12241.

Lu, P., W. Tan, and D. Tang, 2017, Massive dolomite on the Upper Jurassic to Lower Cretaceous carbonate shelf, northeastern Saudi Arabia: Insights from reactive transport modeling: AAPG Annual Convention and Exhibition, Houston, Texas, April 2–5, 2017.

Luczaj, J. A., 2006, Evidence against the Dorag (mixing-zone) model for dolomitization along the Wisconsin arch— A case for hydrothermal diagenesis: AAPG Bulletin, v. 90, p. 1719–1738.

Luczaj, J. A., and R. H. Goldstein, 2000, Diagenesis of the Lower Permian Krider dolomite, southwest Kansas: fluid-inclusion, U-Pb, and fission-track evidence for reflux dolomitization during latest Permian time: Journal of Sedimentary Research, v. 70, p. 762–773.

Lukoczki G, J. Haas, J. M. Gregg, H. G. Machel, S. Kele, and C. M. John, 2019, Multi-phase dolomitization and recrystallization of Middle Triassic shallow marine–peritidal carbonates from the Mecsek Mts. (SW Hungary), as inferred from petrography, carbon, oxygen, strontium and clumped isotope data: Marine and Petroleum Geology, v. 101, p. 440–458.

Machel H. G., 1997, Recrystallization versus neomorphism, and the concept of "significant recrystallization" in dolomite research: Sedimentary Geology, v. 113, p. 161–168.

Machel, H. G., 1987, Baroque dolomite as a by-product of chemical compaction and thermochemical sulfate reduction: Geology, v. 15, p. 936–940.

Machel, H. G., 2004, Concepts and models of dolomitization: A critical reappraisal, in C. J. R. Braithwaite, G. Rizzi, and G. Darke, eds., The geometry and petrogenesis of dolomite hydrocarbon reservoirs: Geological Society (London) Special Publication 235, p. 7–63.

Machel, H. G., and E. W. Mountjoy, 1986, Chemistry and environments of dolomitization—a reappraisal: Earth Science Reviews, v. 23, p. 175–222.

Machel, H. G., and J. Lonnee, 2002, Hydrothermal dolomite— A product of poor definition and imagination: Sedimentary Geology, v. 152, p. 163–171.

Mansurbeg, H., M. Alsuwaidi, N. Salih, S. Shahrokhi, and S. Morad, 2021, Integration of stable isotopes, radiometric dating and microthermometry of baroque dolomite and host dolostones (Cretaceous carbonates, Kurdistan, Iraq): new insights into hydrothermal dolomitization: Marine and Petroleum Geology, v. 127, 104989.

Mattner, J., and M. Al-Husseini, 2002, Essay: Applied cyclo-stratigraphy for the Middle East E&P industry: GeoArabia, v. 7, p. 734–744.

McArthur, J.M., R. J. Howarth, and G.A. Shields, 2012, Strontium isotope stratigraphy in: Gradstein, F.M., Ogg, J.G. And Smith, A.G., Eds., A Geological Timescale 2012, Chapter 7, p. 127–144, Cambridge: Cambridge University Press.

McGuire, M. D., R. B. Koepnick, M. L. Markello, M. L. Stockton, L. E. Waite, M. J. Kompanik, M. J. Al-Shammary, and M. O. AlAmoudi, 1993, Importance of sequence stratigraphic concepts in development of reservoir architecture in Upper Jurassic grainstones, Hadriya and Hanifa reservoirs, Saudi Arabia: Proceedings of 8th Middle East Oil Show, Society of Petroleum Engineers, Paper 25578, p. 489–499.

Morad, S., I. S. Al-Aasm, F. H. Nader, A. Ceriani, M. Gasparrini, and H. Mansurbeg, 2012, Impact of diagenesis on the spatial and temporal distribution of reservoir quality in the Jurassic Arab D and C members, offshore Abu Dhabi oilfield, United Arab Emirates: GeoArabia, v. 17, p. 17–56.

Morrow, D. W., 1982, Diagenesis 2, dolomite—part 2, dolomitization models and ancient dolostones: Geoscience Canada, v. 9, p. 95–107.

Morrow, D. W., 1998, Regional subsurface dolomitization: Models and constraints: Geoscience Canada, v. 25, p. 57–70.

Mountjoy, E. W., and J. E. Amthor, 1994, Has burial dolomitization come of age? Some answers from the Western Canada sedimentary basin, in B. Purser, M. Tucker, and D. Zenger, eds., Dolomites: International Association of Sedimentologists Special Publication 21, p. 203–229.

Murris, R. J., 1980, Middle East stratigraphic evolution and oil habitat: AAPG Bulletin, v. 64, p. 597–618.

Nader, F.H., R. Swennen, and R. Ellam, 2004 Reflux stratabound dolostone and hydrothermal volcanism-associated dolostone: a two-stage dolomitization model (Jurassic, Lebanon): Sedimentology, v. 51, p. 339–360.

Paton, C., J. D. Woodhead, J. C. Hellstrom, J. M. Hergt, A. Greig, and R. Maas, 2010, Improved laser ablation U-Pb zircon geochronology through robust downhole fractionation correction: Geochemistry, Geophysics, Geosystems, v. 11 (3), doi: 10.1029/2009GC002618.

Paton, C., J. Hellstrom, B. Paul, J. Woodhead, and J. Hergt, 2011, Iolite: Freeware for the visualization and processing of mass spectrometric data: Royal Society of Chemistry, v. 26, p. 2508−2518, doi: 10.1039/C1JA10172B.

Qing, H., and E. W. Mountjoy, 1994, Formation of coarsely crystalline, hydrothermal dolomite reservoirs in the Presqu'ile Barrier, Western Canada sedimentary basin: AAPG Bulletin, v. 78, p. 55–77.

Roberts, N. M., E. T. Rasbury, R. R. Parrish, C. J. Smith, M. S. Horstwood, and D. J. Condon, 2017, A calcite reference material for LA-ICP-MS U-Pb geochronology. Geochemistry, Geophysics, Geosystems, v. 18, p. 2807–2814.

Rosales, I., L. Pomar, and S. F. Al-Awwad, 2018, Microfacies, diagenesis and oil emplacement of the Upper Jurassic Arab-D carbonate reservoir in an oil field in central Saudi Arabia (Khurais Complex): Marine and Petroleum Geology, v. 96, p. 551–576, https://doi. org/10.1016/j.marpetgeo.2018.05.010.

Sharland, P. R., R. Archer, D. M. Casey, R. B. Davies, S. H. Hall, A. P. Heward, A. D. Horbury and M. D. Simmons, 2001, Arabian Plate Sequence Stratigraphy: GeoArabia Special Publication v. 2, 371 p

Sharp, Z., 2006, Principles of Stable Isotope Geochemistry, Prentice-Hall, Upper Baroque River, N. J., 344 p.

Sheppard, S. M. F., and H. P. Schwartz, 1970, Fractionation of carbon and oxygen isotopes and magnesium between co-existing metamorphic calcite and dolomite. Contributions to Mineralogy and Petrology, v. 26, p. 161–98.

Smith, L. B. Jr., 2006, Origin and reservoir characteristics of Upper Ordovician Trenton–Black River hydrothermal dolomite reservoirs in New York: AAPG Bulletin, v. 90, p. 1691–1718.

Stacey, J., H. Corlett, G. Holland, A. Koeshidayatullah, C. Cao, P. Swart, S. Crowley, and C. Hollis, 2021, Regional fault-controlled shallow dolomitization of the Middle Cambrian Cathedral Formation by hydrothermal fluids fluxed through a basal clastic aquifer: Geological Society of America Bulletin, v. 133, p. 2235–2377, https://doi.org/10.1130/B35927.1

Stewart, S. A., 2018, Hormuz salt distribution and influence on structural style in NE Saudi Arabia: Petroleum Geoscience, v. 24, p. 143–158, https://doi.org/10.1144/petgeo2017-011.

Tera, F., and G. J. Wasserburg, 1972, U-Th-Pb systematics in three Apollo 14 basalts and the problem of initial Pb in lunar rocks: Earth and Planetary Science Letters, v. 14, p. 281–304.

Urey, H., 1947, The thermodynamic properties of isotopic substances: Journal of the Chemical Society, v. 99, p. 562–581.

Veizer, J., D. Ala, K. Azmy, P. Bruckschen, D. Buhl, F. Bruhn, G. A. F. Carden, A. Diener, S. Ebneth, Y. Godderis, T. Jasper, C. Korte, F. Pawellek, O. G. Podlaha, and H. Strauss, 1999, $^{87}Sr/^{86}Sr$, $\delta^{13}C$ and $\delta^{18}O$ evolution of Phanerozoic seawater: Chemical Geology, v. 161, p. 59–88.

Vermeesch, P., 2018, IsoplotR: A free and open toolbox for geochronology: Geoscience Frontiers, v. 9, p. 1479–1493.

Warren J., 2000, Dolomite: Occurrence, evolution and economically important associations: Earth-Science Reviews, v. 52, p. 1–81.

Whitaker, F. F., and Y. Xiao, 2010, Reactive transport modeling of early burial dolomitization of carbonate platforms by geothermal convection: AAPG Bulletin, v. 94, p. 889–917, doi:10.1306/12090909075

Whitaker, F. F., P. L. Smart, and G. D. Jones, 2004, Dolomitization: From conceptual to numerical models, in C. Braithwaite, G. Rizzi, and G. Darke, eds., The geometry and petrogenesis of dolomite hydrocarbon reservoirs: Geological Society (London) Special Publication 235, p. 99–139.

White, D. E., 1957, Thermal waters of volcanic origin: Geological Society of America Bulletin, v. 68, p. 1637– 1658.

White, T., and I. S. Al-Aasm, 1997, Hydrothermal dolomitization of the Mississippian Upper Debolt Formation, Sikanni gas field, northeastern British Columbia, Canada: Bulletin of Canadian Petroleum Geology, v. 45, p. 297– 316.

Woodhead, J. D., and J. M. Hergt, 2001, Strontium, Neodymium and Lead isotope analyses of NIST glass certified reference materials: SRM 610, 612, 614. Geostandards and Geoanalytical Research, v. 25, p. 261–266, doi:10.1111/j.1751-908x.2001.tb00601.x.

Zenger, D. H., J. B. Dunham, and R. L. Ethington, eds., 1980, Concepts and models of dolomitization: SEPM Special Publication 28, 320 p.

Ziegler, M. A., 2001, Late Permian to Holocene paleofacies evolution of the Arabian plate and its hydrocarbon occurrences: GeoArabia, v. 6, p. 445–504.

Chapter 3

Multiple Episodes of Dolomite Recrystallization in the Hydrothermal Realm: Jurassic Arab Formation, Saudi Arabia

ABSTRACT

Upper Jurassic carbonates in northeast Saudi Arabia contain large volumes of high-temperature dolostones that are composed of equant and baroque dolomites. Equant and baroque dolomites have either uniformly dull cathodoluminescence (CL) (likely attesting to little or no recrystallization) and/or mottled CL (attesting to recrystallization), with the mottled dolomites dominating. Stable isotopic and fluid inclusion values in equant and baroque dolomites, as well as in dull CL and mottled CL dolomites, are nearly identical, indicating precipitation of equant and baroque forms and their recrystallization, are all related to the same processes. Dolostone as a whole has mean $\delta^{18}O$ and $\delta^{13}C$ values of -9.3‰ and 2.8‰, respectively, and fluid inclusion mean homogenization and melting of ice temperatures of 103.5ºC and -24.2ºC (25.1 wt.% NaCl eq.), respectively. Strontium isotope ratios ($^{87}Sr/^{86}Sr$) range from 0.70761 to 0.70779, significantly higher than Late Jurassic seawater. These values, compared to the burial history, indicate hydrothermal conditions during both dolomite precipitation and recrystallization. Uranium–lead (U–Pb) dating on dolomite yielded ages from 52.8 ± 8.7 Ma (recorded in equant dolomite with dull CL) to 11.9 ± 2.4 Ma (recorded in baroque dolomite with mottled CL), whereas, the oldest age obtained in baroque dolomite is 44.8 ± 7.0 Ma, also recorded in a dolomite crystal with dull CL. Thus, at least some equant dolomite predates baroque dolomite, and some dull CL crystals predate mottled ones. Nevertheless, the majority of U–Pb dates on equant and baroque with dull and mottled CL patterns overlap; indicating a temporal connection between the initial hydrothermal formation of equant and baroque dolomites as well as between continued precipitation and recrystallization under hydrothermal conditions. The observations indicate hydrothermal conditions can both precipitate dolomite and recrystallize previously precipitated hydrothermal dolomite.

3.1 INTRODUCTION

Dolomite recrystallization is a common diagenetic process than can occur in most diagenetic realms and can commence almost immediately after initial dolomite formation. The literature includes many examples of recrystallized dolomite, many of which are young, Paleocene–Eocene or even younger, that experienced intensive recrystallization shortly after initial dolomite precipitation and at shallow depth (e.g., Ryan et al., 2022). Processes of initial dolomite precipitation and subsequent recrystallization can potentially alternate, or even overlap, during the duration of dolomite paragenesis. Examples of young recrystallized dolomites of Holocene age (< 3000 years old) have been reported from Ambergris Caye, Belize (Gregg et al., 1992); and older Paleozoic examples of dolomite recrystallization include those of the Devonian carbonates of the Western Canada sedimentary basin (Lonnee and Machel, 2006). In the latter example, recrystallization altered burial dolomites in the presence of hydrothermal fluids at elevated temperatures (Lonnee and Machel, 2006). Examples of recrystallized dolomite are abundant in the geological record (e.g., Banner et al., 1988; Spötl and Burns, 1991; Kupecz and Land, 1994; Durocher and Al-Aasm, 1997; Lukoczki et al., 2019) with Land (1982) stating that "*few (if any) dolomitized rocks exist as they were originally deposited. Most are from two or more processes of formation, and at least one stabilization (recrystallization) event".* This statement, although it highlights the importance and wide spread of recrystallization, might overstate the problem of recrystallization, as there are many examples of pristine, unrecrystallized dolomites in the geological record and in a variety of settings (e.g., Amthor et al., 1993; Al-Aasam, 2000).

Because dolomite recrystallization is capable of causing major alteration to the petrographic and geochemical attributes of the original dolomite (Machel, 1997), there are typically some ambiguities in interpreting dolomite origin. Failure to distinguish between ‘pristine’

and altered dolomite signatures will lead to a flawed interpretation of the origin and timing of dolomite. This is not trivial, as an accurate identification of the origin of dolomite is essential to understand the controls on the lateral and temporal distribution of dolomite in an area. The latter is especially important when such dolomites have an economic importance.

The Jurassic system in Saudi Arabia has immense economic importance, hosting a large fraction of global oil reserves. In the northeast of Saudi Arabia, the Jurassic system contains regionally extensive, high-temperature dolomites that affect the reservoir properties. The dolomite distribution exhibits a discordant relationship to stratigraphic units, mostly cross-cutting some bedded anhydrite units in some locations (Broomhall and Allan, 1987; Lu et al., 2017). Petrographic and geochemical analyses of the dolomites reveal the absence of any early attributes of dolomitization; likely indicating either a late formation of dolomite, a late recrystallization of all dolomites at depth, or a combination of both.

This study employs an integrated analysis of petrographic and geochemical data constrained by U–Pb dating to study the origin of the dolomite in this area, and evaluate the setting and extent of its recrystallization. The novel application of U–Pb dating, in particular, will provide a practical tool to address the problem of dolomite recrystallization in general.

3.2 GEOLOGICAL SETTING

Sedimentation of the Jurassic carbonates in Saudi Arabia, and across neighboring countries, occurred during a tectonically quiescent time that favored the eustatically controlled deposition of thick carbonate and evaporite successions (Sharland et al., 2001; Al-Husseini, 2009). Couplets of carbonate–evaporite successions that are mappable across the majority of the region characterize the Upper Jurassic Series (Figure 3.1; Sharland et al., 2001; Al-Husseini, 2009). The

carbonates are predominantly limestone but, in some areas, there are greater percentages of dolomite. Such an area is the subject of this study (Figure 3.1) where dolomite represents >80% of all carbonates.

Subsequent to sedimentation, the Jurassic strata underwent a rapid and constant burial phase through the entire Cretaceous to recent without any exposure or major uplifts, and present-day depths are the maximum burial depths the rocks have reached (Abu-Ali and Littke, 2005). The rocks in the study area have experienced extensive late diagenetic alteration. This is in part due to the close proximity to known regional fault/fold axes that are recognized to have been active during much of the diagenetic history of these rocks and might have acted as fluid conduits to facilitate alteration (Faqira et al., 2009; Lu et al., 2017; Stewart, 2018). Consequently, the overall diagenetic history of the Jurassic carbonates in the study area is dissimilar from most of the Jurassic carbonates elsewhere, including in Ghawar Field (Broomhall and Allan, 1987; Cantrell et al., 2004; Swart et al., 2005, 2016; Lu and Cantrell, 2016).

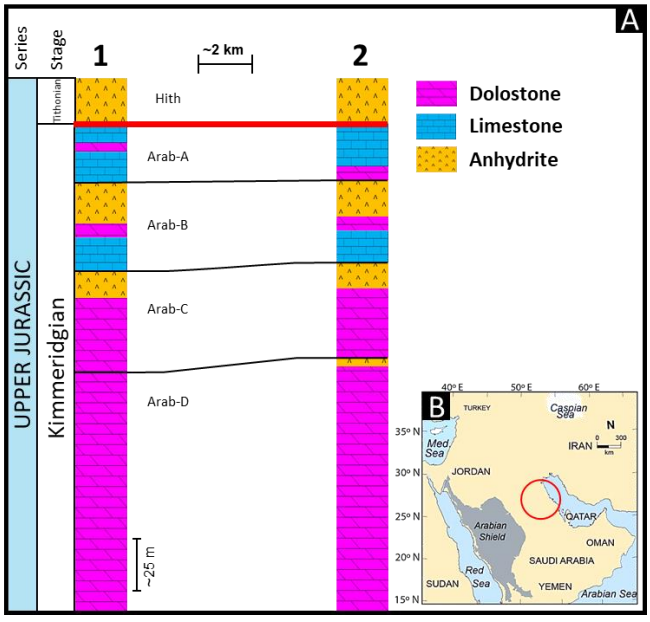

Figure 3.1. (A) Lithological correlation of Arab Formation in the studied wells. The base of the Tithonian Hith (red line) is used as a datum. (B) Base map of Saudi Arabia and neighboring countries, showing the general area of interest in NE Saudi Arabia; due to the proprietary nature of the data, the exact locations of the wells cannot be provided. Map is from Eltom (2020).

3.3 METHODS

This study utilizes a dataset that includes 103 dolostone samples (78 thin and 25 thick sections) taken directly from two subsurface cores located in northeast Saudi Arabia that sampled the Jurassic Arab Formation (Figure 3.1). An additional 42 limestone thin sections were used to help with establishing the overall paragenesis in the section. This study focuses on dolomite recrystallization and relies mostly on the dolostone samples. Prior to plane light petrographic analysis, all thin and thick sections were fully scanned using a DP74 camera attached to an Olympus System (Olympus Corp., Japan) capable of automatically scanning petrographic thin sections. Samples were stained with Alizarin red S to distinguish calcite from other minerals and with potassium ferricyanide to distinguish ferroan from non-ferroan carbonates (Dickson, 1966).

Cathodoluminescence (CL) microscopy was performed on >50 polished thin and thick sections as well as rock chips to decipher the CL attributes of the different dolomite fabrics in dolostone. All analyses were done under a Leitz SM-LUX–POL CL microscope and a Clmk5 imaging system (Cambridge Image Technology Ltd., UK), with the CL unit running a gun current of 350–400 mA, an accelerating potential of 13.5–14.5 kV, and a chamber pressure of <0.05 torr.

Stable isotope analyses were performed on 78 dolostone microsamples (~50–100 μg) taken directly from thin sections from the two cores. An additional 29 analyses on limestone and 5 on dolomite cement in limestone were also taken for reference. All analyses were performed at the University of Kansas Stable Isotope Lab (KPESIL) using a Kiel IV carbonate reaction device and dual inlet Finnigan MAT253 mass spectrometer (Thermo Fisher Scientific, USA). The analyses followed a standard lab procedure where powdered microsamples were heated to release any volatiles, and then were reacted with 100% phosphoric acid at 70°C for 9 min. Values are reported

in per mil (‰) and relative to Vienna Peedee belemnite (VPDB), with a reported precision better than 0.05‰ for both $\delta^{13}C$ and $\delta^{18}O$.

Fluid inclusion petrography and microthermometry analyses were done using a Linkam THMSG 600 stage (Linkam Scientific Instruments, Ltd., UK) and following the procedure of Goldstein and Reynolds (1994). Twenty-five fluid inclusion assemblages (FIAs) were measured from polished dolostone thick sections. The fluid inclusion assemblages include a total of 259 homogenization and 163 melting temperatures of ice (Tm_{ice}).

Strontium isotope ratios ($^{87}Sr/^{86}Sr$) were analyzed for 11 samples (6 dolostone, 3 limestone, and 2 anhydrite). Due to the large sampling size (powdered samples are 10–20 mg), all $^{87}Sr/^{86}Sr$ values are considered 'whole-rock' analyses. Analyses were conducted using a Sector 54 thermal ionization mass spectrometer at the University of Kansas and the NIST 987 reference value of 0.71248 was used to normalize all $^{87}Sr/^{86}Sr$ data and used 3.5-N nitric acid (HNO_3) to dissolve the powder, followed by the separation of Sr using a Sr-spec-filled ion-exchange column via standard column chromatography and evaporated until dry.

Uranium–lead (U–Pb) analyses were conducted on 22 dolomite textural domains that include different dolomite phases (equant and baroque, replacive and cement). The analysis used laser ablation inductively coupled plasma mass spectrometry (LA–ICP–MS) with an Element2 ICP–MS attached to a Photon Machines Analyte G2 193-nm ArF excimer laser ablation system (Thermo Fisher Scientific, USA), at the University of Kansas Isotope Geochemistry Laboratory. Circular spots (130 μm diameter) in individual dolomite phases were ablated at a fluency of 2.7 J cm^{-2} and a repetition rate of 10 Hz, resulting in 20-μm deep pits. The ablated material was carried to the ICP–MS in 1.1-l/min He gas and tied in with ~1.1-l/min Ar gas before entry into the plasma torch. Correction for drift and isotopic and downhole fractionation was done by bracketing the

measurements of the unknowns with a known Pb isotopic ratio glass reference material (SRM NIST614; Woodhead and Hergt, 2001). Uranium–lead elemental fractionation was corrected offline with an in-house Excel spreadsheet, using the calcite reference material DBTL (Hill et al., 2016) for age calibration, and WC1 (Roberts et al., 2017) for validation of the calibration. The data reduction was performed using the U–Pb geochron3 data reduction scheme in IOLITE v. 2.5 (Paton et al., 2010, 2011). Analyses for separate analytical sessions yielded results within 99.1% of the published value for WC1. Tera–Wasserburg Concordia diagrams (Tera and Wasserburg, 1972) were created using IsoplotR (Vermeesch, 2018; http://isoplotr.geo.utexas.edu/) from the $^{238}U/^{206}Pb$ and $^{207}Pb/^{206}Pb$ values of individual dolomite and limestone phases and to calculate the intercept ages.

3.4 RESULTS

3.4.1 Dolostone distribution and general dolomite attributes

The Arab carbonates in the two cored wells have ~75% dolostone and ~25% limestone, with the latter only encountered in the uppermost portion of the reservoir (Figure 3.1A). All the limestone encountered is almost entirely calcite with no replacive dolomite. Some limestone samples, however, contain up to 18% dolomite cement. All dolostone samples contain only dolomite and anhydrite with no calcite. No intermediate lithology was observed (i.e., no dolomitic limestone or calcitic dolostone). Dolostone–to–limestone ratio increases in wells to the north and outside of the study area, with limestone and much of the bedded anhydrite being absent in those wells. Analysis of those wells is not included here but can be found in Chapter 2.

The majority of the replacive dolomite exhibits fabric-preserving textures (~82% of all samples or 64 out of 78 samples are dominated by fabric-preserving dolomite, Figure 3.2A). Fabric-destructive textures are also common but dominate only 14 samples (~18%). Dolomite crystal sizes vary significantly from one sample to another, and even within the same sample. Coarse (100–500 μm) to very coarse (>500 μm) crystal sizes dominate all dolostones, and together account for ~72% of all crystal size populations (Figure 3.2B). Collectively, ~60% of all dolomite crystals analyzed display a nonplanar (anhedral) crystal boundary (Figure 3.2C). Subhedral and euhedral (planar) are mostly limited to areas near pore spaces.

Morphologically, all dolomites encountered in this study (preserving or destructive) can be classified as either equant (ED, ~58% of all dolomites; Figure 3.2D) or baroque (BD, ~42% of all dolomite; Figure 3.2D). Equant and baroque dolomite intercalate with each other stratigraphically, and can co-occur in the same thin sections (Figure 3.3A). The two types of dolomites show no obvious relationship to stratigraphic members. Rather, ED and BD occur in all stratigraphic members (Arab-D to Arab-A). Both ED and BD are either a replacement or a cement phase. All dolomite phases are non-ferroan as they do not stain with potassium ferricyanide.

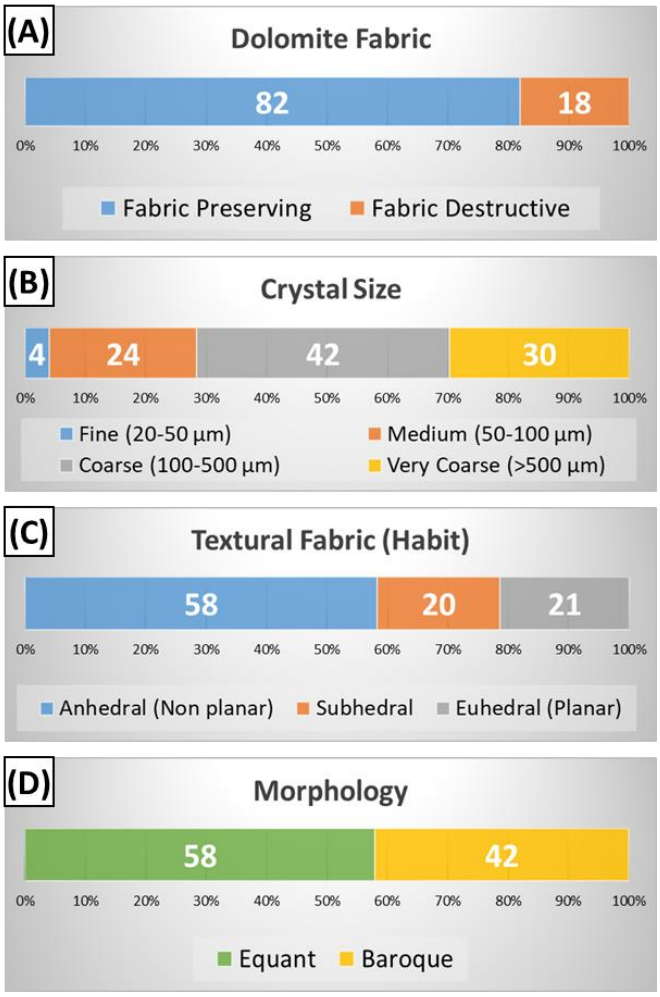

Figure 3.2. General petrographic attributes of dolostones and dolomites. All values are relative % in all 78 dolostone samples.

3.4.2 Equant dolomite (ED)

This dolomite is both a replacement and a cement. Replacive equant dolomite is dominated by nonplanar (anhedral crystals) with sizes of most crystals ranging from 100 to 300 µm. This phase commonly retains the size and overall shape of the grain it has replaced and is typically fluid-inclusion poor, especially in the core of the crystal. A fabric-preserving texture (Figure 3.3B) dominates. Fabric-destructive texture is less common and it is typically interlocking, hydrocarbon-stained, mosaics of relatively uniform dolomite crystals (~200 µm in size; Figure 3.3A, C). All

equant dolomite crystals have unit extinction (i.e., lacks undulose extinction in cross-polarized light)

Equant dolomite cement is less common, and it is either blocky interparticle/intercrystal cement (Figure 3.3B) or a cement overgrowth (Figure 3.3D). The interparticle cement is more common; it is composed of microcrystalline crystals (<10 μm) that filled pores partially or completely. This cement type is found in large quantities in dolostone samples with well-preserved original textures, such as the oolitic dolograinstone (Figure 3.3B). On the other hand, the cement overgrowth (Figure 3.3D) occurs as small dolomite crystals (~100 μm) that overgrew a previously dolomitized grain. This cement was observed in large quantities in peloidal-skeletal dolograinstone facies (Figure 3.3D) where some interparticle pores remained open even after dolomitization.

3.4.3 Baroque dolomite (BD)

Similar to the equant dolomite, baroque dolomite is either a replacement or a cement phase. The replacive baroque dolomite is more common and exhibits either fabric-preserving or fabric-destructive textures with the latter dominating. Unlike the replacive equant dolomite, which replaced individual grains, replacive baroque dolomite replaced patches of grains and cement and formed poikilotopic fabrics (Figure 3.3E, F), with no relationship to the original fabrics, even when the replacement is fabric preserving. Consequently, the sizes of baroque dolomite crystals are much larger than the original grains (Figure 3.3E), with sizes ranging from ~500 μm to over 2000 μm. Most replacive baroque dolomite lacks well-defined curved (saddle) crystal faces, typical of baroque dolomite, and exhibits mostly non-planar (anhedral) crystal boundaries. Recognizing this type of dolomite was still easy under cross-polarized light as most crystals show clear sweeping

(undulose) extinction (Figure 3.3F). This phase is fluid-inclusion rich and appears cloudy in thin section.

Baroque dolomite cement occurs as a cement overgrowth (Figure 3.3G) or as a void-filling cement phase composed of large baroque/saddle crystals (Figure 3.3H). Some baroque dolomite examples are in vugs, solution-enlarged fractures, and have large (>1000 μm), white, hydrocarbon-free crystals, displaying well-developed curved (saddle) crystal faces and cleavages (Figures 3.3H, 3.4A, B). Margins of these vugs and solution-enlarged fractures cut across older equant dolomites (Figure 3.4B). Baroque dolomite cement is the least common of all dolomite fabrics, and is limited to thin (up to 10 cm thick) horizons that cross-cut the more common replacive equant and baroque dolomite. Because not all baroque dolomites exhibit the curved (saddle) crystal faces, typical of this type of dolomite, we describe this dolomite as baroque rather than saddle, albeit saddle crystals are common in some cement phases (Figure 3.3G, H).

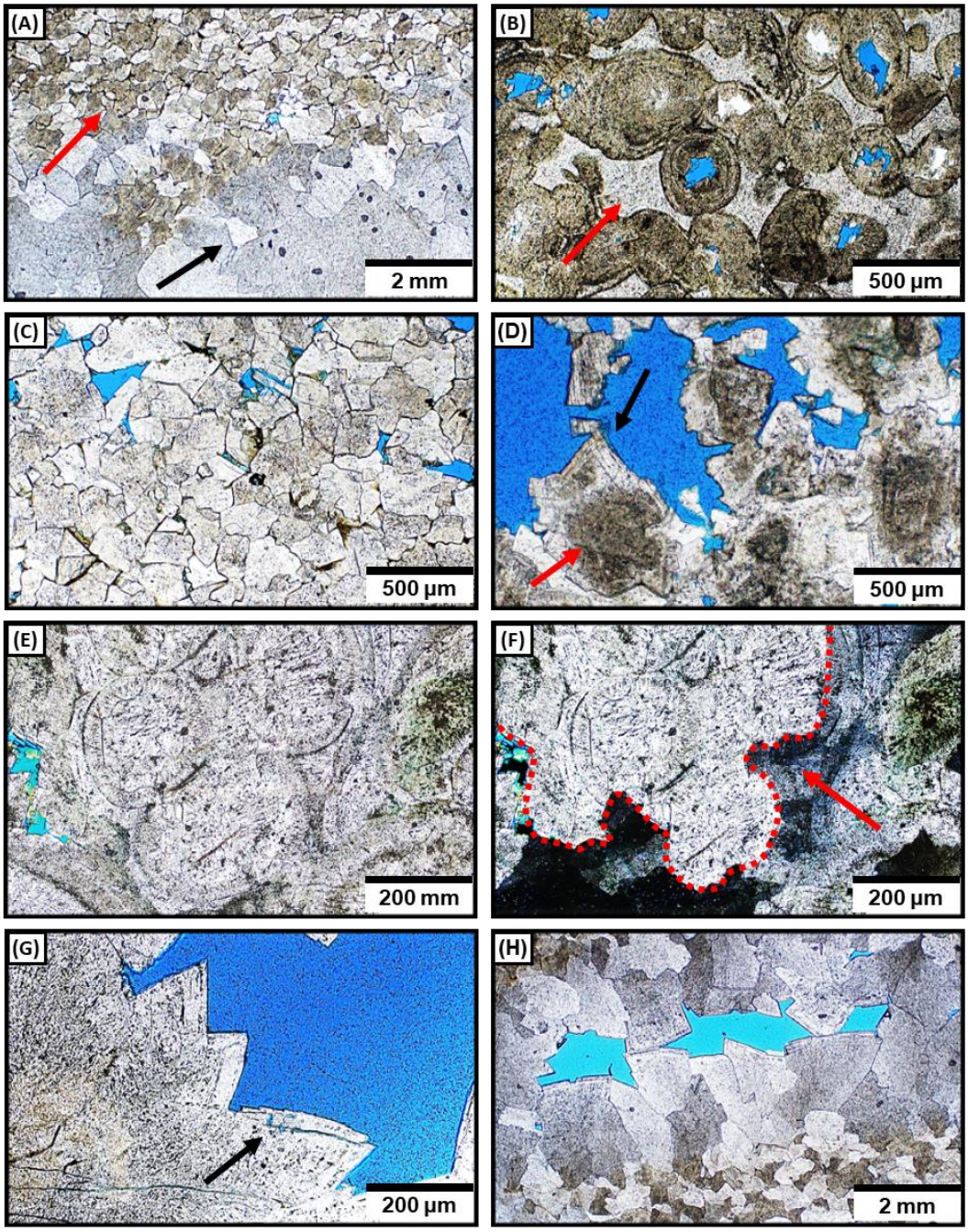

Figure 3.3. Photomicrographs of different dolomite textures encountered in the study. (A) Hydrocarbon-stained equant dolomite ED (red arrow) and baroque dolomite BD (black arrow). (B) Fabric-preserving equant dolomite of oolitic dolograinstone; the sample is 100% dolomite; note the blocky equant dolomite cement (arrow). (C) Fabric-destructive equant dolomite showing interlocking mosaic with crystal sizes between 100 µm and 300 µm. (D) Replacive equant dolomite (red arrow) and equant cement overgrowth (black arrow). Note the fabric preserving nature of dolomite. (E, F) Plane and cross-polarized light images of baroque dolomite replacing patches of grains and cement. Red arrow and red dotted outline in (F) show the outline of one baroque crystal that replaced multiple ooid grains and the cement in between. (G, H) Saddle dolomite cement partially filling some large vugs and voids. The void-filling baroque dolomite exhibits the most pristine look and shows clear crystal curvatures. This phase cross-cuts the hydrocarbon-stained replacive equant dolomite. Note, many of the saddle dolomites also include meso-micropores some of which are distributed along solution-enlarged fractures (black arrow in G). These pores are also observed in equant dolomites.

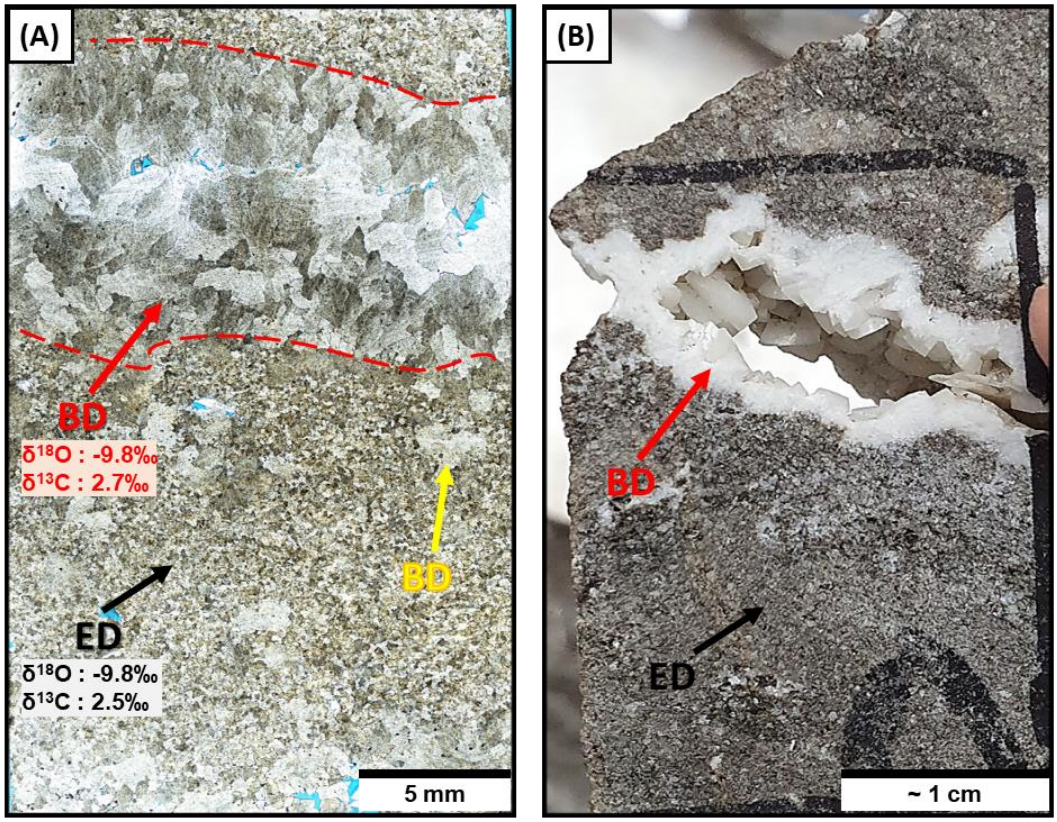

Figure 3.4. (A) Full thin-section scan of a fabric destructive dolomite that includes replacive equant dolomite (ED; black arrow), replacive baroque dolomite (BD; yellow arrow), and void-filling baroque dolomite (BD; red arrow, red dashed outline). The BD cross-cuts equant dolomites. Note the nearly identical stable isotopic values for BD and ED. (B) Hand specimen of equant dolomite (ED; black arrow) that is cross-cut by a solution-enlarged fracture, which is partially filled by baroque dolomite cement (BD; red arrow).

3.4.4 Cathodoluminescence

All dolomite crystals can be grouped, based on their CL pattern, into either uniformly dull (Figure 3.5A) or mottled (Figure 3.5B) crystals. Uniformly dull and mottled crystals co-occur in all samples (Figure 3.5C) with the latter overwhelmingly dominating (a rough estimate that >80% of all crystals are mottled in CL). Crystals with uniformly dull CL (Figure 3.5A) are characterized by a dark to faint orangish color in CL. In contrast, mottled crystals show an abundance of bright reddish spots and some dully luminescent spots within an overall dull–moderate CL crystal (Figure

3.5B). The degree of mottling also varies from one crystal to another with many crystals showing intensive mottling of crystals characterized by a near dominance of the bright reddish patchy CL spots (Figure 3.5D).

There is no relationship between CL patterns and dolomite fabrics as crystals with dull and mottled CL were observed in both equant (Figure 3.5E, F) and baroque (Figure 3.5G, H) dolomites. Similarly, both replacive and cement phases (Figure 3.5E, F) also include dull and mottled CL patterns. Some mottled baroque dolomite crystals show an irregular zonation, characterized by relatively thin very dull and dull outer growth zone (or cement overgrowth), which line some dolomite crystals (Figure 3.5G, H).

Finally, many of the dolomite crystals and especially the mottled ones, show dissolution, and meso-micropores (~5 to ~30 μm in size) in thick sections. Many of these small pores are at or near the bright reddish spots (Figure 3.5E, G). Some of the pores are also observed in the uniformly dull crystals. Some of these pores are distributed along solution-enlarged fractures. Other pores are molds of particular areas of dolomite growth zones. Some are partially filled with infillings of dolomite cement.

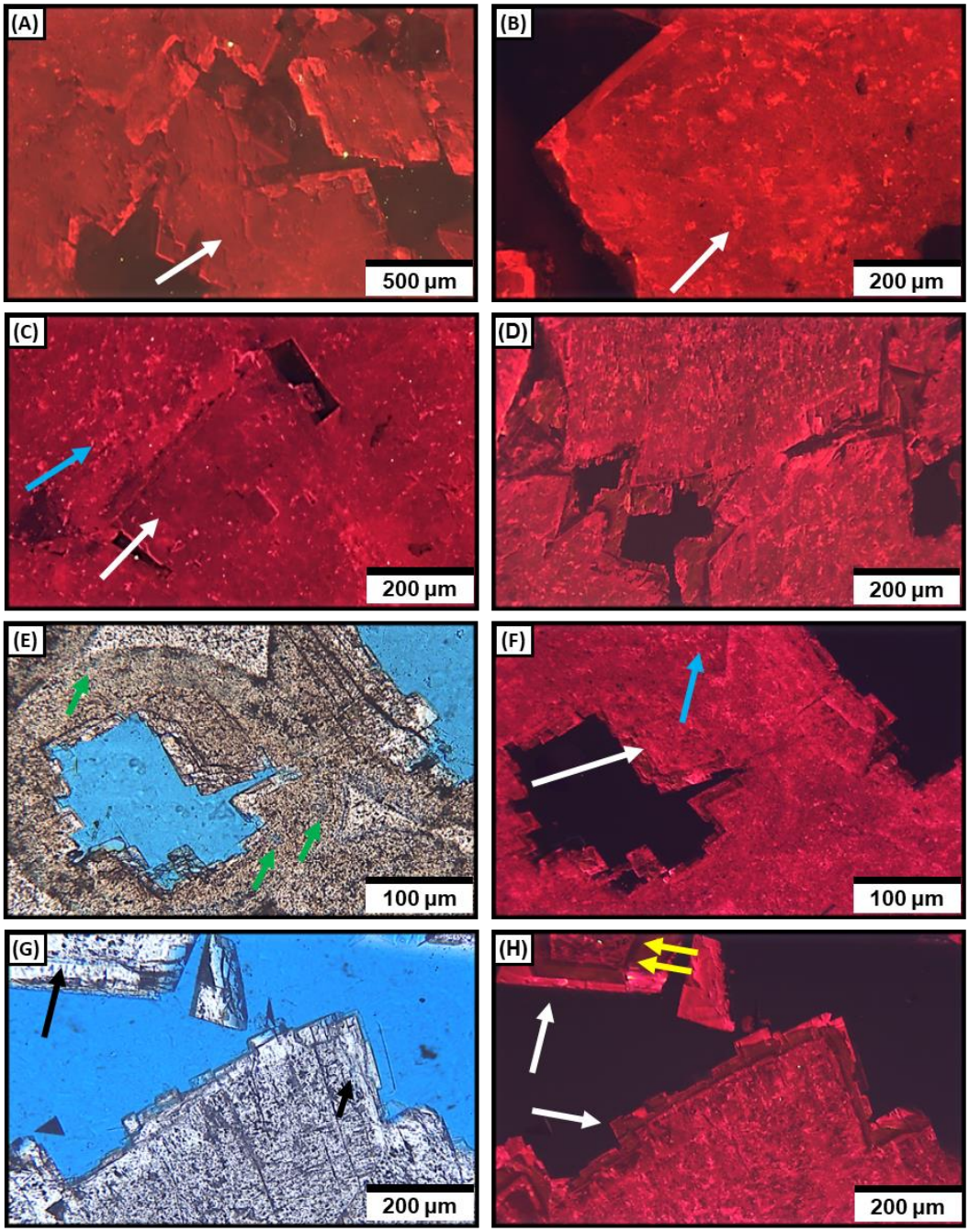

Figure 3.5. Photomicrographs of different cathodoluminescence patterns encountered in the dolostone. (A) Equant dolomite crystal with dull to faint red luminescence. (B) Corroded baroque dolomite crystal with intense bright yellowish red luminescence in the inner core (intense mottling). (C) Example of dull (white arrow) and mottled (blue arrow) dolomite crystals. (D) Mottled baroque dolomite crystals with pervasive yellowish red patchy spots in the crystals. (E, F) Paired plane-light and CL images of fabric-preserving equant dolomite showing mottled crystals in the replaced grain (white arrow) and adjacent cement (blue arrow). Note some mesopores in (E; green arrows). (G, H) Paired plane-light and CL images of baroque dolomite crystals with mottling. Note the very dull (yellow arrows) and dull outer (white arrows) growth zone in H. This feature was observed in a limited number of samples. Dissolution and meso-micropores are also present (black arrows in G).

3.4.5 Fluid inclusion petrography and microthermometry

Primary two-phase (aqueous-vapor) fluid inclusions are abundant in both equant and baroque dolomite and in dull and mottled crystals. Fluid inclusions in the dolomite have a relatively narrow range of homogenization and melting of ice temperatures. Homogenization temperatures (Th) (n = 259) range from 83.5 to 117.1ºC with a mean of 103.5ºC, and melting temperatures of ice (Tm_{ice}) (n = 163) range from -27.9 to -19.9ºC, with a mean of -24.2ºC. When converting the Tm_{ice} values to salinity (Bodnar, 1992), the dolostones range in salinity from 22.3 to 27.4 wt. % NaCl eq. with a mean of 25.1 wt. % NaCl eq..

Equant and baroque dolomite have nearly identical ranges and means of Th, with mean temperatures of 103.4ºC and 103.9ºC for equant and baroque dolomites, respectively. Similarly, Tm_{ice} values, and thus salinity, for the two dolomite fabrics are identical (a mean salinity of 25.1 wt. % NaCl eq. for both equant and baroque dolomite). As a result, microthermometric data for the two dolomite fabrics overlap each other in the salinity vs Th space (Figure 3.6A; Table 3.1). The narrow range observed in Th and salinity in dolostone is not related to whether the crystal is dull or mottled in CL either, as both dull and mottled crystals record nearly identical ranges and means of both Th and salinity (Figure 3.6B; Table 3.1).

Despite the overall comparable means of homogenization temperatures and salinity for equant and baroque dolomite, individual fluid inclusion assemblages (FIAs) show a range of homogenization temperatures and salinity (Figure 3.7). Most FIAs yield consistent Th, using the designation of Goldstein and Reynolds (1994; 90% of the inclusions are within 10–15ºC), indicating the fluid inclusions have not thermally reequilibrated to any significant degree. One consistent FIA in an equant dolomite sample with dull CL, for example, has a temperature range from 91.9ºC to 117.0ºC, a range of ~25.0ºC (FIA # 6; Figure 3.7A). Similarly, one FIA in baroque

dolomite with dull CL has a temperature range from 83.5ºC to 114.2ºC, a range of ~31.0ºC (FIA# 1; Figure 3.7C). Therefore, while ~93% of all fluid inclusions have homogenization temperatures between 95.0ºC and 110.0ºC, there are fluid inclusions, with lower or higher temperatures, existing in the same FIAs where the dominating temperatures fall between the 95.0–110ºC range. Thus, while the means and overall ranges are similar between equant and baroque dolomites, as well as between mottled and dull dolomites, individual assemblages still capture a wide range of fluid inclusion values.

Table 3.1: Fluid Inclusion Statistics for Dolostone

	Th (ºc)				Tm_{ice} (ºc)				Salinity (%)		
Groups	**Count**	**Min**	**Max**	**Mean**	**Count**	**Min**	**Max**	**Mean**	**Min**	**Max**	**Mean**
All Dolostone	259	83.5	117.1	103.5	163	-27.9	-19.9	-24.2	22.3	27.4	25.1
Equant Dolomite (ED)	**187**	**91.8**	**117.1**	**103.4**	**121**	**-27.9**	**-20.2**	**-24.2**	**22.5**	**27.4**	**25.1**
ED (Dull)	53	91.9	117.0	104.1	42	-27.9	-21.6	-24.3	23.4	27.4	25.1
ED (Mottled)	134	91.8	117.1	103.1	79	-27.0	-20.2	-24.2	22.5	26.8	25.1
Baroque Dolomite (BD)	**72**	**83.5**	**117.0**	**103.9**	**42**	**-26.5**	**-19.9**	**-24.2**	**22.3**	**26.5**	**25.1**
BD (Dull)	24	83.5	117.0	102.8	9	-25.5	-23.8	-24.5	24.8	25.9	25.2
BD (Mottled)	48	93.3	111.5	104.4	33	-26.5	-19.9	-24.2	22.3	26.5	25.1
All Dull Dolomite	77	83.5	117.0	103.7	51	-27.9	-21.6	-24.3	23.4	27.4	25.1
All Mottled Dolomite	182	91.8	117.1	103.5	112	-27.0	-19.9	-24.2	22.3	26.8	25.1

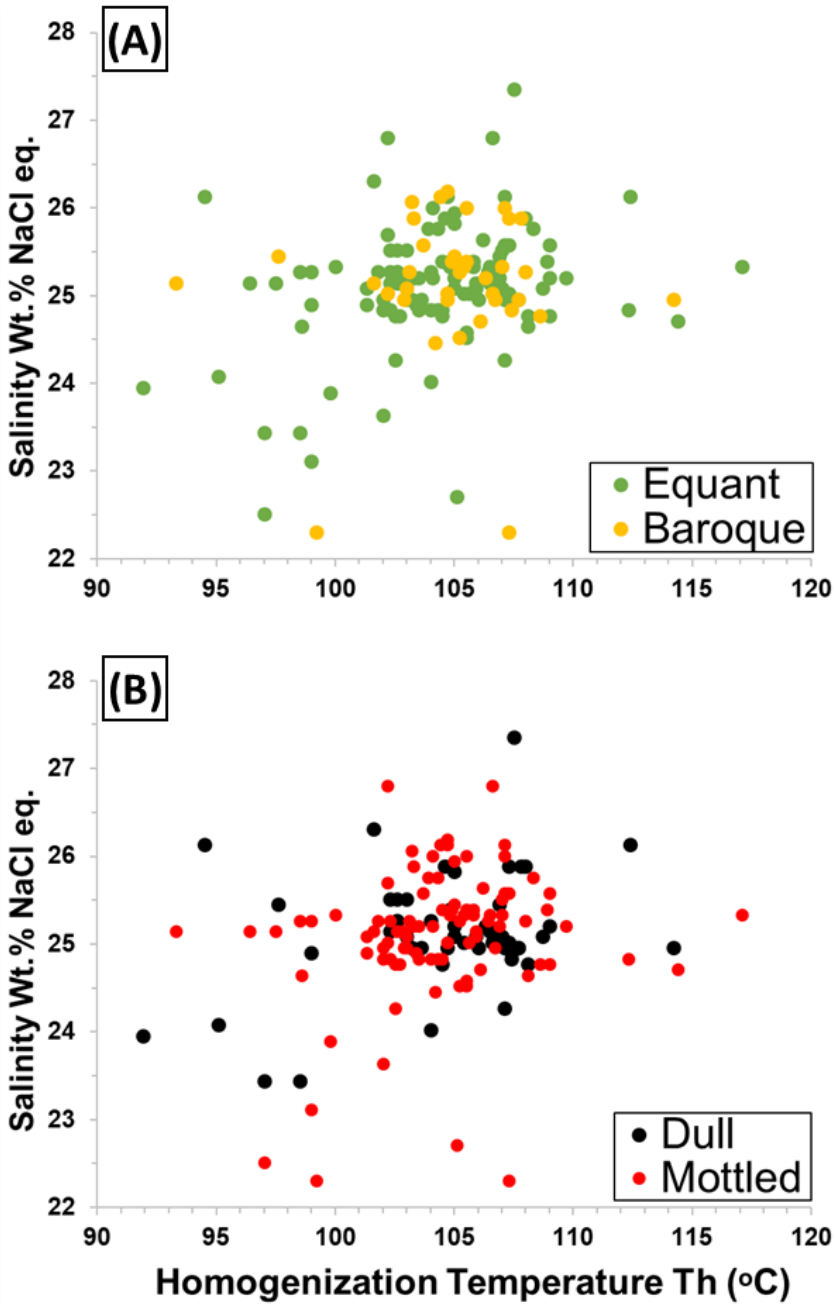

Figure 3.6. (A) Salinity–homogenization temperature cross plot for dolostones coded as a function of dolomite phase (equant vs baroque). (B) The same data coded as a function of CL pattern (dull vs mottled). Note the lack of separation between equant and baroque as well as between dull and mottled dolomites. Ranges and means are provided in Table 3.1. Note the cross-plots only show datapoints with both salinity and homogenization temperatures. Salinity was measured from the temperature of melting of ice data and is presented as wt.% NaCl equivalent. Data points are from multiple samples and multiple fluid inclusion assemblages.

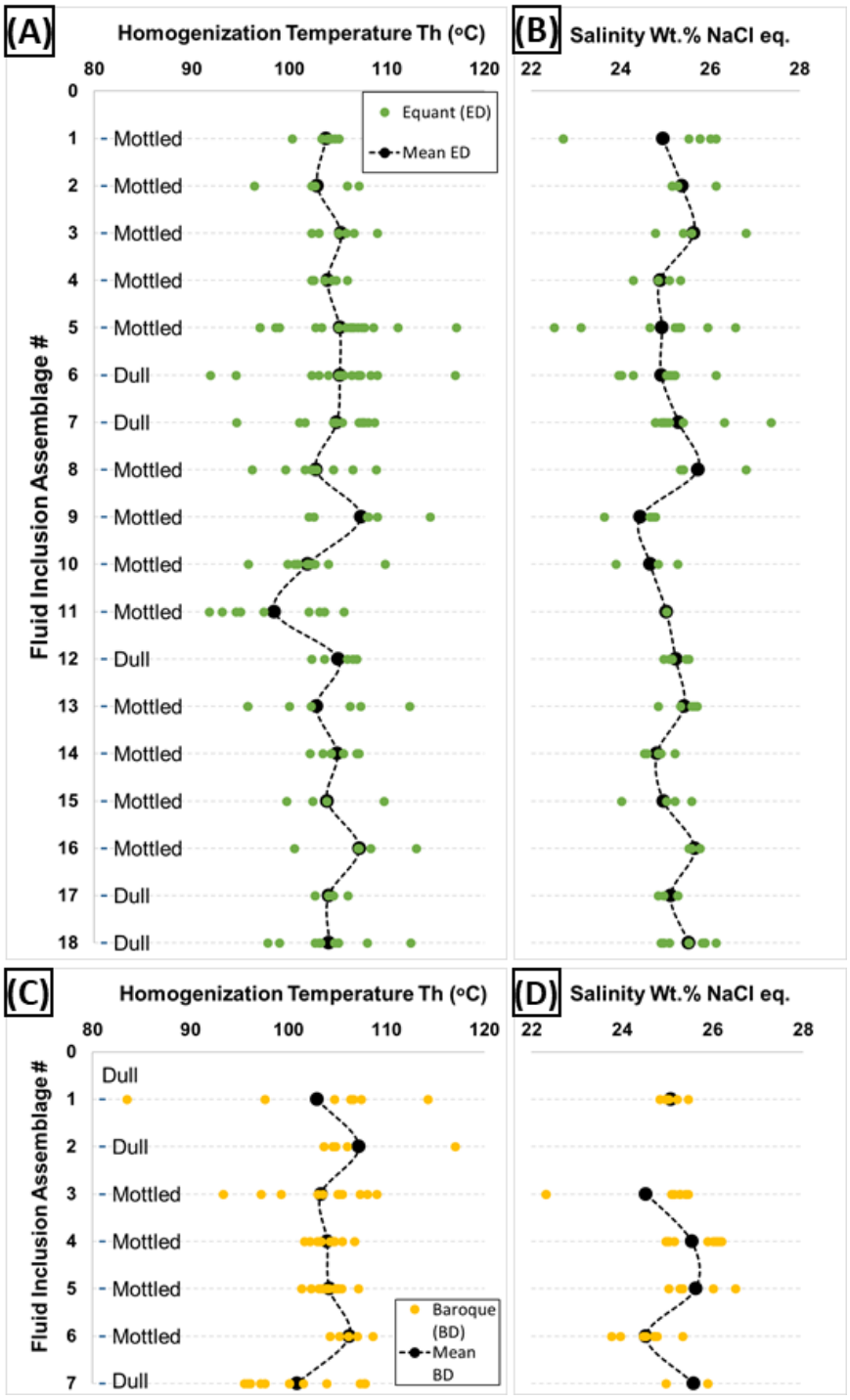

Figure 3.7. Homogenization temperatures and salinity plots for 25 fluid inclusion assemblages [FIAs] (18 for equant dolomites [green dots; top plots], and 7 for baroque dolomite [yellow dots; bottom plots]. All data are from well 2, and sorted from shallow to deep. (A, B) Homogenization temperatures and salinity in equant dolomite FIAs plotted from top to bottom of the reservoir. Note despite little change in Th and salinity between individual FIAs, essentially all FIAs contain a range of Th and salinity values. Some FIAs have as large as 25ºC variation (example FIA# 6). (C, D) Homogenization temperatures and salinity in baroque dolomite FIAs plotted from top to bottom of the reservoir. Note the range of Th and salinity within individual FIAs. FIA# 2 in baroque dolomite does not contain melting temperature of ice measurements; hence, no salinity values.

3.4.6 Oxygen ($\delta^{18}O$) and carbon ($\delta^{13}C$) stable isotope analysis

Oxygen ($\delta^{18}O$) isotope values in dolostone range from -8.0 to -10.0‰ with a mean of -9.3‰, and carbon ($\delta^{13}C$) isotope values have a range of 2.5 to 3.5‰ with a mean of 2.8‰. The $\delta^{18}O$ values in dolostone are noticeably more negative than that of low-temperature Jurassic marine dolomite (Figure 3.8A; Table 3.2; Land, 1980; Veizer et al., 1999). The same is true for limestone $\delta^{18}O$ values, which are outside the range for low-temperature Jurassic marine calcite (Figure 3.8A; Veizer et al., 1999). Five limestone samples contain dolomite cement in interparticle pores; this cement in limestone is less negative than all the dolomite in the dolostone (Figure 3.8A). Limestone diagenesis is not the subject of this paper and stable isotope data are only provided as a reference to help with dolostone analysis.

Similar to the fluid inclusion data, equant and baroque dolomites have nearly identical ranges and means in both $\delta^{18}O$ and $\delta^{13}C$ (Figure 3.8B; Table 3.2). Equant dolomite has mean $\delta^{18}O$ and $\delta^{13}C$ values of -9.2‰ and 2.8‰, respectively, compared to means of -9.3‰ and 2.7‰ for baroque dolomite. There are many examples of petrographic thin sections that contain both textures (e.g., Figure 3.4A), with baroque dolomite cross-cutting the older equant dolomite. Yet, even with the obvious timing and textural differences, the two dolomite phases record nearly identical stable isotopic values (Figure 3.4A).

Due to the relatively large sampling size for stable isotopes, it was not possible to confidently extract samples from purely dull CL or purely mottled CL crystals. However, stable isotope analysis on areas dominated by either dull or mottled CL crystals show the two have identical mean values of $\delta^{13}C$ (Table 3.2). Mean of $\delta^{18}O$ in dull-dominated CL vs mottle-dominated CL samples, however, is separated by ~0.5‰ (Table 3.2), with the mottle-dominated CL being 0.5‰ more negative than the dull-dominated CL samples. Despite this slight difference

between the two $\delta^{18}O$ values, the bulk of the isotopic data in these two groups overlap each other (Table 3.2).

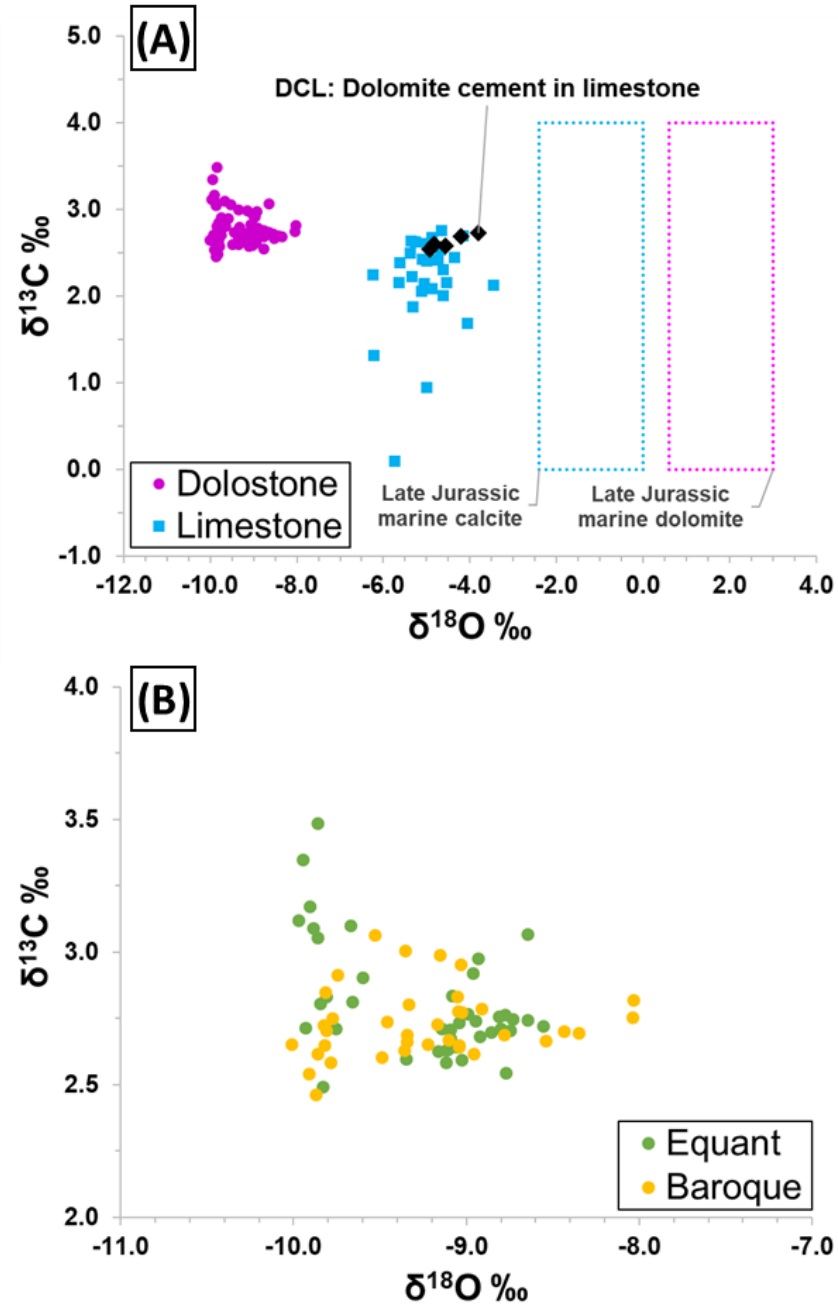

Figure 3.8. (A) Carbon isotope ($\delta^{13}C$) vs oxygen isotope ($\delta^{18}O$) cross plot of dolostone, limestone and dolomite cement in limestone. The data points for both lithologies are outside those expected for Late Jurassic marine calcite and dolomite (Veizer et al., 1999); the dolomite value is based on the fractionation value given by Land (1980). (B) Dolostone data coded as a function of dolomite phase (equant vs baroque). Note the lack of separation between the two dolomite phases. Ranges and mean values are provided in Table 3.2.

Table 3.2: Stable Isotope Statistics for Dolostone

		$\delta^{13}C$ (‰ VPDB)			$\delta^{18}O$ (‰ VPDB)		
Groups	**Count**	**Min**	**Max**	**Mean**	**Min**	**Max**	**Mean**
All Dolostones	**78**	**2.5**	**3.5**	**2.8**	**-10.0**	**-8.0**	**-9.3**
Equant Dolomite	41	2.5	3.5	2.8	-10.0	-8.6	-9.2
Baroque Dolomite	37	2.5	3.1	2.7	-10.0	-8.0	-9.3
Dull	6	2.6	2.9	2.8	-9.1	-8.0	-8.8
Mottled	19	2.5	3.2	2.8	-10.0	-8.4	-9.3
Undifferentiated*	53	2.5	3.5	2.8	-10.0	-8.0	-9.3

* Stable isotope data for samples with no CL analysis

3.4.7 Strontium isotope ratio ($^{87}Sr/^{86}Sr$)

Dolostone's 'whole-rock' strontium isotope ratios ($^{87}Sr/^{86}Sr$) range from 0.70761 to 0.70779, which are much higher than that of Late Jurassic seawater (Figure 3.9A; McArthur et al., 2012). Strontium isotope ratio ($^{87}Sr/^{86}Sr$) for both limestone and anhydrite, however, fall well within the range of Late Jurassic seawater (Figure 3.9A). The limestone's $^{87}Sr/^{86}Sr$ values range from 0.70701 to 0.70714, whereas the anhydrite has a narrow range from 0.70710 to 0.70712 (Figure 3.9A).

Strontium isotope ratios plotted against oxygen isotope values for the same samples suggest a correlation in the limestones, but not in the dolostones. In the limestone, the sample with the least negative $\delta^{18}O$ value records the lowest $^{87}Sr/^{86}Sr$ value of 0.70701, whereas the one with the most negative $\delta^{18}O$ value records the highest $^{87}Sr/^{86}Sr$ value of 0.70714 (Figure 3.9B). In the dolostone, there is no obvious relationship between $\delta^{18}O$ and $^{87}Sr/^{86}Sr$. The limestone and dolostone dataset (together) show that more negative $\delta^{18}O$ coincide with higher $^{87}Sr/^{86}Sr$ (Figure 3.9B). Finally, it was not possible to sample for individual dolomite phases because the $^{87}Sr/^{86}Sr$

analysis requires a very large sample size (~10–20 mg), which equates to many dolomite crystals with multiple textures.

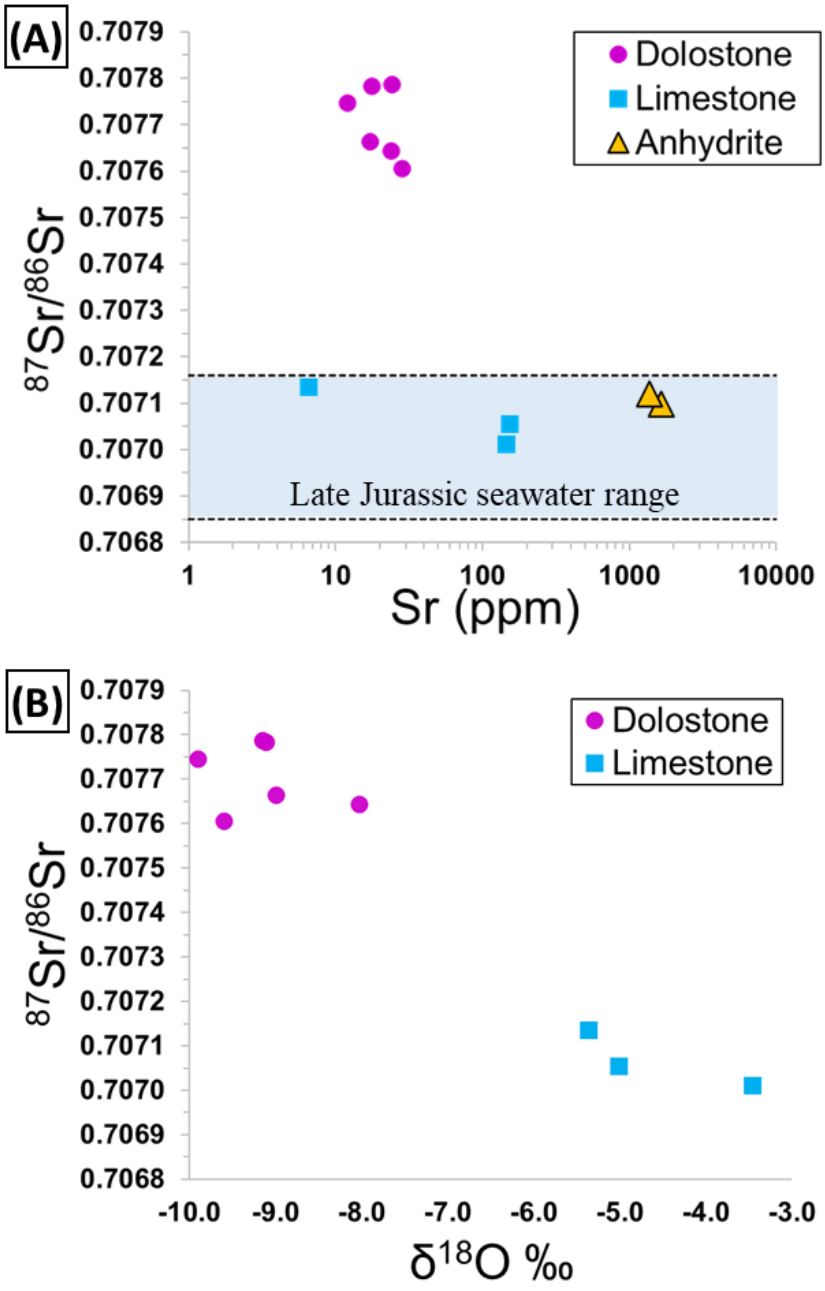

Figure 3.9. (A) Strontium isotope ratio ($^{87}Sr/^{86}Sr$) vs Sr concentration (ppm) for six dolostone, three limestone and two anhydrite samples. Limestone and anhydrite samples fall within the range expected for Late Jurassic seawater (shaded area between two black dotted lines; McArthur et al., 2012). The dolostones record much higher $^{87}Sr/^{86}Sr$ values than expected for Late Jurassic seawater, indicting either a radiogenic influence or formation from seawater-derived fluid of a younger age (e.g., Eocene seawater has $^{87}Sr/^{86}Sr$ values similar to those of the dolostones here; McArthur et al., 2012). (B) Strontium isotope ratio $^{87}Sr/^{86}Sr$ vs $\delta^{18}O$ for dolostone and limestone.

3.4.8 Uranium–lead (U–Pb) dating

Reliable uranium–lead ages were obtained from 22 dolomite crystals from six dolostone samples (Table 3.3). Dolomite U–Pb ages range from 52.8 ± 8.7 Ma to 11.9 ± 2.4 Ma (Figure 3.10; Table 3.3). Because U–Pb dating analysis relies on a high-resolution placement of spots on thick sections, it was possible to sample for individual dolomite phases (i.e., equant or baroque) as well as sampling for dull CL and mottled CL crystals.

Equant dolomite has an age range from 52.8 ± 8.7 Ma to 14.8 ± 0.8 Ma (Table 3.3; Figure 3.10). Baroque dolomite has a range from 44.8 ± 7.0 Ma to 11.9 ± 2.4 Ma. Based on these results, equant dolomite records older maximum ages than baroque dolomite. The bulk of analyses, however show that equant dolomite and baroque dolomite mostly overlap each other in their ages (Figure 3.10).

The majority of dolomite crystals in the study, as mentioned earlier, are mottled in CL (Figure 3.5) and crystals with dull CL are rare (Figure 3.5). This is reflected in the U–Pb dates where the majority of analyzed crystals (18 out of 22) are mottled. The oldest ages recorded in equant dolomite were obtained from two crystals with dull CL that yield ages of 52.8 ± 8.7 Ma and 44.7 ± 16.0 Ma (Figure 3.10; Table 3.3). The oldest age recorded in baroque dolomite also occurs in a crystal with dull CL, an age of 44.8 ± 7.0 Ma. Another baroque dolomite crystal with dull CL records an age of 25.2 ± 7.4 Ma.

Despite the general overlap in U–Pb dates between equant and baroque dolomite (Figure 3.10), there are a few observations worthy of note. First, U–Pb dates in dull dolomites are different between equant and baroque dolomite, with equant dolomite recording slightly older ages. Second, both equant and baroque dolomites record a wide range of ages within the same sample. For example, in sample number 560 (Table 3.3) three equant dolomite crystals were analyzed for U–

Pb dating and yielded ages from 52.8 ± 8.7 Ma to 15.3 ± 2.8 Ma, a possible range as high as 49 million years and as low as 31 million years, when all uncertainties (errors) are considered (Table 3.3). Similarly, in sample number 364 (Table 3.3) four different mottled baroque dolomite crystals that are relatively near one another were analyzed. The ages for those crystals range from 35.2 ± 4.4 Ma to 11.9 ± 2.4 Ma. Third, three of the samples with dull CL yield old ages (> ~44.0 Ma), one yields an intermediate age (25.2 ± 7.8 Ma), and none yield any younger ages; with all younger ages (ages younger than ~25Ma) recorded in the mottled dolomites.

Table 3.3: Uranium–Lead (U–Pb) Dating Data for Dolostone

Analysis #	Sample ID	Dolomite Phase	CL Pattern	U–Pb Age	Error (±)*	Total Error (±)
All Equant Dolomite						
1	560	Equant	Dull	52.8	8.7	17.0
2	540	Equant	Dull	44.7	16.0	31.4
3	560	Equant	Mottled	36.7	12.5	24.6
4	480	Equant	Mottled	30.6	4.5	8.9
5	364	Equant	Mottled	27.8	2.3	4.4
6	520	Equant	Mottled	26.1	6.9	13.5
7	520	Equant	Mottled	25.5	5.3	10.4
8	520	Equant	Mottled	25.2	6.3	12.4
9	520	Equant	Mottled	24.0	12.9	25.2
10	540	Equant	Mottled	22.0	7.9	15.4
11	560	Equant	Mottled	15.3	2.8	5.5
12	540	Equant	Mottled	14.9	0.8	3.0
All Baroque Dolomite						
13	439	Baroque	Dull	44.8	7.0	13.6
14	439	Baroque	Mottled	40.9	7.8	23.2
15	480	Baroque	Mottled	37.3	10.4	20.3
16	439	Baroque	Mottled	35.3	2.3	6.0
17	364	Baroque	Mottled	35.2	4.4	8.6
18	364	Baroque	Mottled	33.7	5.0	9.7
19	480	Baroque	Mottled	26.7	6.8	13.3
20	439	Baroque	Dull	25.2	7.4	14.4
21	364	Baroque	Mottled	21.0	1.9	11.3
22	364	Baroque	Mottled	11.9	2.4	10.8

* Internal uncertainty (error) as reported in the text. Refer to Appendix C for discussion of the uncertainty.

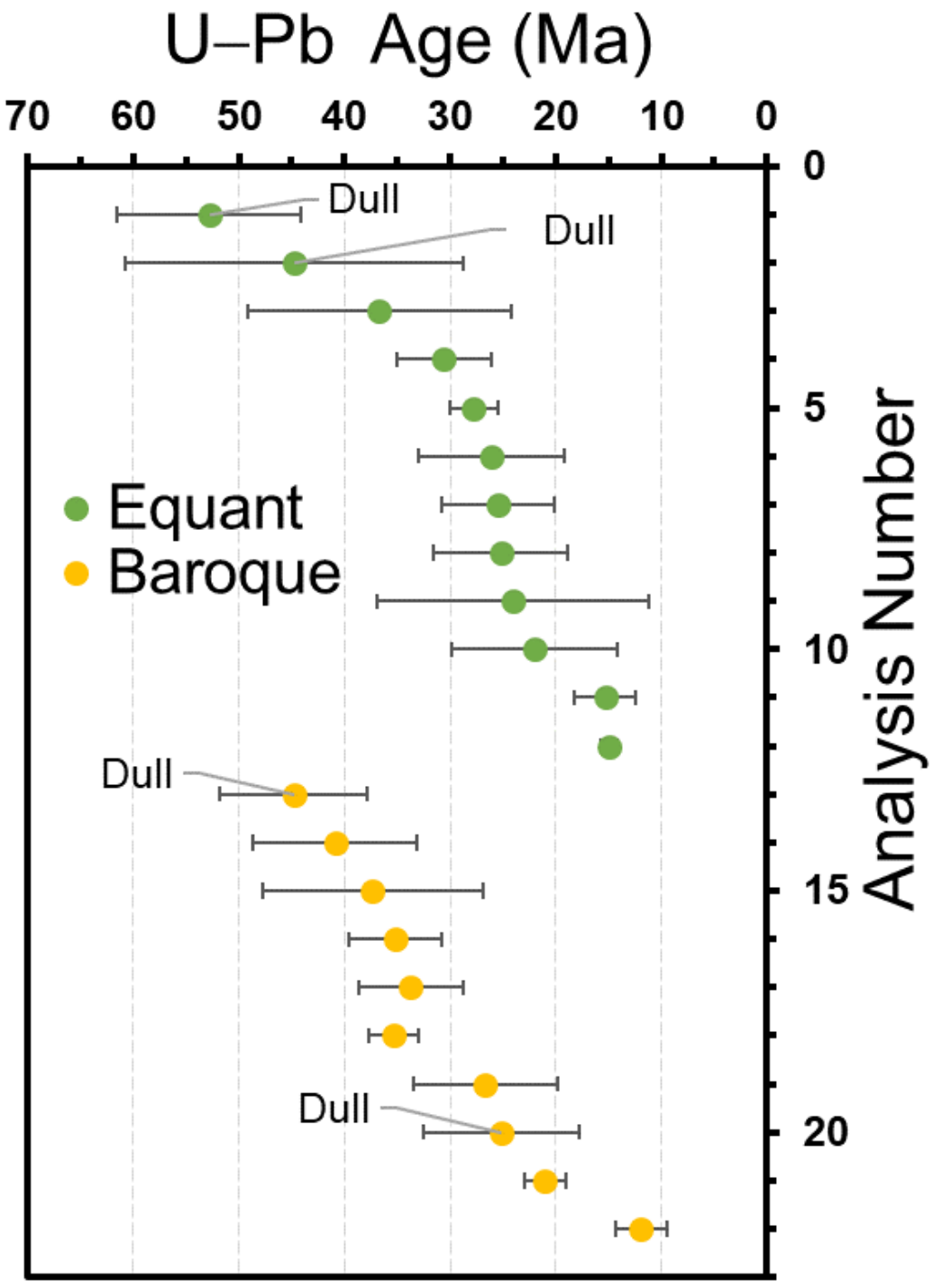

Figure 3.10. Uranium–lead (U–Pb) ages for 22 dolomite analyses, color coded for equant (green) and baroque (yellow) dolomites. The data are sorted from oldest to youngest for each dolomite type. All crystals are mottled in CL except those labeled 'Dull'. Note how dull dolomites are older in general but still overlap with the mottled dolomites. All data in the plot are presented in Table 3.3.

3.5 DISCUSSION

3.5.1 Recognizing recrystallization and petrographic evidence of original dolomite

Cathodoluminescence petrography reveals an abundance of dolomite crystals with moderate to intensive mottling, with > 80% of all dolomites showing CL mottling (Figure 3.5). Despite the dominance of mottled CL crystals, unmottled with uniformly dull CL crystals are also present in essentially all dolomite samples, but with a much smaller proportion. Mottled and dull CL crystals are also present in all stratigraphic positions, indicating no stratigraphic control. Some dolomite with intense CL mottling is also coated with a thin, and minor dolomite phase characterized by alternating dull, very dull, and bright CL and truncation from dissolution (Figure 3.5G, H). The latter indicates at least some dull dolomites are very late, and further supports some temporal overlap. The presence of micro- to mesopores in the vicinity of mottled areas in dolomite attests that some of the mottling is associated with dissolution and reprecipitation events. These features are consistently observed in both equant and baroque dolomites (Figure 3.5E–H).

Previous studies have used the mottling of dolomite crystals in CL as an indication of recrystallization, or a dissolution and precipitation event (i.e.., neomorphic replacement) (Banner et al., 1988; Reinhold, 1998; Gaswirth et al., 2007; Choquette and Hiatt, 2008). Other textural criteria used to infer recrystallization are the coarsening of dolomite crystals (McKenzie, 1981; Gregg, 1992), and the increase of the proportion of non-planar crystal boundaries (Gregg and Sibley, 1984; Gregg and Shelton, 1990). These criteria are also used here to infer recrystallization has happened in the area as dolomite is dominated by coarse crystals (Figure 3.2B) with non-planar (anhedral) crystal boundaries (Figure 3.2C). Relying on the criteria above, the rare occurrence of dull and unmottled dolomites argues that not all dolomite has undergone extensive recrystallization. Rather, some dolomites likely preserved some or all of their original geochemical

signatures. This is not unusual as many studies have demonstrated that despite some recrystallization, some dolomites still retain original or near original geochemical signatures (Reinhold, 1998; Al-Aasm and Packard, 2000; Ryan et al., 2021). The degree of mottling in CL can be used as a general guideline to distinguish between unrecrystallized to minimally recrystallized (dull and unmottled in CL) and intensively recrystallized (mottled in CL) dolomites. Using this approach, the geochemical attributes of the unrecrystallized to minimally recrystallized dolomites (i.e., dull CL) would represent conditions of, or at least very close to, initial formation in these dolomites. Additionally, the petrographic observations in this study argue for an overlap between dolomite formation, dolomite cementation, dissolution, and reprecipitation; essentially indicating a temporal overlap between the processes of dolomite formation and recrystallization.

3.5.2 Interpreting geochemical attributes of recrystallized dolomite

There are challenges in interpreting geochemical data from dolomite that has undergone extensive recrystallization; as the process of recrystallization is capable of altering all or some of the original petrographic and geochemical attributes in dolomites (Machel, 1997). The following sections illustrate how recrystallization processes interfere with the geochemical signatures associated with dolomites.

3.5.2.1 *Equant vs. baroque dolomite*

Petrographic evidence shows that at least some of the equant dolomite is cross cut by fractures and dissolution, and then followed by precipitation of baroque dolomite (Figure 3.4). Thus, at least some of the equant dolomite predates baroque dolomite. This evidence, however,

does not exclude the possibility that some equant dolomite formed at the same time or even after baroque dolomite. Equant dolomite has mean homogenization temperature of 103.4ºC, and $\delta^{18}O$ of -9.2‰ (Tables 3.1 and 3.2). Baroque dolomites have comparable mean values (Th: 103.9ºC, $\delta^{18}O$: -9.3‰; Tables 3.1 and 3.2). Despite the relatively comparable Th means between equant and baroque dolomites, as well as relatively uniform Th means for individual FIAs (Figure 3.7A, C), FIAs with consistent Th values have ranges from 91.8 to 117.1ºC in equant dolomite and ranges from 83.5 to 117.0ºC in baroque dolomite. These ranges indicate that, at an FIA scale (roughly one growth zone in a dolomite crystal), homogenization temperatures vary. In some cases, Th varies as much as ~30.0ºC within one consistent FIA. Thus, Th values likely record ranges of dolomite precipitation and recrystallization for both dolomite types; with all temperatures indicating late precipitation or recrystallization at depth in the presence of high-temperature fluids that varied in temperature. Homogenization temperatures, melting temperatures of ice (Figure 3.6A; Table 3.1), as well as, the means and ranges in $\delta^{18}O$ and $\delta^{13}C$ values (Figure 3.8B; Table 3.2) all attest that the sets of conditions that formed equant and baroque dolomites are essentially the same.

3.5.2.2 *Dull vs. mottled CL dolomite*

Equant and baroque dolomites contain both dull and mottled crystals, with dull and mottled crystals recording similar geochemical values, with some minor distinctions. The evenly dull CL dolomite has textures suggesting that it has not recrystallized; whereas, the mottled crystals have been subject to multiple events of recrystallization, or internal dissolution followed by cementation. Fluid inclusion data for both CL textures are similar; however, the dull baroque dolomite shows the lowest recorded Th (Th: 83.5ºC; Table 3.1; Figure 3.7C). Consistent FIAs show ranges from 83.5 to 117.0ºC in evenly dull and from 91.8 to 117.1ºC in mottled dolomites.

It was not possible to confidently separate dull and mottled crystals for stable isotopes, but predominantly dull CL and mottled CL dolomites have negative $\delta^{18}O$ values (means are -8.8‰ and -9.3‰ for dull and mottled CL fabrics, respectively). This ~0.5‰ variation between the two fabrics is minor and can be achieved by a small variation of the parent fluid composition. If, however, we assume the parent fluid's $\delta^{18}O$ composition was identical for both mottled and dull CL dolomites, then a variation of a temperature as little as ~3.0ºC can to produce the small variation in $\delta^{18}O$ (fractionation of Sheppard and Schwartz, 1970). Overall, both the dull CL fabrics and the mottled CL fabrics show similar condition of formation, with the responsible fluids characterized by a high temperature, albeit with some temperature variation (Figure 3.7A, C; Table 3.1).

3.5.3 Timing of dolomitization and recrystallization

Uranium–lead dating on dolomite yields the timing of dolomite precipitation and recrystallization. The results should indicate the timing and duration of the variably high temperature conditions that led to both dolomite precipitation and recrystallization. The U–Pb ages range from 52.8 ± 8.7 Ma (recorded in equant dolomite with dull CL) to 11.9 ± 2.4 Ma (recorded in baroque dolomite with mottled CL; Figure 3.11).

In equant dolomite, crystals with dull CL (likely indicating little or no recrystallization) record the oldest U–Pb ages of 52.8 ± 8.7 Ma and 44.7 ± 16.0 Ma (Table 3.3). The mottled equant dolomite crystals have an age range from 36.7 ± 12.5 Ma to as young as 14.9 ± 0.8 Ma. Based on these values, the oldest dolomitization commenced at or slightly before the 52.8 ± 8.7 Ma date (Figure 3.11). Recrystallization of equant dolomite could have commenced around the same time frame; however, the oldest preserved mottled equant dolomite is at 36.7 ± 12.5 Ma. These data

show a likely age separation between the start of dull (unrecrystallized) and mottled (recrystallized) equant dolomite crystals, with dull crystals recording ages that are up to ~12 Ma older than the mottled crystals (Figure 3.11).

In baroque dolomite, the oldest recorded age is also found in a dull CL crystal, giving an age of 44.8 ± 7.0 Ma. Another dull CL baroque dolomite yields a younger age of 25.2 ± 7.4 Ma, indicating precipitation of dull CL baroque dolomite spanned a range of ages, and was unlikely just a single event. All other baroque dolomite crystals are mottled and range from 40.9 Ma ± 7.8 Ma to 11.9 ± 2.4 Ma (Figure 3.11). The overlap in ages of dull and mottled dolomite indicate dolomite precipitation and recrystallization have a temporal overlap. In summary, Equant dolomitization (initial replacement and cement) likely commenced around 52.8 ± 8.7 Ma and lasted until at least 44.7 ± 16.0 Ma, whereas baroque dolomitization commenced around 44.8 ± 7.0 Ma, and lasted until 25.2 ± 7.4 Ma (Figure 3.11). The mottled CL fabrics coincide with recrystallization or cementation of internal pores with new dolomite. For equant dolomite, this commenced around 36.7 ± 12.5 and lasted until 14.9 ± 0.8 Ma. For baroque dolomite, it likely commenced around 40.9 Ma ± 7.8 Ma and continued until 11.9 ± 2.4 Ma age.

Using the $^{87}Sr/^{86}Sr$ curve (Figure 3.12; McArthur et al., 2012) as a rough estimator to determine the age of dolomite formation or recrystallization, all dolostone samples would fall within the ~75 Ma to ~34 Ma age range. However, replacement dolomites likely reflect a mixture of the Jurassic Sr from the rock and younger Sr from the dolomitizing or recrystallizing fluid. The ~75 Ma rough age is at least 13 Ma older than the oldest possible age obtained from U–Pb dating (i.e., 52.8 ± 8.7 = maximum age of 61.5 Ma; Figure 3.11; Table 3.3). Thus, this $^{87}Sr/^{86}Sr$ value likely reflects a mixture between Jurassic limestone Sr and the later dolomitizing fluid Sr. Furthermore, high salinity fluids, known from our fluid inclusion data, were not forming through

evaporation at 75 Ma (Sharland et al., 2001). Instead, evaporites and their residual brines are known to form later during the Paleocene and Eocene. All other $^{87}Sr/^{86}Sr$ values fall well within the ages obtained by U–Pb dating and are consistent with the time of Paleocene and Eocene evaporation, however, a single $^{87}Sr/^{86}Sr$ value can yield multiple ages when plotted in the $^{87}Sr/^{86}Sr$ curve (Figure 3.12). Similarly, it is difficult to conclusively determine the origin of all $^{87}Sr/^{86}Sr$ values in the dolostones, and whether they are from the dolomitizing fluids or are mixtures. Thus, the ages obtained by $^{87}Sr/^{86}Sr$ can only be used as a rough estimator of the source of the fluid and must be constrained with other datasets.

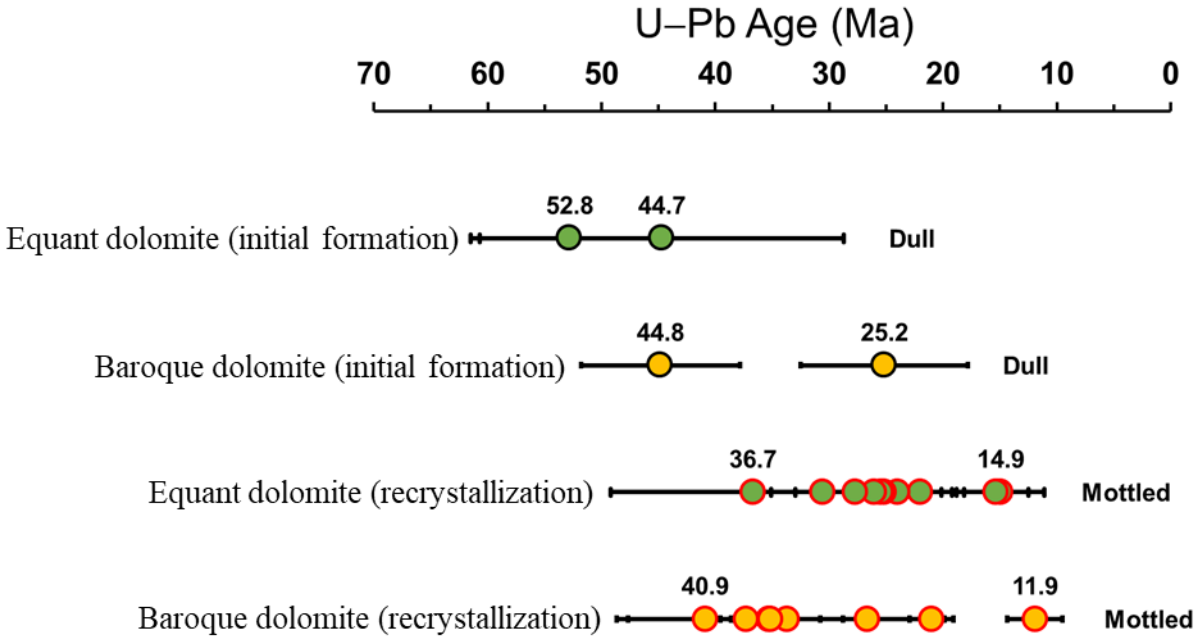

Figure 3.11. Summary of U–Pb dates for equant and baroque dolomite. Note how some equant predates baroque dolomite, but with some overlap. Some dull CL dolomites predate mottled CL dolomites, but the majority of data overlap; indicating an overlap between dolomitization and recrystallization. Refer to text for discussion and interpretation of data.

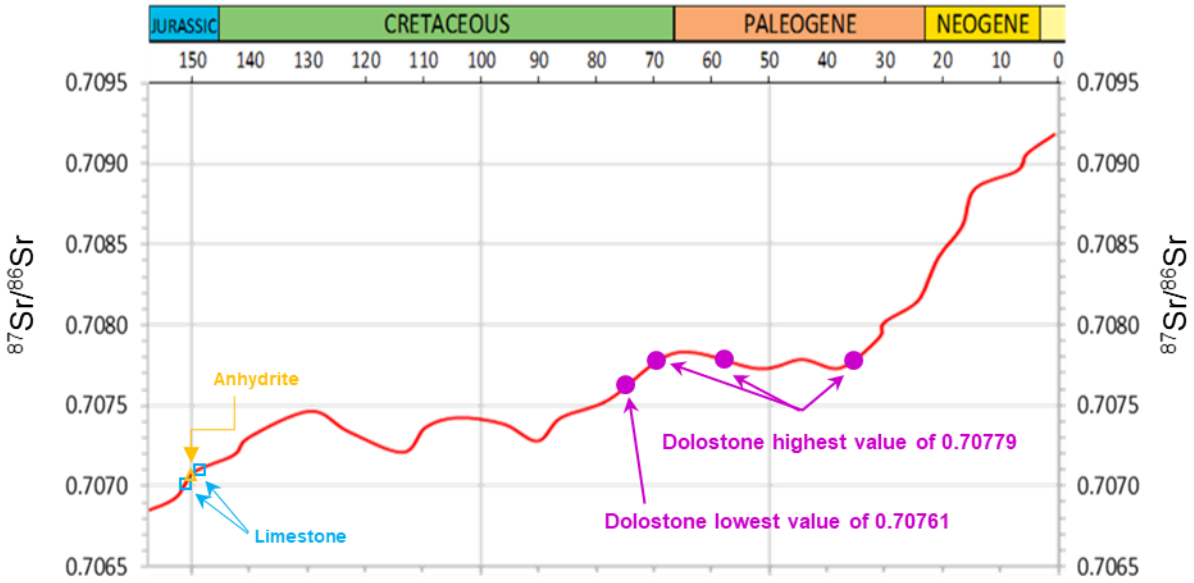

Figure 3.12. Strontium isotope ratio curve from the Late Jurassic to present showing the overall increase in $^{87}Sr/^{86}Sr$ values. Dolostone (purple dots) are only the minimum and maximum values; note a single $^{87}Sr/^{86}Sr$ value can yield multiple ages, refer to discussion for interpretation of all strontium isotope ratio data, and integration with U–Pb dates. Curve is from McArthur et al. (2012).

3.5.4 Hydrothermal origin of dolomitization and recrystallization

3.5.4.1 *Identifying hydrothermal conditions*

Numerous studies have interpreted the dolomite in their respective areas as hydrothermal in origin (Qing and Mountjoy, 1994; White and Al-Asam, 1997; Al-Aasam, I., 2003; Lavoie et al., 2005; Luczaj, 2006; Davies and Smith, 2006; Smith, 2006; Hiemstra and Goldstein, 2015). Others dispute the degree to which these hydrothermal systems are always correctly identified. Machel and Lonnee (2002) have insisted on using a restrictive definition for hydrothermal systems that requires that the dolomitizing fluids were at least 5–10ºC warmer than ambient burial temperature (e.g., White, 1957). Meeting this strict requirement is typically not possible in most studies because the ambient temperature at the time of dolomite precipitation cannot be estimated without knowing the burial depth of dolomite precipitation, which requires knowing the absolute age of

dolomitization. Additional criteria have been suggested by Goldstein (2012) and include any of the following with caveats: (1) a repeated record of temperature increase and decrease inconsistent with the burial history; (2) determined paleotemperature that is higher than the most liberal maximum burial temperature; (3) a determined pressure–temperature relationship or paleogeothermal gradient that is inconsistent with normal burial; (4) data showing local high paleotemperature at the same depth within a region; and (5) data showing higher paleotemperatures focused in proposed conduits for fluid flow. In our study, we are able to meet Machel and Lonnee's (2002) criteria, because of the U–Pb dates, and meet Goldstein's (2012) criteria (1) and (2).

The carbonates in this study have undergone a history of constant burial since Early Cretaceous that continued until early Paleogene, with present-day burial depths being the maximum burial depths for the Arab Formation (Abu-Ali and Littke, 2005). The temperatures at the time of dolomite formation and recrystallization (anywhere from 52.8 ± 8.7 Ma to 11.9 ± 2.4 Ma; Table 3.3; Figures 3.10 and 3.11) were likely the same or slightly colder than present-day bottom-hole temperatures, because carbonates at that time span were either as deep as, or slightly shallower than, today's depth. Today's bottom-hole temperature (at the Arab Formation depth) is ~85ºC (Aramco internal data). Dolomite homogenization temperatures range from 83.5–117.1ºC, with a mean of ~103.5ºC (Table 3.1; Figure 3.6). Integrating the fluid inclusion and U–Pb dating results, with the established burial history in the region reveals that all dolomite, equant and baroque, including those with dull CL and mottled CL, have formed and recrystallized at a temperature on average ~18 to ~19ºC above the ambient burial temperature. These temperature differences are based on mean values for each group as reported in Table 3.1.

Similarly, barring one lone Th measurement of 83.5ºC (Table 3.1) which cannot be considered hydrothermal, all other 258 out of 259 Th measurements record temperatures at least

5ºC higher than the ambient temperature of 85ºC. The highest Th measurement of 117.1ºC is ~32ºC higher than the ambient temperature. Thus, virtually all homogenization datapoints, regardless of dolomite fabric, show elevated temperatures well above the 5–10ºC criteria. Moreover, the fluid inclusion Th data within FIAs is typically consistent, evidence that fluid inclusions have not thermally reequilibrated by the criteria of Goldstein and Reynolds (1994). Comparing Th values in each FIA to other FIAs reveals mean temperature fluctuations back and forth of approximately ~10ºC, with individual FIAs containing Th variability as much as 30ºC (Figure 3.7A, C). Recalling that the rocks did not experience any major unroofing; this variation in temperature is inconsistent with the burial history of the rocks in this area. In fact, there is no possible burial and unroofing scenario that could lead to the Th variation observed here, and therefore there must have been repeated pulses of hot hydrothermal fluid flow (with temperatures much higher than ambient temperature) alternating with cooling of that fluid to temperatures slightly above the ambient temperature.

3.5.4.2 *Is the dolomite hydrothermal or recrystallized low-temperature dolomite?*

There have been some questions regarding whether hydrothermal processes are capable of widespread dolomitization. Many studies that reported high-temperature dolomites concluded that those dolomites are actually early-formed, low-temperature, dolomites, likely produced from seawater-derived fluids, that have experienced a later recrystallization event at depth, in the presence of high-temperature fluids (Spötl and Burns, 1991; Montanez and Read, 1992; Smith and Dorobek, 1993; Kupecz and Land, 1994; Ronchi et al., 2011; Rott and Qing, 2013). The concerns expressed for the hydrothermal origin of the dolomite are typically Mg budgets (whether a hydrothermal fluid has enough Mg to dolomitize a region) and if the rocks were simply

dolomitized at low temperature and then recrystallized at high temperature. We resolve the answers to these questions below for the current study.

Earlier, it was established that the processes of dolomitization, dolomite cementation, dissolution, and recrystallization all show petrographic evidence of having formed after burial at significant depth, and in close temporal association with one another. Petrographic evidence from evenly dull CL dolomite indicates relatively pristine preservation, whereas mottled CL dolomites show evidence of internal dissolution followed by cementation of the pores, or recrystallization. This late, high-temperature origin is supported by fluid inclusion, stable isotopic, $^{87}Sr/^{86}Sr$, and U–Pb dating analyses. Fluid inclusion Th are higher than maximum burial temperature and pulse up and down (Figures 3.7 and 3.8), dolomite oxygen isotopes lack any signature of low-temperature fluids (Figure 3.8A), $^{87}Sr/^{86}Sr$ shows no signature of Jurassic seawater and indicate a much younger source of seawater-derived brine (Figure 3.9A), and all radiometric ages are post deep burial (Figure 3.10). Thus, we interpret all dolomitization to have been from hydrothermal fluids. The dolomitization and dolomite cementation was closely associated with dissolution and cementation of internal pores with later dolomite. Similarly, some of the dolomite may also recrystallize, but all dolomite shows evidence of the same range of hydrothermal conditions. Thus, we interpret that dolomitization, dolomite cementation, dissolution and recrystallization all took place in approximately the same hydrothermal setting. It is not simply a low-temperature dolomite that has recrystallized at depth.

Producing a large amount of hydrothermal dolomite at depth, as observed here, typically has been regarded as challenging because the rocks are separated from a source of Mg-rich fluids such as seawater. A fault-controlled mechanism (sensu Corbella et al., 2014; Hollis et al., 2017) was offered as a likely mechanism to explain the large volume of fluids needed to produce such

dolomites. Surface-breaching faults could serve as conduits to allow the sinking of large volumes evaporated seawater. The water would be heated geothermally after it sank and charged an underlying aquifer. Dolomitization could then commence from the vertical expulsion along fault systems of these Mg-rich fluids, that now have high-temperature. This dolomitization model is capable of producing large volumes of high-temperature dolomite from rising hydrothermal fluids (Dewit et al., 2012; Corbella et al., 2014; Hollis et al., 2017; Hirani et al., 2018; Lukoczki et al., 2019; Koeshidayatullah et al., 2020; Stacey et al., 2021; Afify et al., 2022). This mechanism has been invoked as a main producer of dolomite in rifted areas in particular, where large strike-slip and extensional faults are common (Hirani et al., 2018; Afify et al., 2022).

Our study area could have operated in similar fashion, but with some significant differences constrained by the dataset herein [see Chapter 2 for details]. The area is situated in a structurally active region, where such faults were likely present (Broomhall and Allan, 1987; Faqira et al., 2009; Stewart, 2018). The Upper Triassic Minjur sandstone, which is interpreted to have served as an aquifer [Chapter 2], is many 100s of meters deeper than the Jurassic Arab Formation. Present-day bottom-hole temperatures in the Minjur Sandstone is ~120ºC (Aramco internal data). Present-day depth of the Triassic sandstone is very close to its burial depth during the 52.8 ± 8.7 Ma to 11.9 ± 2.4 Ma period during which dolomitization and dolomite recrystallization took place. The $^{87}Sr/^{86}Sr$ values of the dolomite show that a seawater-derived source fluid may have been as young as ~34 Ma and may have been older, but how much older is unknown from $^{87}Sr/^{86}Sr$ because the lower $^{87}Sr/^{86}Sr$ values of dolomite likely represents a mixture between the high value of the dolomitizing fluid and the low value from the Jurassic limestone that has been dolomitized (Figure 3.11). Evaporites in the overlying section are known in Paleogene rocks (Umm Er Radhuma, Rus, and Dammam Formations) which spanned an age from ~58 to ~35 Ma (Stewart, 2018). This age

range of the overlying evaporites and carbonates overlaps with the older ages obtained from U–Pb (Figure 3.11), and are also consistent with the roughly estimated ages from $^{87}Sr/^{86}Sr$ (Figure 3.12). Thus, it is interpreted that while evaporated brines were generated at the surface, large volumes of those brines sank due to their high density along fault-damage zone fluid conduits. They charged the underlying Triassic sandstone aquifer where they would have been heated to a temperature of ~120ºC based on the burial depth at that time for the Minjur Sandstone (Abu-Ali and Littke, 2005). Based on the distribution of the dolomite data in the region and the U–Pb dates, those fluids ascended through seismic pumping or local geothermal convection cells might have developed in the fault-damage zones. This process continued for approximately 40 million years, leading to extensive dolomitization and recrystallization of the Arab Formation.

3.5.5 Causes of recrystallization

The petrographic and geochemical data, constrained by U–Pb dating, indicate that recrystallization was multi episodic and spanned a period of approximately 30 million years (Figure 3.11; the mottled dolomites). Petrographic evidence shows the presence of meso- and micropores in the vicinity of mottled areas within dolomite crystals (Figure 3.7). Thus, recrystallization of some, and perhaps most dolomite, likely proceeded through microscale dissolution of metastable dolomite phases followed by precipitation of more stable phases as fillings of those pores. Dolomites with variable Ca concentrations and variable solubilities could have contributed to the overall dissolution of some dolomite phases as demonstrated in previous studies on dolomite recrystallization (e.g., Nielsen et al., 1994; Rott and Qinq, 2013).

Sustaining continued dissolution and reprecipitation for millions of years, however, would also implicate a sustained and repeated change in the saturation state of the fluid; a change from

supersaturation to undersaturation states with respect to dolomite. The fluctuation observed in the fluid inclusion data supports repeated pulses of warm fluids with slight variations in temperature, salinity, and likely some variations in overall chemistries (Figure 3.7). The fluctuation of saturation state of fluids could have been achieved by the repeated tapping of the sandstone aquifer by fractures or seismic pumping to release renewed warm Mg-rich fluids. It is possible that each pulse of Mg-rich fluid would have had relatively distinct chemical, isotopic, and salinity compositions, as well as, different saturation states with respect to dolomite. This is also supported by the nature of dolomitization in the area, where the parent fluids that sank down through the faults, during the Paleogene (~58 to 35 Ma; see previous discussion) could themselves have had variable Mg concentrations. As an alternative and a simpler explanation, it remains possible that the hot fluids injected from the underlying aquifer were all supersaturated with respect to dolomite at the moment of injection into the Arab Formation, but once they reached their shallow destination, they cooled. This is supported by the fluid inclusion data, which shows repeated pulses of fluid flow with 10–30ºC temperature fluctuations. The repeated temperature fluctuations could be all the explanation needed for the system to go back and forth between supersaturated and undersaturated conditions, explaining the nature of recrystallization.

Some previous studies that dealt with intensive recrystallization processes ascribed these processes to Ostwald's ripening where larger nano- and microparticles grow at the expense of smaller particles to achieve a higher thermodynamic stability (Morse and Casey, 1988; Gregg et al., 1992). Others suggest that increases of burial, and thus ambient temperatures and pressures, as well as evolved pore-fluid composition should lead to progressive recrystallization of essentially all early-formed dolomites (Land, 1985; Kupecz and Land, 1994). Many of the mentioned studies, however, dealt with an early, low-temperature, and presumably non-ideal dolomite that would

naturally be prone to subsequent stabilization processes through recrystallization. In our study, however, all the dolomite is interpreted to be of late burial and hydrothermal origin. Although some studies argued that burial dolomites tend to resist subsequent recrystallization and retain original conditions due to lack of a thermodynamic drive (e.g., Amthor et al., 1993), our study demonstrates that recrystallization processes can operate at depth, and cause extensive alteration to late burial dolomites; likely through the repeated changes of fluid temperatures and/or composition.

3.6 CONCLUSIONS

1. The Upper Jurassic carbonates in northeast Saudi Arabia contain large volumes of equant and baroque dolomites, both of which exhibit evenly dull and/or mottled CL textures. All dolomite fabrics and textures (equant and baroque, dull and mottled) have nearly identical fluid inclusion and stable isotopic values; characterized by high homogenization temperatures (mean: 103.5ºC, which is at least ~18ºC higher than ambient temperature) and very negative oxygen isotopic values (mean: -9.3‰). This indicates a common hydrothermal origin for equant and baroque dolomites, as well as a common origin of dolomite formation and recrystallization.
2. The maximum U–Pb dating age in equant and baroque dolomite are 52.8 ± 8.7 Ma and 44.8 ± 7.0 Ma, respectively. This indicates some equant dolomite formation likely predates baroque dolomite. The bulk of U–Pb dating ages in equant and baroque dolomites, however, overlap each other; indicating a temporal association between the two dolomites.

3. Uranium–lead dating shows that some dolomites with dull CL are older (ages: 52.8 ± 8.7 Ma and 44.7 ± 16.0 Ma) than those with mottled CL (ages from 36.7 ± 12.5 Ma to 14.8 ± 0.8 Ma). Although some of the dull CL dolomite predates mottled dolomite, dull and mottled dolomites overlap each other during the majority of the diagenetic history when age uncertainties are considered. This indicates precipitation and recrystallization (from dissolution and cementation) have a temporal association, with the two processes operating over a 40−million−year time span.
4. The source of Mg-rich fluid is evaporated seawater, that coincided with the formation of Paleogene strata ~58 to ~35 million years ago; the fluid sank along fault-damage zones and charged an underlying sandstone aquifer where it was heated to ambient burial temperature. Those hot fluids were then injected through faults and fractures as pulses over a 40−million−year time span.
5. The injection of repeated pulses of hot fluids was responsible for the extensive recrystallization, causing the chemistry to shift back and forth between supersaturated and undersaturated. Temperature fluctuation in the hydrothermal realm could have been the lone driver for the dissolution and reprecipitation that caused recrystallization, but fluctuations in chemical composition from different fluid sources cannot be discounted.

3.7 REFERENCES

Abu-Ali, M., and R. Littke, 2005, Paleozoic petroleum systems of Saudi Arabia: A basin modeling approach: GeoArabia, v. 10, p. 131–168.

Afify, A. M., M. E. Sanz-Montero, and L. Gonzalez-Acebron, 2022, Dolomite–magnesite formation and polymetallic mineralization in a rift-sag basin on the western margin of the Red Sea: paleoenvironmental, hydrothermal, and tectonic implications: Journal of Sedimentary Research, v. 92, p. 144–165, DOI: 10.2110/jsr.2021.100.

Al-Aasam, I. S., 2000, Chemical and isotopic constraints for recrystallization of sedimentary dolomites from the Western Canada sedimentary basin: Aquatic Geochemistry, v. 6, p. 227–248.

Al-Aasam, I., 2003, Origin and characterization of hydrothermal dolomite in the Western Canada Sedimentary Basin: Journal of Geochemical Exploration, v. 78, p. 9–15, https://doi.org/10.1016/S0375–6742(03)00089-X.

Al-Husseini, M., 2009, Update to Late Triassic–Jurassic stratigraphy of Saudi Arabia for the Middle East geologic time scale: GeoArabia, v. 14, p. 145–186.

Amthor, J. E., E. W. Mountjoy, and H. G. Machel, 1993, Subsurface dolomites in Upper Devonian Leduc Formation buildups, central part of Rimbey-Meadowbrook reef trend, Alberta, Canada: Bulletin of Canadian Petroleum Geology, v. 41, p. 164–185.

Banner, J. L., G. N. Hanson, and W. J. Meyers, 1988, Water-rock interaction history of regionally extensive dolomites of the Burlington-Keokuk Formation (Mississippian): isotopic evidence, in V. Shukla and P. A. Baker, eds., Sedimentology and geochemistry of dolostones: SEPM Special Publication 43, p. 97–114.

Bodnar, R. J., 1992, Revised equation and table for freezing point depressions of H,O-salt fluid inclusions (Abstract): PACROFI IV, Fourth Biennial Pan-American Conference on Research on Fluid Inclusions, Program and Abstracts, Lake Arrowhead, CA, v. 14, p. 15.

Broomhall, R. W., and J. R. Allen, 1987, Regional caprock-destroying dolomite on the Middle Jurassic to Early Cretaceous Arabian Shelf: Society of Petroleum Engineers Formation Evaluation, v. 2, p. 435–441.

Cantrell, D., P. K. Swart, and R. M. Hagerty, 2004, Genesis and characterization of dolomite, Arab-D reservoir, Ghawar field, Saudi Arabia: GeoArabia, v. 9, p. 1–26.

Choquette, P.W., and E. E. Hiatt, 2008, Shallow-burial dolomite cement: a major component of many ancient sucrosic dolomites: Sedimentology, v. 55, p. 423–460.

Corbella, M., E. Gomez-Rivas, J.D. Martin-Martin, S.L. Stafford, A. Teixell, A. Griera, A. Trave, E. Cardellach, and R. Salas, 2014, Insights to controls on dolomitization by means of reactive transport models applied to the Benicàssim case study (Maestrat Basin, eastern Spain): Petroleum Geoscience, v. 20, p. 41–54.

Davies, G. R., and L. B. Smith, 2006, Structurally controlled hydrothermal dolomite reservoir facies: An overview: AAPG Bulletin, v. 90, p. 1641–1690.

Dewit, J., M. Huysmans, P. Muchez, D. W. Hunt, J. B. Thurmond, J. Verges, E. Saura, N. Fernandez, I. Romaire, P. Esestime, and R. Swennen, 2012, Reservoir characteristics of fault-controlled hydrothermal dolomite bodies: Ramales Platform case study, in J. Garland, J. E. Neilson, S. E. Laubach, and K. J. Whidden, eds., Advances in Carbonate Exploration and Reservoir Analysis: Geological Society, London, Special Publications, v. 370, p. 83–109, doi:10.1144/SP370.1.

Dickson, J. A. D., 1966, Carbonate identification and genesis as revealed by staining: Journal of Sedimentary Petrology, v. 36, p. 491–505.

Durocher, S., and I. S. Al-Aasm, 1997, Dolomitization and neomorphism of Mississippian (Visean) upper Debolt Formation, Blueberry field, northeastern British Columbia; geologic, petrologic, and chemical evidence: AAPG Bulletin, v. 81, p. 954–977.

Faqira, M., M. Rademakers, and A. M. Afifi, 2009, New insights into the Hercynian Orogeny, and their implications for the Paleozoic Hydrocarbon System in the Arabian Plate: GeoArabia, v. 14, p. 199–228.

Gaswirth, S. B., D. A. Budd, and L. G. Farmer, 2007, The role and impact of regionally extensive freshwater-seawater mixing zones in the maturation of regional dolomite bodies within the proto-Floridan aquifer: Sedimentology, v. 54, p. 1065–1092.

Goldstein, R. H., 2012, Fluid inclusion geothermometry in sedimentary systems: From paleoclimate to hydrothermal, in Analyzing the thermal history of sedimentary basins: Methods and case studies: Tulsa, Oklahoma, SEPM Special Publication 103, p. 45–63.

Goldstein, R. H., and T. J. Reynolds, 1994, Systematics of fluid inclusions in diagenetic minerals: Tulsa, Oklahoma, SEPM Short Course 31, 199 p.

Gregg, J. M., and D. F. Sibley, 1984, Epigenetic dolomitization and the origin of xenotopic dolomite texture: Journal of Sedimentary Petrology, v. 54, p. 908–931.

Gregg, J. M., and K. L. Shelton,1990, Dolomitization and dolomite neomorphism in the back reef facies of the Bonneterre and Davis formations (Cambrian), southeastern Missouri: Journal of Sedimentary Research, v. 60, p. 549–562.

Gregg, J. M., S. A Howard, and S. J. Mazzullo, 1992, Early diagenetic recrystallization of Holocene (< 3000 years old) peritidal dolomites, Ambergris Cay, Belize: Sedimentology, v. 39, p. 143–160.

Hiemstra, E. J., and R. H. Goldstein, 2015, Repeated injection of hydrothermal fluids into downdip carbonates: a diagenetic and stratigraphic mechanism for localization of reservoir porosity, Indian Basin Field, New Mexico, USA: Geological Society of London, Special Publication 406, p. 141–177.

Hill, C. A., V. J. Polyak, Y. Asmerom, and P. Provencio, 2016, Constraints on a Late Cretaceous uplift, denudation, and incision of the Grand Canyon region, southwestern Colorado Plateau, USA, from U-Pb dating of lacustrine limestone: Tectonics, v. 35, p. 896–906.

Hirani, J., E. Bastesen, A. Boyce, H. Corlett, R. Gawthorpe, C. Hollis, and F. Whitaker, 2018, Controls on the formation of stratabound dolostone bodies, Hammam Faraun Fault block, Gulf of Suez: Sedimentology, v. 65, p. 1973–2002, https://doi.org/10.1111/ sed.12454.

Hollis, C., E. Bastesen, A. Boyce, H. Corlett, R. Gawthorpe, J. Hirani, and F. Whitaker, 2017, Fault-controlled dolomitization in a rift basin: Geology, v. 45, p. 219–222, https://doi.org/10.1130/G38s394.1.

Koeshidayatullah, A., H. Corlett, J. Stacey, P.K. Swart, A. Boyce, H. Robertson, F. Whitaker, and C. Hollis, 2020, Evaluating new fault-controlled hydrothermal dolomitization models:

Insights from the Cambrian Dolomite, Western Canadian Sedimentary Basin: Sedimentology, v. 67, p. 2945–2973, https://doi.org/10.1111/sed.12729.

Kupecz J. A. Land L. S., 1994, Progressive recrystallization and stabilization of early-stage dolomite: Lower Ordovician Ellenburger Group, west Texas, in Purser B. H. Tucker M. E. Zenger D. H., eds., Dolomites: A volume in honor of Dolomieu: Cambridge, Blackwell Scientific Publications, International Association of Sedimentologists Special Publication 21, p. 255–279.

Land, L. S., 1980, The isotopic and trace element geochemistry of dolomite: the state of the art. In: Concepts and Models of Dolomitization (Eds D.L. Zenger, J.B. Dunham and R.L. Ethington): SEPM Special Publication 28, p. 87–110.

Land, L. S., 1982, Dolomitization: AAPG Education Course Note Series 24, 20 p.

Land, L. S., 1985, The origin of massive dolomite: Journal of Geological Education, v. 33, p. 112–125.

Lavoie, D., G. Chi, P. Brennan-Alpert, A. Desrochers, and R. Bertrand, 2005, Hydrothermal dolomitization in the Lower Ordovician Romaine Formation of the Anticosti Basin: Significance for hydrocarbon exploration: Canadian Society of Petroleum Geologists Bulletin, v. 53, p. 454–472.

Lonnee, J., and H. G. Machel, 2006, Pervasive dolomitization with subsequent hydrothermal alteration in the Clarke Lake gas field, Middle Devonian Slave Point Formation, British Columbia, Canada: AAPG Bulletin, v. 90, p. 1739– 1761.

Lu, P., and D. Cantrell, 2016, Reactive transport modelling of reflux dolomitization in the Arab-D reservoir, Ghawar Field, Saudi Arabia: Sedimentology, v. 63, p. 865–892, doi:10.1111/sed.12241.

Lu, P., W. Tan, and D. Tang, 2017, Massive dolomite on the Upper Jurassic to Lower Cretaceous carbonate shelf, northeastern Saudi Arabia: Insights from reactive transport modeling: AAPG Annual Convention and Exhibition, Houston, Texas, April 2–5, 2017.

Luczaj, J. A., 2006, Evidence against the Dorag (mixing-zone) model for dolomitization along the Wisconsin arch— A case for hydrothermal diagenesis: AAPG Bulletin, v. 90, p. 1719–1738.

Lukoczki G, J. Haas, J. M. Gregg, H. G. Machel, S. Kele, and C. M. John, 2019, Multi-phase dolomitization and recrystallization of Middle Triassic shallow marine–peritidal carbonates from the Mecsek Mts. (SW Hungary), as inferred from petrography, carbon, oxygen, strontium and clumped isotope data: Marine and Petroleum Geology, v. 101, p. 440–458.

Machel H. G., 1997, Recrystallization versus neomorphism, and the concept of "significant recrystallization" in dolomite research: Sedimentary Geology, v. 113, p. 161–168.

Machel, H. G., and J. Lonnee, 2002, Hydrothermal dolomite— A product of poor definition and imagination: Sedimentary Geology, v. 152, p. 163–171.

McArthur, J.M., R. J. Howarth, and G.A. Shields, 2012, Strontium isotope stratigraphy in: Gradstein, F.M., Ogg, J.G. And Smith, A.G., Eds., A Geological Timescale 2012, Chapter 7, pp. 127–144, Cambridge: Cambridge University Press.

McKenzie, J. A.,1981, Holocene dolomitization of calcium carbonate sediments from coastal sabkhas of Abu Dhabi, U.A.E.: a stable isotope study. Journal of Geology, v. 89, p. 185–198.

Montanez, I. P., and F. J. Read, 1992, Fluid-rock interaction history during stabilization of early dolomites, Upper Knox Group (Lower Ordovician) U.S. Appalachians: Journal of Sedimentary Petrology, v. 62, p. 753–778.

Morse, J. W., and W. H. Casey, 1988, Ostwald processes and mineral paragenesis in sediments: American Journal of Science, v. 288, p. 537–560.

Nielsen, P., R. Swennen, R, and E. Keppens, 1994, Multiple recrystallizations within massive ancient dolomite units: an example from the Dinantian of Belgium: Sedimentology, v. 41, p. 567–584.

Paton, C., J. D. Woodhead, J. C. Hellstrom, J. M. Hergt, A. Greig, and R. Maas, 2010, Improved laser ablation U–Pb zircon geochronology through robust downhole fractionation correction: Geochemistry, Geophysics, Geosystems, v. 11, doi: 10.1029/2009GC002618.

Paton, C., J. Hellstrom, B. Paul, J. Woodhead, and J. Hergt, 2011, Iolite: Freeware for the visualization and processing of mass spectrometric data: Royal Society of Chemistry, v. 26, p. 2508–2518, doi: 10.1039/C1JA10172B.

Qing, H., and E. W. Mountjoy, 1994, Formation of coarsely crystalline, hydrothermal dolomite reservoirs in the Presqu'ile Barrier, Western Canada sedimentary basin: AAPG Bulletin, v. 78, p. 55–77.

Reinhold, C., 1998, Multiple episodes of dolomitization and dolomite recrystallization during shallow burial in Upper Jurassic shelf carbonates: eastern Swabian Alb, southern Germany: Sedimentary Geology, v. 121, p. 71– 95.

Roberts, N.M., E. T. Rasbury, R. R. Parrish, C. J. Smith, M. S. Horstwood, and D. J. Condon, 2017, A calcite reference material for LA-ICP-MS U-Pb geochronology. Geochemistry, Geophysics, Geosystems, v. 18, p. 2807–2814.

Ronchi, P., F. Jadouol, A. Ceriani, A. Di Giulio, P. Scotti, A. Orttenzi, and E. P. Massara, 2011, Multistage dolomitization and distribution of dolomitized bodies in Early Jurassic carbonate platforms (Southern Alps, Italy): Sedimentology, v. 58, p. 532–565.

Rott, C. M., and H. Qing, 2013, Early dolomitization and recrystallization in shallow marine carbonates, Mississippian Alida beds, Williston Basin (Canada): Evidence from petrography and isotope geochemistry: Journal of Sedimentary Research, v. 83, p. 928–941.

Ryan, B. H., S. E. Kaczmarek, and J. M. Rivers, 2021, Multi-episodic recrystallization and isotopic resetting of early-diagenetic dolomites in near-surface settings: Journal of Sedimentary Research, v. 91, p. 146–166, doi:10.2110/jsr.2020.056.

Ryan, B. H., S. E. Kaczmarek, J. M. Rivers, and C. J. Manche, 2022, Extensive recrystallization of Cenozoic dolomite during shallow burial: A case study from the Palaeocene–Eocene Umm er Radhuma formation and a global meta-analysis: Sedimentology, Early view, March 2022.

Sharland, P.R., R. Archer, D. M. Casey, R. B. Davies, S. H. Hall, A. P. Heward, A. D. Horbury and M. D. Simmons, 2001, Arabian Plate Sequence Stratigraphy: GeoArabia Special Publication v. 2, 371 p

Sheppard, S. M. F., and H. P. Schwartz, 1970, Fractionation of carbon and oxygen isotopes and magnesium between co-existing metamorphic calcite and dolomite. Contributions to Mineralogy and Petrology, v. 26, p. 161–98.

Smith, L. B. Jr., 2006, Origin and reservoir characteristics of Upper Ordovician Trenton–Black River hydrothermal dolomite reservoirs in New York: AAPG Bulletin, v. 90, p. 1691–1718.

Smith, T. D. and S. L. Dorobek, 1993, Alteration of early formed dolomite during shallow to deep burial: Mississippian Mission Canyon Formation, central to southwestern Montana: Geological Society of America Bulletin, v. 105, p. 1389–1399.

Spötl, C., and S. J. Burns, 1991, Formation of ^{18}O-depleted dolomite within a marine evaporitic sequence, Triassic Reichenhall Formation, Austria: Sedimentology, v. 38, p. 1041–1057.

Stacey, J., H. Corlett, G. Holland, A. Koeshidayatullah, C. Cao, P. Swart, S. Crowley, and C. Hollis, 2021, Regional fault-controlled shallow dolomitization of the Middle Cambrian Cathedral Formation by hydrothermal fluids fluxed through a basal clastic aquifer: Geological Society of America Bulletin, v. 133, p. 2235–2377, https://doi.org/10.1130/B35927.1.

Stewart, S. A., 2018, Hormuz salt distribution and influence on structural style in NE Saudi Arabia: Petroleum Geoscience, v. 24, p. 143–158, https://doi.org/10.1144/petgeo2017–011.

Swart, P. K., D. L. Cantrell, H. Westphal, C. R. Handford, and C. G. Kendall, 2005, Origin of dolomite in the Arab-D reservoir from the Ghawar field, Saudi Arabia: Evidence from petrographic and geochemical constraints: Journal of Sedimentary Research, v. 75, p. 476–491, https://doi.org/10.2110/jsr.2005.037.

Swart, P. K., D. L. Cantrell, M. M. Arienzo, and S. T. Murray, 2016, Evidence for high temperature and ^{18}O-enriched fluids in the Arab-D of the Ghawar field, Saudi Arabia: Sedimentology, v. 63, p. 1739–1752.

Tera, F., and G. J. Wasserburg, 1972, U-Th-Pb systematics in three Apollo 14 basalts and the problem of initial Pb in lunar rocks: Earth and Planetary Science Letters, v. 14, p. 281–304.

Veizer, J., D. Ala, K. Azmy, P. Bruckschen, D. Buhl, F. Bruhn, G. A. F. Carden, A. Diener, S. Ebneth, Y. Godderis, T. Jasper, C. Korte, F. Pawellek, O. G. Podlaha, and H. Strauss, 1999, $^{87}Sr/^{86}Sr$, $\delta^{13}C$ and $\delta^{18}O$ evolution of Phanerozoic seawater: Chemical Geology, v. 161, p. 59–88.

Vermeesch, P., 2018, IsoplotR: A free and open toolbox for geochronology: Geoscience Frontiers, v. 9, p. 1479–1493.

White, D. E., 1957, Thermal waters of volcanic origin: Geological Society of America Bulletin, v. 68, p. 1637–1658.

White, T., and I. S. Al-Aasm, 1997, Hydrothermal dolomitization of the Mississippian Upper Debolt Formation, Sikanni gas field, northeastern British Columbia, Canada: Bulletin of Canadian Petroleum Geology, v. 45, p. 297– 316.

Woodhead, J. D., and J. M. Hergt, 2001, Strontium, Neodymium and Lead isotope analyses of NIST glass certified reference materials: SRM 610, 612, 614. Geostandards and Geoanalytical Research, v. 25, p. 261–266, doi:10.1111/j.1751–908x.2001.tb00601.x.

Chapter 4

Impact of Mesogenetic Dissolution on Porosity and Permeability in a Heavily Dolomitized Jurassic Carbonate, Saudi Arabia

ABSTRACT

The question of whether dolostones contain additional pore space or merely inherit porosity from precursor limestones remains an open question. Here, this question and the question of what controls dolostone porosity and permeability are addressed by systematically analyzing petrographic and petrophysical attributes of dolomitized and undolomitized grainy carbonates from the Jurassic Arab Formation in northeast Saudi Arabia. Dolostone and limestone facies exhibit nearly identical median porosity and permeability (11.5% and 3.3 mD vs 11.9% and 2.4 mD, respectively). The relationships between porosity and permeability in the two lithologies are also similar (correlation coefficients R = 0.73 and 0.72, in dolostone and limestone, respectively). The controls on reservoirs properties are different, however. In limestones, depositional textures, mechanical compaction, and cementation are the main controls, whereas, late dissolution and late cementation are the main controls in dolostone. Late dissolution events in dolostone in particular appear to alter the petrophysical properties in dolostone and these events formed moldic pores within anhydrite, saddle dolomite, dolomite growth zones, as well as vugs that cross-cut stylolites and multiple diagenetic phases. Collectively, these pores account for ~4.5% porosity in the dolostones and such pores are missing in the limestones. Through the integration of petrographic and geochemical analyses that are constrained by uranium–lead (U–Pb) dating on dolomites, we interpret a large fraction of pore spaces in dolostone to have developed through mesogenetic dissolution events, which operated at depth. Mesogenetic dissolution events are unrelated to and absent from the limestone facies; and thus, models for porosity and permeability distribution in the limestones cannot guide those in the dolostones.

4.1 INTRODUCTION

The impact of dolomitization on reservoir properties has received considerable attention in carbonate research (Schmoker et al., 1985; Purser et al., 1994; Lucia and Major, 1994; Sun, 1995; Saller and Henderson, 1998; Braithwaite et al., 2004; Ehrenberg, 2004; Vandeginste et al., 2009; Maliva et al., 2011). This is not surprising, as dolomitized carbonate platforms contain a large proportion of global hydrocarbon reserves, with early estimates indicating that dolomite reservoirs represent ~50% of global and ~80% of North American carbonate reservoirs (Zegnar, 1980; Sun, 1995; Warren, 2000). Nevertheless, the exact roles that dolomitization processes play in controlling the petrophysical properties of carbonate platforms remains unclear; in part due to the many independent factors that jointly determine the final petrophysical properties of dolomitized reservoirs (Sun, 1995). Such factors include the origin of dolomite fabric, crystal size(s), textural fabric (i.e., crystal shape), original depositional textures, position within the platform, burial history, degree of compaction, and post-dolomitization diagenesis of the dolomite (Schmoker et al., 1985; Purser et al., 1994; Lucia and Major, 1994; Sun, 1995; Saller and Henderson, 1998).

The literature includes many examples where dolomitization has improved, degraded, or had no to minimal impact on reservoir quality and properties (e.g., Sun, 1995). Many studies have also demonstrated that the effects of dolomite are non-uniform, even within the same reservoir unit, and consequently, relying on average values of porosity and permeability when comparing limestone and dolostone reservoir properties can be misleading (Meyer et al., 2000; Cantrell et al., 2001; Alqattan and Budd, 2017). Although some studies have argued for a minimal impact of dolomitization on porosity, and attributed pore spaces observed in dolostones to precursor limestones (e.g., Lucia, 2004), the majority have noted the variable and heterogeneous impacts of dolomitization on reservoir properties.

The Upper Jurassic (Arab Formation) carbonates in northeast Saudi Arabia provide an exceptional example of carbonates that contain both dolostone and limestone, with the latter including well-preserved original fabrics with no replacive dolomite. The majority of the dolomites is interpreted to have formed or recrystallized during burial diagenesis, thus, dolomitization largely began after limestone diagenesis (Broomhall and Allan, 1987). In this study, we employ qualitative and quantitative techniques to: (1) determine the controls on reservoir quality in both limestone and dolostone; (2) determine the impact of dolomite on reservoir quality; and (3) determine the origin of pore spaces in dolostone. The results of the study provide insight to understanding the controls on carbonate reservoir quality in the study area, but are also applicable to other carbonate reservoirs worldwide.

4.2 MATERIALS AND METHODS

The data for this study include 151 thin sections (118 dolostones and 33 limestones), prepared from core plug samples, each of which also have petrophysical lab measurements (helium porosity and permeability). The plugs were taken directly from three cored subsurface wells (Figure 4.1) that sampled the Upper Jurassic Arab Formation, located in an area away from the main producing fields in Saudi Arabia. These cores are characterized by an abundance of dolomite (~85% of the reservoir facies are dolostones). Plug porosity used the helium expansion method and permeability measurements used nitrogen as the injected fluid in an airtight Hassler sleeve apparatus. The data show that median and mean porosity values are essentially the same, because data are normally distributed. The mean and median permeability values differ substantially, however, with the arithmetic means recording higher values due to non-normality. Because of this,

for permeability values, the medians better represent the total permeability. Therefore, in this paper, the median values are used to describe both porosity and permeability.

All thin sections were scanned under plane- and cross-polarized light using an Olympus BX53 microscope equipped with a DP74 camera and automated mechanical stage capable of scanning petrographic thin sections. The images were then used to record the quantitative abundances of mineralogy, types of grains, pores, cements, and dolomite types, using point counting (300 points) and digital image analysis toolbox in the JMicroVision v. 1.3.1 software (Roduit, 2019). Samples were stained with Alizarin Red S to distinguish calcite from other minerals and with potassium ferricyanide to distinguish ferroan from non-ferroan carbonate minerals (Dickson, 1966). Cathodoluminescence (CL) microscopy was performed on >30 polished thin and thick sections with an accelerating potential of 13.5–14.5 kV, a gun current of 350–400 mA, and an air chamber pressure of <0.05 torr using a Leitz Ortholux–Pol microscope and a CITL mk5 CL system.

Stable isotope analyses were conducted on 137 microsamples (112 dolostones, 20 limestones, and 5 dolomite cements in limestone). The microsamples were heated under vacuum at high temperature to release volatile organic compounds and then were reacted with 100% phosphoric acid at 70°C for 9 min in a Kiel IV Carbonate Device. The isotopic ratios of the released CO_2 gas were measured with a dual inlet Finnigan MAT253 mass spectrometer at the Keck Paleoenvironmental and Environmental Stable Isotope Laboratory, University of Kansas. All values are reported in per mil (‰) and relative to the Vienna Peedee belemnite (VPDB), with reported standard deviations of <0.05‰ for both $\delta^{13}C$ and $\delta^{18}O$.

Fluid inclusion petrography and microthermometry was performed on 35 polished thick sections using a Linkam THMSG 600 stage following the procedure of Goldstein and Reynolds

(1994). Tens of different fluid inclusion assemblages, which include a total of 307 homogenization and 200 melting temperature of ice measurements, were recorded for different diagenetic phases in the dolostone.

Strontium isotope ratios $^{87}Sr/^{86}Sr$ were analyzed in 12 samples (9 dolostones and 3 limestones). Powdered samples (10–20 mg) were dissolved in 3.5 N HNO_3 and a Sr-spec-filled ion-exchange column was used to separate the Sr. The NIST 987 standard of 0.71248 was used to normalize all $^{87}Sr/^{86}Sr$ data.

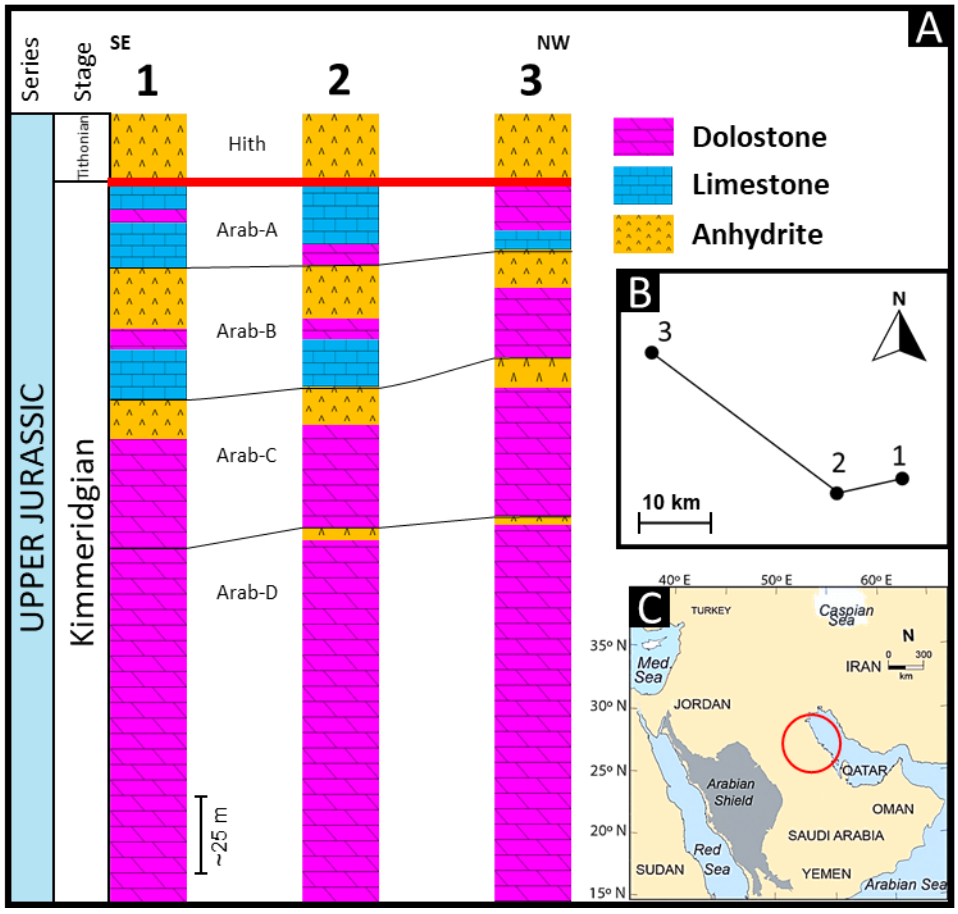

Figure 4.1. (A) Southeast–northwest lithological correlation of the Arab Formation in the studied wells (1–3). The base of the Tithonian Hith (red line) is used as a datum. (B) Transect showing the distribution of wells. (C) Base map of Saudi Arabia and neighboring countries, from Eltom (2020). The wells are located in northeast Saudi Arabia; due to the proprietary nature of the data, the exact locations of the wells cannot be provided, the red circle shows the general area of interest.

4.3 RESULTS

4.3.1 Depositional and diagenetic facies

There are more dolostone than limestone samples in the study because dolostone is extensive laterally and stratigraphically (~85% of the area is completely dolomitized; Figure 4.1). Five main facies, 4 dolostone (facies D1 to D4) and 1 limestone (facies L), (Figure 4.2; Table 4.1) are described here: (1) peloidal–skeletal dolograinstone (facies D1; Figure 4.2A); (2) oolitic dolograinstone (D2; Figure 4.2B); (3) sponge dolorudstone (D3; Figure 4.2C); and (4) fabric-destructive dolostone (D4; Figure 4.2D). The fabric-destructive facies D4 could have started as any depositional texture (i.e., mudstone to grainstone). This facies shows some lamination and contains an abundance of what could be poorly preserved fenestral pores or vugs. The lone limestone facies is peloidal–skeletal grain-dominated packstone (GDP) to grainstone (facies L; the undolomitized counterpart of facies D1; Table 4.1).

The limestone facies (L) is divided into two subfacies based on texture; a grainstone (Lg; Figure 4.2E) and a grain-dominated packstone (Lp; Figure 4.2F) subfacies, with the former dominating (24 out of 33 samples are grainstone; Table 4.1). The subfacies also exhibit variation in packing of grains, and include samples with open packing where grains show one or two contact points (Lgo and Lpo subfacies; Table 4.1), or compacted packing with multiple contact points and some suturing at grain contacts (Lgc and Lpc subfacies; Table 4.1). Examples of these differing compaction fabrics will be shown in sections of this paper that follow. Because of the extensive dolomitization, it was not possible to subdivide the dolostone facies into subfacies based on their original textures with as much confidence as with the limestone; thus, the dominating texture in each facies was used as an identifier.

Table 4.1. Facies Description and Distribution

Facies and Subfacies Name	Lithology	Facies Code	No of Samples	Stratigraphic Distribution	Lateral Distribution	Texture	Grains
Peloidal-Skeletal Dolograinstone	Dolostone	D1	47	A, B, C, D	Wells 1, 2, 3	Grainstone	Green algae, Foraminifera
Oolitic Dolograinstone		D2	30	A, B, C, D	Wells 1, 2, 3	Grainstone	Green Algae
Sponge Dolorudstone		D3	17	D	Well 2	Rudstone	Stromatoporoids, Green Algae
Fabric Destructive Dolostone		D4	24	A, B, C, D	Wells 1, 2, 3	n/a	n/a
Peloidal-Skeletal Facies	Limestone	**L**	**33**	A, B	Wells 1, 2	-	Foraminifera, Gastropods, Brachiopods, Green Algae
Peloidal-Skeletal Grainstone (Open-Packing)		Lgo	10			Grainstone	
Peloidal-Skeletal Grainstone (Compacted)		Lgc	14			Grainstone	
Peloidal-Skeletal Grain-Dominated Packstone (Open-Packing)		Lpo	4			GDP	
Peloidal-Skeletal Grain-Dominated Packstone (Compacted)		Lpc	5			GDP	

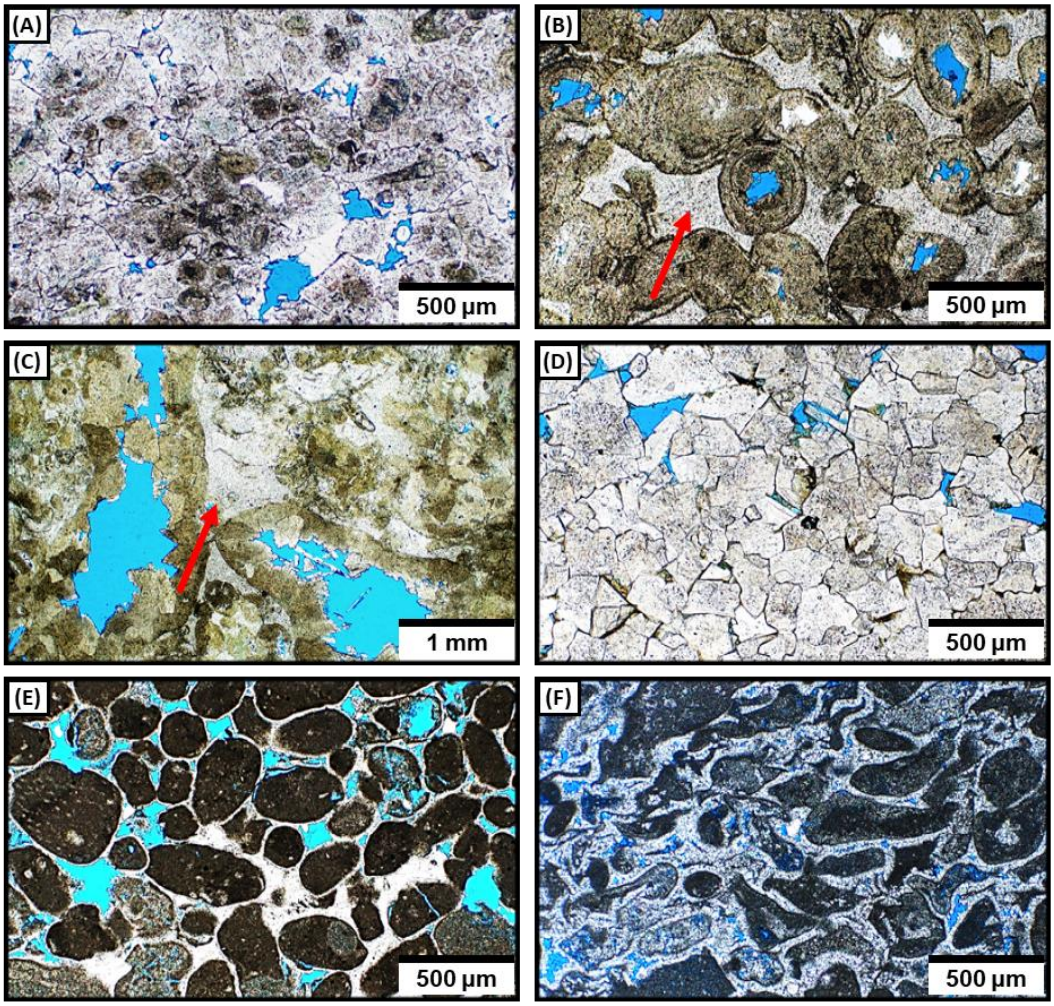

Figure 4.2. Photomicrographs of the dolostone and limestone facies encountered in the study. (A) Peloidal-skeletal dolograinstone (Facies D1). (B) Oolitic dolograinstone (Facies D2); note the oomolds and blocky dolomite cement (arrow). This sample is 100% dolomite. (C) Sponge dolorudstone (Facies D3); note the large molds inside the grain (possibly stromatoporoids) and the blocky dolomite cement (arrow). This sample is 100% dolomite. (D) Fabric-destructive dolostone (Facies D4). (E) Peloidal–skeletal grainstone (Facies Lg). (F) Peloidal-skeletal grain-dominated packstone (Facies Lp). Facies Lg and Lp are likely the undolomitized counterparts of Facies D1 (A).

4.3.2 Dolomite petrography

The majority of dolostone facies (94 out of 118 samples) contain replacive dolomite crystals that preserved the grains and depositional fabrics either partially or completely (Figure 4.2A, B, C). Fabric-destructive (FD) dolomite dominates 24 of the 118 dolostone samples (Figure 4.2D). Nonplanar-A (anhedral) and planar-S (subhedral) crystals dominate all dolostone facies and

together account for 89% of all dolomite crystals (Table 4.2). Nonplanar-E (euhedral) crystals are limited to some dolomite rhombs that were observed near and inside large pores. All dolomites can be grouped into either equant (lacking undulose extinction; ~63%) or baroque (with undulose extinction; ~37%) dolomites. Equant and baroque each comprise cement and replacement phases, with both commonly co-occurring in the same thin section. Dolostones dominated by baroque dolomite contain a greater proportion of large crystals (> 500 μm in size), whereas dolostones dominated by equant dolomite contain a greater proportion of fine and medium crystal sizes (< 100 μm in size; Table 4.2). Dolomite crystal sizes also vary as function of dolostone facies (Table 4.2), with the fabric-destructive dolostone containing the greatest proportion of coarse dolomite crystals > 500 μm (Table 4.2).

Most dolomite lacks zoning in cathodoluminescence, with mottled appearance characterized by dull luminescence with bright spots in the inner parts of the crystals (Figure 4.3). The mottling was observed in both equant and baroque dolomite and in both replacive and cement phases (Figure 4.A, B). Rare examples of CL growth zonation, dolomite dissolution, and overgrowth are observable in the outer parts of a few crystals (Figure 4.3C, D).

Table 4.2. Statistics of Different Petrographic Attributes in Dolostone

		Habit (%)		Crystal Size (%)					Textural Fabric (%)		
Group	**Count**	**Matrix**	**Saddle**	**Very Fine**	**Fine**	**Medium**	**Coarse**	**Very Coarse**	**Anhedral**	**Subhedral**	**Euhedral**
All Dolostones	**118**	**63.0**	**37.0**	**2.2**	**11.5**	**27.6**	**35.4**	**23.4**	**74.3**	**14.7**	**11.0**
Facies D1	47	73.4	26.6	4.7	15.8	32.4	33.8	13.3	76.7	14.9	8.4
Facies D2	30	65.7	34.3	0.0	12.7	26.3	39.5	21.5	77.3	13.0	9.7
Facies D3	17	34.7	65.3	0.0	2.9	20.6	41.8	34.7	57.1	20.0	22.9
Facies D4	24	60.0	40.0	1.7	7.9	25.0	28.8	36.7	78.1	12.7	9.2

Very Fine = 5 – 20 µm, Fine = 20 – 50 µm, Medium = 50 – 100 µm, Coarse = 100 – 500 µm, Very Coarse = > 500 µm. D1 = Peloidal-skeletal dolograinstone, D2 = Oolitic dolograinstone, D3 = Sponge dolorudstone, and D4 = Fabric-destructive dolostone

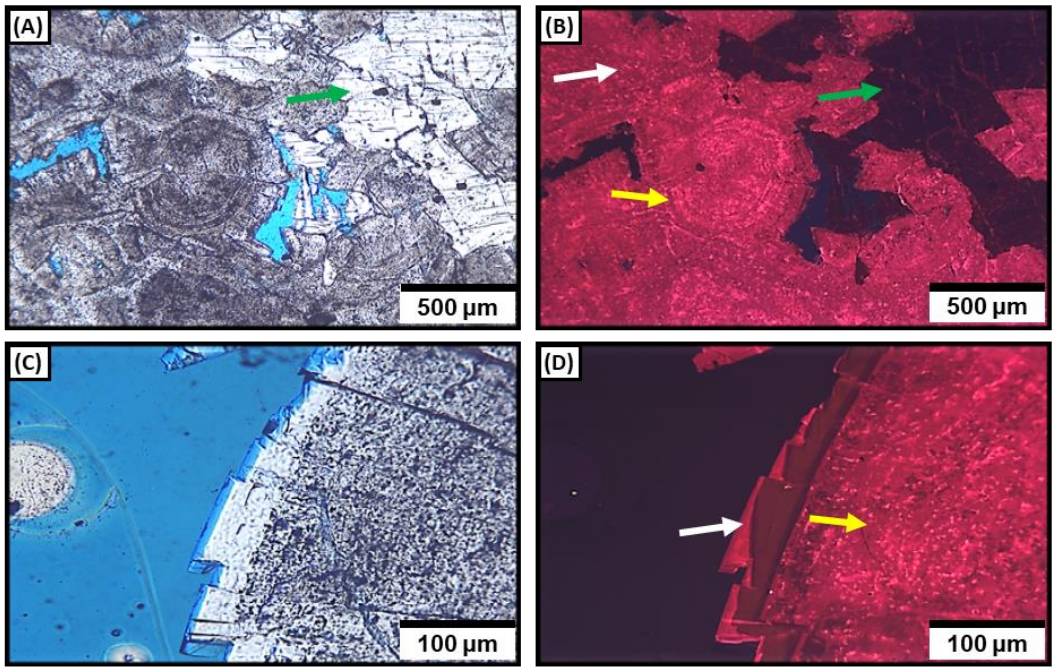

Figure 4.3. Paired plane light (A, C) and cathodoluminescence (CL) (B, D) images of dolostone. (A, B) Oolitic dolograinstone sample showing the same bright CL pattern in both the replacement dolomite (replacing ooids; yellow arrow) and the interparticle pore-reducing dolomite cement (white arrow). Both dolomite phases also show some mottling in CL, probably indicative of recrystallization. Green arrow in (A, B) is anhydrite (C, D) Bright CL in saddle dolomite with some mottling in CL (yellow arrow), similar to those of other replacement and pore-reducing dolomite phases. Two growth zones of very dull CL are in the outer banded dolomite cement (white arrow) and similarly very dull luminescent areas are observed as mottles, and patches within the mottled dolomite.

4.3.3 Main diagenetic alteration

This section addresses diagenetic processes and products that have a detectable impact on porosity in limestones and dolostones. It does not include the many minor diagenetic processes that have little impact.

4.3.3.1 *Limestones*

The studied limestones experienced diagenetic events and processes that modified their pore networks significantly, and produced distinct diagenetic facies. Three main diagenetic processes dominate limestone diagenesis: (1) cementation (by calcite, dolomite, and anhydrite), (2) compaction, and (3) dissolution.

Cementation has the greatest negative impact on porosity, with total cement percentages varying between 4.5% and 26.5%, with a mean of ~16.7%. The amount of cement also varies slightly between grainstone and GDP. Mean total cement (includes total calcite, dolomite, and anhydrite) are ~17.0% and ~15.0% for grainstone and GDP, respectively. Calcite is the main cement in all limestone samples; it is either isopachous or circumgranular rim cement that surrounds the grains but does not fill pores (Figure 4.4A, B). There are also examples of spalled calcite rim cement (Figure 4.4C). Calcite cement averages ~10.7% of all constituents in limestone with a range from 3% to 19%. Dolomite cements are pore-reducing, either as irregular patches of fine crystalline dolomite masses that encrust calcite cement (Figure 4.4D) or as rare coarse baroque crystals that partially fill pores (Figure 4.4E, F). Together, all dolomite cement accounts for a mean of 4.7% (range from 0 to 18%) of all constituents in limestone. There is a small quantity of anhydrite cement; it accounts for ~1.3% of all constituents (Figure 4.4F).

The amount of compaction, including mechanical compaction and grain–to–grain pressure dissolution, is uneven among the limestone samples and can be nonuniform even within the same thin section. Quantification of compaction requires multiple assumptions; thus, we rely on a qualitative assessment using grain packing textures as a proxy for the degree of compaction. Grainstone and grain-dominated packstone samples exhibit either open (diagenetic subfacies Lgo and Lpo) or compacted (Lgc and Lpc) packing of grains (Table 4.1). Samples with minor compaction (14 of 33 limestone samples) exhibit open grain packing with well-preserved rounded peloids that are covered by undeformed, thick, isopachous or circumgranular calcite cements (Figure 4.5A). Samples with moderate to intense compaction (19 of 33 limestone samples) are characterized by the presence of squashed peloids and pellets and only partial rim cements preserved (Figure 4.5B). Locally, areas with even more intense compaction were also observed. In these areas, the fabric is not only composed of densely packed grains, but the shape of the grains is more elongate, pore sizes are reduced, and spalled rim cements are abundant. Compaction bands (Figure 4.5C) are common in these samples and localized deformation of the original grains are observed at the thin section scale. In some samples, compaction bands develop near replacive anhydrite; and in areas where the bands develop, the initially connected interparticle pores have the two-dimensional appearance of isolated pores (Figure 4.5D).

Dissolution is the main porosity-enhancing diagenetic process observed in limestones. In the studied samples, dissolution either enhanced primary interparticle pores, leading to the creation of small dissolution-enhanced interparticle pores (~300 μm in size), or created moldic pores (Figure 4.5E). Dissolution in limestone did not generate large vuggy pores, as those were observed only in the dolostones.

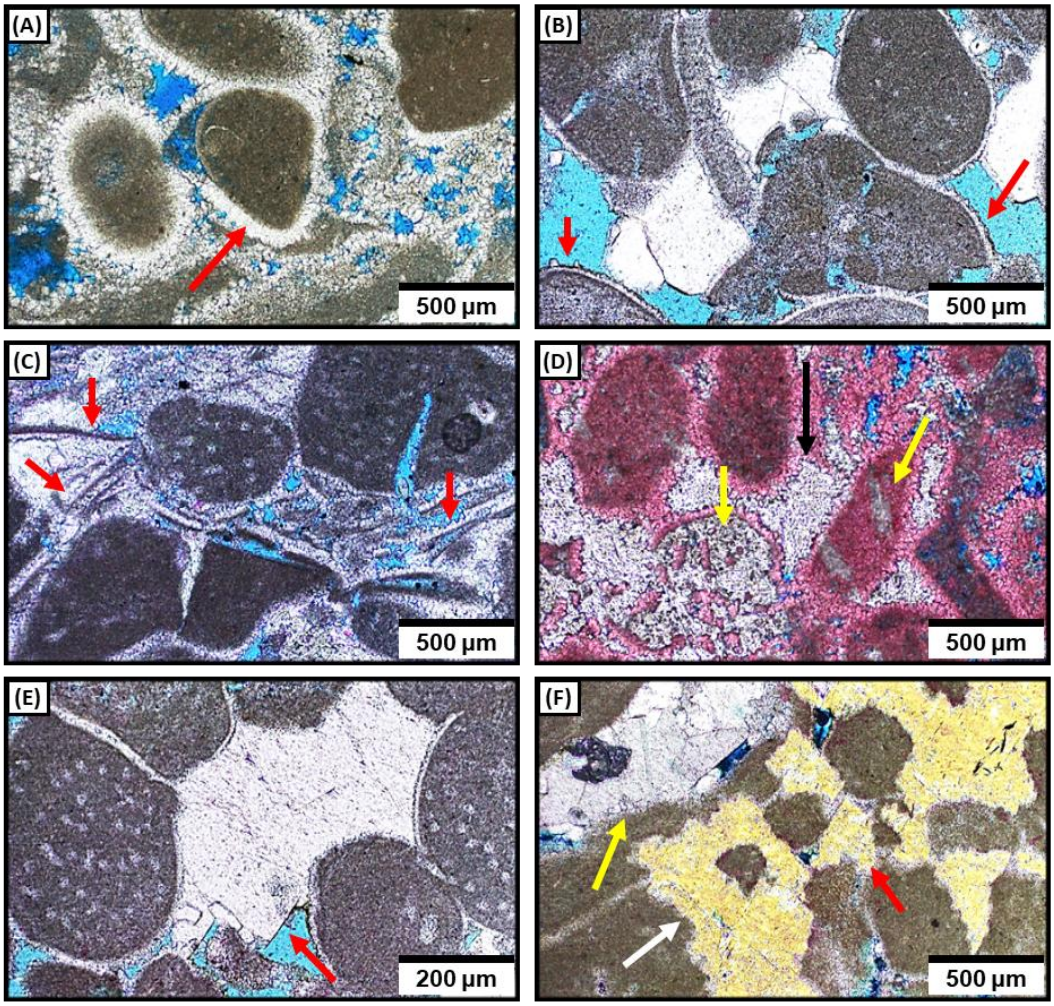

Figure 4.4. Photomicrographs of different cements and diagenetic phases observed in limestone. (A) Isopachous calcite rim cement surrounding peloids (arrow). (B) Thin circumgranular rim cement composed of sparse equant calcite crystals. (C) Detached circumgranular rim cement (arrows); the white cement is dolomite. (D) Dolomite cement in limestone; the sample is stained with Alizarin red and the red is calcite. Note the dolomite-filled interparticle pores (black arrow) and moldic pores (yellow arrows). (E) Saddle dolomite partially filling interparticle pores in limestone (arrow). (F) Cross- polar image of saddle dolomite partially filling moldic pores in limestone (yellow arrow), anhydrite replacing peloids (white arrow), and anhydrite filling interparticle pores (red arrow).

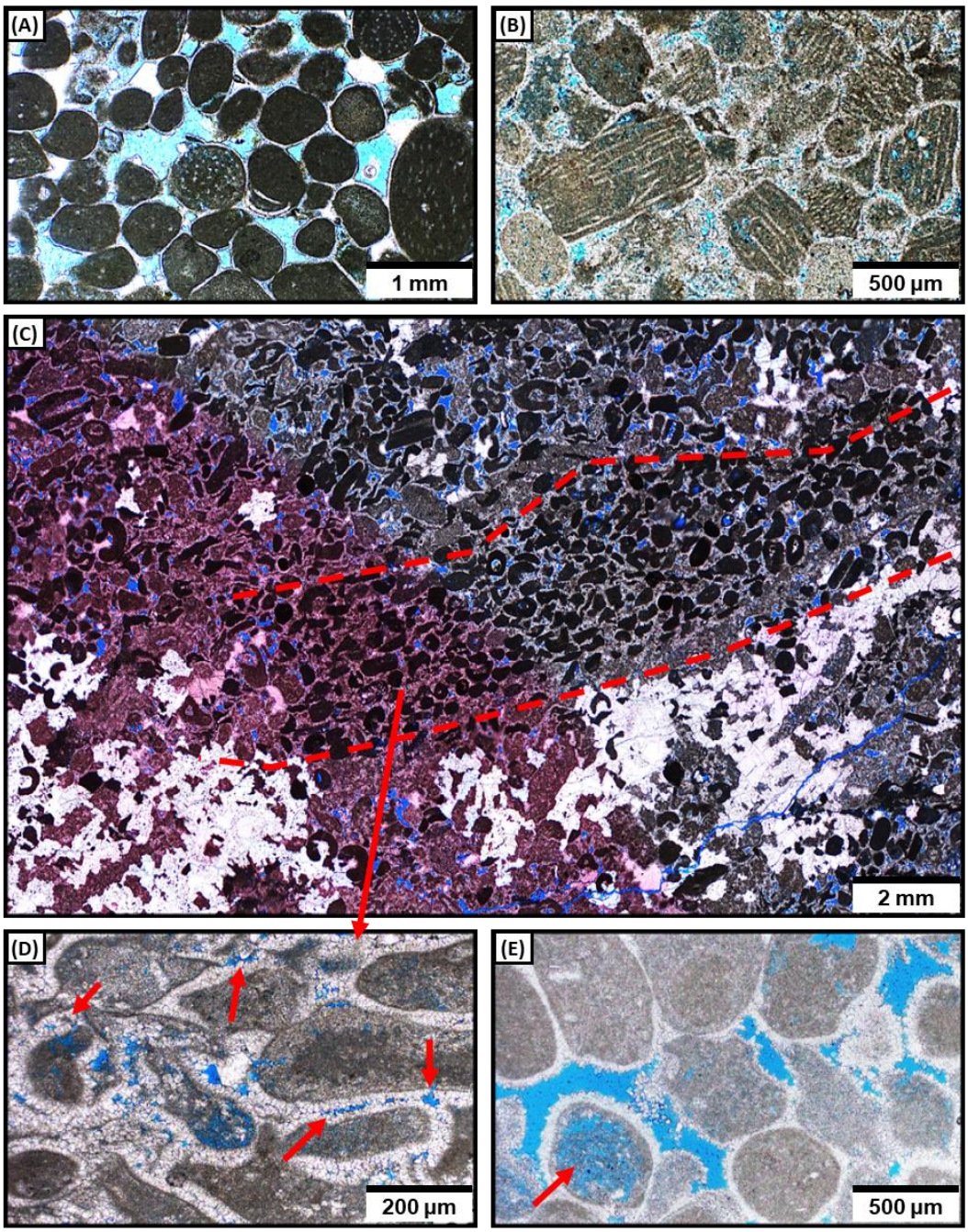

Figure 4.5. Photomicrographs of mechanical and chemical compaction and dissolution in limestone. (A) Peloidal-skeletal grainstone (subfacies Lgo), with open packing of grains and minor grain–to–grain pressure dissolution. (B) Peloidal-skeletal grainstone with more compaction (subfacies Lgc), grain is Faverina. (C) Full thin section scan of a peloidal– skeletal grain-dominated packstone (subfacies Lpc) showing well-developed compaction bands (area between the two dashed lines). Compaction is more intense within the band. The area within the band also contains modified pore spaces, where interparticle pores appear to be isolated from each other. The white mineral is anhydrite. (D) Peloids within the compaction bands showing deformation and reorientation. Note that the pore throats of main interparticle pores between grains are reduced in size (arrows), leading initially connected pores to appear isolated, at least in 2-D. (E) Example of a moldic pore in limestone (arrow).

4.3.3.2 *Dolostones*

In the dolostones, cementation and dissolution are the two main diagenetic processes impacting the pore networks. All dolostone facies contain dolomite and anhydrite cements. Calcite cement is not present in any dolostone sample. Dolomite cement is pore reducing (Figure 4.6A), as overgrowths that reduce either primary (Figure 4.6B) or secondary (Figure 4.6A, C) pores. Some of the dolomite cements have baroque or saddle morphologies, whereas others do not. Most of the dolomite shows mottling in CL, lacks thin concentric growth zones, but shows cloudy areas constrained by growth-zone boundaries. Anhydrite cement forms either tabular or rounded and internally felted, pore-reducing masses, and is closely associated with replacive anhydrite (Figure 4.6D). Replacive anhydrite cross-cuts some dolomite phases, and younger baroque dolomite phases cut across it (Figure 4.6E). Overall, dolomite cement varies from ~7% to ~30% (mean: ~15%) of the rock volume and anhydrite cement varies between 0% and 20% (mean: 2.9%), with total amount of cement in individual samples varying between ~8.0% to ~35.0% (mean: ~18%). Mean total cement in facies D1 is ~15%, D2 is ~25.0%, D3 is 19.0%, and D4 cannot be determined.

All dolostone samples include pore spaces that were created or enhanced by dissolution. These pore spaces range from small (~10 μm), isolated moldic pores found mostly within the masses of dolomite crystals and characterized by round or nondescript shapes, to large (up to 1 cm) vuggy pores (Figure 4.6F). The vugs are only observed in the dolostone and not in the limestone. Dissolution-related pores are either fabric selective (e.g., moldic pores within dolomitized ooids; Figure 4.2B) or non-fabric selective (e.g., large vugs cross-cutting multiple dolomite phases; Figure 4.6F). Some moldic pores are within anhydrite nodules (Figure 4.7A), baroque dolomite crystals (Figure 4.7B), or along certain dolomite crystal growth zones (Figure 4.7C). Some vugs cross-cut stylolites (Figure 4.7D) and are preferentially distributed close to

stylolite seams. The majority of baroque dolomite crystal terminations show some etching of the outermost growth surface (Figure 4.7E, F). Together, these observations highlight some noticeable differences between the dissolution pores in the dolostone and limestone.

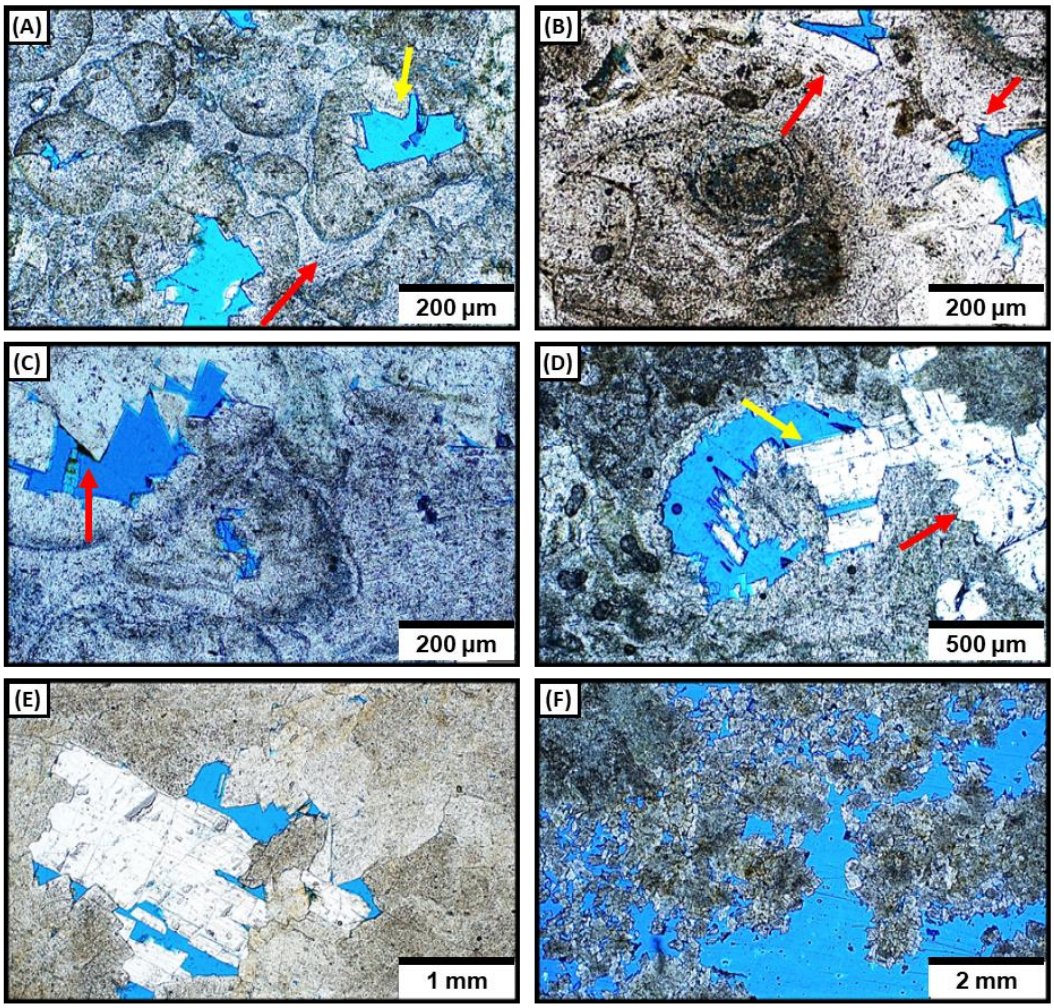

Figure 4.6. Photomicrographs of cement and dissolution-related products in dolostones. (A) Blocky pore-reducing dolomite cement between stromatoporoid grains (red arrow) and dolomite crystal overgrowth partially filling secondary pores (yellow arrows) in a sponge dolorudstone facies (Facies D3). (B) Dolomite cement overgrowth partially filling interparticle pores between dolomitized ooids and dolomitized composite ooids (red arrows) in an oolitic dolograinstone facies (Facies D2). (C) Large saddle dolomite crystal partially filling secondary pores in a sponge facies; the grain is likely stromatoporoid and the sample is from Facies D3. (D) Replacive (red arrow) and pore-filling (yellow arrow) anhydrite partially filling primary and secondary pores in an oolitic dolograinstone sample (Facies D2). (E) Anhydrite crystals partially filling pores in dolostone observed in fabric-destructive facies (Facies D4). (F) Large nonfabric-selective vug in a peloidal–skeletal dolograinstone sample (Facies D1).

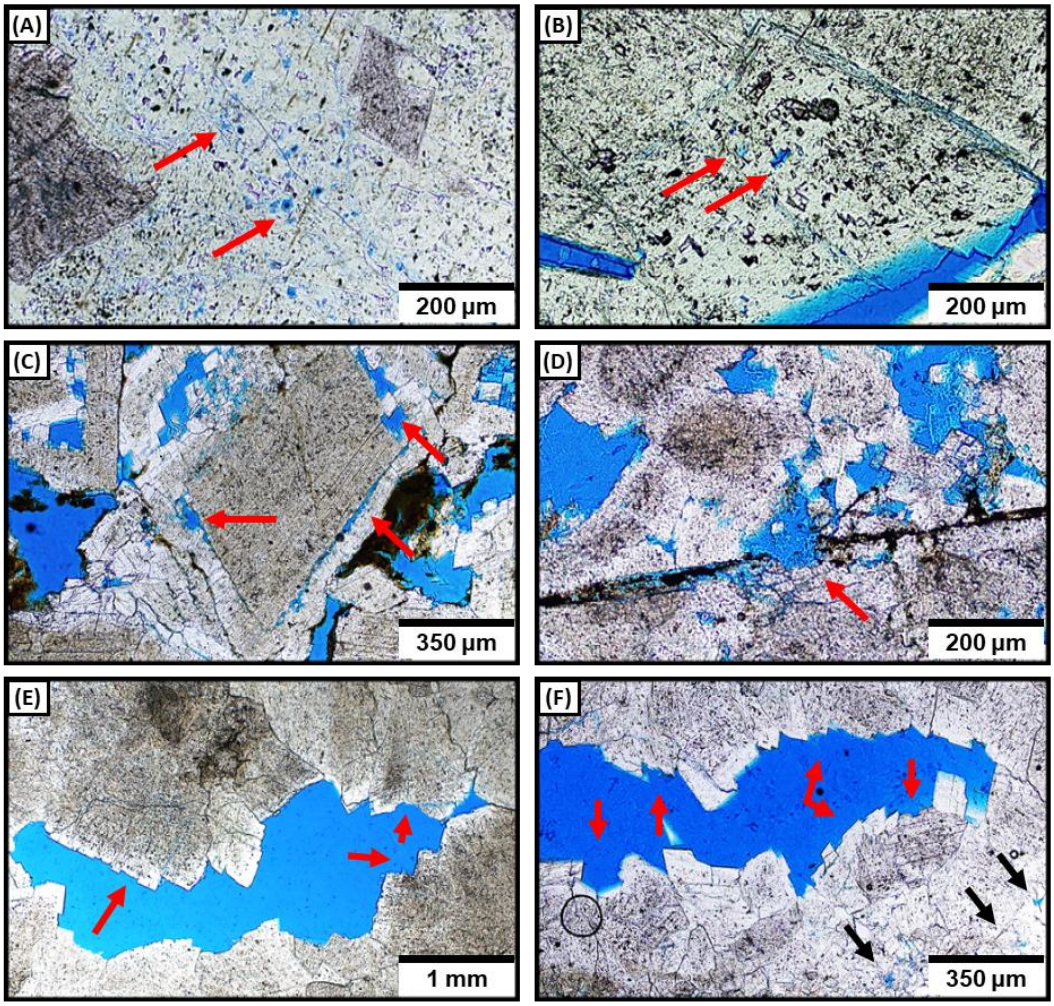

Figure 4.7. Photomicrographs of diagenetic phases and products unique to dolostones. (A) Small (~10 to 20 µm) moldic pores within a coarse anhydrite phase. (B) Small (~10 to 20 µm) moldic pores within saddle dolomite crystal (arrow), with solution-enlarged microfractures. (C) Molds within dolomite crystal growth zone (arrows), with solution-enlarged microfractures. (D) Vug cross-cutting a stylolite seam (arrow). (E, F) Corroded outer growth zones in saddle dolomite crystals (arrows); black arrows in (F) show moldic pores within the masses of saddle dolomite crystals.

4.3.4 Geochemistry

Oxygen isotope ($\delta^{18}O$) values in limestones (n = 20) vary between -6.3‰ and -4.1‰ (mean: -5.0‰) and carbon isotope ($\delta^{13}C$) values range from 1.7‰ to 2.8‰ (mean: 2.4‰) (Figure 4.8A). Dolomite cements in limestone (n = 5) show an $\delta^{18}O$ range of -3.8‰ to -4.9‰ and $\delta^{13}C$ range of 2.5 to 2.7‰ (Figure 4.8A). The dolostone samples (n = 112) have more negative $\delta^{18}O$

values than the limestones and dolomite cement in the limestone, with values ranging from -10.0‰ to -6.4‰ (mean: -8.1‰) The $\delta^{13}C$ values in dolostone vary between 1.4‰ and 3.5‰ (mean: 2.6‰), which is slightly more positive than the majority of the $\delta^{13}C$ values in limestone. Despite the range of $\delta^{18}O$ values in limestones and dolostones, all values are more negative than those expected for low-temperature marine dolomites and calcites produced by coeval Late Jurassic seawater (Figure 4.8A; Veizer et al., 1999). Different dolomite phases (e.g., equant replacive and cement, and baroque replacive and cements) record comparable $\delta^{18}O$ and $\delta^{13}C$ values.

Dolostones contain an abundance of primary, two-phase, fluid inclusions that are concentrated in certain growth zones of dolomite phases. Homogenization temperatures Th (n = 307 measurements) average 102.1°C, with a range of 83.5–117.1°C (Figure 4.8B). Despite this range, approximately 90% of the values are between 95°C and 110°C. Melting temperatures of ice Tm_{ice} (n = 200 measurements) average -23.3°C (equating to a salinity of 24.5 wt.% NaCl eq.; Bodnar, 1992) and range from -27.9°C to -17.5°C (i.e., salinities of 27.4–20.6 wt.% NaCl eq.; Figure 4.8B). Similar to the stable isotopes, the different dolomite phases also record comparable Th and Tm_{ice} values. Limestone phases lack measurable primary fluid inclusions.

Strontium isotope ratios ($^{87}Sr/^{86}Sr$) measured in 12 whole-rock samples (9 dolostone and 3 limestone) were obtained to determine the origin of the fluid responsible for dolomitization, as well as the fluids that produced calcite cement. Limestone samples record values between 0.70701 and 0.70714, which are within the range for Late Jurassic seawater (Figure 4.8C; McArthur et al., 2001). The dolostone $^{87}Sr/^{86}Sr$ values vary between 0.70761 to 0.70787, which are notably higher than those of Late Jurassic seawater (Figure 4.8C; McArthur et al., 2001).

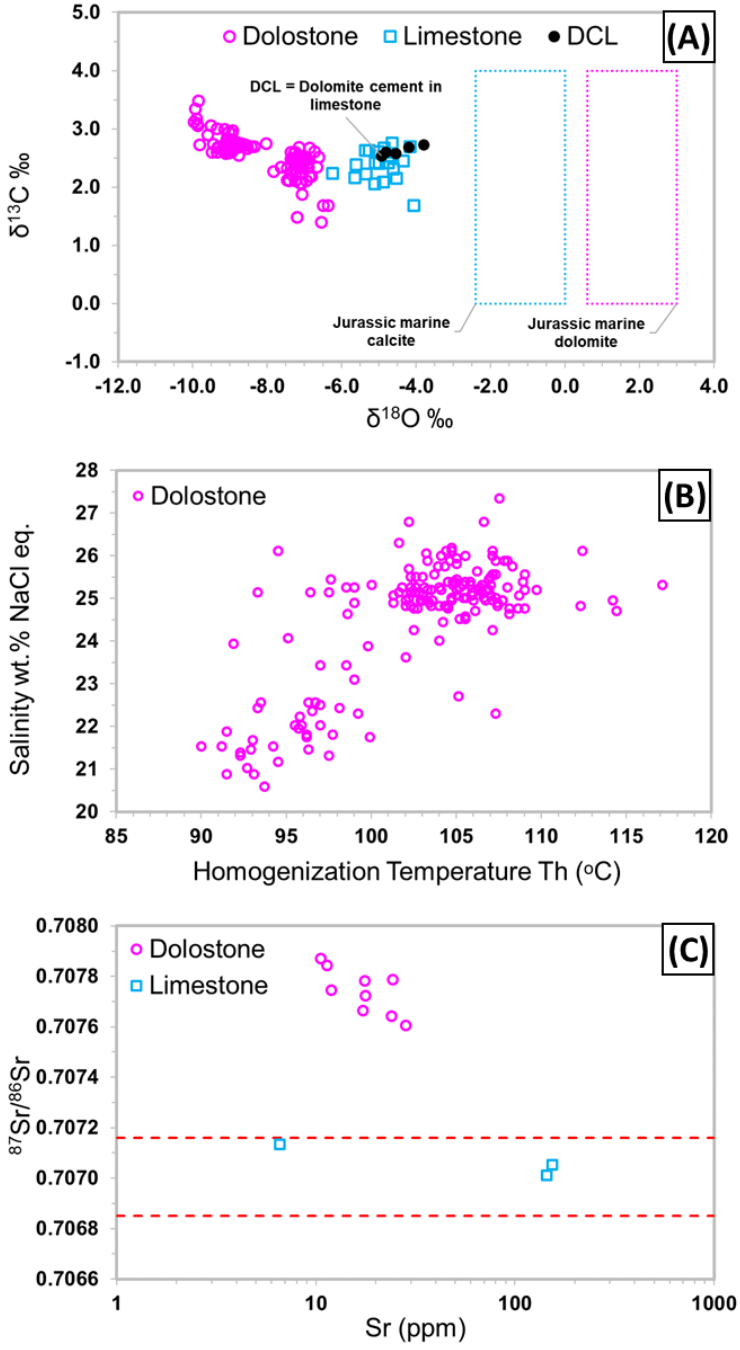

Figure 4.8. (A) Carbon isotope ($\delta^{13}C$) vs. oxygen isotope ($\delta^{18}O$) cross plot of limestone and dolostone. The data points for both lithologies are outside those expected for Late Jurassic, low-temperature, marine calcite and dolomite (Veizer et al., 1999); the dolomite value is based on the fractionation value given by Land (1980). (B) Salinity–homogenization temperature cross plot for dolomite in dolostone. Salinity was measured from the temperature of melting of ice data and is presented as wt.% NaCl equivalent. Data points are from multiple samples and multiple fluid inclusion assemblages. (C) Strontium isotope ratio ($^{87}Sr/^{86}Sr$) vs Sr concentration (ppm) for nine dolostone and three limestone samples. Limestone samples fall within the range expected for Late Jurassic seawater (area between two red dashed lines; McArthur et al., 2001). The dolostones record much higher $^{87}Sr/^{86}Sr$ values than expected for Late Jurassic seawater, indicating either a radiogenic influence or formation from seawater-derived fluid of a younger age (e.g., Eocene seawater has $^{87}Sr/^{86}Sr$ values similar to those of the dolostones here; McArthur et al., 2001).

4.3.5 Reservoir petrophysics

Limestone (n = 33 samples) has median porosity and permeability values of 11.9% and 2.6 mD, respectively (Table 4.3). As discussed earlier, in this study limestone contains only one facies; the peloidal-skeletal GDP to grainstone (Figure 4.2E, F). This facies is divided based on its texture into a grainstone subfacies (Lg) and a GDP subfacies (Lp). Each subfacies is then further subdivided based on the degree of grain compaction into 'open-packed' subfacies, where the majority of grains show open-packing (Lgo and Lpo) or compacted subfacies, where grains showed more compaction fabrics, characterized by more contact points between grains (Lgc and Lpc, Figure 4.5B, C). These divisions are used here for the petrophysical analysis of the limestones (Figure 4.9A; Table 4.3). Subfacies Lgo has the highest median porosity and permeability values of all limestone subfacies (porosity = 14.7%, permeability = 15.1 mD; Figure 4.9A; Table 4.3), while subfacies Lpc has the lowest median values (porosity = 11.3%; permeability = 0.3 mD; Figure 4.9A; Table 4.3). The relationship between porosity and permeability in the limestone's subfacies (Lgo, Lgc, Lpo, and Lpc), as depicted by the regression slopes and correlation coefficients (*R*), is wide-ranging (Table 4.3). Subfacies Lgo and Lpc (the two facies with the highest and lowest porosity and permeability median values, respectively) record the lowest *R* value (*R* = +0.32). The two other limestone subfacies (Lgc and Lpo) record higher *R* values of +0.68 and +0.92, respectively (Table 4.3).

Dolostone (n = 118) has median porosity and permeability values of 10.4% and 1.5 mD, respectively. Both porosity and permeability show a wider range of values in dolostone than in limestone (Table 4.3). The four dolostone facies (D1 to D4) have similar porosity and permeability values and overlap each other in permeability–porosity space (Figure 4.9B), yet facies D2 and D4 show slightly lower values than D1 and D3 (Table 4.3). Samples with permeabilities > 100 mD

are only observed in the dolostone facies (Figure 4.9B) and not the limestone facies (Figure 4.9A). There is a strong relationship between porosity and permeability in all four dolostone facies with the correlation coefficients (*R*) for each varying between +0.73 to +0.89 (Table 4.3).

Table 4.3. Statistics of Petrophysical Values for Dolostone Facies and Limestone Facies and Subfacies

	Porosity (%)						Permeability (mD)					R^2	R
Group	**Count**	**Min**	**Max**	**Mean**	**Geometric**	**Median**	**Min**	**Max**	**Mean**	**Geometric**	**Median**		
Limestones (Facies L)	**33**	**5.6**	**19.6**	**12.7 (8.0)***	**12.1**	**11.9**	**0.1**	**56.0**	**7.3**	**2.2**	**2.6**	**0.52**	**0.72**
Subfacies Lg	**24**	**5.6**	**19.6**	**13.2 (8.7)***	**12.5**	**13.6**	**0.1**	**56.0**	**9.4**	**3.5**	**3.5**	**0.50**	0.71
Subfacies Lgo	10	11.4	19.6	15.7	15.4	14.7	2.9	56.0	19.1	11.9	15.1	0.10	0.32
Ssubfacies Lgc	14	5.6	16.7	11.5	10.8	11.7	0.1	7.9	2.5	1.5	2.1	0.46	0.68
Subfacies Lp	**9**	**6.9**	**16.6**	**11.4 (6.4)***	**11.1**	**11.3**	**0.2**	**7.6**	**1.5**	**0.7**	**0.4**	**0.62**	0.79
Subfacies Lpo	4	6.9	16.6	12.1	11.5	12.5	0.4	7.6	2.8	1.4	1.6	0.84	0.92
Subfacies Lpc	5	8.8	11.8	10.9	10.8	11.3	0.2	0.9	0.4	0.4	0.3	0.10	0.32
Dolostones	**118**	**2.0**	**23.7**	**10.8**	**10.2**	**10.4**	**0.1**	**3150.0**	**105.2**	**3.1**	**1.5**	**0.58**	**0.76**
Facies D1	47	2.0	23.7	11.7	10.9	11.5	0.1	3150.0	132.1	4.3	3.3	0.54	0.73
Facies D2	30	5.6	20.1	10.5	9.9	9.4	0.1	2250.0	126.8	1.6	1.2	0.79	0.89
Facies D3	17	8.3	15.8	12.0	11.8	11.8	0.3	498.0	65.6	5.4	2.1	0.55	0.74
Facies D4	24	4.9	16.4	8.9	8.4	8.4	0.1	974.0	54.6	2.5	1.0	0.60	0.77

*(x.x) = primary pore percentage. Code: Facies L = Peloidal-skeletal limestone, Lg = L grainstone, Lp = L packstone, Lgo = Lg open-packing of grains, Lgc = Lg compacted grains. Facies D1 = Peloidal-skeletal dolograinstone (dolomitized counterpart of Facies L), Facies D2 = Oolitic dolograinstone, Facies D3 = Sponge dolorudstone, Facies D4 = Fabric-destructive dolostone. R2 values are based on linear regression between porosity and log permeability.

The peloidal-skeletal dolograinstone (facies D1) and its undolomitized counterpart (i.e., the limestone facies L, including all subfacies) have some petrophysical similarities and differences (Figure 4.9C; Table 4.3). The dolomitized (D1) and undolomitized (L) facies have two main similarities. First, the median porosity and permeability values of the two facies are nearly identical (11.5% and 3.3 mD and 11.9% and 2.5 mD, for D1 and L, respectively; Figure 4.9C; Table 4.3). Second, the correlation coefficients between porosity and permeability in the two facies are also nearly identical (R = +0.73 and +0.72, for D1 and L, respectively; Table 4.3). On the other hand, the two facies (D1 and L) have two noticeable differences. First, the dolomitized facies has

a much wider range of permeability values, and includes samples with much higher values, than does the undolomitized facies. The dolomitized facies (D1) contains six samples with permeabilities >100 mD (Figure 4.9C), while the undolomitized facies (L) does not contain any sample with a permeability > 100 mD, with the highest permeability recorded in this facies being 56 mD (Figure 4.9C; Table 4.3). Second, while the correlations coincide at low values, the dolomite dataset has a much higher slope. As described in the foregoing, the main difference between the two facies is the configuration of pore types in each facies (Table 4.4) as observed petrographically. The pore network in the dolomitized D1 facies is dominated by moldic and vuggy pores (together representing ~77% of total porosity; Table 4.4), with ~25 to ~50% of those moldic and vuggy pores showing diagenetic relationships similar to those shown in Figure 4.7. The undolomitized facies, on the other hand, is dominated by interparticle pores (represent ~53% of total porosity). Moldic pores are common in the undolomitized facies (Figure 4.5E), but no vugs were observed in the limestone facies (Table 4.4).

In limestone (facies L), amount of interparticle porosity shows a positive relationship with permeability (R^2 = 0.37, R = +0.61; Figure 4.10A). No other pore type yields correlations with permeability (Figure 4.10B, C, D; Table 4.5). In facies D1, interparticle, intercrystal, and vuggy porosity are all correlated with permeability (Figure 4.10E, F, H). Intercrystal porosity shows the strongest relationship to permeability (R^2 = 0.60, R = +0.78; Figure 4.10F). The correlation of interparticle porosity in D1 (Figure 4.10E) shows a much steeper slope than for the limestone (Figure 4.10A). In dolostone, vugs show a strong positive relationship with permeability (Figure 4.10E, G; Table 4.5). Although, intercrystal pores are not common in the facies D1 (nor in any dolostone facies), with a relative proportion of only 8.3% of total pore volume in facies D1 (Table 4.4), it is still positively correlated with permeability. Moldic pores, which dominate the dolostone

facies (~54% of total pore volume) show a poor correlation with permeability (Figure 4.10G). Much of the pores within the dolomite crystal masses in dolostones are described as moldic as they are clearly dissolution-produced and not crystal-supported pores. Moldic pores were observed in all dolostone samples (118 of 118) but vuggy pores were observed in only 62 of 118 samples (~52% of the samples).

The relationships among porosity, main pore types, permeability, and cement types are variable in both the limestone and dolostone facies (Table 4.5). In the limestone, calcite cement shows no correlation to extant porosity but a moderately negative correlation to permeability. Dolomite and anhydrite cements in limestone account for a smaller fraction of total cement than calcite and generally show a weak relationship to porosity. In the dolostone, dolomite and anhydrite cements show moderate negative correlations with both porosity and permeability (Table 4.5).

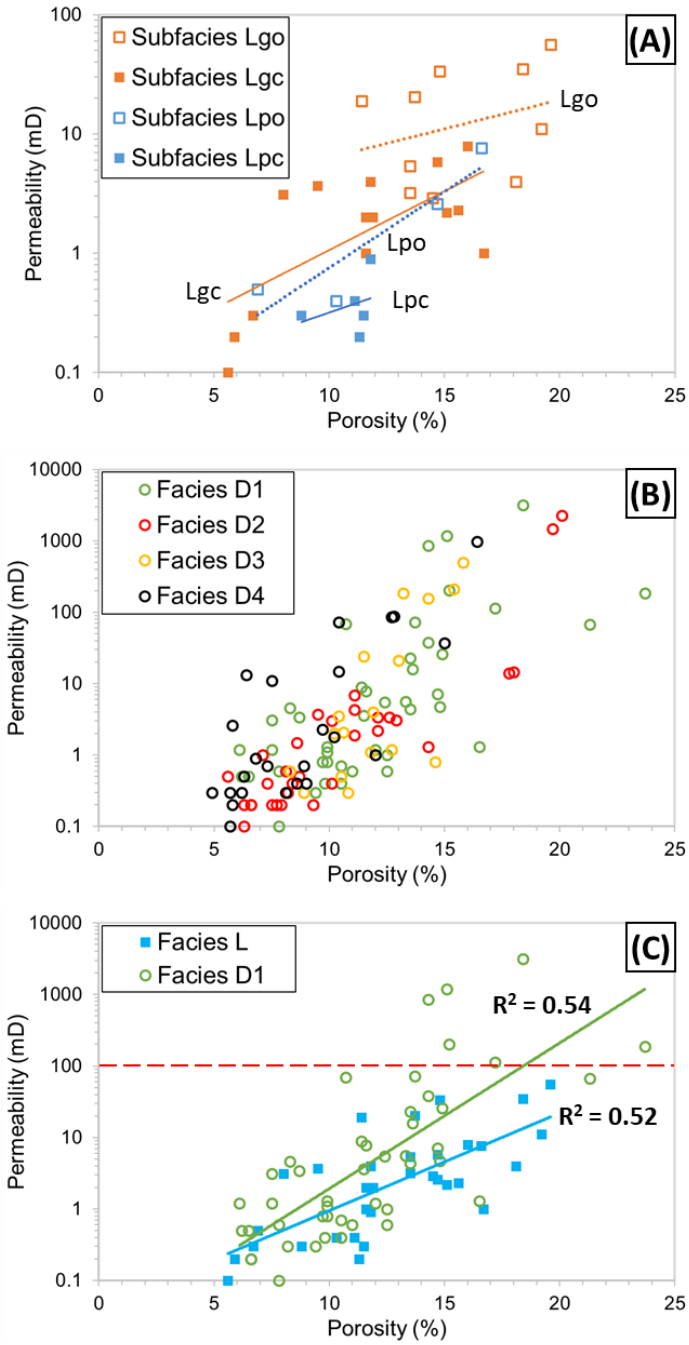

Figure 4.9. Porosity–permeability cross plots of the limestone and dolostone facies. (A) Porosity–permeability cross plot of undolomitized peloidal–skeletal subfacies. Highest porosity and permeability values were observed in subfacies Lgo, and lowest in subfacies Lpc. (B) Porosity–permeability cross plots of the four dolostone facies, showing an overlap in values. (C) Cross plot comparing Facies L with the dolomitized counterpart facies (Facies D1). Both the dolomitized and undolomitized facies show similar means (Table 4.3) but permeabilities > 100mD were only observed in Facies D1 and not Facies L. Code: Facies L = Peloidal-skeletal limestone, g = grainstone, p = packstone, o = open-packing of grains, c = compacted grains. Facies D1 = Peloidal-skeletal dolograinstone (dolomitized counterpart of Facies L), Facies D2 = Oolitic dolograinstone, Facies D3 = Sponge dolorudstone, Facies D4 = Fabric-destructive dolostone. R^2 values are based on linear regression between porosity and log permeability.

Table 4.4. Statistics of Pore Type Proportions in Limestone and Dolostone

Group	Main Texture	Count	Mean Porosity (%)	Proportion of Pore Types (Mean %)							
				Interparticle	Intraparticle	Moldic	Vug	Intercrystal	Fenestral	Undifferentiated	
Facies L	Grainstone	33	12.7	6.7	1.3	4.3	0.4*	-	-	-	= 12.7
				52.6	10.6	33.8	3.0*	-	-	-	= 100%
Facies D1	Grainstone	47	11.7	1.5	0.0	6.3	2.7	1.0	0.1	0.2	= 11.7
				12.6	0.0	54.1	22.9	8.3	0.7	1.4	= 100%
Facies D2	Grainstone	30	10.5	0.0	0.0	6.1	3.5	0.4	0.0	0.4	= 10.5
				0.0	0.0	58.3	33.6	4.1	0.0	4.0	= 100%
Facies D3	Rudstone	17	12.0	0.0	0.0	8.8	2.8	0.4	0.0	0.0	= 12.0
				0.0	0.0	73.1	23.4	3.6	0.0	0.0	= 100%
Facies D4	-	24	8.9	0.2	0.0	3.9	2.7	1.1	0.6	0.3	= 8.9
				2.4	0.0	43.5	30.9	12.2	7.2	3.8	= 100%

L = Peloidal-skeletal grainstone (and grain-dominated packstone), D1 = Peloidal-skeletal dolograinstone, D2 = Oolitic dolograinstone, D3 = Sponge dolorudstone, and D4 = Fabric-destructive dolostone

* Facies L1 does not contain vugs but contains solution-enlarged interparticle pores, here counted as vug

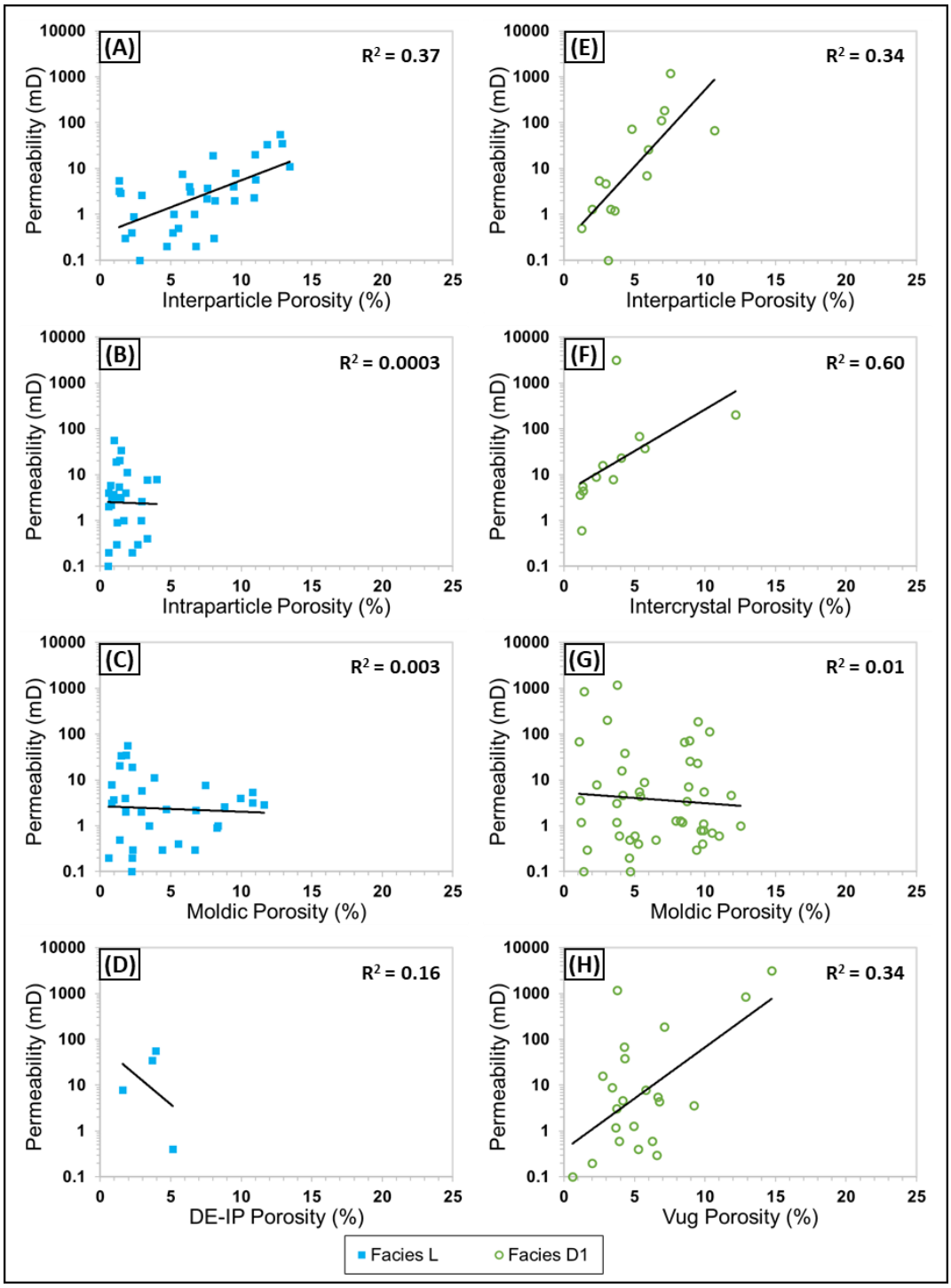

Figure 4.10. Relationship of four most common pore types (as a % of total extant porosity) to permeability in limestone (A, B, C, D) and dolostone (E, F, G, H) samples. Interparticle pore in limestone (A) is the only pore type with good correlation with permeability and a positive trend. In the dolostone, intercrystal pores exhibit the best correlation with permeability. Facies L = Peloidal–skeletal grain-dominated packstone to grainstone, Facies D1 = Peloidal–skeletal dolograinstone. DE–IP in (D) is dissolution-enlarged interparticle pores as limestone does not contain any vuggy pores. R^2 values are based on linear regression between percent of the extant pore space and log permeability.

Table 4.5. Relationship among pore types, cement type, and porosity and permeability

Facies	Porosity		Permeability	
	R^2	R	R^{2*}	R
Facies L				
Total Porosity			**0.52**	**0.72 (+)**
Interparticle porosity	0.25	0.50 (+)	**0.37**	**0.61 (+)**
Intraparticle porosity	0.08	0.28 (+)	**0.00**	**0.05 (-)**
Moldic porosity	0.09	0.30 (+)	**0.00**	**0.05 (-)**
DE-Interparticle porosity	0.17	0.41 (+)	**0.16**	**0.40 (-)**
Calcite cement	0.00	0.00	0.09	0.30 (-)
Dolomite cement	0.04	0.20 (-)	0.02	0.14 (+)
Anhydrite cement	0.19	0.44 (-)	0.01	0.09 (-)
Total cement	0.06	0.25 (-)	0.02	0.14 (-)
Facies D1				
Total Porosity			**0.54**	**0.73 (+)**
Interparticle porosity	0.62	0.79 (+)	**0.34**	**0.58 (+)**
Intercrystal porosity	0.10	0.32 (+)	**0.60**	**0.77 (+)**
Moldic porosity	0.13	0.36 (+)	**0.01**	**0.10 (-)**
Vuggy porosity	0.31	0.56 (+)	**0.34**	**0.58 (+)**
Calcite cement				
Dolomite cement	0.29	0.54 (-)	0.20	0.45 (-)
Anhydrite cement	0.03	0.17 (-)	0.00	0.00
Total cement	0.31	0.56 (-)	0.17	0.41 (-)

(+) = positive trend, (-) = negative trend. R^2 values are based on linear regression between porosity and log permeability. Values in bold are also shown by cross-plots in Figure 4.10

4.4 DISCUSSION

4.4.1 Overall paragenesis

The paragenesis of the carbonates studied here can be divided into two stages, predolomitization and post–onset of dolomitization stages (Figure 4.11). Limestones were mostly impacted by early, predolomitization events, that are dominated by near-surface diagenesis. The calcite cements (Figures 4.4 and 4.5), show isopachous and bladed fabrics, and are likely

submarine cements (e.g., James and Ginsburg, 1979; Friedman, 1985; Pierson and Shinn, 1985). This is supported by $^{87}Sr/^{86}Sr$ in limestone, which is within the range of Late Jurassic seawater (Figure 4.8C; McArthur et al., 2001). Moldic pores are of unknown origin. Limestone $\delta^{18}O$ is more negative than low-temperature marine calcite (Figure 4.8A), however, uranium–lead (U–Pb) dating, which was obtained in a different study [Chapter 2 of this dissertation], yields ages from 140 ± 6 Ma to 111 ± 11 Ma for the limestones (event 8; Figure 4.11) indicating recrystallization during Cretaceous burial heating. The minor dolomite cement phase in the limestone postdates mold formation and some compaction. It has more negative $\delta^{18}O$ values than that of low-temperature Jurassic marine dolomites (Figure 4.8A) but it is still less negative than the dolostones in the same wells. This dolomite likely represents a minor burial dolomite phase that formed well before the dolomite in the dolostone. Uranium–lead (U–Pb) dating in the dolomite cement in the limestone yielded ages of 129 ± 19 Ma to 112 ± 6 Ma (event 9; Figure 4.11), supporting a shallow burial origin, or an early origin with a subsequent recrystallization in a shallow burial setting [Chapter 2 of this dissertation].

Dolostones have negative $\delta^{18}O$ values (mean: -8.1‰; Figure 4.8A), high homogenization temperatures (mean: 102.1ºC; Figure 4.8B), and elevated $^{87}Sr/^{86}Sr$ values outside those expected for Late Jurassic seawater (Figure 4.8C). All indicating that the bulk of dolomites in the dolostones have formed or significantly recrystallized during deep burial, well after the majority of the limestone diagenesis has ceased (Figure 4.11). A deep burial environment for all dolostones is also supported by uranium–lead dating (U–Pb), which yields ages from 58 ± 6 Ma to 12 ± 2 Ma for different dolomite phases in dolostones [Figure 4.11; Chapter 2 of this dissertation]. This age range likely records the time of some dolomite formation but also a subsequent time of recrystallization as the two processes could have overlapped (Figure 4.11). Details of the paragenesis, along with

complete interpretations of the geochemical data and origin of dolomite are beyond the scope of this paper but can be found in Chapter 2. The petrographic observations presented here, however, show that: (1) there are multiple events of dolomite precipitation alternating with dissolution to form molds and vugs; and (2) dolomite precipitation, fracturing, and solution enlargement are all closely associated with one another, and they postdate stylolization, and therefore are late.

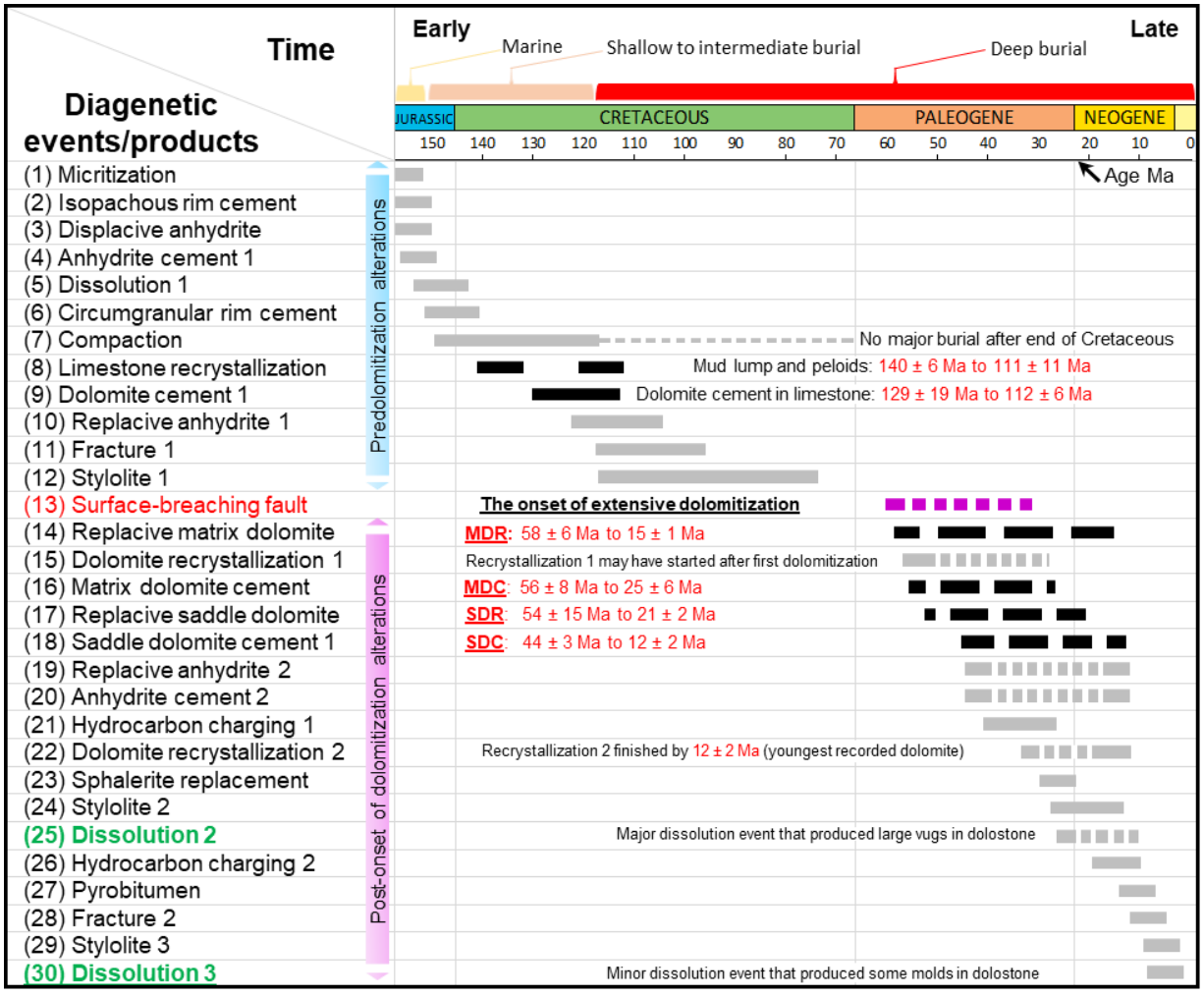

Figure 4.11. Paragenesis of the Upper Jurassic Arab Formation in northeast Saudi Arabia. The diagenetic history of the carbonates can be grouped generally into predolomitization and post onset of dolomitization stages. Bars in black are constrained by U–Pb dating with the ages provided by the red text. All other events are constrained by cross-cutting relationships, geochemical analyses, and knowledge of published structural and burial history of the region.

4.4.2 Controls on porosity and permeability in limestone

Limestone is born with large volumes of pore space, with modern surface packstones and grainstones that experienced little diagenetic alteration recording porosities between 40% and 67% (Enos and Sawatsky, 1981). Subsurface limestones, however, retain only a small fraction of their initial pore space. For example, field observations by Meyers (1980) showed a reduction of up to 38% of limestone porosity in Mississippian packstones and grainstones. The mean porosity of subsurface limestone reservoirs decreases with burial depth, so deep burial processes are typically regarded as detrimental to reservoir properties (Schmoker et al., 1985; Goldhammer, 1997).

Mechanical and chemical compaction and cementation can obliterate porosity, while dissolution can either enhance primary pores or create new secondary pores. A number of empirical studies have shown that mechanical compaction can reduce carbonate porosity from an upper limit of ~70% to as low as 30% (Shinn and Robbin, 1983; Croizé et al., 2013). Other diagenetic processes, such as cementation and chemical compaction, can also diminish porosity to nearly 0% in some carbonates (Croizé et al., 2013). Because the relationships between diagenetic processes and initial depositional facies are nonlinear, depositional facies can display variable diagenetic modifications that lead to complex and nonuniform pore systems. Diagenesis can also modify the same depositional facies unevenly leading to petrophysical heterogeneity even within the same facies.

As an example, the limestones in this study exhibit a range of petrophysical properties that vary as a function of their depositional and diagenetic textures. The peloidal–skeletal facies contains both grainstone (subfacies Lg) and grain-dominated packstone (GDP) (subfacies Lp) textures (Figure 4.9A; Tables 4.1 and 4.3), with the grainstone recording slightly higher porosity and permeability than the GDP subfacies (median porosity and permeability of 13.6% and 3.5 mD

for grainstone, and 11.3% and 0.4 mD for the GDP; Table 4.3). Depositional texture alone, however, could not explain all of the petrophysical variability observed in the limestone samples.

The combination of depositional texture, degree of compaction, and cementation explains nearly all of the porosity and permeability range observed in the limestone. Samples with the highest porosity and permeability values are those with open-grain packing and a grainstone texture (subfacies Lgo; Figure 4.9A; Table 4.3). In contrast, heavily compacted grain-dominated packstones (subfacies Lpc) recorded the lowest petrophysical values (Table 4.3). A Student's *t*-Test (two populations assuming equal variance) of porosity in the Lpc and Lgo at $\alpha = 95\%$ yielded a *p*–value of 0.004, indicating that the values are statistically different (i.e., the null hypothesis that the two groups are the same can be rejected). Similarly, a Kruskal–Wallis test for nonparametric populations of unequal sizes was used for permeability and yielded a *p*–value of 0.002, indicating that the permeability values are statistically different between Lgo and Lpc subfacies (i.e., the null hypothesis that the two groups are the same can be rejected). Such statistically significant differences do not exist between grainstone and grain-dominated packstone alone, nor between open-grain vs compacted grains within the same texture. These findings show that, not surprisingly, there are differences in porosity preservation between packstones and grainstones, but that the two facies also reacted differently to compaction, with grainstones showing a strong relationship between compaction and petrophysical properties, and packstones not showing such a relationship.

Compaction also produced local compaction bands. These bands are characterized by tabular zones of purely localized compressive deformation where grains rotate and push against each other or against a more stable surface (Figure 4.5C; Baud et al., 2009, 2017; Abdullah et al., 2020; Chen et al., 2020). Compaction bands in this study occur mostly in the vicinity of replacive

anhydrite layers and display petrophysical heterogeneity at a thin section scale (Figure 4.5C), with the areas near the bands exhibiting lower porosity than surrounding areas. Thin section analysis reveals that compaction reduced the size of the interparticle pores between cement-surrounded grains and also reduced some pore throats in the initially connected interparticle pores (Figure 4.5C, D). The blockage and/or reduction of pore throats in interparticle pores has degraded the overall permeability in these samples. The overall impact of compaction bands observed here is consistent with many previous studies focused on this phenomenon in carbonates. Past studies have documented major fluid flow anomalies in areas where compaction bands develop, probably because of reduced permeability (Abdullah et al., 2020; Chen et al., 2020).

Quantity of porosity reduction from compaction could not be measured directly, but it can be estimated based on an assumption of initial porosity and our quantification of total cement. Enos and Sawatsky (1981) reported that the mean porosities of modern packstone and grainstone are 54.7% and 44.5%, respectively. The packstone in this study has a mean cement percentage of ~15%, and a mean primary porosity of 6.4% (Table 4.3). Together these values indicate a mean porosity of up to ~21.4% after compaction. If the packstone started with 54.7% porosity, as that of modern packstone, then compaction has reduced 54.7% – 21.4% = ~33% of the porosity. In the grainstone, the mean cement percentage is ~17%, and the mean primary porosity in grainstone is 8.7% (Table 4.3). Using the same method, the porosity reduction in grainstone due to compaction is 44.5% – 25.7% = ~19%. These values only represent rough estimates, especially considering the presence of small amounts of cement in secondary pores and the wide range of possible initial primary porosity in both packstones and grainstones. For example, Enos and Sawatsky (1981) reported a porosity range of 45% to 67% in packstone and a range from 40% to 53% in grainstone. Nevertheless, the two values obtained here (~33% and ~19% porosity reduction by compaction)

are still consistent with field (e.g., Meyers, 1980) and empirical (e.g., Shinn and Robbin, 1983; Croizé et al., 2013) studies, which showed that compaction can reduce porosity in limestones by up to ~40%.

Dissolution did create pore spaces in the limestone, mostly in the form of molds within peloids (Figure 4.5E). Collectively, moldic pores account for ~4.3% porosity in the limestone (which equates to ~34% relative proportion of all pores; Table 4.4) and were observed in larger quantities in the packstone samples. Moldic pores certainly enhanced the overall porosity (Table 4.5), but maybe only had a minimal impact on permeability based on the lack of correlation between moldic porosity and permeability (R^2 = 0.003; Figure 4.10C; Table 4.5). Except for a few minor solution-enlarged interparticle pores, observed in only four samples, dissolution in the limestones was fabric selective. Vugs were not observed in the limestone samples but are abundant in the dolostones.

4.4.3 Controls on porosity and permeability in dolostone

All four dolostone facies (D1 to D4) have similar medians and ranges of porosity and permeability (Figure 4.9B; Table 4.3). The fabric-destructive dolostone (D4) has slightly lower values than the other facies (median porosity and permeability of 8.4% and 1.0 mD). This facies could have started as any depositional texture (i.e., mudstone to grainstone), but the laminated textures and possible fenestral pores (Table 4.4), might indicate and origin as microbialite; which has been encountered frequently in the undolomitized Upper Jurassic limestones in this region (Hughes, 2004). As such, the original limestone facies could have started with a lower porosity than the other dolomitized facies. All other dolostone facies (D1 to D3) are composed primarily of grainstone and rudstone textures, yet, even with relatively uniform textures, facies D1 to D3

contain samples with low and high porosities (Figure 4.9B; Table 4.3). Original depositional textures in these rocks do not seem to control petrophysical properties. As an example, Facies D1 is all grainstone texture, composed of dolomitized peloids and skeletal grains, yet, it shows a wide range in porosity (a range from 2.0% to 23.7%; Table 4.3).

Part of the reason for the wide range of porosity and permeability in facies D1, and all other dolostone facies, is that the original limestone facies likely included samples with a wide range of petrophysical values too. This is demonstrated in the corresponding grainstone facies in the limestone (Facies L) where a wide range of porosity was observed. Thus, porosity from the precursor limestone likely had some control on porosity in the dolostone, because dolomitization took place after limestone diagenesis. The correlations between porosity and permeability for limestone vs dolostone show different slopes, and there is a long and complex history of dissolution and cementation after dolomitization had begun. This leads to the conclusion that post limestone diagenetic processes control the final porosity (and permeability) values in dolostone.

Cementation and dissolution countered each other in either enhancing or degrading the porosity and permeability in dolostones. This is demonstrated by a negative correlation between cementation versus porosity and permeability, and a positive correlation between secondary pores versus porosity and permeability in facies D1 (Table 4.5). The balance between the amount of cementation and dissolution must also have determined the final petrophysical values of individual samples, albeit with variable starting initial porosities, amount of total cement, and amount of porosity from late dissolution, with the majority of porosity in dolostone developed through late dissolution events. Those processes, clearly led to higher permeabilities in dolostone than in limestone (Figure 4.9), originating from dissolution and minor intercrystalline and fracture porosity (Figure 4.10).

4.4.4 Dolostone porosity: Inherited or created?

Petrophysical analysis of facies D1 and its undolomitized facies L indicates nearly identical median porosity and permeability for the two facies. The dolomitized facies (facies D1) has median porosity and permeability values of 11.5% and 3.3 mD compared to 11.9% and 2.6 mD for the undolomitized facies (facies L; Figure 4.9C; Table 4.3). Relying only on median (or mean) petrophysical values might lead to the conclusion that dolostone indeed only passively inherited all of its porosity from the precursor limestone. This very conclusion has been drawn in previous studies on dolomite reservoirs, in which it has been argued that while dolomite might change pore types and alter pore networks, the overall porosity will mimic that of original limestone (Lucia, 2004). The notion that dolomitization of limestone would produce an additional ~13% porosity due to the smaller molar volume in dolomite compared to calcite has long been rejected (Landes, 1946; Weyl, 1960; Lucia, 2004).

While the initial dolomitization of limestone in the Arab Formation (i.e., the conversion of calcite to dolomite) may or may not have generated additional porosity, it is clear that once the rock was dolomitized, it experienced a set of diagenetic processes missing from the limestones. In thin sections, dolostone contains pore types that are certainly not related to those in the precursor limestone (Figures 4.6 and 4.7; Table 4.4). All the pore spaces that could have been inherited from the precursor limestones were also altered after dolomitization, including the primary interparticle, secondary oomoldic, and even some fenestral pores observed in facies D4.

To demonstrate the case that dolostone porosity is most likely generated and not inherited we use the quantitative data from this study. The dolomitized facies D1 has mean total cement of ~15%, all of which is late in origin and postdates the limestone diagenesis (Figure 4.11). This

amount of cement is sufficient to occlude all of the pores the dolostone could have inherited from the limestone because the mean porosity value in limestone is only ~13% (Table 4.3). Despite having ~15% cement, the dolomitized facies has a mean porosity of ~12% (Figure 4.9B). The only possible explanation is that late dissolution produced extensive moldic and vuggy pores, some of which have been partially cemented (Figure 4.7). Meaning, at one point during its history, facies D1 could have had a porosity of ~27% (~13% inherited, and ~14% generated), with later cement partially filling up to ~15% of those pores. This would lead to the present-day porosity of ~12%.

There will always be some ambiguities on how or even if dolomitization alters porosity in carbonates, however, the data presented here argue that the final petrophysical properties in dolostones have no clear relationship to those of the precursor limestone. The final porosity may be partially controlled by the inherited porosity, but it is controlled more by dolomitization, dolomite cementation, and dissolution, that yield pore origin and porosity–permeability relationships distinct from the precursor limestone.

4.4.5 Mesogenetic (deep burial) dissolution

Mesogenetic dissolution occurs during burial diagenesis in the presence of corrosive fluids and is typically unrelated to marine or meteoric alteration (Mazzullo and Harris, 1991, 1992; Wright and Harris, 2013). The literature contains many examples of carbonate pore spaces that were created through what has been interpreted as mesogenetic dissolution (Elliott, 1982; Mazzullo and Harris, 1992; Liu et al., 2008; Beavington-Penney et al., 2008; Jin et al., 2009; Poteet et al., 2016; Rosales et al., 2018; Aschwanden et al., 2019; Xiang et al., 2021; Lai et al., 2021; Hollis and Al Hajri, 2022). It has been suggested, however, that some of these studies may have incorrectly interpreted low-temperature meteoric dissolution as mesogenetic porosity (Ehrenberg

et al., 2012). This includes a previous study of Jurassic carbonates from Saudi Arabia (Rosales et al., 2018) in which the pore volumes generated are volumetrically small and could have formed prior to deep burial (Ehrenberg et al., 2019). Critically, the dissolution of late diagenetic phases alone does not necessitate the need for mesogenetic dissolution, as many carbonate platforms can precipitate burial phases and then undergo dissolution in the telogenetic realm through uplift and sometimes exposure. An example of this is the hydrothermal dolostone from the Cretaceous Benassale Formation in the Maestrate Basin, Spain, where the dolostones developed vugs through a telogenetic dissolution event that occurred many millions of years after the formation of hydrothermal dolomite at depth (Martin-Martin et al., 2015). Due to this uncertainty, along with mass balance limitations (Bjørlykke and Jahren, 2012), the mesogenetic dissolution hypothesis has received some criticism (Ehrenberg et al., 2012).

The carbonates in this study have undergone a history of constant burial that did not include a telogenetic phase (major uplift) after deposition (Abu-Ali and Littke, 2005). The integration of petrographic and geochemical data presented here supports the interpretation that mesogenetic dissolution indeed created pore spaces in the dolostone. Based on the interpretation of stable isotopes (Figure 4.8A), fluid inclusions (Figure 4.8B), and $^{87}Sr/^{86}Sr$ (Figure 4.9C) data, all dolomite phases in the dolostone are interpreted to have formed and/or recrystallized in a deep burial setting, after limestone diagenesis has ceased (Figure 4.11). Along the same line, pores that are unique to the dolostones, must be interpreted to have occurred during or after the formation of late dolomite. These late-generated pores dominate all dolostone facies (Table 4.4).

Petrographic support for mesogenetic dissolution includes the presence of moldic pores within burial anhydrite (Figure 4.7A), within late baroque (saddle) dolomite (Figure 4.7B), truncation visible in CL in dolomite followed by further cementation, molds within dolomite

crystal growth zones (Figure 4.7C), the cross-cutting of stylolites by vuggy pores (Figure 4.7D), and the presence of corroded baroque (saddle) dolomite crystals (Figure 4.7E, F). Large vugs that cross-cut burial diagenetic phases must also have formed through mesogenetic dissolution (Figure 4.6F).

Earlier, we estimated that for facies D1 ~14% mesogenetic porosity could have been generated at one point during the diagenetic history of the dolostone. This value, however, is based on an assumed mean of initial dolostone porosity, mean cement, and present-day mean porosity in dolostone. Of course, this value is not likely to be applicable to all dolostone samples as there are examples of preserved inherited pores in the dolostone (e.g., oomoldic pores in dolostone; Figure 4.2A). The ~14% mesogenetic porosity generation estimated for facies D1, may represent the total porosity that could have developed at depth and is comparable to that reported by other studies of mesogenetic porosity in carbonate. For example, Aschwanden et al. (2019) reported a value of ~15% porosity generation by mesogenetic dissolution for the Cenozoic Muschelkalk dolostone in the Swiss Molasse Basin. These authors, however, invoked freshwater that penetrated deep to generate the late dissolution mostly by dissolving anhydrite; we do not invoke freshwater, nor do we assume all pores to be dissolved anhydrite in this study.

Petrographic estimation of pore types that are mesogenetic in origin must include an interpretation of their origin, which is not always a straightforward task. Nevertheless, a rough, petrography-based, estimation of minimum amount of mesogenetic porosity that is extant can be based on the fraction of pore types (e.g., moldic, vuggy, intercrystal) that show conclusive evidence of late formation (e.g., molds within late dolomite crystals or vugs that cross-cut stylolites; See Figure 4.7). This analysis yields minimum porosity values of 2.3% to 4.5% (out of ~12% total) in facies D1 that must be mesogenetic in origin. Pores where there is no conclusive

evidence of mesogenetic origin are not counted in this, even though they likely formed through the same mesogenetic processes as the other pores. This minimum estimate of 2.3% to 4.5% indicates that at least relative percentages of ~20% to ~38% (of total present-day dolostone porosity) must have originated from mesogenetic dissolution.

4.5 CONCLUSIONS

The integration of petrographic, geochemical, and petrophysical analyses of Upper Jurassic carbonates in this study provides new insights into the reservoir quality controls of undolomitized limestone as well as the origin of dolostone porosity, the key results are as follows:

1. Depositional textures, compaction, and cementation explain the majority of the petrophysical variability observed in the limestone. Mechanical compaction is estimated to have reduced porosity by ~19% and ~33% in grainstone and grain-dominated packstone, respectively.
2. Differential compaction produced diagenetic subfacies in the limestone that exhibit petrophysical differences at statistically significant levels. The decrease in porosity and permeability is more predictable in grainstones than in packstones.
3. Dolostone has similar median porosity and permeability values to the limestone, yet most of the porosity in the dolostone was not inherited from the precursor limestone, but rather developed from dissolution during or after late dolomitization.
4. Mesogenetic dissolution produced moldic pores within anhydrite crystals, moldic pores within both baroque dolomite crystals and those that cross-cut stylolites, as well as large vuggy pores that cross-cut multiple deep burial diagenetic phases. Collectively, a

minimum of 2.3% to 4.5% of the mean dolostone porosity (mean: ~12%) is interpreted to have developed through mesogenetic dissolution events.

4.6 REFERENCES

Abdallah, Y., J. Sulem, M. Bornert, S. Ghabezloo, and I. Stefanou, 2020, Compaction banding in high-porosity carbonate rocks: 1. Experimental observations: Journal of Geophysical Research: Solid Earth, v. 125. doi/10.1029/2020JB020610.

Abu-Ali, M., and R. Littke, 2005, Paleozoic petroleum systems of Saudi Arabia: A basin modeling approach: GeoArabia, v. 10, p. 131–168.

Al-Husseini, M. I., 1997, Jurassic sequence stratigraphy of the western and southern Arabian Gulf: GeoArabia, v. 2, p. 361–382.

Al-Husseini, M., 2009, Update to Late Triassic–Jurassic stratigraphy of Saudi Arabia for the Middle East geologic time scale: GeoArabia, v. 14, p. 145–186.

Alqattan, M. A., and D. A. Budd, 2017, Dolomite and dolomitization of the Permian Khuff-C reservoir in Ghawar field, Saudi Arabia: AAPG Bulletin, v. 101, p. 1715–1745.

Alsharhan, A. S., 2014, Petroleum systems in the Middle East, in H. R. Rollinson, M. P. Searle, I. A. Abbasi, A. Al-Lazki, and M. H. Al Kindi, eds., Tectonic evolution of the Oman Mountains: Geological Society, London, Special Publications 2014, v. 392, p. 361–408.

Archie, G. E., 1952, Classification of carbonate reservoir rocks and petrophysical considerations: AAPG Bulletin, v. 36, p. 278–298.

Aschwanden, L., L. W. Diamond, M. Mazurek, and D. W. Davis, 2019, Creation of Secondary Porosity in Dolostones by Upwelling Basement Water in the Foreland of the Alpine Orogen: Geofluids, p. 1–23.

Baud, P., A. Schubnel, M. Heap, and A. Rolland, 2017, Inelastic compaction in high porosity limestone monitored using acoustic emissions. Journal of Geophysical Research: Solid Earth, v. 122, p. 9989–9910. https://doi.org/10.1002/2017JB014627.

Baud, P., S. Vinciguerra, C. David, A. Cavallo, E. Walker, and T. Reuschle, 2009, Compaction and failure in high porosity carbonates: mechanical data and microstructural observations: Pure Applied Geophysics, v. 166, p. 869–898.

Beavington-Penney, S. J., P. Nadin, V. P. Wright, E. Clarke, J. McQuilken, and H. W. Bailey, 2008, Reservoir quality variation on an Eocene carbonate ramp, El Garia Formation, offshore Tunisia: Structural control of burial corrosion and dolomitization: Sedimentary Geology, v. 209, p. 42–57, doi:10.1016/j.sedgeo.2008.06.006.

Bjørlykke, K., and J. Jahren, 2012, Open or closed geochemical systems during diagenesis in sedimentary basins: Constraints on mass transfer during diagenesis and the prediction of porosity in sandstone and carbonate reservoirs: AAPG Bulletin, v. 96, p. 2193–2214, doi:10.1306/04301211139.

Bodnar, R. J., 1992, Revised equation and table for freezing point depressions of H,O-salt fluid inclusions (Abstract): PACROFI IV, Fourth Biennial Pan-American Conference on Research on Fluid Inclusions, Program and Abstracts, Lake Arrowhead, CA, v. 14, p. 15.

Braithwaite, C. J. R., G. Rizzi, and G. Darke, eds., 2004, The geometry and petrogenesis of dolomite hydrocarbon reservoirs: Geological Society (London) Special Publication 235, 413 p.

Broomhall, R. W., and J. R. Allen, 1987, Regional caprock-destroying dolomite on the Middle Jurassic to Early Cretaceous Arabian Shelf: Society of Petroleum Engineers Formation Evaluation, v. 2, p. 435–441.

Cantrell, D. L., P. K. Swart, R. C. Handford, C. G. Kendall, and H. Westphal, 2001, Geology and production significance of dolomite, Arab-D reservoir, Ghawar field, Saudi Arabia: GeoArabia, v. 6, p. 45–60.

Chang, D., H. Vinegar, C. Morriss, and C. Straley, 1995, Effective porosity, producible fluid and permeability in carbonates from NMR logging: Paper A, Society of Professional Well Log Analysts 36th Annual Logging Symposium, 21 p.

Chen, X., H. Roshan, A. Lv, M. Hu, and K. Regenauer-Lieb, 2020, The dynamic evolution of compaction bands in highly porous carbonates: the role of local heterogeneity for nucleation and propagation: Progress in Earth and Planetary Science, v.7, p. 1–19.

Choquette, P. W., A. Cox, and W. J. Meyers, 1992, Characteristics, distribution and origin of porosity in shelf dolostones: Burlington Keokuk Formation (Mississippian), U.S. mid-continent: Journal of Sedimentary Petrology, v. 62, p. 167–189.

Choquette, P. W., and L. C. Pray, 1970, Geologic nomenclature and classification of porosity in sedimentary carbonates: AAPG Bulletin, v. 54, p. 207–244.

Croizé, D., F. Renard, and J. P. Gratier, 2013, Compaction and porosity reduction in carbonates: A review of observations, theory, and experiments. Advances in Geophysics, v. 54, p. 181–238, https://doi.org/10.1016/B978-0-12-380940-7.00003-2.

Dickson, J. A. D., 1966, Carbonate identification and genesis as revealed by staining: Journal of Sedimentary Petrology, v. 36, p. 491–505.

Ehrenberg, S. N., 2004, Porosity and permeability in Miocene carbonate platforms on the Marion Plateau, offshore NE Australia: Relationships to stratigraphy, facies and dolomitization, in C. J. R. Braithwaite, G. Rizzi, and G. Darke, eds., The geometry and petrogenesis of dolomite hydrocarbon reservoirs: Geological Society (London) Special Publication 235, p. 233–253.

Ehrenberg, S. N., O. Walderhaug, and K. Bjørlykke, 2012, Carbonate porosity creation by mesogenetic dissolution: Reality or illusion?: AAPG Bulletin, v. 96, p. 217–233, doi:10.1306/05031110187.

Ehrenberg, S.N., O. Walderhaug, and K. Bjørlykke, 2019, Discussion of "Microfacies, diagenesis and oil emplacement of the Upper Jurassic Arab-D carbonate reservoir in an oil field in central Saudi Arabia (Khurais Complex)" by Rosales et al. (2018): Marine and Petroleum Geology, v. 100, p. 551–553.

Elliott, T. L., 1982, Carbonate facies, depositional cycles, and the development of secondary porosity during burial diagenesis: Mission Canyon Formation, Haas field, North Dakota, in J. E. Christopher and J. Kaldi, eds., Fourth International Williston Basin Symposium: Saskatchewan Geological Society Special Publication 6, p. 131–151.

Eltom, H., 2020, Limitation of laboratory measurements in evaluating rock properties of bioturbated strata: A case study of the Upper Jubaila Member in central Saudi Arabia: Sedimentary Geology, v. 398, 105573.

Enos, P., and L. H. Sawatsky, 1981, Pore networks in Holocene carbonate sediments: Journal of Sedimentary Petrology, v. 51, p. 961–985.

Friedman, G. M., 1985, The problems of submarine cement in classifying reef rock: an experience in frustration, in N. Schneidermann and P. M. Harris eds., Carbonate Cements: International Association of Sedimentologists Special Publication 36, p. 117–121.

Goldhammer, R. K., 1997, Compaction and decompaction algorithms for sedimentary carbonates: Journal of Sedimentary Research, v. 67, p. 26–35.

Goldstein, R. H., and T. J. Reynolds, 1994, Systematics of fluid inclusions in diagenetic minerals: Tulsa, Oklahoma, SEPM Short Course 31, 199 p.

Hollis, C, and Al Hajri, A, 2022, Post-compactional porosity in a hydrocarbon-bearing carbonate succession: Potential timing and processes controlling porosity creation in the Aptian Shuaiba Formation, Oman: Sedimentary Geology, v. 428, 106046, https://doi.org/10.1016/j.sedgeo.2021.106046.

Hughes, G. W., 2004, Middle to Upper Jurassic Saudi Arabian carbonate petroleum reservoirs: Biostratigraphy, micropalaeontology and palaeoenvironments: GeoArabia, v. 9, p. 79–114.

James, N. P., and R. N Ginsburg, 1979, The seaward margin of Belize barrier and atoll reefs: Morphology, sedimentology, organism distribution and late Quaternary history: International Association of Sedimentologists Special Publication 3, Oxford, London, Edinburgh, Melbourne, Blackwell Scientific Publications, 191 p.

Jin, Z., D. Zhu, W. Hub, X. Zhang, J. Zhang, and Y. Song, 2009, Mesogenetic dissolution of the Middle Ordovician limestone in the Tahe oil field of Tarim Basin, northwest China: Marine and Petroleum Geology, v. 26, p. 753–763, doi:10.1016/j.marpetgeo.2008.08.005.

Lai, J, S. Liu, Y. Xin, S. Wang, C. Xiao, Q. Song, X. Chen, K. Yang, G. Wang, X. Ding, 2021, Geological-petrophysical insights in the deep Cambrian dolostone reservoirs in Tarim Basin, China: AAPG Bulletin, v. 105, p. 2263–2296, doi: https://doi.org/10.1306/03122119135.

Land, L. S., 1980, The isotopic and trace element geochemistry of dolomite: The state of the art, in D. H. Zenger, J. B. Dunham, and R. L. Ethington, eds., Concepts and models of dolomitization: Tulsa, Oklahoma, SEPM Special Publication 28, p. 87–110, doi:10.2110/pec.80.28.0087.

Landes, K. K., 1946, Porosity through dolomitization: AAPG Bulletin, v. 30, p. 305–318.

Lindsay, R. F., D. L. Cantrell, G. W. Hughes, T. H. Keith, H. W. Mueller III, and D. Russell, 2006, Ghawar Arab-D Reservoir: Widespread porosity in shoaling-upward carbonate cycles: AAPG Memoir 88, p. 97–138.

Liu, C., C. Lin, Y. Wang, and M. Wu, 2008, Burial Dissolution of Ordovician Granule Limestone in the Tahe Oilfield of the Tarim Basin, NW China, and Its geological significance: Acta Geologica Sinica, v. 82, p. 520–529.

Lønøy, A., 2006, Making sense of carbonate pore system: AAPG Bulletin, v. 90, p. 1381–1405, doi:10.1306 /03130605104.

Lucia, F. J., 1995, Rock-fabric/petrophysical classification of carbonate pore space for reservoir characterization: AAPG Bulletin, v. 79, p. 1275–1300.

Lucia, F. J., 2004, Origin and petrophysics of dolostone pore space, in C. J. R. Braithwaite, G. Rizzi, and G. Darke, eds., The geometry and petrogenesis of dolomite hydrocarbon reservoirs. Geological Society (London) Special Publication 235, p. 141–155.

Lucia, F. J., 2007, Carbonate reservoir characterization: An integrated approach: New York, Springer, 227 p.

Lucia, F. J., and R. P. Major, 1994, Porosity evolution through hypersaline reflux dolomitization, in B. Purser, M. Tucker, and D. Zenger, eds., Dolomites: International Association of Sedimentologists Special Publication 21, p. 325–341.

Maliva, R. G., D. A. Budd, E. A. Clayton, T. M. Missimer, and J. A. D. Dickson, 2011, Insights into the dolomitization process and porosity modification in sucrosic dolostones, Avon Park Formation (middle Eocene), east-central Florida, U.S.A: Journal of Sedimentary Research, v. 81, p. 218–232, doi: https://doi.org/10.2110/jsr.2011.18.

Martin-Martin, J. D., A. Trave, E. Gomez-Rivas, R. Salas, J.-P. Sizun, J. Verges, M. Corbella, S. L. Stafford, and P. Alfonso, 2015, Fault-controlled and stratabound dolostones in the Late Aptian–Earliest Albian Benassal Formation (Maestrat Basin, E Spain): Petrology and geochemistry constrains: Marine and Petroleum Geology, v. 65, p. 83–102, doi:10.1016/j.marpetgeo.2015.03.019.

Mazzullo, S. J., and P. M. Harris, 1991, An overview of dissolution porosity development in the deep-burial environment, with examples from carbonate reservoirs in the Permian Basin, in M. P. Candellaria, ed., Permian Basin plays: Tomorrow's technology today: West Texas Geological Society Publication No. 91-89, p. 125–138.

Mazzullo, S. J., and P. M. Harris, 1992, Mesogenetic dissolution: Its role in porosity development in carbonate reservoirs: AAPG Bulletin, v. 76, p. 607–620.

McArthur, J. M., R. J. Howarth and T. R. Bailey, 2001, Strontium isotope stratigraphy: LOWESS Version 3: Best fit to the marine Sr-isotope curve for 0-590 Ma and accompanying look-up table for deriving numerical age: Journal of Geology, v. 109, p. 155–169.

McGuire, M. D., R. B. Koepnick, M. L. Markello, M. L. Stockton, L. E. Waite, M. J. Kompanik, M. J. Al-Shammary, and M. O. AlAmoudi, 1993, Importance of sequence stratigraphic concepts in development of reservoir architecture in Upper Jurassic grainstones, Hadriya and Hanifa reservoirs, Saudi Arabia: Proceedings of 8th Middle East Oil Show, Society of Petroleum Engineers, Paper 25578, p. 489–499.

Meyer, F. O., R. C. Price, and S. M. Al-Raimi, 2000, Stratigraphic and petrophysical characteristics of cored Arab-D super-k intervals, Hawiyah area, Ghawar field, Saudi Arabia: GeoArabia, v. 5, p. 355–384.

Meyers, W. J, 1980, Compaction in Mississippian skeletal limestones, southwestern New Mexico: Journal of Sedimentary Petrology, v. 50, p. 457–474.

Pierson, B. J. and E. A. Shinn, 1985, Cement distribution and carbonate mineral stabilization in Pleistocene limestones of Hogsty Reef, Bahamas, in N. Schneidermann and P. M. Harris eds., Carbonate Cements: International Association of Sedimentologists Special Publication 36, p. 153–168.

Poteet, J. E., R. H. Goldstein, and E. K. Franseen, 2016, Diagenetic controls on the location of reservoir sweet spots relative to palaeotopographical and structural highs: Geological Society, London, Special Publications 435, p. 177–215.

Purser, B. H., A. Brown, and D. M. Aissaoui, 1994, Nature, origins and porosity in dolomites, in B. Purser, M. Tucker, and D. Zenger, eds., Dolomites, a volume in honour of Dolomieu: International Association of Sedimentologists Special Publication 21, p. 283–308.

Roduit, N., 2019, JMicroVision: Image analysis toolbox for measuring and quantifying components of high-definition images. Version 1.3.1. https://jmicrovision.github.io.

Saller, A. H., and N. Henderson, 1998, Distribution of porosity and permeability in platform dolomites: Insight from the Permian of west Texas: AAPG Bulletin, v. 82, p. 1528–1550.

Schmoker, J. W., K. B. Krystinik, and R. B. Halley, 1985, Selected characteristics of limestone and dolomite reservoirs in the United States: AAPG Bulletin, v. 69, p. 733–741.

Shinn, R. A., and D. M. Robbin, 1983, Mechanical and chemical compaction in fine-grained shallow-water limestones: Journal of Sedimentary Petrology, v. 53, p. 595–618.

Sun, S. Q., 1995, Dolomite reservoirs: porosity evolution and reservoir characteristics: AAPG Bulletin, v. 79, p. 186–204.

Vandeginste V., R. Swennen, M. H. Reed, R. M. Ellam, K. Osadetz, and F. Roure, 2009, Host rock dolomitization and secondary porosity development in the Upper Devonian Cairn Formation of the Fairholme carbonate complex (South-west Alberta, Canadian Rockies): diagenesis and geochemical modeling: Sedimentology, v. 56, p. 2044– 2060.

Veizer, J., Ala, D., Azmy, K., Bruckschen, P., Buhl, D., Bruhn, F., Carden, G.A., Diener, A., Ebneth, S., Godderis, Y. and Jasper, T., 1999, $^{87}Sr/^{86}Sr$, $\delta^{13}C$ and $\delta^{18}O$ evolution of Phanerozoic seawater: Chemical geology, v. 161, p. 59–88.

Warren J., 2000, Dolomite: Occurrence, evolution and economically important associations: Earth-Science Reviews, v. 52, p. 1–81.

Weyl, P. K., 1960, Porosity through dolomitization: Conservation of-mass requirements: Journal of Sedimentary Petrology, v. 30, p. 85–90.

Woody, R. E., J. M. Gregg, and L. K. Koederitz, 1996, Effect of texture on petrophysical properties of dolomite; Evidence from the Cambrian–Ordovician of southeastern Missouri: AAPG Bulletin, v. 80, p 119–132.

Wright, P., and P. M. Harris, 2013, Carbonate dissolution and porosity development in the burial (mesogenetic) environment. In: AAPG Annual Convention and Exhibition, Search and Discovery. Article #50860, Pittsburgh, PA, 19–22 May.

Xiang, P., H. Ji, Y. Shi, Y. Du, P. Chen, Q. Weng, X. Xu, Y. Sun, Y. Huang, and S. Zou, 2021, Characteristics and formation mechanism of mesogenetic dissolution: A case study of Ordovician carbonate in the western slope of the Shulu Sag, Jizhong Depression, Bohai Bay Basin: Journal of Petroleum Science and Engineering, p.109045.

Zenger, D. H., J. B. Dunham, and R. L. Ethington, eds., 1980, Concepts and models of dolomitization: SEPM Special Publication 28, 320 p.

Ziegler, M. A., 2001, Late Permian to Holocene paleofacies evolution of the Arabian plate and its hydrocarbon occurrences: GeoArabia, v. 6, p. 445–504.

Chapter 5

Conclusions and Recommendations

5.1 CONCLUSIONS

The integration of petrographic, geochemical, and petrophysical analyses of Upper Jurassic carbonates in this study provides new insights into the reservoir quality controls of undolomitized limestone as well as the origin of dolostone porosity, the key results are as follows:

1. Oxygen isotope data in all dolostones are more negative than those of Late Jurassic marine dolomite. Primary homogenization temperatures (Th) in dolostones average 100.4^{o}C and salinities average 24.3 wt. % NaCl equivalent. The mean Th is greater than the maximum burial temperatures the rocks were exposed to. The salinity indicates hypersaline fluids (6 to ~8 times more saline than seawater) were responsible for the bulk of dolomitization.

2. Nearly all dolomites in the study area (including equant and baroque, dull in CL or mottled) are interpreted to be a mixture of hydrothermally formed (dull CL) and hydrothermally recrystallized dolomite (mottled in CL). Hydrothermal formation and subsequent recrystallization overlapped each other during the majority of dolostone diagenetic history.

3. There is a spatial trend in stable isotope and fluid inclusion data in dolostones. Dolostones located to the north in the study area, and closest to a known regional fault, recorded less negative $\delta^{18}O$, less positive $\delta^{13}C$, and lower Th and salinity values than

wells to the south. Likely indicating some localized control on dolomitizing fluid source.

4. The results of integrated $^{87}Sr/^{86}Sr$ and U–Pb analyses indicate that fluids charged a Triassic sandstone reservoir by sinking through faulted and fractured rocks. Those fluids were evaporated seawater that penetrated downward due to density contrast between ~58 Ma and ~32 Ma.

5. Depositional textures, compaction, and cementation explain the majority of the petrophysical variability observed in the limestone. Mechanical compaction is estimated to have reduced porosity by ~19% and ~33% in grainstone and grain-dominated packstone, respectively.

6. Dolostone has similar median porosity and permeability values to the limestone, yet most of the porosity in the dolostone was not inherited from the precursor limestone, but rather developed from dissolution during or after late dolomitization.

7. Mesogenetic dissolution produced moldic pores within anhydrite crystals, moldic pores within both saddle dolomite crystals and those that cross-cut stylolites, as well as large vuggy pores that cross-cut multiple deep burial diagenetic phases. Collectively, a minimum of 2.3% to 4.5% of the mean dolostone porosity (mean: ~12%) is interpreted to have developed through mesogenetic dissolution events.

5.2 RECOMMENDATIONS

1. The study shows the utility of geochemical analyses to accurately infer the origin of dolomite. The available extensive datasets provided sufficient information to understand the dolomite in the Arab Formation. Future work might want to include dolomites in the older and especially younger stratigraphic units to have a more complete understanding of the dolomite history.

2. All dolomite phases in this study contain an abundance of two-phase fluid inclusions. Previous studies in Ghawar either lacked fluid inclusion analysis, or discarded the results as they are not consistent with an assumed early-reflux origin of the dolomite. It is recommended to petrographically analyze the dolomites elsewhere in the country and build a better fluid-inclusion database for these dolomites.

3. A better integration of structural, burial, and sequence stratigraphic analysis of the area is needed to fully understand the details of the dolomitization process in the area.

4. The application of uranium–lead dating not only proved useful here, but also crucial in providing constraints to dolomite timing. Without such data, the interpretations of stable isotope, fluid inclusion, and strontium isotope ratio data would have been tentative. The chemistry of the dolomites in the area allows for successful application of this technique. It is recommended to explore U–Pb in nearby dolomites, including those in the Ghawar field.

5. The study demonstrated the feasibility of a ‘fault-controlled’ mechanism to produce large volumes of subsurface dolomites. This mechanism might have been overlooked

in other basins worldwide. More studies are likely needed before the importance of such mechanisms is realized.

6. The study revealed the presence of large volumes of pores of mesogenetic origin. Only a few regional studies have made similar conclusions. Petrographic analysis of the Arab pore system in the country needs to be addressed, as some mesogenetic pores could have developed after hydrocarbon charging has ceased.

Chapter 6

Appendices

APPENDIX A: Stable Isotope Data

Analysis #	Well No	W Analysis	Plug	Member	Lithology	Dolomite Phase	$\delta^{18}O$ VPDB	$\delta^{13}C$ VPDB
1	1	1	Np	B	Dol	MDR	-9.76	2.71
2	1	2	Np	B	Dol	MDR	-9.93	2.71
3	1	3	357	B	Dol	MDR	-9.67	3.10
4	1	4	359	B	Dol	SDR	-9.78	2.75
5	1	5	361	B	Dol	SDR	-9.83	2.73
6	1	6	np	B	Dol	MDR	-9.83	2.49
7	1	7	Np	B	Dol	SDC	-9.81	2.71
8	1	8	np	B	Dol	SDC	-9.36	2.63
9	1	9	364	B	Dol	SDC	-9.82	2.65
10	1	10	np	B	Dol	MDR	-9.85	2.81
11	1	11	Np	B	Dol	SDC	-9.86	2.62
12	1	12	np	B	Dol	SDC	-9.79	2.58
13	1	13	np	B	Dol	MDR	-9.66	2.81
14	1	14	Np	B	Dol	MDR	-9.81	2.83
15	1	15	Np	B	Dol	SDC	-10.01	2.65
16	1	16	np	B	Dol	SDR	-9.87	2.46
17	1	17	366	B	Dol	SDR	-9.91	2.54
18	2	1	432	A	Dol	SDR	-9.81	2.85
19	2	2	434	A	Dol	SDR	-9.74	2.91
20	2	3	437	A	Dol	SDR	-9.34	2.80
21	2	4	439	A	Dol	SDR	-8.03	2.82
22	2	5	441	A	Dol	SDR	-8.04	2.75
23	2	6	443	A	Dol	SDR	-8.44	2.70
24	2	7	445	A	Dol	SDR	-9.17	2.73
25	2	8	461	C	Dol	MDR	-9.89	3.09
26	2	9	463	C	Dol	MDR	-9.97	3.12
27	2	10	465	C	Dol	MDR	-9.86	3.06
28	2	11	467	C	Dol	MDR	-9.95	3.35
29	2	12	469	C	Dol	MDR	-9.86	3.49
30	2	13	471	C	Dol	MDR	-9.90	3.17
31	2	14	473	D	Dol	MDR	-8.65	3.07
32	2	15	475	D	Dol	SDR	-9.05	2.83
33	2	16	477	D	Dol	MDR	-8.93	2.98
34	2	17	478	D	Dol	MDR	-9.08	2.83
35	2	18	480	D	Dol	SDC	-9.15	2.99
36	2	19	482	D	Dol	SDC	-9.03	2.95
37	2	20	484	D	Dol	SDC	-9.49	2.61
38	2	21	486	D	Dol	SDC	-9.36	3.01
39	2	22	488	D	Dol	SDC	-9.53	3.06
40	2	23	490	D	Dol	MDR	-9.60	2.90
41	2	24	492	D	Dol	SDR	-9.05	2.65
42	2	25	494	D	Dol	SDR	-8.54	2.67
43	2	26	496	D	Dol	MDR	-8.75	2.71
44	2	27	498	D	Dol	SDR	-9.04	2.64
45	2	28	500	D	Dol	SDR	-8.96	2.62

46	2	29	502	D	Dol	SDR	-9.05	2.78
47	2	30	504	D	Dol	SDR	-8.35	2.70
48	2	31	506	D	Dol	SDR	-8.78	2.69
49	2	32	508	D	Dol	SDR	-9.34	2.69
50	2	33	510	D	Dol	MDC	-8.96	2.92
51	2	34	512	D	Dol	MDC	-9.12	2.58
52	2	35	514	D	Dol	MDC	-8.77	2.55
53	2	36	516	D	Dol	MDC	-8.86	2.70
54	2	37	518	D	Dol	MDR	-8.65	2.74
55	2	38	520	D	Dol	MDC	-8.78	2.76
56	2	39	522	D	Dol	MDC	-8.56	2.72
57	2	40	524	D	Dol	MDC	-8.92	2.68
58	2	41	526	D	Dol	MDC	-8.81	2.76
59	2	42	528	D	Dol	SDR	-8.92	2.79
60	2	43	530	D	Dol	SDR	-9.03	2.78
61	2	44	532	D	Dol	MDR	-9.16	2.63
62	2	45	534	D	Dol	MDR	-9.09	2.71
63	2	46	536	D	Dol	MDR	-8.73	2.75
64	2	47	538	D	Dol	MDC	-8.95	2.74
65	2	48	540	D	Dol	MDC	-8.99	2.77
66	2	49	541	D	Dol	SDR	-9.34	2.66
67	2	50	543	D	Dol	SDR	-9.46	2.74
68	2	51	545	D	Dol	MDC	-9.12	2.63
69	2	52	547	D	Dol	MDC	-9.15	2.71
70	2	53	548	D	Dol	MDC	-9.10	2.68
71	2	54	550	D	Dol	MDC	-9.35	2.60
72	2	55	552	D	Dol	SDR	-9.23	2.65
73	2	56	554	D	Dol	SDR	-9.11	2.67
74	2	57	556	D	Dol	MDC	-9.06	2.64
75	2	58	558	D	Dol	MDC	-8.80	2.71
76	2	59	560	D	Dol	MDC	-9.11	2.63
77	2	60	562	D	Dol	MDC	-9.03	2.60
78	2	61	564	D	Dol	MDC	-9.05	2.73
79	3	1	NA	B	Dol	MDR	-6.81	2.29
80	3	2	NA	B	Dol	SDR	-6.88	2.31
81	3	3	NA	B	Dol	SDR	-6.77	2.18
82	3	4	NA	B	Dol	MDR	-6.95	1.92
83	3	5	NA	B	Dol	SDR	-7.03	1.99
84	3	6	NA	B	Dol	SDR	-6.54	2.20
85	3	7	NA	B	Dol	SDR	-7.31	1.93
86	3	8	NA	B	Dol	MDR	-6.72	2.18
87	3	9	NA	B	Dol	SDC	-6.19	2.05
88	3	10	NA	B	Dol	SDR	-7.32	2.03
89	3	11	NA	B	Dol	SDR	-6.47	2.12
90	3	12	NA	B	Dol	SDR	-6.86	2.15
91	3	13	NA	B	Dol	SDR	-6.59	2.05
92	3	14	NA	B	Dol	SDR	-5.92	2.03
93	3	15	NA	B	Dol	SDR	-6.29	2.05
94	4	1	229	A	Dol	MDC	-7.21	1.49
95	4	2	231	A	Dol	MDC	-6.55	1.40
96	4	3	233	A	Dol	MDC	-6.51	1.69
97	4	4	235	A	Dol	MDC	-6.36	1.69
98	4	5	237	A	Dol	MDC	-6.53	1.88
99	4	6	237	A	Dol	MDC	-6.64	1.82
100	4	7	239	A	Dol	MDR	-7.08	1.88
101	4	8	242	A	Dol	MDR	-6.90	2.23
102	4	9	244	A	Dol	MDR	-7.28	2.33
103	4	10	246	A	Dol	MDR	-6.66	2.35
104	4	11	248	A	Dol	MDR	-6.95	2.12
105	4	12	250	A	Dol	SDR	-7.26	2.11
106	4	13	252	A	Dol	SDR	-6.91	2.34

107	4	14	254	A	Dol	MDR	-6.87	2.19
108	4	15	256	A	Dol	MDR	-6.78	2.35
109	4	16	256	A	Dol	SDC	-6.66	2.34
110	4	17	258	A	Dol	MDR	-7.14	2.19
111	4	18	258	A	Dol	MDR	-7.07	2.21
112	4	19	258	A	Dol	MDR	-7.16	2.09
113	4	20	260	A	Dol	MDR	-7.18	2.39
114	4	21	262	A	Dol	MDR	-6.93	2.41
115	4	22	264	A	Dol	MDR	-6.62	2.52
116	4	23	266	A	Dol	MDR	-6.95	2.46
117	4	24	266	A	Dol	MDR	-6.96	2.49
118	4	25	268	A	Dol	MDR	-7.46	2.13
119	4	26	270	A	Dol	MDR	-6.81	2.18
120	4	27	272	A	Dol	MDR	-6.96	2.25
121	4	28	274	A	Dol	MDR	-7.15	2.40
122	4	29	276	A	Dol	MDR	-7.06	2.37
123	4	30	278	A	Dol	MDR	-7.09	2.35
124	4	31	280	A	Dol	MDR	-7.23	2.27
125	4	32	282	A	Dol	MDR	-7.06	2.34
126	4	33	284	A	Dol	MDR	-7.13	2.08
127	4	34	286	A	Dol	MDR	-7.09	2.07
128	4	35	286	A	Dol	MDR	-6.75	2.05
129	4	36	288	B	Dol	MDR	-7.12	2.54
130	4	37	290	B	Dol	MDR	-7.18	2.53
131	4	38	292	B	Dol	MDR	-7.27	2.61
132	4	39	294	B	Dol	MDR	-7.31	2.65
133	4	40	296	B	Dol	MDR	-7.15	2.57
134	4	41	298	B	Dol	MDR	-7.37	2.60
135	4	42	300	B	Dol	MDR	-7.23	2.44
136	4	43	302	B	Dol	MDR	-7.08	2.44
137	4	44	304	B	Dol	MDR	-7.15	2.68
138	4	45	307	B	Dol	MDR	-7.83	2.28
139	4	46	309	B	Dol	MDR	-7.37	2.23
140	4	47	309	B	Dol	MDR	-6.99	2.24
141	4	48	311	B	Dol	MDR	-7.16	2.33
142	4	49	313	B	Dol	MDR	-7.08	2.52
143	4	50	313	B	Dol	MDR	-7.32	2.43
144	4	51	315	B	Dol	MDR	-7.28	2.48
145	4	52	317	B	Dol	MDR	-7.30	2.49
146	4	53	319	B	Dol	MDR	-7.29	2.58
147	4	54	321	B	Dol	MDR	-7.25	2.60
148	4	55	323	B	Dol	MDR	-7.25	2.32
149	4	56	325	B	Dol	MDR	-7.12	2.45
150	4	57	327	B	Dol	MDR	-7.64	2.35
151	4	58	329	B	Dol	MDR	-7.21	2.49
152	4	59	331	B	Dol	MDR	-7.10	2.49
153	4	60	333	B	Dol	MDR	-7.30	2.51
154	4	61	335	B	Dol	MDR	-7.04	2.41
155	4	62	335	B	Dol	MDR	-7.10	2.55
156	4	63	337	B	Dol	MDR	-7.20	2.47
157	4	64	341	C	Dol	MDR	-7.30	2.47
158	4	65	345	C	Dol	MDR	-7.42	2.12
159	4	66	347	C	Dol	MDR	-6.74	2.61
160	4	67	343	C	Dol	MDR	-6.02	2.65
161	4	68	349	C	Dol	MDR	-6.50	2.63
162	4	69	351	C	Dol	MDR	-5.65	2.75
163	4	70	353	C	Dol	MDR	-7.26	2.59
164	4	71	355	C	Dol	MDR	-7.14	2.35
165	4	72	357	C	Dol	MDR	-7.47	2.32
166	4	73	357	C	Dol	MDR	-7.39	2.34
167	4	74	359	C	Dol	SDC	-7.46	2.25

168	4	75	359	C	Dol	MDR	-7.26	2.30
169	4	76	361	C	Dol	MDR	-7.13	2.44
170	4	77	361	C	Dol	MDR	-6.68	2.29
171	4	78	363	C	Dol	MDR	-6.86	2.62
172	4	79	367	C	Dol	MDR	-7.14	2.50
173	4	80	369	C	Dol	MDR	-7.37	2.49
174	4	81	371	C	Dol	MDR	-7.10	2.73
175	4	82	373	C	Dol	MDR	-7.04	2.44
176	4	83	376	C	Dol	MDR	-7.07	2.44
177	4	84	378	C	Dol	SDR	-7.06	2.57
178	4	85	380	C	Dol	SDR	-6.87	2.68
179	4	86	382	C	Dol	SDR	-7.24	2.98
180	4	87	384	C	Dol	SDR	-7.34	2.95
181	4	88	386	C	Dol	SDR	-7.24	3.06
182	4	89	388	C	Dol	SDR	-6.39	2.71
183	4	90	390	C	Dol	MDR	-7.06	2.57
184	4	91	390	C	Dol	MDR	-6.73	2.60
185	4	92	392	C	Dol	MDR	-6.73	2.64
186	4	93	394	C	Dol	MDR	-8.04	2.45
187	4	94	399	C	Dol	MDR	-7.00	2.45
188	5	1	NA	A	Dol	MDR	-3.98	1.53
189	5	2	NA	A	Dol	SDR	-2.69	1.34
190	5	3	NA	A	Dol	SDR	-4.41	1.85
191	5	4	NA	B	Dol	MDR	-2.75	1.55
192	5	5	NA	B	Dol	MDR	-4.14	1.58
193	5	6	NA	B	Dol	MDR	-3.87	1.47
194	5	7	NA	B	Dol	MDR	-2.68	1.50
195	5	8	NA	B	Dol	MDR	-4.26	1.61
196	5	9	NA	B	Dol	MDR	-3.30	1.68
197	5	10	NA	B	Dol	MDR	-3.61	1.48
198	5	11	NA	B	Dol	MDR	-4.53	1.69
199	6	1	NA	D	Dol	SDC	-5.85	1.69
200	6	2	NA	D	Dol	SDR	-5.55	1.74
201	6	3	NA	D	Dol	SDR	-5.59	1.50
202	6	4	NA	D	Dol	SDR	-4.56	1.26
203	6	5	NA	D	Dol	SDR	-4.84	1.66
204	6	6	NA	D	Dol	SDR	-5.11	1.43
205	6	7	NA	D	Dol	SDR	-5.66	1.48
206	6	8	NA	D	Dol	SDR	-4.97	1.11
207	6	9	NA	D	Dol	SDR	-3.85	0.96
208	6	10	92	D	Dol	SDR	-4.23	1.56
209	6	11	NA	D	Dol	SDR	-4.47	1.18
210	6	12	NA	D	Dol	MDR	-3.04	0.36
211	6	13	NA	D	Dol	SDR	-5.21	0.88
212	6	14	NA	D	Dol	SDR	-5.22	0.82
213	6	15	NA	D	Dol	SDR	-4.87	1.32
214	6	16	NA	D	Dol	SDR	-5.16	1.35
215	6	17	NA	D	Dol	SDR	-4.83	0.58
216	6	18	NA	D	Dol	SDR	-6.23	1.38
217	6	19	NA	D	Dol	SDR	-5.75	1.60
218	6	20	NA	D	Dol	SDR	-6.26	1.16
219	6	21	NA	D	Dol	SDR	-5.53	1.63
220	6	22	94	D	Dol	SDR	-4.92	1.55
221	1	1	NP	A	Lim		-6.23	1.32
222	1	2	NP	A	Lim		-5.07	2.15
223	1	3	NP	A	Lim		-5.33	1.88
224	1	4	325	A	Lim		-4.77	2.57
225	1	5	327	A	Lim		-4.17	2.70
226	1	6	329	A	Lim		-5.35	2.23
227	1	7	331	A	Lim		-5.65	2.16
228	1	8	np	A	Lim		-5.39	2.51

229	1	9	339	A	Lim		-5.62	2.39
230	1	10	347	A	Lim		-4.63	2.01
231	1	11	np	A	Lim		-5.00	0.95
232	1	12	351	A	Lim		-4.07	1.69
233	2	1	404	A	Lim		-4.55	2.16
234	2	2	406	A	Lim		-4.88	2.09
235	2	3	410	A	Lim		-4.63	2.31
236	2	4	412	A	Lim		-4.36	2.45
237	2	5	418	A	Lim		-5.13	2.06
238	2	6	420	A	Lim		-6.26	2.25
239	2	7	422	A	Lim		-4.68	2.54
240	2	8	424	A	Lim		-5.00	2.42
241	2	9	426	A	Lim		-5.10	2.43
242	2	10	428	A	Lim		-4.75	2.42
243	2	11	447	A	Lim		-3.46	2.13
244	2	12	449	A	Lim		-5.75	0.10
245	2	13	456	B	Lim		-5.27	2.63
246	2	14	457	B	Lim		-5.02	2.61
247	2	15	458	B	Lim		-4.66	2.76
248	2	16	459	B	Lim		-5.37	2.64
249	2	17	460	B	Lim		-4.88	2.68
250	1	1	NP	A	Lim/dol		-6.59	1.67
251	1	2	NP	A	Lim/dol		-5.62	2.16
252	1	3	343	A	Lim/dol		-5.56	2.33
253	1	4	343	A	Lim/dol		-6.11	2.48
254	1	5	345	A	Lim/dol		-6.16	2.33
255	1	6	349	A	Lim/dol		-5.41	2.29
256	1	7	343	A	Lim/dol		-8.24	2.12
257	1	8	343	A	Lim/dol		-8.04	2.68
258	1	9	345	A	Lim/dol		-8.69	3.19
259	1	10	349	A	Lim/dol		-8.86	2.66
260	2	1	414	A	Lim		-4.27	2.33
261	2	2	422	A	Lim		-4.24	2.62
262	2	3	424	A	Lim		-4.33	2.61
263	2	4	428	A	Lim		-4.45	2.55
264	2	5	414	A	Dol in Lim		-3.80	2.73
265	2	6	422	A	Dol in Lim		-4.21	2.69
266	2	7	424	A	Dol in Lim		-4.56	2.58
267	2	8	428	A	Dol in Lim		-4.82	2.60
268	2	9	428	A	Dol in Lim		-4.94	2.54

APPENDIX B: Fluid Inclusion Data

Analysis #	Well #	measurement	Plug	FIA	FI number	Dolomite Phase	Th	Tm	Salinity Wt%
1	1	1	361	1	1	MDR	98.7		
2	1	2	361	1	2	MDR	99.3		
3	1	3	361	1	3	MDR	99.3		
4	1	4	361	1	4	MDR	99.7		
5	1	5	361	1	5	MDR	101.4		
6	1	6	361	2	1	MDR	98.5	-24.5	25.3
7	1	7	361	2	2	MDR	99.0	-24.5	25.3
8	1	8	361	2	3	MDR	97.5	-24.3	25.1
9	1	9	361	2	4	MDR	102.0	-23.8	24.8
10	1	10	361	2	5	MDR	101.3	-23.9	24.9
11	1	11	361	2	6	MDR	102.0	-24.0	25.0
12	1	12	361	2	7	MDR	99.8		
13	1	13	361	2	8	MDR	97.5		
14	1	14	361	2	9	MDR	98.8		
15	1	15	361	2	10	MDR		-24.0	25.0
16	1	16	361	2	11	MDR		-23.9	24.9
17	1	17	364	1	1	SDR	107.1		
18	1	18	364	1	2	SDR	105.8		
19	1	19	364	1	3	SDR	106.0		
20	1	20	364	1	4	SDR	111.5		
21	1	21	364	1	5	SDR	104.9	-24.7	25.4
22	1	22	364	1	6	SDR	103.7	-25.0	25.6
23	1	23	364	1	7	SDR	104.5		
24	1	24	364	1	8	SDR	104.5		
25	1	25	366	1	1	MDR	103.5	-23.8	24.8
26	1	26	366	1	2	MDR	101.3	-24.2	25.1
27	1	27	366	1	3	MDR	102.8	-24.3	25.1
28	1	28	366	1	4	MDR	103.5	-24.4	25.2
29	1	29	366	1	5	MDR	102.5	-23.7	24.8
30	1	30	366	1	6	MDR	104.1	-24.4	25.2
31	1	31	366	1	7	MDR	101.5		
32	1	32	366	1	8	MDR	102.1		
33	1	33	366	1	9	MDR	102.7	-23.7	24.8
34	1	34	366	1	10	MDR	102.6		
35	1	35	366	1	11	MDR	103.0	-24.0	25.0
36	1	36	366	1	12	MDR	103.1		
37	1	37	366	1	13	MDR	102.2		
38	1	38	366	1	14	MDR	102.2		
39	1	39	366	1	15	MDR		-24.3	25.1
40	1	40	366	1	16	MDR		-24.4	25.2
41	2	1	439	1	1	SDC	83.5		
42	2	2	439	1	2	SDC	97.6	-24.8	25.5
43	2	3	439	1	3	SDC	107.4	-23.8	24.8
44	2	4	439	1	4	SDC	114.2	-24.0	25.0
45	2	5	439	1	5	SDC	106.6	-24.1	25.0
46	2	6	439	1	6	SDC	106.3	-24.4	25.2
47	2	7	439	1	7	SDC	104.7	-24.0	25.0
48	2	8	439	2	1	SDR	104.5		
49	2	9	439	2	2	SDR	117.0		

50	2	10	439	2	3	SDR	103.6		
51	2	11	439	2	4	SDR	104.8		
52	2	12	439	2	5	SDR	106.0		
53	2	13	443	1	1	SDR	99.2	-19.9	22.3
54	2	14	443	1	2	SDR	107.3	-19.9	22.3
55	2	15	443	1	3	SDR	97.2		
56	2	16	443	1	4	SDR	105.5	-24.7	25.4
57	2	17	443	1	5	SDR	105.0	-24.8	25.5
58	2	18	443	1	6	SDR	108.0	-24.5	25.3
59	2	19	443	1	7	SDR	105.2	-24.5	25.3
60	2	20	443	1	8	SDR	103.0	-24.2	25.1
61	2	21	443	1	9	SDR	109.0		
62	2	22	443	1	10	SDR	93.3	-24.3	25.1
63	2	23	443	1	11	SDR	103.5		
64	2	24	461	2	1	MDR	104.1	-25.7	26.0
65	2	25	461	2	2	MDR	103.9	-25.3	25.8
66	2	26	461	2	3	MDR	104.7	-25.9	26.1
67	2	27	461	2	4	MDR	104.3	-25.3	25.8
68	2	28	461	2	5	MDR	100.3		
69	2	29	461	2	6	MDR	104.1		
70	2	30	461	2	7	MDR	103.3		
71	2	31	461	2	8	MDR	105.1	-20.5	22.7
72	2	32	461	2	9	MDR	104.1		
73	2	33	461	2	10	MDR		-24.9	25.5
74	2	34	461	2	11	MDR		-20.5	22.7
75	2	35	463	1	1	MDR	102.6	-24.3	25.1
76	2	36	463	1	2	MDR	96.4	-24.3	25.1
77	2	37	463	1	3	MDR	102.3	-24.5	25.3
78	2	38	463	1	4	MDR	105.9	-24.3	25.1
79	2	39	463	1	5	MDR	107.1	-25.9	26.1
80	2	40	471	1	1	MDR	106.6	-27.0	26.8
81	2	41	471	1	2	MDR	105.8	-24.7	25.4
82	2	42	471	1	3	MDR	109.0	-25.0	25.6
83	2	43	471	1	4	MDR	103.0		
84	2	44	471	1	5	MDR	102.3		
85	2	45	471	1	6	MDR	105.0		
86	2	46	471	1	7	MDR		-23.7	24.8
87	2	47	480	1	1	SDC	106.7	-24.0	25.0
88	2	48	480	1	2	SDC	105.5	-25.7	26.0
89	2	49	480	1	3	SDC	104.7	-26.0	26.2
90	2	50	480	1	4	SDC	104.2		
91	2	51	480	1	5	SDC	102.9	-24.0	25.0
92	2	52	480	1	6	SDC	103.3	-25.5	25.9
93	2	53	480	1	7	SDC	104.7	-24.1	25.0
94	2	54	480	1	8	SDC	102.2	-24.1	25.0
95	2	55	480	1	9	SDC	103.2	-25.8	26.1
96	2	56	480	1	10	SDC	101.6	-24.3	25.1
97	2	57	480	1	11	SDC	104.4	-25.9	26.1
98	2	58	486	1	1	SDC	105.4	-24.6	25.3
99	2	59	486	1	2	SDC	105.1		
100	2	60	486	1	3	SDC	107.1	-25.7	26.0
101	2	61	486	1	4	SDC	103.1	-24.5	25.3
102	2	62	486	1	5	SDC	104.9		

103	2	63	486	1	6	SDC	102.3		
104	2	64	486	1	7	SDC	103.4		
105	2	65	486	1	8	SDC	101.3		
106	2	66	486	1	9	SDC	103.8		
107	2	67	486	1	10	SDC	103.8		
108	2	68	486	1	11	SDC	105.1		
109	2	69	486	1	12	SDC	104.1		
110	2	70	486	1	13	SDC		-26.5	26.5
111	2	71	486	1	14	SDC	104.7	-24.1	25.0
112	2	72	490	1	1	SDR	104.2	-23.2	24.5
113	2	73	490	1	2	SDR	106.1	-23.6	24.7
114	2	74	490	1	3	SDR	105.2	-23.3	24.5
115	2	75	490	1	4	SDR	107.0	-24.6	25.3
116	2	76	490	1	5	SDR	108.6	-23.7	24.8
117	2	77	490	1	6	SDR		-22.4	24.0
118	2	78	490	1	7	SDR		-22.1	23.8
119	2	79	490	1	8	SDR		-23.6	24.7
120	2	80	498	1	1	MDC	102.3	-23.8	24.8
121	2	81	498	1	2	MDC	104.4		
122	2	82	498	1	3	MDC	102.5	-22.9	24.3
123	2	83	498	1	4	MDC	105.9	-24.2	25.1
124	2	84	498	1	5	MDC	104.8	-24.6	25.3
125	2	85	498	1	6	MDC	103.6		
126	2	86	502	1	1	MDC	103.3	-24.4	25.2
127	2	87	502	1	2	MDC	106.6		
128	2	88	502	1	3	MDC	99.0	-21.1	23.1
129	2	89	502	1	4	MDC	97.0		
130	2	90	502	1	5	MDC	117.1	-24.6	25.3
131	2	91	502	1	6	MDC	98.6	-23.5	24.6
132	2	92	502	1	7	MDC	102.7		
133	2	93	502	1	8	MDC	108.6		
134	2	94	502	1	9	MDC	111.1		
135	2	95	502	1	10	MDC	107.4		
136	2	96	502	1	11	MDC	107.7		
137	2	97	502	1	12	MDC	105.0	-25.6	25.9
138	2	98	502	1	13	MDC	106.4	-24.5	25.3
139	2	99	502	1	14	MDC	106.4		
140	2	100	502	1	15	MDC	105.8	-24.6	25.3
141	2	101	502	1	16	MDC	106.2		
142	2	102	502	1	17	MDC	107.0		
143	2	103	502	1	18	MDC	97.0	-20.2	22.5
144	2	104	502	1	19	MDC		-26.6	26.6
145	2	105	502	1	20	MDC		-24.6	25.3
146	2	106	510	1	1	MDC	109.0	-24.4	25.2
147	2	107	510	1	2	MDC	103.0	-24.2	25.1
148	2	108	510	1	3	MDC	102.3	-24.3	25.1
149	2	109	510	1	4	MDC	107.3	-24.1	25.0
150	2	110	510	1	5	MDC	117.0		
151	2	111	510	1	6	MDC	91.9	-22.4	24.0
152	2	112	510	1	7	MDC	106.4		
153	2	113	510	1	8	MDC	107.1	-22.9	24.3
154	2	114	510	1	9	MDC	108.3		
155	2	115	510	1	10	MDC	107.0	-24.2	25.1

156	2	116	510	1	11	MDC	104.0	-22.5	24.0
157	2	117	510	1	12	MDC	105.0	-24.4	25.2
158	2	118	510	1	13	MDC	105.6		
159	2	119	510	1	14	MDC	94.5	-25.9	26.1
160	2	120	510	1	15	MDC	107.1		
161	2	121	510	1	16	MDC	107.1		
162	2	122	510	1	17	MDC	105.3		
163	2	123	512	1	1	MDC	104.5	-23.7	24.8
164	2	124	512	1	2	MDC	107.4	-23.9	24.9
165	2	125	512	1	3	MDC	107.7	-24.0	25.0
166	2	126	512	1	4	MDC	108.7	-24.2	25.1
167	2	127	512	1	5	MDC	101.0		
168	2	128	512	1	6	MDC	104.8	-24.7	25.4
169	2	129	512	1	7	MDC	107.5	-27.9	27.4
170	2	130	512	1	8	MDC	105.4	-24.1	25.0
171	2	131	512	1	9	MDC	108.1	-23.7	24.8
172	2	132	512	1	10	MDC	107.1	-24.0	25.0
173	2	133	512	1	11	MDC	101.6	-26.2	26.3
174	2	134	512	1	12	MDC	94.6		
175	2	135	512	1	13	MDC		-23.7	24.8
176	2	136	520	1	1	MDC	102.2	-27.0	26.8
177	2	137	520	1	2	MDC	104.5	-24.7	25.4
178	2	138	520	1	3	MDC	106.5	-24.6	25.3
179	2	139	520	1	4	MDC	96.2		
180	2	140	520	1	5	MDC	108.9	-24.7	25.4
181	2	141	520	1	6	MDC	102.4		
182	2	142	520	1	7	MDC	101.6		
183	2	143	520	1	8	MDC	99.6		
184	2	144	520	1	9	MDC	102.8		
185	2	145	524	1	1	MDC	109.0	-23.7	24.8
186	2	146	524	1	2	MDC	108.1	-23.5	24.6
187	2	147	524	1	3	MDC	114.4	-23.6	24.7
188	2	148	524	1	4	MDC	108.0		
189	2	149	524	1	5	MDC	102.5		
190	2	150	524	1	6	MDC	102.0	-21.9	23.6
191	2	151	528	1	1	MDC	102.1		
192	2	152	528	1	2	MDC	104.0	-23.8	24.8
193	2	153	528	1	3	MDC	101.8	-24.5	25.3
194	2	154	528	1	4	MDC	100.8		
195	2	155	528	1	5	MDC	102.5		
196	2	156	528	1	6	MDC	102.6		
197	2	157	528	1	7	MDC	101.9		
198	2	158	528	1	8	MDC	99.8	-22.3	23.9
199	2	159	528	1	9	MDC	100.9		
200	2	160	528	1	10	MDC	95.8		
201	2	161	528	1	11	MDC	100.5		
202	2	162	528	1	12	MDC	109.8		
203	2	163	532	1	1	MDC	94.5		
204	2	164	532	1	2	MDC	103.1		
205	2	165	532	1	3	MDC	105.6	-24.1	25.0
206	2	166	532	1	4	MDC	91.8		
207	2	167	532	1	5	MDC	97.4		
208	2	168	532	1	6	MDC	102.0		

209	2	169	532	1	7	MDC	93.1		
210	2	170	532	1	8	MDC	95.0		
211	2	171	532	1	9	MDC	103.6		
212	2	172	536	1	1	SDR	96.1		
213	2	173	536	1	2	SDR	95.5		
214	2	174	536	1	3	SDR	100.1		
215	2	175	536	1	4	SDR	100.1		
216	2	176	536	1	5	SDR	103.9		
217	2	177	536	1	6	SDR	107.3	-25.5	25.9
218	2	178	536	1	7	SDR	107.7	-24.0	25.0
219	2	179	536	1	8	SDR	107.8	-25.5	25.9
220	2	180	536	1	9	SDR	101.5		
221	2	181	536	1	10	SDR	97.1		
222	2	182	536	1	11	SDR	97.6		
223	2	183	536	1	12	SDR	95.8		
224	2	184	540	1	1	MDR	102.3	-24.9	25.5
225	2	185	540	1	2	MDR	105.9	-24.2	25.1
226	2	186	540	1	3	MDR	106.9	-24.8	25.5
227	2	187	540	1	4	MDR	106.5	-24.3	25.1
228	2	188	540	1	5	MDR	103.6	-24.0	25.0
229	2	189	545	1	1	MDR	100.0	-24.6	25.3
230	2	190	545	1	2	MDR	112.3	-23.8	24.8
231	2	191	545	1	3	MDR	102.2	-25.2	25.7
232	2	192	545	1	4	MDR	106.2	-25.1	25.6
233	2	193	545	1	5	MDR	95.7		
234	2	194	545	1	6	MDR	95.7		
235	2	195	545	1	7	MDR	107.3	-25.0	25.6
236	2	196	545	2	1	MDC	103.4	-23.9	24.9
237	2	197	545	2	2	MDC	104.3	-23.8	24.8
238	2	198	545	2	3	MDC	105.5	-23.3	24.5
239	2	199	545	2	4	MDC	105.5	-23.4	24.6
240	2	200	545	2	5	MDC	106.9	-24.4	25.2
241	2	201	545	2	6	MDC	102.1		
242	2	202	545	2	7	MDC	104.3		
243	2	203	545	2	8	MDC	107.1		
244	2	204	548	1	2	MDR		-24.1	25.0
245	2	205	548	1	3	MDR	103.8		
246	2	206	548	1	4	MDR	109.7	-24.4	25.2
247	2	207	548	1	5	MDR	102.4		
248	2	208	548	1	6	MDR	99.7		
249	2	209	548	1	7	MDR		-25.0	25.6
250	2	210	548	1	8	MDR		-22.5	24.0
251	2	211	556	1	1	MDC	107.1	-25.0	25.6
252	2	212	556	1	2	MDC	113.0		
253	2	213	556	1	3	MDC	107.0	-24.9	25.5
254	2	214	556	1	4	MDC	108.3	-25.3	25.8
255	2	215	556	1	5	MDC		-25.3	25.8
256	2	216	556	1	6	MDC	100.5		
257	2	217	560	1	1	MDC	104.5	-23.8	24.8
258	2	218	560	1	2	MDC	104.5		
259	2	219	560	1	3	MDC	106.0	-24.0	25.0
260	2	220	560	1	4	MDC	102.6	-24.5	25.3
261	2	221	560	1	5	MDC	104.0	-24.5	25.3

262	2	222	560	1	6	MDC	102.6	-24.5	25.3
263	2	223	560	2	1	MDC	105.0	-24.2	25.1
264	2	224	560	2	2	MDC	99.0	-23.9	24.9
265	2	225	560	2	3	MDC	103.2	-24.0	25.0
266	2	226	560	3	1	MDC	105.0	-25.4	25.8
267	2	227	560	3	2	MDC	104.6	-25.5	25.9
268	2	228	560	3	3	MDC	97.8		
269	2	229	560	4	1	MDC	102.6	-24.9	25.5
270	2	230	560	4	2	MDC	103.0	-24.9	25.5
271	2	231	560	4	3	MDC	112.4	-25.9	26.1
272	2	232	560	4	4	MDC	108.0	-25.5	25.9
273	2	233	564	1	1	MDR	95.1	-22.6	24.1
274	2	234	564	1	2	MDR	95.5		
275	2	235	564	1	3	MDR	97.0	-21.6	23.4
276	2	236	564	1	4	MDR	98.5	-21.6	23.4
277	4	1	231	1	1	SDR		-20.1	22.4
278	4	2	231	1	2	SDR		-20.0	22.4
279	4	3	231	1	3	SDR	97.0	-19.5	22.0
280	4	4	231	1	4	SDR	97.7	-19.2	21.8
281	4	5	231	1	5	SDR		-19.0	21.7
282	4	6	231	1	6	SDR		-18.2	21.1
283	4	7	231	1	7	SDR	95.5		
284	4	8	231	1	8	SDR	95.5		
285	4	9	231	1	9	SDR	95.7		
286	4	10	231	1	10	SDR	96.9		
287	4	11	280	1	1	SDR	96.7	-20.3	22.6
288	4	12	280	1	2	SDR	96.3	-20.3	22.6
289	4	13	280	1	3	SDR	96.5	-20.0	22.4
290	4	14	280	1	4	SDR	95.8	-19.8	22.2
291	4	15	280	1	5	SDR	95.5	-19.5	22.0
292	4	16	280	1	6	SDR	95.9	-19.5	22.0
293	4	17	288	1	1	SDR	93.3	-20.1	22.4
294	4	18	288	1	2	SDR	93.0	-19.0	21.7
295	4	19	288	1	3	SDR	92.9	-18.7	21.5
296	4	20	288	1	4	SDR	92.3	-18.6	21.4
297	4	21	288	1	5	SDR	91.5	-17.9	20.9
298	4	22	288	1	6	SDR	93.1	-17.9	20.9
299	4	23	327	1	1	SDC	93.5	-20.3	22.6
300	4	24	327	1	2	SDC	91.5	-19.3	21.9
301	4	25	327	1	3	SDC	91.2	-18.8	21.5
302	4	26	327	1	4	SDC	90.0	-18.8	21.5
303	4	27	327	1	5	SDC	92.3	-18.5	21.3
304	4	28	327	1	6	SDC	92.2		
305	4	29	327	1	7	SDC	93.0		
306	4	30	327	1	8	SDC	92.0		
307	4	31	327	1	9	SDC	93.8		
308	4	32	327	1	10	SDC	96.5		
309	4	33	327	1	11	SDC	90.7		
310	4	34	351	1	1	SDR	95.7	-19.4	22.0
311	4	35	351	1	2	SDR	96.2	-19.2	21.8
312	4	36	351	1	3	SDR	99.9	-19.1	21.8
313	4	37	351	1	4	SDR	96.2	-19.1	21.8
314	4	38	351	1	5	SDR	96.3	-18.7	21.5

315	4	39	351	1	6	SDR	97.5	-18.5	21.3
316	4	40	351	1	7	SDR	94.5	-18.3	21.2
317	4	41	351	1	8	SDR	96.1		
318	4	42	351	1	9	SDR	97.3		
319	4	43	351	1	10	SDR	94.5		
320	4	44	394	1	1	MDR	98.1	-20.1	22.4
321	4	45	394	1	2	MDR		-19.4	22.0
322	4	46	394	1	3	MDR	94.2	-18.8	21.5
323	4	47	394	1	4	MDR	92.7	-18.1	21.0
324	4	48	394	1	5	MDR		-17.9	20.9
325	4	49	394	1	6	MDR		-17.9	20.9
326	4	50	394	1	7	MDR	93.7	-17.5	20.6
327	4	51	394	1	8	MDR	90.3		
328	4	52	394	1	9	MDR	91.2		
329	4	53	394	1	10	MDR	92.5		
330	4	54	394	1	11	MDR	95.0		
331	4	55	394	1	12	MDR	96.1		
332	6	1	92	1	1	SDR	75.8	-18.7	21.5
333	6	2	92	1	2	SDR	75.4	-19.3	21.9
334	6	3	92	1	3	SDR	83.2	-18.7	21.5
335	6	4	92	1	4	SDR		-19.3	21.9
336	6	5	92	1	5	SDR	82.2		
337	6	6	92	1	6	SDR	83.5	-20.4	22.6
338	6	7	92	1	7	SDR	83.7		
339	6	8	92	1	8	SDR	88.1		
340	6	9	92	1	9	SDR	75.2	-18.9	21.6
341	6	10	92	1	10	SDR	75.7	-18.7	21.5
342	6	11	92	1	11	SDR	76.0	-19.0	21.7
343	6	12	92	1	12	SDR		-19.7	22.2
344	6	13	92	1	13	SDR	80.1	-18.4	21.3
345	6	14	92	1	14	SDR		-18.0	21.0
346	6	15	92	1	15	SDR		-18.6	21.4
347	6	16	92	2	1	SDR	78.0	-20.3	22.6
348	6	17	92	2	2	SDR	77.5	-19.5	22.0
349	6	18	92	2	3	SDR	76.1		
350	6	19	92	2	4	SDR		-18.2	21.1
351	6	20	94	1	1	MDR	79.2		
352	6	21	94	1	2	MDR	79.7		
353	6	22	94	1	3	MDR	77.5		
354	6	23	94	1	4	MDR	83.3		
355	6	24	94	1	5	MDR	83.5		
356	6	25	94	1	6	MDR	81.5		
357	6	26	94	1	7	MDR	87.0		
358	6	27	94	1	8	MDR	86.7	-22.0	23.7
359	6	28	94	1	9	MDR	90.1		
360	6	29	94	1	10	MDR	84.0		
361	6	30	94	1	11	MDR	85.0		
362	6	31	94	1	12	MDR	90.1	-21.9	23.6
363	6	32	94	1	13	MDR	90.3	-21.9	23.6
364	6	33	94	1	14	MDR		-22.0	23.7
365	6	34	94	1	15	MDR	85.5	-22.1	23.8
366	6	35	94	1	16	MDR	90.8	-22.1	23.8
367	6	36	94	1	17	MDR	89.0	-21.3	23.2

APPENDIX C: Uranium–Lead (U–Pb) Data

Analysis	Well	ID	W Analysis #	Spot #	$^{238}U/^{206}Pb$		$^{207}Pb/^{206}Pb$		err.corr.		omit	Description
						Prop2SE		Prop2SE	rho			
1	1	364	1	364-1.FIN2								Baroque
2	1	364	2	364-2.FIN2								Baroque
3	1	364	3	364-3.FIN2	2.6615	0.6008	1.01	0.18	0.5382			Baroque
4	1	364	4	364-4.FIN2	1.337	0.1752	0.8	0.0691	0.1559			Baroque
5	1	364	5	364-5.FIN2	7.9474	1.2333	1.06	0.21	0.4755			Baroque
6	1	364	6	364-6.FIN2	6.0774	1.1119	1.27	0.27	0.8821			Baroque
7	1	364	7	364-7.FIN2	3.9737	0.5341	0.96	0.18	0.6563			Baroque
8	1	364	8	364-8.FIN2	15.0129	1.5767	0.693	0.0301	0.0909			Baroque
9	1	364	9	364-9.FIN2	103.316	14.2443	0.466	0.047	0.1505			Baroque
10	1	364	10	364-9.FIN2	88.099	8.3888	0.378	0.042	-0.045			Baroque
11	1	364	11	364-10.FIN2	13.4494	1.615	0.94	0.16	0.3334			Baroque
12	1	364	12	364-11.FIN2	1.222	0.1987	0.731	0.0361	0.4298			Baroque
13	1	364	13	364-12.FIN2	5.4118	0.8831	0.91	0.15	0.2899			Baroque
14	1	364	14	364-13.FIN2	5.571	0.746	0.74	0.31	0.9406			Baroque
15	1	364	15	364-14.FIN2	9.3924	1.7955	1.09	0.46	0.969			Baroque
16	1	364	16	364-15.FIN2	8.6097	1.187	0.82	0.11	0.5529			Baroque
17	1	364	17	364-16.FIN2	6.8877	1.4677	0.82	0.16	0.2598			Baroque
18	1	364	18	364-17.FIN2	5.5438	0.7388	0.89	0.13	0.3215			Baroque
19	1	364	19	364-18.FIN2	7.428	1.1268	1.02	0.23	0.9484			Baroque
20	1	364	20	364-19.FIN2								Baroque
21	1	364	21	364-20.FIN2	5.7109	1.2395	1.07	0.41	0.8146			Baroque
22	1	364	22	364-21.FIN2	7.8922	1.652	1.33	0.72	0.9176		x	Baroque
23	1	364	23	364-22.FIN2	14.3858	2.0243	0.73	0.12	0.7002			Baroque
24	1	364	24	364-23.FIN2	7.6274	1.0861	0.78	0.0651	0.6207			Baroque
25	1	364	25	364-23.FIN2	9.8824	1.0506	0.83	0.13	0.3417			Baroque
26	1	364	26	364-24.FIN2	4.1028	0.4667	0.729	0.0421	0.3731			Baroque
27	1	364	27	364-25.FIN2	98.8241	9.664	0.408	0.028	0.2539			Baroque
28	1	364	28	364-26.FIN2	0.6765	0.0541	0.753	0.0461	0.4392			Transcet
29	1	364	29	364-27.FIN2	1.9197	0.2495	0.734	0.072	0.347			Transcet
30	1	364	30	364-27.FIN2	3.5185	0.8852	0.84	0.31	0.5305			Transcet
31	1	364	31	364-28.FIN2	2.2549	0.29	0.91	0.13	0.4298			Transcet
32	1	364	32	364-29.FIN2	1.6052	0.1465	0.762	0.097	0.479			Transcet
33	1	364	33	364-29.FIN2	2.8845	0.4286	0.88	0.15	0.4214			Transcet
34	1	364	34	364-30.FIN2	2.5143	0.2773	0.766	0.0551	0.4214			Transcet
35	1	364	35	364-31.FIN2	5.5984	0.35	0.742	0.0082	0.133			Transcet
36	1	364	36	364-32.FIN2	6.6074	1.0459	0.744	0.0491	0.35			Transcet
37	1	364	37	364-33.FIN2	3.4861	0.3599	0.71	0.0162	0.2134			Transcet
38	1	364	38	364-34.FIN2	2.3193	0.4757	0.95	0.3	0.7835			Baroque
39	1	364	39	364-35.FIN2	4.7751	0.6097	0.78	0.1	0.2016			Baroque
40	1	364	40	364-36.FIN2	3.1136	0.2471	0.819	0.0371	0.4699			Baroque
41	1	364	41	364-37.FIN2	26.2466	2.7794	0.595	0.0231	0.321			Baroque
42	1	364	42	364-37.FIN2	44.0495	3.5302	0.574	0.0251	0.2235			Baroque
43	1	364	43	364-38.FIN2	0.924	0.1291	0.847	0.0591	-0.011			Baroque
44	1	364	44	364-39.FIN2	2.7188	0.5556	0.688	0.087	0.5947			Baroque
45	1	364	45	364-40.FIN2	3.7632	0.2966	0.714	0.0591	0.4449			Baroque
46	1	364	46	364-41.FIN2	41.7823	3.9331	0.523	0.0261	-0.17			Baroque
47	1	364	47	364-42.FIN2	65.6923	5.114	0.58	0.0151	-0.209			Baroque
48	1	364	48	364-43.FIN2	109.277	9.1016	0.56	0.0291	-0.25			Baroque
49	1	364	49	364-44.FIN2	99.0826	5.2403	0.6	0.0161	-0.22			Baroque
50	1	364	50	364-45.FIN2	38.3945	5.632	0.56	0.0291	-0.25			Baroque
51	1	364	51	364-46.FIN2	34.5434	4.7767	0.639	0.0241	0.0208			Baroque
52	1	364	52	364-47.FIN2	6.6461	1.0195	0.79	0.11	0.6885			Baroque
53	1	364	53	364-48.FIN2	3.8137	0.7208	1.03	0.23	0.6519			Baroque
54	1	364	54	364-49.FIN2	76.2736	7.3326	0.449	0.0221	-0.358			Baroque
55	1	364	55	364-50.FIN2	134.019	7.6161	0.372	0.0111	0.1177			Baroque
56	1	364	56	364-51.FIN2	11.7163	1.1956	0.793	0.088	0.5			Baroque
57	1	364	57	364-52.FIN2	93.9237	14.1021	0.392	0.028	-0.647			Equant
58	1	364	58	364-52.FIN2	102.385	9.2761	0.403	0.027	0.0449			Equant
59	1	364	59	364-53.FIN2	50.7356	5.9786	0.579	0.0181	-0.322			Equant
60	1	364	60	364-54.FIN2	25.5388	2.8597	0.608	0.0341	0.2036			Equant
61	1	364	61	364-55.FIN2	59.1915	5.0774	0.591	0.054	0.2688			Equant
62	1	364	62	364-56.FIN2	73.3211	9.1106	0.466	0.035	-0.197			Equant
63	1	364	63	364-56.FIN2	118.754	9.7351	0.385	0.031	-0.313			Equant
64	1	364	64	364-57.FIN2	117.405	7.8896	0.397	0.0191	0.1356			Equant
65	1	364	65	364-58.FIN2	37.7567	4.21	0.571	0.046	0.4908			Equant
66	1	364	66	364-58.FIN2	79.4739	13.4358	0.449	0.042	0.302			Equant
67	1	364	67	364-59.FIN2	1.9903	0.3129	0.97	0.18	0.3545			Baroque
68	1	364	68	364-60.FIN2	0.9631	0.1321	0.824	0.0681	0.3294			Baroque

69	1	364	69	364-61.FIN2	1.4759	0.461	1.01	0.36	0.3964			Baroque
70	1	364	70	364-62.FIN2	0.8949	0.1911	0.79	0.1	0.1962			Baroque
71	1	364	71	364-63.FIN2	0.9639	0.0809	0.801	0.0551	0.1926			Baroque
72	1	364	72	364-64.FIN2	0.4716	0.0964	0.743	0.086	0.1696			Baroque
73	1	364	73	364-65.FIN2	84.8117	10.2726	0.529	0.0281	-0.016			Baroque
74	1	364	74	364-66.FIN2	36.8986	4.9688	0.605	0.0421	0.2559			Baroque
75	1	364	75	364-67.FIN2	30.9667	3.8489	0.638	0.0251	0.3315			Baroque
76	1	364	76	364-68.FIN2	8.1177	1.8628	0.645	0.0182	-0.419		x	Baroque
77	1	364	77	364-68.FIN2	75.7652	7.7316	0.645	0.0241	0.331			Baroque
78	1	364	78	364-69.FIN2	89.0656	7.0762	0.546	0.0141	0.0951			Baroque
79	1	364	79	364-70.FIN2	4.2092	3.5866	2	2.1	0.7551		x	Baroque
80	1	364	80	364-71.FIN2	2.9673	0.392	0.678	0.073	0.6326			Baroque
81	1	364	81	364-72.FIN2	9.0918	1.1066	0.828	0.098	0.5665			Baroque
82	1	364	82	364-73.FIN2	16.6639	2.0561	0.86	0.16	0.5031			Baroque
83	1	364	83	364-74.FIN2	8.0601	1.0984	0.74	0.14	0.4341			Baroque
84	1	364	84	364-75.FIN2	4.5826	0.3991	0.791	0.0791	0.7871			Baroque
85	1	364	85	364-76.FIN2	8.1761	1.4215	0.98	0.2	0.8449			Baroque
86	1	364	86	364-77.FIN2	32.7515	5.0465	0.672	0.077	0.4949			Baroque
87	1	364	87	364-77.FIN2	20.1146	2.9126	0.7	0.13	0.8073			Baroque
88	1	364	88	364-78.FIN2	7.428	1.2231	0.91	0.14	0.3672			Baroque
89	1	364	89	364-78.FIN2	3.6899	0.2625	0.723	0.083	0.5819			Baroque
90	2	414	1	414-01.FIN2	13.3807	0.6838	0.621	0.0122	0.1422			Peloids
91	2	414	2	414-02.FIN2	15.182	1.1	0.632	0.0142	-0.069			Peloids
92	2	414	3	414-03.FIN2	13.885	1.1291	0.611	0.0132	-0.141			Peloids
93	2	414	4	414-04.FIN2	4.7132	0.2032	0.741	0.0092	0.3021			Peloids
94	2	414	5	414-05.FIN2	7.3195	0.5406	0.696	0.0099	-0.105			Peloids
95	2	414	6	414-06.FIN2	10.1306	0.8539	0.69	0.0182	-0.156			Peloids
96	2	414	7	414-07.FIN2	10.2718	0.7644	0.752	0.0133	0.3168			Peloids
97	2	414	8		32.1293	5.8971	0.733	0.0232	0.0188			Peloids
98	2	414	9	414-08.FIN2	8.0911	0.4666	0.714	0.0391	0.3272			Peloids
99	2	414	10	414-09.FIN2	12.4325	1.1012	0.636	0.0152	-0.011			Peloids
100	2	414	11	414-10.FIN2	10.7201	0.8009	0.667	0.0142	0.2442			Peloids
101	2	414	12		21.0123	2.1325	0.619	0.0182	0.4703			Peloids
102	2	414	13	414-11.FIN2	18.1784	1.1574	0.454	0.0151	-0.438			Mud Lump
103	2	414	14	414-12.FIN2	18.1188	0.9467	0.473	0.0201	-0.499			Mud Lump
104	2	414	15	414-13.FIN2	12.4465	1.1037	0.547	0.0191	-0.23			Mud Lump
105	2	414	16	414-14.FIN2	20.5819	0.9532	0.422	0.0161	-0.16			Mud Lump
106	2	414	17	414-15.FIN2	23.5159	1.0889	0.391	0.0151	0.2585			Mud Lump
107	2	414	18	414-16.FIN2	3.4976	0.3897	0.698	0.0162	-0.365			Mud Lump
108	2	414	19	414-17.FIN2	13.645	1.0742	0.541	0.0201	-0.414			Mud Lump
109	2	414	20		18.9255	1.6366	0.439	0.0221	-0.127			Mud Lump
110	2	414	21	414-18.FIN2	19.4586	1.088	0.447	0.0151	-0.128			Mud Lump
111	2	414	22	414-19.FIN2	22.6485	0.9237	0.406	0.0161	-0.146			Mud Lump
112	2	414	23	414-20.FIN2	22.5561	1.4983	0.438	0.0181	-0.291			Mud Lump
113	2	414	24	414-21.FIN2	23.4162	1.3209	0.433	0.0271	0.3788			Dolomite Cement
114	2	414	25	414-22.FIN2	18.5444	1.1426	0.507	0.047	0.2496			Dolomite Cement
115	2	414	26	414-23.FIN2	20.8144	1.1263	0.472	0.042	-0.033			Dolomite Cement
116	2	414	27	414-24.FIN2	3.5653	0.6111	0.87	0.17	0.202			Dolomite Cement
117	2	414	28	414-25.FIN2	17.5158	1.3767	0.697	0.077	0.2488			Dolomite Cement
118	2	414	29	414-26.FIN2	30.1157	1.5217	0.34	0.02	0.1793			Dolomite Cement
119	2	414	30		21.4611	1.0739	0.487	0.0341	0.5416			Dolomite Cement
120	2	414	31	414-27.FIN2	17.5158	2.5073	0.73	0.2	0.1347			Dolomite Cement
121	2	414	32	414-28.FIN2	13.9905	1.7791	0.62	0.11	0.7803			Dolomite Cement
122	2	414	33	414-29.FIN2	2.5703	0.3898	0.92	0.14	0.6928			Dolomite Cement
123	2	414	34	414-30.FIN2	25.5253	1.9699	0.463	0.052	0.34			Dolomite Cement
124	2	414	35	414-31.FIN2	18.8609	1.1181	0.491	0.037	0.5776			Dolomite Cement
125	2	414	36	414-32.FIN2	16.8483	1.0727	0.506	0.0311	0.3055			Dolomite Cement
126	2	414	37	414-33.FIN2	11.8844	1.5403	0.77	0.16	0.1057			Dolomite Cement
127	2	414	38	414-34.FIN2	17.4055	1.8486	0.567	0.088	0.8749			Dolomite Cement
128	2	414	39	414-35.FIN2	5.0011	0.569	0.91	0.16	0.1386			Dolomite Cement
129	2	414	40	414-36.FIN2	2.1672	0.553	0.9	0.2	0.7465			Dolomite Cement
130	2	414	41	414-37.FIN2	20.4675	2.2124	0.552	0.077	0.1693			Dolomite Cement
131	2	414	42	414-38.FIN2	23.975	1.5872	0.448	0.043	0.1267			Dolomite Cement
132	2	414	43	414-39.FIN2	17.0038	1.4535	0.432	0.035	0.7828			Dolomite Cement
133	2	414	44		0.3838	0.0429	0.709	0.0162	-0.293			Dolomite Cement
134	2	414	45	414-40.FIN2	2.2105	0.8404	0.82	0.22	0.5337			Dolomite Cement
135	2	414	46		25.0056	4.7054	0.58	0.12	0.5076			Dolomite Cement
136	2	414	47	414-41.FIN2	28.5593	1.5881	0.392	0.0221	0.2486			Dolomite Cement
137	2	414	48	414-42.FIN2	26.3154	1.6601	0.399	0.031	-0.122			Dolomite Cement
138	2	414	49	414-43.FIN2	37.7217	3.7616	0.482	0.058	0.5868			Dolomite Cement
139	2	414	50	414-44.FIN2	26.7614	1.3991	0.376	0.028	0.1757			Dolomite Cement
140	2	414	51	414-45.FIN2	27.84	1.511	0.409	0.0241	0.545			Dolomite Cement
141	2	414	52	414-46.FIN2	24.3446	1.5829	0.396	0.033	0.1374			Dolomite Cement
142	2	414	53	414-47.FIN2	21.5029	1.078	0.439	0.0281	0.6353			Dolomite Cement
143	2	414	54	414-48.FIN2	20.7753	2.512	0.508	0.074	0.4393			Dolomite Cement

144	2	414	55	414-49.FIN2	23.4162	1.1279	0.413	0.034	0.3072			Dolomite Cement
145	2	414	56	414-50.FIN2	19.9144	1.0683	0.432	0.032	0.1614			Dolomite Cement
146	2	439	1	439-1.FIN2	5.571	0.6382	0.697	0.082	0.4139			Baroque
147	2	439	2	439-2.FIN2	2.6931	0.2238	0.89	0.0581	0.6261			Baroque
148	2	439	3	439-3.FIN2	14.206	1.7991	0.96	0.16	0.4004			Baroque
149	2	439	4	439-4.FIN2	18.6308	3.3809	0.641	0.079	0.1951			Baroque
150	2	439	5	439-5.FIN2	1.5962	0.2088	0.748	0.0311	0.7636			Baroque
151	2	439	6	439-6.FIN2	1.9973	0.3255	0.772	0.0371	0.0353			Baroque
152	2	439	7	439-7.FIN2	7.1477	0.8221	0.734	0.092	0.5936			Baroque
153	2	439	8	439-8.FIN2	0.7731	0.0753	0.737	0.0301	0.106			Baroque
154	2	439	9	439-9.FIN2	0.5361	0.0567	0.779	0.0252	-0.024			Baroque
155	2	439	10	439-10.FIN2	4.8986	0.7876	0.762	0.0391	0.0766			Baroque
156	2	439	11	439-12.FIN2	0.6013	0.0773	0.768	0.0271	0.3105			Baroque
157	2	439	12	439-11.FIN2	0.3529	0.021	0.805	0.0182	0.1906			Baroque
158	2	439	13	439-13.FIN2	1.836	0.1993	0.825	0.0381	0.3043			Baroque
159	2	439	14	439-14.FIN2	2.9519	0.3502	0.896	0.0971	0.2444			Baroque
160	2	439	15	439-15.FIN2	2.9751	0.3556	0.845	0.0921	0.4618			Baroque
161	2	439	16	439-16.FIN2	13.063	2.2678	0.86	0.19	0.3238			Baroque
162	2	439	17	439-16.FIN2	40.7339	6.1877	0.54	0.17	0.5284			Baroque
163	2	439	18	439-17.FIN2	18.9413	4.122	0.69	0.16	0.2061			Baroque
164	2	439	19	439-18.FIN2	4.3879	0.5829	1.03	0.2	0.0823		x	Baroque
165	2	439	20	439-18.FIN2	8.8787	1.2616	0.84	0.18	0.4241			Baroque
166	2	439	21	439-19.FIN2	0.6045	0.0498	0.857	0.0531	0.1906			Baroque
167	2	439	22	439-20.FIN2	7.6274	1.0861	0.96	0.17	0.675			Baroque
168	2	439	23	439-21.FIN2	11.1419	1.7624	0.87	0.19	0.1345			Baroque
169	2	439	24	439-22.FIN2	2.4078	0.411	0.92	0.1101	-0.031			Baroque
170	2	439	25	439-23.FIN2	2.7385	0.1867	1	0.1101	0.5229			Baroque
171	2	439	26	439-24.FIN2	4.8986	0.6412	0.866	0.0911	0.232			Baroque
172	2	439	27	439-25.FIN2	1.2326	0.1151	0.877	0.0451	0.3183			Baroque
173	2	439	28	439-26.FIN2	24.1804	5.6806	1.61	0.9	0.5754		x	Baroque
174	2	439	29	439-27.FIN2	42.8859	6.8527	0.625	0.088	0.1466			Baroque
175	2	439	30	439-28.FIN2	2.7992	0.329	0.83	0.0631	0.2805			Baroque
176	2	439	31	439-29.FIN2	2.4923	0.5326	1	0.16	0.159		x	Baroque
177	2	439	32	439-30.FIN2	102.849	8.1832	0.321	0.029	-0.391		x	Baroque
178	2	439	33	439-31.FIN2	56.5412	6.0181	0.652	0.0172	-0.28			Baroque
179	2	439	34	439-32.FIN2	50.7356	4.2055	0.606	0.0241	-0.455			Baroque
180	2	439	35	439-33.FIN2	68.0525	5.082	0.647	0.0162	-0.331			Baroque
181	2	439	36	439-34.FIN2	27.3192	6.198	1.15	0.34	0.3378		x	Baroque
182	2	439	37	439-35.FIN2	2.8555	0.2858	0.8	0.0641	0.2816			Baroque
183	2	439	38	439-36.FIN2	43.5432	4.5907	0.555	0.06	0.1626			Baroque
184	2	439	39	439-37.FIN2	9.3154	1.3874	0.642	0.091	0.3785			Baroque
185	2	439	40	439-38.FIN2	36.0786	2.9559	0.76	0.0172	-0.082			Baroque
186	2	439	41	439-39.FIN2	20.2942	4.7292	0.585	0.0411	-0.073			Baroque
187	2	439	42	439-40.FIN2	8.6097	1.0582	0.79	0.0232	0.1059			Baroque
188	2	439	43	439-41.FIN2	48.9861	5.5795	0.586	0.0181	0.0486			Baroque
189	2	439	44	439-42.FIN2	18.9413	2.6796	0.745	0.0321	0.1262			Baroque
190	2	439	45	439-43.FIN2	12.116	1.2263	0.798	0.0114	0.0544			Baroque
191	2	439	46	439-44.FIN2	6.1765	1.2818	0.768	0.0321	-0.032			Baroque
192	2	439	47	439-44.FIN2	23.6766	6.4305	0.71	0.072	0.1993			Baroque
193	2	439	48	439-45.FIN2	10.1471	1.4642	0.739	0.086	0.754			Baroque
194	2	439	49	439-46.FIN2	30.4686	3.4863	0.587	0.0381	-0.295			Baroque
195	2	439	50	439-47.FIN2	4.4743	0.5189	0.87	0.13	0.2172			Baroque
196	2	439	51	439-48.FIN2	0.693	0.0649	0.833	0.0321	0.268			Baroque
197	2	439	52	439-49.FIN2	0.8675	0.1009	0.882	0.0621	-0.066			Baroque
198	2	439	53	439-50.FIN2	3.9876	0.6765	1.09	0.3	0.4793		x	Baroque
199	2	439	54	439-51.FIN2	1.3261	0.151	0.804	0.0571	0.3299			Baroque
200	2	439	55	439-52.FIN2	26.3073	4.2962	0.654	0.0311	0.2306			Baroque
201	2	439	56	439-53.FIN2	36.0786	3.8502	0.596	0.0381	0.139			Baroque
202	2	439	57	439-54.FIN2	15.5682	3.0024	0.738	0.074	0.0073			Baroque
203	2	439	58	439-55.FIN2	28.1306	5.2535	0.41	0.057	-0.269		x	Baroque
204	2	439	59	439-56.FIN2	11.8383	1.7431	0.659	0.0541	0.2716			Baroque
205	2	439	60	439-56.FIN2	25.947	3.2422	0.72	0.12	0.58			Baroque
206	2	439	61	439-57.FIN2	13.2149	1.5599	0.751	0.0162	0.2976			Baroque
207	2	439	62	439-58.FIN2	22.594	2.8226	0.754	0.0361	0.2034			Baroque
208	2	439	63	439-59.FIN2	26.8671	3.5986	0.782	0.0232	0.1509			Baroque
209	2	439	64	439-59.FIN2	70.1529	8.3506	0.723	0.0461	-0.137			Baroque
210	2	439	65	439-60.FIN2	10.5229	1.9604	0.75	0.0212	-0.489			Baroque
211	2	439	66	439-61.FIN2	3.9324	0.4427	0.808	0.0331	0.2214			Baroque
212	2	439	67	439-62.FIN2	19.4602	3.2564	0.633	0.0291	-0.073			Baroque
213	2	439	68	439-62.FIN2	4.0444	0.5816	0.812	0.0311	0.1347			Baroque
214	2	439	69	439-63.FIN2	2.3627	0.3229	0.814	0.0143	0.0984			Baroque
215	2	439	70	439-64.FIN2	5.8581	0.6749	0.812	0.0282	-0.189			Baroque
216	2	439	71	439-65.FIN2	9.7972	1.5333	0.722	0.0241	-0.017			Baroque
217	2	439	72	439-66.FIN2	13.8595	2.2152	0.655	0.0521	0.2055			Baroque
218	2	439	73	439-67.FIN2	3.4861	0.9011	0.866	0.0841	-0.108			Baroque

219	2	439	74	439-68.FIN2	8.4183	1.0738	0.75	0.12	0.1583			Baroque
220	2	439	75	439-69.FIN2	10.8236	1.4598	0.759	0.088	0.25			Baroque
221	2	439	76	439-70.FIN2	6.4208	0.8087	0.761	0.0232	0.1952			Baroque
222	2	439	77	439-71.FIN2	2.476	0.3703	0.793	0.0212	0.035			Baroque
223	2	439	78	439-72.FIN2	26.5532	3.1487	0.777	0.0301	-0.333			Baroque
224	2	439	79	439-73.FIN2	12.6275	1.4264	0.698	0.0311	-0.019			Baroque
225	2	439	80	439-74.FIN2	23.4325	2.7473	0.653	0.0421	0.0924			Baroque
226	2	439	81	439-75.FIN2	11.7163	1.3498	0.74	0.11	0.9082			Baroque
227	2	439	82	439-76.FIN2	32.5638	3.4237	0.726	0.0411	0.1553			Baroque
228	2	439	83	439-76.FIN2	59.5014	7.8816	0.77	0.0331	0.3258			Baroque
229	2	439	84	439-77.FIN2	18.0393	2.4897	0.712	0.073	-0.188			Baroque
230	2	439	85	439-78.FIN2	28.2004	3.7528	0.738	0.0381	0.2115			Baroque
231	2	439	86	439-79.FIN2	39.737	4.1095	0.689	0.0261	-0.078			Baroque
232	2	439	87	439-80.FIN2	7.9474	0.6862	0.804	0.0521	0.0935			Baroque
233	2	439	88	439-81.FIN2	4.1326	0.7113	0.799	0.0242	-0.039			Baroque
234	2	439	89	439-82.FIN2	16.8118	1.701	0.772	0.0731	0.4092			Baroque
235	2	480	1	480-01.FIN2	14.0975	1.7884	0.699	0.0661	0.1496			Baroque
236	2	480	2	480-02.FIN2	5.2134	0.5203	0.694	0.0261	0.0871			Baroque
237	2	480	3	480-03.FIN2	10.3294	1.1652	0.8	0.12	0.247			Baroque
238	2	480	4	480-04.FIN2	24.0794	2.9001	0.72	0.11	0.2514			Baroque
239	2	480	5	480-05.FIN2	23.1708	3.3151	0.69	0.13	0.6148			Baroque
240	2	480	6	480-06.FIN2	7.2238	1.1365	0.634	0.092	0.4259			Baroque
241	2	480	7		59.4219	13.7563	0.61	0.16	0.1258			Baroque
242	2	480	8	480-07.FIN2	21.5869	2.0825	0.625	0.065	0.5463			Baroque
243	2	480	9	480-08.FIN2	17.6275	1.2554	0.676	0.0541	0.5673			Baroque
244	2	480	10	480-09.FIN2	20.8537	2.6875	0.67	0.078	-0.031			Baroque
245	2	480	11	480-10.FIN2	6.8225	0.7626	0.667	0.0551	0.6594			Baroque
246	2	480	12	480-11.FIN2	4.5297	0.6891	0.685	0.0521	0.3684			Baroque
247	2	480	13	480-12.FIN2	16.0181	2.1677	0.714	0.086	0.5869			Baroque
248	2	480	14	480-13.FIN2	5.9104	1.1401	0.78	0.11	0.2873			Baroque
249	2	480	15	480-14.FIN2	6.3887	0.5593	0.683	0.082	0.6814			Baroque
250	2	480	16		8.3101	0.6947	0.721	0.0771	0.2668			Baroque
251	2	480	17	480-15.FIN2	14.4477	1.7088	0.76	0.11	0.7801			Baroque
252	2	480	18		25.7633	4.7546	0.8	0.24	0.745			Baroque
253	2	480	19	480-16.FIN2	13.4132	0.878	0.787	0.0601	0.6218			Baroque
254	2	480	20	480-17.FIN2	31.1337	3.354	0.69	0.11	0.777			Baroque
255	2	480	21	480-18.FIN2	8.9133	1.1552	0.844	0.0951	0.734			Baroque
256	2	480	22	480-19.FIN2	28.4125	3.0145	0.54	0.36	0.8813			Baroque
257	2	480	23	480-20.FIN2	43.1737	5.59	0.67	0.14	0.5005			Baroque
258	2	480	24	480-21.FIN2	5.5821	0.5959	0.801	0.0921	0.0255			Baroque
259	2	480	25	480-22.FIN2	14.7366	2.1688	0.68	0.11	0.2831			Baroque
260	2	480	26	480-23.FIN2	13.7298	1.4254	0.82	0.11	0.1126			Baroque
261	2	480	27		8.187	0.7345	0.594	0.063	0.204			Baroque
262	2	480	28	480-24.FIN2	26.0058	3.0149	0.93	0.21	0.6136			Baroque
263	2	480	29	480-25.FIN2	43.859	3.8659	0.577	0.091	0.2084			Baroque
264	2	480	30	480-26.FIN2	40.9351	4.1236	0.707	0.096	0.5342			Baroque
265	2	480	31	480-27.FIN2	24.3984	3.4597	0.78	0.14	0.5739			Baroque
266	2	480	32	480-28.FIN2	14.1698	2.0057	0.67	0.1	0.2387			Baroque
267	2	480	33	480-29.FIN2	33.0912	6.3536	0.587	0.099	-0.091			Baroque
268	2	480	34	480-30.FIN2	28.0519	3.3636	0.7	0.11	0.5612			Baroque
269	2	480	35	480-31.FIN2	16.5704	2.1955	0.87	0.14	0.3134			Baroque
270	2	480	36	480-32.FIN2	3.4324	1.0135	0.86	0.2	0.55			Baroque
271	2	480	37	480-33.FIN2	10.1399	2.6077	1.08	0.29	0.9331			Baroque
272	2	480	38	480-34.FIN2	83.1013	14.4063	0.449	0.044	0.0735			Baroque
273	2	480	39	480-35.FIN2	22.3734	2.0561	0.739	0.085	0.338			Baroque
274	2	480	40	480-36.FIN2	14.5427	2.1123	0.78	0.17	0.5382			Baroque
275	2	480	41		23.5159	3.2647	0.72	0.15	0.1182			Baroque
276	2	480	42	480-37.FIN2	21.0925	3.3909	0.68	0.11	0.2477			Baroque
277	2	480	43	480-38.FIN2	9.9572	1.5298	0.668	0.0251	0.2412			Eqant
278	2	480	44	480-39.FIN2	40.784	3.9441	0.488	0.0221	-0.22			Eqant
279	2	480	45	480-40.FIN2	9.528	1.1557	0.644	0.0142	-0.086			Eqant
280	2	480	46	480-41.FIN2	8.7027	1.1697	0.678	0.0271	0.0823			Eqant
281	2	480	47	480-42.FIN2	5.1647	0.3674	0.678	0.0491	0.015			Eqant
282	2	480	48	480-43.FIN2	23.667	2.4999	0.531	0.046	-0.054			Eqant
283	2	480	49		9.6108	1.0927	0.656	0.0281	0.1538			Eqant
284	2	480	50	480-44.FIN2	9.528	1.5649	0.667	0.0221	0.25			Eqant
285	2	480	51	480-45.FIN2	36.8416	4.0772	0.572	0.0221	-0.074			Eqant
286	2	480	52	480-46.FIN2	9.1343	2.2674	0.612	0.0311	-0.428			Eqant
287	2	480	53	480-47.FIN2	16.4227	2.1081	0.633	0.0251	0.2715			Eqant
288	2	480	54	480-48.FIN2	30.198	2.4207	0.464	0.0301	0.1116			Eqant
289	2	480	55	480-49.FIN2	7.5702	0.9894	0.657	0.0172	0.072			Eqant
290	2	480	56	480-50.FIN2	9.4466	1.2969	0.649	0.0221	0.0462			Eqant
291	2	480	57	480-51.FIN2	3.2797	0.4494	0.687	0.0291	0.0024			Eqant
292	2	480	58		11.513	1.9239	0.669	0.0261	0.1315			Eqant
293	2	480	59	480-52.FIN2	6.6985	0.8564	0.677	0.0172	0.1198			Eqant

294	2	480	60	480-53.FIN2	9.2878	1.1762	0.659	0.0202	-0.233			Eqant
295	2	480	61	480-54.FIN2	13.3807	1.5153	0.637	0.0251	0.1316			Eqant
296	2	480	62	480-55.FIN2	12.1456	1.6084	0.647	0.0152	0.0139			Eqant
297	2	480	63	480-56.FIN2	12.1322	1.3134	0.659	0.0251	0.2549			Eqant
298	2	480	64	480-57.FIN2	14.0796	1.4628	0.637	0.0221	0.0987			Eqant
299	2	480	65	480-58.FIN2	11.7579	1.3833	0.652	0.0172	-0.33			Eqant
300	2	480	66	480-59.FIN2	22.1049	1.7887	0.624	0.0231	-0.151			Eqant
301	2	480	67	480-60.FIN2	23.074	1.6616	0.623	0.0122	-0.096			Eqant
302	2	480	68	480-61.FIN2	12.4746	1.2622	0.652	0.0212	-0.084			Eqant
303	2	480	69	480-62.FIN2	8.1268	0.9612	0.677	0.0271	-0.06			Eqant
304	2	480	70	480-63.FIN2	25.5253	3.668	0.617	0.0221	0.0467			Eqant
305	2	480	71	480-64.FIN2	20.8144	2.8727	0.642	0.0261	-0.158			Eqant
306	2	480	72	480-65.FIN2	12.6894	1.465	0.67	0.0222	0.0695			Eqant
307	2	480	73	480-66.FIN2	80.0903	8.7597	0.456	0.084	-0.174			Eqant
308	2	480	74		6.1403	0.7881	0.708	0.0192	0.0961			Eqant
309	2	480	75	480-67.FIN2	16.8226	2.237	0.663	0.0311	-0.004			Eqant
310	2	480	76	480-68.FIN2	2.2789	0.2739	0.702	0.0232	0.1722			Eqant
311	2	480	77	480-69.FIN2	11.0084	1.0284	0.662	0.0162	-0.268			Eqant
312	2	480	78	480-70.FIN2	16.7462	2.7984	0.642	0.0281	-0.02			Eqant
313	2	480	79	480-71.FIN2	11.2665	1.1338	0.652	0.0202	0.1815			Eqant
314	2	480	80	480-72.FIN2	4.3859	0.7676	0.679	0.0172	-0.058			Eqant
315	2	480	81	480-73.FIN2	14.5427	2.1123	0.668	0.0271	-0.062			Eqant
316	2	480	82	480-74.FIN2	7.6753	0.5937	0.637	0.0431	0.208			Eqant
317	2	480	83		18.9579	2.2232	0.598	0.057	-0.176			Eqant
318	2	480	84	480-75.FIN2	15.6329	2.0651	0.657	0.0361	0.1641			Eqant
319	2	480	85		34.9762	6.2129	0.625	0.0261	0.1713			Eqant
320	2	480	86	480-76.FIN2	16.206	1.675	0.642	0.0241	-0.189			Eqant
321	2	480	87	480-77.FIN2	13.0029	1.6901	0.64	0.0152	-0.289			Eqant
322	2	520	1	520-01.FIN2	6.1403	0.9921	0.829	0.0781	-0.186		x	Eqant
323	2	520	2	520-02.FIN2	13.645	3.3732	1.45	0.77	0.9912		x	Eqant
324	2	520	3	520-03.FIN2	7.0849	0.8672	0.736	0.0701	0.2123			Eqant
325	2	520	4	520-04.FIN2	14.7366	3.3451	1.15	0.45	0.1461		x	Eqant
326	2	520	5	520-05.FIN2	37.3394	7.8342	1.84	0.76	0.1294		x	Eqant
327	2	520	6		18.733	7.6236	0.81	0.37	0.3206		x	Eqant
328	2	520	7	520-06.FIN2	11.91	1.1132	0.81	0.17	0.6668		x	Eqant
329	2	520	8		153.507	57.5951	0.5	0.21	-0.329			Eqant
330	2	520	9	520-07.FIN2	2.2556	0.5991	0.663	0.0461	-0.541			Eqant
331	2	520	10		134.786	37.8413	0.283	0.081	-0.552			Eqant
332	2	520	11	520-08.FIN2	11.8844	4.4749	0.89	0.27	0.0392		x	Eqant
333	2	520	12	520-09.FIN2	18.1188	2.9784	0.67	0.11	-0.072			Eqant
334	2	520	13	520-10.FIN2	10.4269	1.285	0.702	0.075	0.588			Eqant
335	2	520	14	520-11.FIN2	7.5702	0.8347	0.637	0.0411	0.086			Eqant
336	2	520	15	520-12.FIN2	18.1188	3.2747	0.93	0.16	0.0127		x	Eqant
337	2	520	16		31.669	7.4508	0.8	0.51	0.1691		x	Eqant
338	2	520	17	520-13.FIN2	25.5253	5.138	0.567	0.079	0.3161			Eqant
339	2	520	18		124.185	34.9161	0.51	0.17	-0.241			Eqant
340	2	520	19	520-14.FIN2	8.6347	0.8163	0.733	0.0621	0.7816			Eqant
341	2	520	20	520-15.FIN2	10.4269	1.579	0.737	0.0621	0.053			Eqant
342	2	520	21	520-16.FIN2	9.7809	1.8216	-0.04	-0.17	-0.37		x	Eqant
343	2	520	22		16.4962	3.6986	-0.47	-0.16	-0.503		x	Eqant
344	2	520	23	520-17.FIN2	36.0015	5.529	1.07	0.36	0.4932		x	Eqant
345	2	520	24	520-18.FIN2	9.9572	2.1563	1.18	0.27	0.2787		x	Eqant
346	2	520	25	520-19.FIN2	52.8826	5.1012	0.558	0.074	0.3766			Eqant
347	2	520	26	520-20.FIN2	28.0519	4.4274	0.568	0.055	-0.14			Eqant
348	2	520	27	520-21.FIN2	32.6032	4.0587	0.557	0.0221	0.2316			Eqant
349	2	520	28	520-22.FIN2	65.7885	13.7292	0.8	0.32	0.3797		x	Eqant
350	2	520	29	520-23.FIN2	9.3665	1.9084	0.585	0.0281	-0.111			Eqant
351	2	520	30		25.2339	3.987	0.617	0.0251	0.0466			Eqant
352	2	520	31	520-24.FIN2	5.2134	0.618	0.746	0.0212	0.1294			Eqant
353	2	520	32	520-25.FIN2	22.883	3.0448	0.675	0.0431	0.2863			Eqant
354	2	520	33		51.647	13.0475	0.639	0.082	-0.393			Eqant
355	2	520	34	520-26.FIN2	11.3943	2.0017	0.773	0.0511	0.2657			Eqant
356	2	520	35		23.2684	3.2454	0.68	0.14	-0.361			Eqant
357	2	520	36	520-27.FIN2	19.8073	3.4162	0.73	0.1	-0.053			Eqant
358	2	520	37	520-28.FIN2	32.9924	3.7638	0.581	0.0421	0.1602			Transect
359	2	520	38	520-29.FIN2	19.3225	1.305	0.588	0.0064	0.0379			Transect
360	2	520	39	520-30.FIN2	13.7983	1.0981	0.613	0.0341	0.1643			Transect
361	2	520	40		41.0872	6.2822	0.562	0.0411	-0.23			Transect
362	2	520	41	520-31.FIN2	85.678	13.9864	0.543	0.0361	0.0615			Transect
363	2	520	42	520-32.FIN2	26.0058	2.6501	0.562	0.0261	0.0803			Transect
364	2	520	43	520-33.FIN2	68.2251	8.0445	0.455	0.051	-0.186			Transect
365	2	520	44	520-34.FIN2	15.7892	2.4886	0.663	0.0261	-0.016			Transect
366	2	520	45		34.2182	8.3795	0.59	0.12	-0.11			Transect
367	2	520	46	520-35.FIN2	61.4026	7.2024	0.53	0.052	0.0612			Transect
368	2	520	47	520-36.FIN2	26.2529	3.0722	0.511	0.05	-0.102			Transect

369	2	520	48		43.5137	6.7021	0.467	0.043	0.2289				Transect
370	2	520	49	520-37.FIN2	20.2056	3.0021	0.626	0.0301	-0.178				Equant
371	2	520	50	520-38.FIN2	27.7004	2.8662	0.683	0.07	0.0628				Equant
372	2	520	51	520-39.FIN2	52.8826	9.6365	0.67	0.12	0.2928				Equant
373	2	520	52	520-40.FIN2	43.1737	7.6072	0.593	0.062	0.1981				Equant
374	2	520	53	520-41.FIN2	19.9503	3.1783	0.668	0.0371	-0.032				Equant
375	2	520	54	520-42.FIN2	28.2672	1.6979	0.617	0.0122	0.0501				Equant
376	2	520	55	520-43.FIN2	52.8826	8.1223	0.475	0.042	-0.075				Equant
377	2	520	56	520-44.FIN2	12.1456	2.1406	0.615	0.0521	-0.209				Equant
378	2	520	57		32.6996	4.7571	0.573	0.0431	0.22				Equant
379	2	520	58	520-45.FIN2	37.8509	4.8182	0.546	0.0361	0.2504				Equant
380	2	520	59	520-46.FIN2	96.1084	19.2571	0.49	0.063	-0.215				Equant
381	2	540	1	540-01.FIN2	7.5187	1.333	0.661	0.0351	0.1788				Equant
382	2	540	2	540-02.FIN2	4.5297	0.9298	0.681	0.0531	-0.035				Equant
383	2	540	3	540-03.FIN2	7.2238	1.3249	0.71	0.0571	0.355				Equant
384	2	540	4		23.3174	4.191	0.67	0.13	0.1516				Equant
385	2	540	5	540-04.FIN2	9.9572	1.7982	0.656	0.0411	-0.162				Equant
386	2	540	6		43.1737	6.0939	0.74	0.15	0.0309				Equant
387	2	540	7	540-05.FIN2	34.8658	5.9544	0.578	0.0441	-0.063				Equant
388	2	540	8	540-06.FIN2	49.5626	13.5709	0.659	0.0551	-0.018				Equant
389	2	540	9	540-07.FIN2	20.4675	4.5551	0.55	0.0391	-0.241				Equant
390	2	540	10	540-08.FIN2	2.2194	0.3176	0.67	0.0401	0.4939				Equant
391	2	540	11		8.5019	1.6382	0.58	0.079	-0.134				Equant
392	2	540	12	540-09.FIN2	9.7809	2.1672	0.602	0.0341	0.2937				Equant
393	2	540	13	540-10.FIN2	25.2339	5.7693	0.69	0.11	0.1273				Equant
394	2	540	14	540-11.FIN2	75.1869	13.84	0.61	0.14	-0.03				Equant
395	2	540	15	540-12.FIN2	6.6182	0.7967	0.713	0.0501	0.7078				Equant
396	2	540	16	540-13.FIN2	70.8491	9.1239	0.689	0.0601	0.2409				Equant
397	2	540	17	540-14.FIN2	28.0519	6.0614	0.496	0.0281	-0.555				Equant
398	2	540	18		374.66	15.9057	0.135	0.013	0.475				Equant
399	2	540	19		225.101	7.8286	0.313	0.048	-0.727				Equant
400	2	540	20	540-15.FIN2	64.6343	10.9895	0.526	0.0281	-0.052				Equant
401	2	540	21	540-16.FIN2	36.5976	7.6475	0.586	0.0281	0.1232				Equant
402	2	540	22	540-17.FIN2	5.7866	0.9418	0.744	0.0761	0.5712				Baroque
403	2	540	23		32.0361	5.863	0.91	0.25	0.452				Baroque
404	2	540	24	540-18.FIN2	6.5015	0.6929	0.823	0.0621	0.4954				Baroque
405	2	540	25	540-19.FIN2	6.7807	0.9189	0.751	0.0391	0.3422				Baroque
406	2	540	26	540-20.FIN2	21.2547	4.0956	0.703	0.0471	0.0031				Baroque
407	2	540	27	540-21.FIN2	14.3539	2.4296	0.722	0.0192	-0.305				Baroque
408	2	540	28	540-22.FIN2	5.5262	1.1073	0.722	0.0581	0.328				Baroque
409	2	540	29		21.6715	7.6533	0.67	0.0411	-0.126				Baroque
410	2	540	30	540-23.FIN2	10.943	2.7119	0.83	0.21	-0.186				Baroque
411	2	540	31	540-24.FIN2	13.0029	3.0636	0.746	0.0421	-8E-04				Baroque
412	2	540	32	540-25.FIN2	7.2238	1.8435	0.745	0.0381	-0.246				Equant
413	2	540	33		1.417	0.273	0.635	0.0261	0.2941				Equant
414	2	540	34	540-26.FIN2	12.0136	1.7038	0.86	0.17	-0.077				Equant
415	2	540	35		7.0398	0.7225	0.789	0.0651	0.0695				Equant
416	2	540	36	540-27.FIN2	6.6985	0.7756	0.765	0.0681	0.1686				Equant
417	2	540	37	540-28.FIN2	19.4586	2.8191	0.668	0.0501	0.1089				Equant
418	2	540	38		10.0477	1.3756	0.697	0.08	0.499				Equant
419	2	540	39	540-29.FIN2	2.293	0.3342	0.765	0.0202	0.2722				Equant
420	2	540	40	540-30.FIN2	7.5702	0.8862	0.821	0.0731	-0.011				Equant
421	2	540	41	540-31.FIN2	10.4269	1.3829	0.778	0.0461	-0.078				Equant
422	2	540	42	540-32.FIN2	6.352	1.6446	0.696	0.0241	-0.051				Equant
423	2	540	43		1.4737	0.2757	0.766	0.0192	0.0071				Equant
424	2	540	44	540-33.FIN2	8.0675	1.6517	0.719	0.0401	0.4457				Equant
425	2	540	45		4.0634	0.4806	0.77	0.0451	0.1227				Equant
426	2	540	46	540-34.FIN2	61.0634	15.8736	0.627	0.0401	-0.037				Equant
427	2	540	47		18.4208	2.8028	0.709	0.0251	0.3121				Transect
428	2	540	48	540-35.FIN2	5.3653	0.8879	0.673	0.081	-0.013				Transect
429	2	540	49	540-36.FIN2	46.2446	10.2705	0.542	0.09	0.0078				Transect
430	2	540	50	540-37.FIN2	9.4466	1.9412	0.569	0.0421	-0.013				Transect
431	2	540	51	540-38.FIN2	51.4068	11.2551	0.51	0.0371	0.0393				Transect
432	2	540	52	540-39.FIN2	15.5669	2.8565	0.536	0.073	0.1905				Transect
433	2	540	53		218.861	38.2307	0.67	0.12	-0.227				Transect
434	2	540	54	540-40.FIN2	42.6736	13.0266	0.533	0.0321	0.137				Transect
435	2	540	55		4.9122	1.5512	0.532	0.06	0.1265				Transect
436	2	540	56	540-41.FIN2	8.9857	1.2467	0.567	0.056	0.2335				Transect
437	2	540	57		23.566	4.6818	0.601	0.059	-0.035				Transect
438	2	540	58	540-42.FIN2	3.9193	0.6272	0.651	0.0331	-0.049				Transect
439	2	540	59	540-43.FIN2	38.112	4.2309	0.598	0.0291	0.0766				Transect
440	2	540	60	540-44.FIN2	3.9757	1.0165	0.715	0.0511	-0.12				Transect
441	2	540	61		51.1688	13.0439	0.81	0.14	0.3395				Transect
442	2	560	1	560-01.FIN2	25.7633	3.9759	0.97	0.24	0.5934			x	Equant
443	2	560	2	560-02.FIN2	14.9358	4.2424	0.67	0.14	0.3108				Equant

444	2	560	3	560-03.FIN2	5.2631	1.7305	1.06	0.22	0.0801		x	Equant
445	2	560	4	560-04.FIN2	7.3683	0.9865	0.624	0.0341	-0.101			Equant
446	2	560	5	560-05.FIN2	41.395	14.1174	0.59	0.1	-0.056			Equant
447	2	560	6	560-06.FIN2	12.2805	3.5508	1.43	0.38	0.3312		x	Equant
448	2	560	7	560-07.FIN2	9.1343	2.9462	1.81	0.62	0.2515		x	Equant
449	2	560	8	560-08.FIN2	5.4446	1.3962	1.05	0.25	0.3724		x	Equant
450	2	560	9	560-09.FIN2	28.0519	3.4345	0.63	0.12	0.3103			Equant
451	2	560	10	560-10.FIN2	33.4923	3.2731	0.65	0.11	0.1085			Equant
452	2	560	11	560-11.FIN2	10.0477	1.1029	0.787	0.0821	0.2379			Equant
453	2	560	12	560-12.FIN2	15.8345	2.0056	0.541	0.06	0.4562			Equant
454	2	560	13	560-13.FIN2	17.7979	2.5599	0.625	0.0471	0.5657			Equant
455	2	560	14	560-14.FIN2	47.6399	5.5744	0.637	0.093	0.3581			Equant
456	2	560	15	560-15.FIN2	58.1709	7.3818	0.573	0.081	0.2788			Equant
457	2	560	16	560-16.FIN2	13.4622	1.5011	0.606	0.0211	0.0875			Equant
458	2	560	17	560-17.FIN2	14.3725	1.5239	0.653	0.064	0.069			Equant
459	2	560	18		23.82	3.554	0.598	0.0481	0.1618			Equant
460	2	560	19	560-18.FIN2	5.0933	0.427	0.733	0.0401	0.2091			Equant
461	2	560	20	560-19.FIN2	7.5187	0.7219	0.754	0.0331	0.272			Equant
462	2	560	21	560-20.FIN2	9.6951	1.6201	0.617	0.0331	-0.116			Equant
463	2	560	22	560-21.FIN2	13.1421	1.2603	0.669	0.0441	0.1957			Equant
464	2	560	23	560-22.FIN2	5.879	0.785	0.592	0.0301	0.1838			Equant
465	2	560	24		12.8667	1.0897	0.634	0.0401	0.3754			Equant
466	2	560	25	560-23.FIN2	14.0617	1.034	0.691	0.0461	0.4724			Equant
467	2	560	26	560-24.FIN2	5.3914	0.9491	0.748	0.0311	0.049			Equant
468	2	560	27	560-25.FIN2	8.9133	1.1552	0.702	0.0291	-0.657			Equant
469	2	560	28	560-26.FIN2	8.2481	1.5421	0.792	0.0192	0.1866			Equant
470	2	560	29	560-27.FIN2	6.0728	0.6714	0.747	0.0262	-0.261			Equant
471	2	560	30	560-28.FIN2	1.5501	0.134	0.773	0.0163	0.3048			Equant
472	2	560	31	560-29.FIN2	2.4507	0.214	0.784	0.0173	-0.197			Equant
473	2	560	32	560-30.FIN2	3.7981	0.2394	0.77	0.0311	0.7031			Equant
474	2	560	33	560-31.FIN2	5.2134	0.618	0.726	0.0321	0.1221			Equant
475	2	560	34	560-32.FIN2	15.7892	2.9386	0.735	0.0431	-0.036			Equant
476	2	560	35	560-33.FIN2	7.1769	0.7507	0.693	0.0192	0.1363			Equant
477	2	560	36	560-34.FIN2	10.0113	0.8521	0.662	0.0251	0.0839			Equant
478	2	560	37	560-35.FIN2	8.5019	0.8564	0.695	0.0291	0.2587			Equant
479	2	560	38	560-36.FIN2	6.5399	1.2023	0.731	0.0222	0.2627			Equant
480	2	560	39		12.4465	1.187	0.71	0.0222	-0.017			Equant
481	2	560	40	560-37.FIN2	14.1698	2.9117	0.561	0.0461	-0.18			Equant
482	2	560	41	560-38.FIN2	8.6347	1.1516	0.692	0.0401	0.2839			Equant
483	2	560	42		16.4716	1.9252	0.709	0.0481	0.5662			Equant
484	2	560	43	560-39.FIN2	2.535	0.2923	0.747	0.0301	0.3157			Equant
485	2	560	44	560-40.FIN2	19.3903	7.4877	0.604	0.07	-0.088			Equant
486	2	560	45	560-41.FIN2	17.2425	2.5372	0.676	0.0581	0.0112			Equant
487	2	560	46	560-42.FIN2	20.317	1.551	0.566	0.0441	0.4055			Equant
488	2	560	47	560-43.FIN2	6.2798	0.6114	0.649	0.0331	0.2821			Equant
489	2	560	48	560-44.FIN2	7.2238	0.9014	0.624	0.0291	0.1742			Equant
490	2	560	49	560-45.FIN2	5.3137	0.5403	0.614	0.0221	0.2701			Equant
491	2	560	50	560-46.FIN2	9.8683	1.2393	0.582	0.0391	-0.009			Equant
492	2	560	51		369.648	61.977	0.149	0.028	0.4386		x	Equant
493	2	560	52	560-47.FIN2	9.2878	0.6806	0.588	0.0301	0.3555			Equant
494	2	560	53	560-48.FIN2	15.8118	1.7299	0.592	0.0371	-0.106			Equant
495	2	560	54	560-49.FIN2	8.9133	0.9407	0.594	0.0261	0.3747			Equant
496	2	560	55	560-50.FIN2	9.6108	1.259	0.583	0.0321	0.2599			Equant
497	2	560	56	560-51.FIN2	19.056	1.8544	0.583	0.0471	0.1155			Equant
498	2	560	57	560-52.FIN2	9.5775	0.7068	0.662	0.0371	0.4456			Equant
499	2	560	58	560-53.FIN2	11.1641	0.9123	0.611	0.0481	0.2928			Equant
500	2	560	59	560-54.FIN2	32.8942	2.8671	0.501	0.0351	0.0052			Equant
501	2	560	60	560-55.FIN2	29.3169	3.2854	0.585	0.058	0.0698			Equant
502	2	560	61		7.2238	0.62	0.556	0.0431	0.5367			Equant
503	2	560	62	560-56.FIN2	5.6104	0.6019	0.605	0.0191	-0.044			Equant
504	2	560	63	560-57.FIN2	17.0826	1.5454	0.571	0.0311	0.1134			Equant
505	2	560	64		32.4119	5.6217	0.524	0.053	-0.144			Equant
506	2	560	65	560-58.FIN2	39.3326	4.6438	0.397	0.044	0.2369			Equant
507	2	560	66	560-59.FIN2	34.6472	3.501	0.465	0.0311	-0.08			Equant
508	2	560	67	560-60.FIN2	14.5046	1.8927	0.643	0.0371	0.2038			Equant
509	2	560	68		41.395	8.5419	0.54	0.1	0.1204			Equant
510	2	560	69	560-61.FIN2	22.4188	2.0193	0.523	0.057	0.2063			Equant
511	2	560	70		50.4679	6.2522	0.385	0.063	-0.043			Equant
512	4	231	1	231-1.FIN2	37.2616	3.8623	0.597	0.057	0.2564			Equant
513	4	231	2	231-2.FIN2	31.0513	2.458	0.668	0.0411	0.1781			Equant
514	4	231	3	231-3.FIN2	35.4043	2.9566	0.668	0.0491	0.3801			Equant
515	4	231	4	231-4.FIN2	34.2312	1.886	0.628	0.0381	0.5336			Equant
516	4	231	5	231-5.FIN2	25.6541	2.318	0.673	0.0321	0.2371			Equant
517	4	231	6	231-6.FIN2	31.1364	2.143	0.609	0.0381	0.2574			Equant
518	4	231	7	231-7.FIN2	12.0773	0.5233	0.769	0.0242	0.4231			Equant

519	4	231	8	231-8.FIN2	29.9073	1.328	0.688	0.0351	0.0847			Equant
520	4	231	9	231-9.FIN2	32.7515	1.8248	0.664	0.0411	0.2547			Equant
521	4	231	10	231-10.FIN2	75.7652	13.2227	0.66	0.24	0.0265		x	Equant
522	4	231	11	231-11.FIN2	70.5886	7.1604	0.495	0.074	0.2309			Equant
523	4	231	12	231-12.FIN2	44.3936	5.2801	0.594	0.058	0.3685			Equant
524	4	231	13	231-13.FIN2	31.9235	2.0769	0.632	0.0421	0.5303			Equant
525	4	231	14	231-13.FIN2	50.5101	3.0938	0.579	0.085	0.0681			Equant
526	4	231	15	231-14.FIN2	35.0765	2.1771	0.592	0.0421	0.3781			Equant
527	4	231	16	231-15.FIN2	23.9258	1.8289	0.719	0.0271	0.0797			Equant
528	4	231	17	231-16.FIN2	31.7452	2.0549	0.689	0.0281	0.1611			Equant
529	4	231	18	231-17.FIN2	44.3936	3.0831	0.614	0.052	0.3281			Equant
530	4	231	19	231-18.FIN2	56.5412	3.566	0.553	0.053	0.116			Equant
531	4	231	20	231-19.FIN2	55.1688	5.4724	0.462	0.046	0.4349			Equant
532	4	231	21	231-20.FIN2	22.7751	1.4454	0.736	0.072	0.291			Equant
533	4	231	22	231-21.FIN2	107.723	7.6711	0.306	0.077	-0.081			Equant
534	4	231	23	231-22.FIN2	43.5432	2.8123	0.641	0.082	0.159			Equant
535	4	231	24	231-23.FIN2	28.918	1.7223	0.692	0.0281	0.231			Equant
536	4	231	25	231-24.FIN2	47.7511	3.1623	0.606	0.0461	0.2082			Equant
537	4	231	26	231-25.FIN2	37.1398	3.4813	0.587	0.0321	0.2515			Equant
538	4	231	27	231-26.FIN2	25.829	2.6933	0.683	0.0461	0.1916			Equant
539	4	231	28	231-27.FIN2	15.3786	1.3883	0.735	0.0212	0.0017			Equant
540	4	231	29	231-28.FIN2	22.9128	1.8609	0.662	0.0201	0.2498		x	Equant
541	4	231	30	231-29.FIN2	28.1306	2.3004	0.696	0.0212	0.2549			Equant
542	4	231	31	231-30.FIN2	11.7163	0.5065	0.781	0.0104	-0.092			Equant
543	4	231	32	231-31.FIN2	18.6921	1.6432	0.752	0.0123	-0.031			Equant
544	4	231	33	231-32.FIN2	11.5378	0.6418	0.795	0.0101	0.1237			Equant
545	4	231	34	231-33.FIN2	8.7895	0.3661	0.778	0.0114	0.3728			Equant
546	4	231	35	231-34.FIN2	27.3192	3.3302	0.677	0.0411	-0.223			Equant
547	4	231	36	231-35.FIN2	35.7383	2.6851	0.617	0.0291	0.0109			Equant
548	4	231	37	231-36.FIN2	22.5045	1.0819	0.726	0.0182	0.3951			Equant
549	4	231	38	231-37.FIN2	23.2408	1.323	0.713	0.0281	0.5235			Equant
550	4	231	39	231-38.FIN2	29.1404	2.2464	0.678	0.0251	-0.007			Equant
551	4	231	40	231-39.FIN2	16.5186	1.0629	0.705	0.0192	0.3226		x	Equant
552	4	231	41	231-39.FIN2	23.6274	1.5034	0.689	0.0182	0.3255			Equant
553	4	231	42	231-40.FIN2	25.7121	2.898	0.657	0.0251	-0.087			Equant
554	4	231	43	231-41.FIN2	13.9274	0.9154	0.756	0.0172	-0.198			Equant
555	4	231	44	231-42.FIN2	12.8706	1.2948	0.723	0.0281	-0.019		x	Equant
556	4	231	45	231-42.FIN2	19.7305	1.6925	0.698	0.0202	0.3856			Equant
557	4	231	46	231-43.FIN2	21.1634	1.9016	0.719	0.0231	0.3007			Equant
558	4	231	47	231-44.FIN2	19.1649	1.1355	0.727	0.0241	0.2519			Equant
559	4	231	48	231-45.FIN2	30.8825	2.1097	0.682	0.0221	0.505			Equant
560	4	231	49	231-46.FIN2	22.2403	1.5474	0.717	0.0222	0.0862			Equant
561	4	231	50	231-47.FIN2	16.4231	0.8953	0.738	0.0241	0.1708			Equant
562	4	231	51	231-48.FIN2	9.0197	1.4434	0.742	0.0202	-0.234		x	Equant
563	4	231	52	231-49.FIN2	14.5702	2.8176	0.743	0.0232	-0.399			Equant
564	4	231	53	231-50.FIN2	27.3192	1.4868	0.673	0.0221	0.3527			Equant
565	4	231	54	231-51.FIN2	24.8682	2.2877	0.684	0.0162	-0.129			Equant
566	4	231	55	231-52.FIN2	24.5991	1.8782	0.689	0.0231	0.2747			Equant
567	4	231	56	231-53.FIN2	20.7386	1.2823	0.733	0.0172	-0.139			Equant
568	4	231	57	231-54.FIN2	19.4936	1.2673	0.717	0.0182	0.1904			Equant
569	4	231	58	231-55.FIN2	47.7511	4.7157	0.549	0.045	0.4547			Equant
570	4	231	59	231-55.FIN2	21.9822	1.7585	0.707	0.0281	0.2555			Equant
571	4	231	60	231-56.FIN2	38.9205	2.5264	0.611	0.0291	0.2553			Equant
572	4	231	61	231-57.FIN2	44.7432	6.058	0.577	0.085	0.0583			Baroque
573	4	231	62	231-58.FIN2	25.4245	1.4597	0.674	0.0231	0.366			Baroque
574	4	231	63	231-59.FIN2	11.1748	0.76	0.767	0.0212	0.1873			Baroque
575	4	231	64	231-60.FIN2	29.8288	2.3501	0.651	0.0291	-0.012			Baroque
576	4	231	65	231-61.FIN2	10.4938	0.9072	0.768	0.0222	0.3041			Baroque
577	4	231	66	231-62.FIN2	24.1804	1.966	0.678	0.0411	0.1616			Baroque
578	4	231	67	231-63.FIN2	63.847	4.1537	0.467	0.038	0.2882			Baroque
579	4	231	68	231-64.FIN2	21.5242	1.2989	0.68	0.0152	0.1313			Baroque
580	4	231	69	231-65.FIN2	23.4809	1.1251	0.703	0.0202	-0.067			Baroque
581	4	231	70	231-66.FIN2	34.2312	2.079	0.619	0.0271	0.1336			Baroque
582	4	231	71	231-67.FIN2	18.2128	1.619	0.71	0.0301	0.313			Baroque
583	4	231	72	231-67.FIN2	27.7867	1.4091	0.665	0.0251	0.4115			Baroque
584	4	231	73	231-68.FIN2	24.5991	1.422	0.679	0.0162	0.1245			Baroque
585	4	231	74	231-69.FIN2	36.1935	1.6695	0.603	0.0261	0.2159			Baroque
586	4	231	75	231-70.FIN2	34.5434	1.9182	0.659	0.0221	0.3598			Baroque
587	4	231	76	231-71.FIN2	17.0899	1.8322	0.677	0.0301	0.1783		x	Baroque
588	4	231	77	231-72.FIN2	28.1306	2.5711	0.677	0.0391	0.315			Baroque
589	4	231	78	231-73.FIN2	9.7804	0.7751	0.788	0.0114	-0.238			Equant
590	4	231	79	231-74.FIN2	8.7287	0.6033	0.79	0.0104	0.0666			Equant
591	4	231	80	231-75.FIN2	16.3522	0.9539	0.762	0.0123	-0.079			Equant
592	4	231	81	231-76.FIN2	8.3688	0.6393	0.79	0.0123	0.0151			Equant
593	4	231	82	231-77.FIN2	23.2408	1.7751	0.706	0.0152	-0.002			Equant

594	4	231	83	231-78.FIN2	26.4297	1.8617	0.726	0.0182	-0.019		x	Equant
595	4	231	84	231-79.FIN2	35.2943	3.1519	0.717	0.0192	0.3256		x	Equant
596	4	231	85	231-80.FIN2	21.606	1.2697	0.723	0.0241	0.0848			Equant
597	4	231	86	231-80.FIN2	14.4959	0.9527	0.759	0.0143	-0.058			Equant
598	4	231	87	231-81.FIN2	15.4413	1.095	0.773	0.0114	0.0659			Equant
599	4	231	88	231-82.FIN2	33.4258	1.6238	0.661	0.0241	0.1288			Equant
600	4	231	89	231-82.FIN2	27.719	1.2198	0.723	0.0401	0.7135			Equant
601	4	231	90	231-83.FIN2	81.1769	6.5883	0.377	0.063	-0.086			Equant
602	4	231	91	231-83.FIN2	51.8939	4.1642	0.548	0.04	0.2043			Equant
603	4	231	92	231-84.FIN2	32.5638	2.0683	0.657	0.0391	0.5695			Equant
604	4	231	93	231-84.FIN2	22.2839	1.1826	0.718	0.0222	0.3445			Equant
605	4	231	94	231-85.FIN2	20.2942	1.3338	0.741	0.0192	0.2068			Equant
606	4	231	95	231-86.FIN2	26.3073	1.1115	0.689	0.0301	0.25			Equant
607	4	231	96	231-87.FIN2	17.1673	0.9242	0.723	0.0142	0.0363			Equant
608	4	231	97	231-88.FIN2	16.2819	0.7323	0.715	0.0142	0.4036			Equant
609	4	338	1	338-01.FIN2	0.1273	0.0033	0.843	0.0077	0.5216			Equant
610	4	338	2	338-02.FIN2	0.1249	0.0037	0.854	0.01	0.5697			Equant
611	4	338	3	338-03.FIN2	0.1175	0.0033	0.847	0.0085	0.5924			Equant
612	4	338	4	338-04.FIN2	0.134	0.0033	0.849	0.0067	0.6298			Equant
613	4	338	5	338-05.FIN2	0.1167	0.0034	0.845	0.0094	0.5755			Equant
614	4	338	6	338-06.FIN2	4.2347	0.4572	0.734	0.0114	0.2282			Equant
615	4	338	7	338-07.FIN2	20.8537	2.0226	0.726	0.0212	0.408			Equant
616	4	338	8	338-08.FIN2	11.9875	1.1018	0.693	0.0202	0.1322			Equant
617	4	338	9		25.5844	3.508	0.659	0.0212	-0.168			Equant
618	4	338	10	338-09.FIN2	19.9503	1.4607	0.724	0.0123	0.1455			Equant
619	4	338	11	338-10.FIN2	17.6839	1.627	0.689	0.0162	0.126			Equant
620	4	338	12	338-11.FIN2	36.0015	2.2706	0.581	0.0191	0.1166			Equant
621	4	338	13	338-12.FIN2	34.2182	3.3103	0.628	0.0251	0.0075			Equant
622	4	338	14	338-13.FIN2	25.3497	2.2307	0.611	0.0201	-0.561			Equant
623	4	338	15	338-14.FIN2	27.4937	1.6751	0.612	0.0201	0.3426			Equant
624	4	338	16	338-15.FIN2	20.7753	2.512	0.685	0.0222	0.1051			Equant
625	4	338	17	338-16.FIN2	27.29	1.7831	0.625	0.0172	0.1352			Equant
626	4	338	18	338-17.FIN2	8.9133	1.2268	0.704	0.0291	-0.01			Equant
627	4	338	19		29.791	3.3919	0.657	0.0441	-0.24			Equant
628	4	338	20	338-18.FIN2	19.9864	1.0056	0.662	0.0221	0.4183			Equant
629	4	338	21	338-19.FIN2	15.2448	0.8407	0.718	0.0162	0.1121			Equant
630	4	338	22	338-20.FIN2	9.9752	0.5976	0.727	0.0172	0.212			Equant
631	4	338	23	338-21.FIN2	10.5262	0.6248	0.731	0.0162	0.0767			Equant
632	4	338	24	338-22.FIN2	16.3498	1.0113	0.651	0.0192	0.457			Equant
633	4	338	25	338-23.FIN2	22.8357	1.3499	0.649	0.0192	0.0703			Equant
634	4	338	26	338-24.FIN2	5.1647	0.4867	0.705	0.0182	-0.001			Equant
635	4	338	27	338-25.FIN2	26.1907	2.626	0.635	0.0201	-0.22			Equant
636	4	338	28	338-26.FIN2	30.2807	2.6801	0.569	0.0251	0.155			Equant
637	6	92	1	92-1.FIN2	22.4157	1.6556	0.576	0.0231	-0.224			Equant
638	6	92	2	92-2.FIN2	64.5726	2.8518	0.344	0.021	0.2258			Equant
639	6	92	3	92-3.FIN2	19.7648	3.1878	0.497	0.043	0.1698			Equant
640	6	92	4	92-4.FIN2	35.9645	2.6085	0.498	0.046	0.2198			Equant
641	6	92	5	92-5.FIN2	9.9256	0.6725	0.657	0.0191	-0.014			Equant
642	6	92	6	92-5.FIN2	18.4793	1.0604	0.594	0.0241	0.1394			Equant
643	6	92	7	92-6.FIN2	38.2652	2.2034	0.48	0.0231	0.4529			Equant
644	6	92	8	92-7.FIN2	21.8553	1.8203	0.538	0.0191	-0.036			Equant
645	6	92	9	92-8.FIN2	52.3722	4.943	0.417	0.023	0.0269			Equant
646	6	92	10	92-9.FIN2	38.9205	3.9456	0.437	0.047	0.5731			Equant
647	6	92	11	92-10.FIN2	34.8613	2.973	0.493	0.0191	-0.279			Equant
648	6	92	12	92-11.FIN2	41.4773	2.7081	0.505	0.0321	0.0724			Equant
649	6	92	13	92-12.FIN2	27.719	2.5642	0.5	0.043	0.1368			Equant
650	6	92	14	92-13.FIN2	19.1005	1.7452	0.547	0.041	0.1644			Equant
651	6	92	15	92-14.FIN2	25.7121	1.3288	0.531	0.0201	-0.142			Equant
652	6	92	16	92-15.FIN2	55.7097	3.7265	0.41	0.0171	-0.502			Equant
653	6	92	17	92-16.FIN2	31.6567	3.5855	0.508	0.0241	-0.166			Equant
654	6	92	18	92-17.FIN2	41.0281	3.0776	0.441	0.0181	-0.158			Equant
655	6	92	19	92-18.FIN2	42.8859	2.5794	0.482	0.053	-0.134			Equant
656	6	92	20	92-18.FIN2	59.5014	3.9292	0.435	0.078	0.5151			Equant
657	6	92	21	92-19.FIN2	51.6581	3.901	0.424	0.028	-0.177			Equant
658	6	92	22	92-20.FIN2	29.9862	2.6042	0.493	0.0201	-0.098			Equant
659	6	92	23	92-21.FIN2	18.5094	1.1202	0.574	0.0171	-0.079			Equant
660	6	92	24	92-22.FIN2	39.0542	2.9281	0.586	0.049	0.2447			Equant
661	6	92	25	92-23.FIN2	42.2482	2.6557	0.506	0.037	0.1151			Equant
662	6	92	26	92-24.FIN2	56.2612	4.3316	0.375	0.028	0.0145			Equant
663	6	92	27	92-25.FIN2	35.7383	3.5589	0.565	0.0261	0.3313			Equant
664	6	92	28	92-26.FIN2	31.3079	2.4141	0.548	0.0381	-0.061			Equant
665	6	92	29	92-27.FIN2	61.7651	6.8301	0.335	0.036	0.1188			Equant
666	6	92	30	92-28.FIN2	51.8939	3.4812	0.503	0.0241	0.0536			Equant
667	6	92	31	92-29.FIN2	17.8411	1.1244	0.622	0.0122	0.18			Equant
668	6	92	32	92-30.FIN2	42.4059	4.0487	0.507	0.0201	0.1068			Equant

669	6	92	33	92-31.FIN2	34.1284	3.3522	0.558	0.0321	0.0765			Equant
670	6	92	34	92-32.FIN2	40.3006	3.9446	0.479	0.0251	-0.246			Equant
671	6	92	35	92-33.FIN2	61.1009	4.7639	0.439	0.033	0.1275			Equant
672	6	92	36	92-34.FIN2	63.847	5.1868	0.482	0.0201	0.0174			Equant
673	6	92	37	92-35.FIN2	55.4379	4.7335	0.438	0.034	0.2019			Equant
674	6	92	38	92-36.FIN2	29.3663	2.1341	0.57	0.0361	0.2897			Equant
675	6	92	39	92-37.FIN2	25.4815	2.7348	0.608	0.0301	0.1378			Equant
676	6	92	40	92-38.FIN2	44.92	4.5318	0.494	0.034	-0.062			Equant
677	6	92	41	92-39.FIN2	38.3945	3.5882	0.578	0.0191	-0.07			Equant
678	6	92	42	92-40.FIN2	45.278	4.074	0.545	0.0201	-0.232			Equant
679	6	92	43	92-41.FIN2	47.5513	4.2886	0.528	0.0241	0.0107			Equant
680	6	92	44	92-42.FIN2	40.1582	3.2269	0.527	0.0231	0.4827			Equant
681	6	92	45	92-43.FIN2	19.6283	1.5114	0.609	0.0181	-0.077			Equant
682	6	92	46	92-44.FIN2	35.6262	3.1012	0.497	0.0281	0.2375			Equant
683	6	92	47	92-45.FIN2	38.6557	2.6189	0.593	0.089	-0.087			Baroque
684	6	92	48	92-45.FIN2	52.8594	4.0779	0.513	0.059	0.4416			Baroque
685	6	92	49	92-46.FIN2	62.1026	4.5889	0.47	0.068	0.2425			Baroque
686	6	92	50	92-47.FIN2	64.9416	7.1734	0.363	0.055	0.5329			Baroque
687	6	92	51	92-48.FIN2	43.2121	2.7718	0.467	0.032	0.1976			Baroque
688	6	92	52	92-49.FIN2	88.718	7.1568	0.252	0.052	0.2604			Baroque
689	6	92	53	92-50.FIN2	72.6648	3.9136	0.337	0.044	0.1784			Baroque
690	6	92	54	92-51.FIN2	71.9289	6.0963	0.397	0.066	0.0057			Baroque
691	6	92	55	92-51.FIN2	93.9237	8.7495	0.247	0.063	0.0448			Baroque
692	6	92	56	92-52.FIN2	46.3868	2.9926	0.529	0.054	0.1917			Baroque
693	6	92	57	92-53.FIN2	62.8235	3.7004	0.44	0.04	0.2496			Baroque
694	6	92	58	92-54.FIN2	72.3871	5.7252	0.418	0.079	0.0368			Baroque
695	6	92	59	92-55.FIN2	101.744	5.8437	0.219	0.026	0.0351			Baroque
696	6	92	60	92-56.FIN2	14.7212	1.109	0.659	0.0261	0.1662			Baroque
697	6	92	61	92-57.FIN2	28.3411	1.4613	0.556	0.0261	0.1867			Baroque
698	6	92	62	92-58.FIN2	84.4964	6.2106	0.31	0.058	0.3207			Baroque
699	6	92	63	92-59.FIN2	54.6383	5.3699	0.456	0.055	0.193			Baroque
700	6	92	64	92-60.FIN2	20.4035	1.5581	0.623	0.052	0.3424			Baroque
701	6	92	65	92-61.FIN2	27.8548	2.6554	0.55	0.0311	0.2509			Baroque
702	6	92	66	92-62.FIN2	77.1016	5.4607	0.43	0.1	0.1285			Baroque
703	6	92	67	92-63.FIN2	53.6074	5.1735	0.397	0.045	0.5705			Baroque
704	6	92	68	92-64.FIN2	32.6574	2.3481	0.581	0.05	0.4066			Baroque
705	6	92	69	92-65.FIN2	35.851	2.4844	0.564	0.0411	0.4397			Baroque
706	6	92	70	92-66.FIN2	20.9296	2.2757	0.652	0.076	0.3139			Baroque
707	6	92	71	92-67.FIN2	68.0525	4.6913	0.43	0.075	0.1278			Baroque
708	6	92	72	92-68.FIN2	63.847	4.4958	0.401	0.036	0.2609			Baroque
709	6	92	73	92-69.FIN2	69.2974	5.671	0.366	0.039	0.134			Baroque
710	6	92	74	92-70.FIN2	59.1915	3.5985	0.424	0.056	0.3314			Baroque
711	6	92	75	92-71.FIN2	56.5412	3.8334	0.5	0.046	0.6738			Baroque
712	6	92	76	92-72.FIN2	43.8794	2.2202	0.496	0.0291	0.4146			Baroque
713	6	92	77	92-72.FIN2	59.5014	6.0414	0.417	0.05	0.8281			Baroque
714	6	92	78	92-73.FIN2	60.4509	4.9774	0.43	0.045	0.3425			Baroque
715	6	92	79	92-74.FIN2	42.0918	3.5349	0.457	0.038	-0.19			Baroque
716	6	92	80	92-75.FIN2	76.582	3.374	0.316	0.032	-0.118			Baroque
717	6	92	81	92-76.FIN2	59.8146	4.5722	0.491	0.061	0.0786			Baroque
718	6	92	82	92-77.FIN2	55.4379	5.2604	0.417	0.045	0.0976			Baroque
719	6	92	83	92-78.FIN2	58.5813	4.6835	0.414	0.045	0.1313			Baroque
720	6	92	84	92-79.FIN2	63.4903	4.7884	0.42	0.062	0.4528			Baroque
721	6	92	85	92-80.FIN2	39.0542	2.5429	0.551	0.042	0.0837			Baroque

Continued Appendix C:

Comments on the use of internal uncertainties

In this study, we relied on internal uncertainties when reporting the ages of the different samples, as this practice would provide a better relative comparison between the results. Total (propagated) uncertainties were reported in Tables 2.4 and 3.3, as well as the Tera-Wasserburg plots to follow. As summarized by Roberts et al., 2020, reporting total uncertainty is essential to provide an absolute age value to a specific sample and to better compare results between different laboratories. Roberts et al. (2020) stated *"However, it should be noted that through this practice* **[i.e., reporting internal uncertainties]** *results can only be compared in a relative sense within session or between sessions if validation materials are compiled and used. To compare data in an absolute sense, i.e. to assign an age and total uncertainty to a material for comparison between laboratories and/or with other methods, the uncertainty from the primary reference material must be included to reflect the accuracy with which the matrix-matched normalisation is known. In this way, the uncertainty of the primary reference material constitutes a limiting uncertainty in any sample age."*. The limiting uncertainty caused by the reference material would, thus, always lead to lower precision in dating the unknowns.

The legend below is an excerpt from Isoplot R (http://isoplotr.geo.utexas.edu/) (Vermeesch. 2018) that is used for the Tera-Wasserburg plots to follow.

Legend:

1. **age = τ ± x | y | z**
   $(^{207}Pb/^{206}Pb)_o = \tau \pm x \mid y \mid z$
   where:
   - τ: the Maximum Likelihood estimate of the age or initial Pb-ratio using the algorithm of Ludwig (1998).
   - x: the analytical uncertainty (σ) of τ.
   - y: the 100(1-α)% confidence interval for τ.
   - z: the studentized 100(1-α)% confidence interval for τ with overdispersion, calculated as $z = t\ y\ \sqrt{MSWD}$, where t is the 1-α/2 quantile of a t-distribution with the appropriate degrees of freedom (only reported if the p-value for the chi-square test is < α)
2. **MSWD = u, p(χ^2)**
   where:
   - u: the Mean Square of the Weighted Deviates (MSWD) for the isochron fit.
   - v: the chi-squared p-value for the isochron fit

Well 1 Sample 364 Multiple Phases

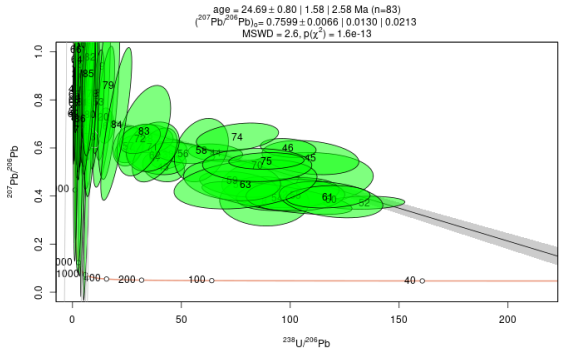

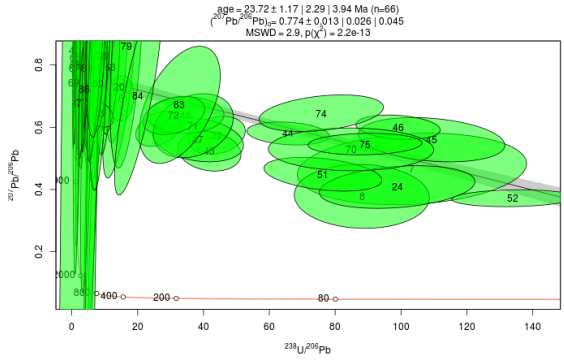

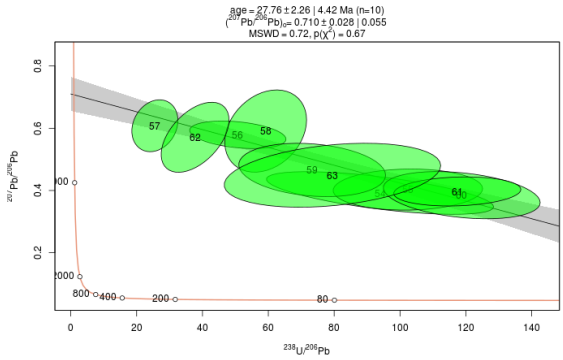

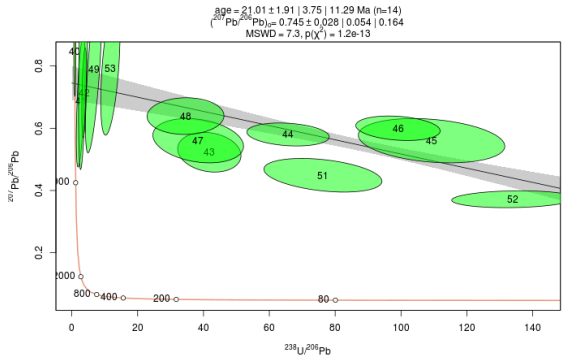

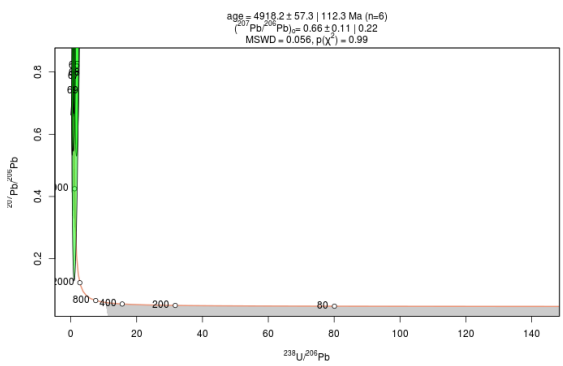

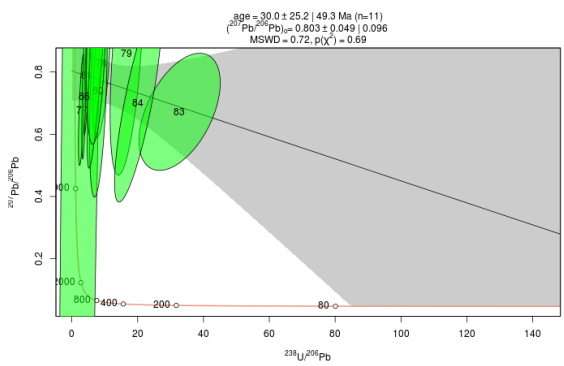

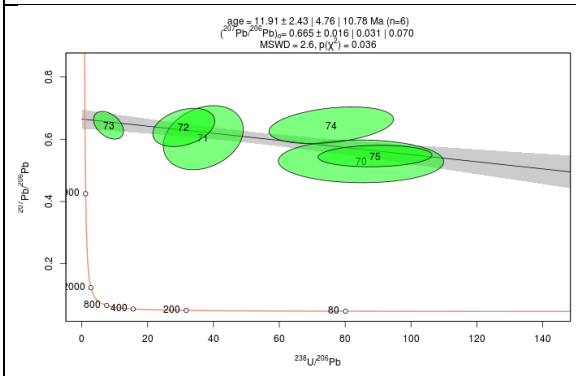

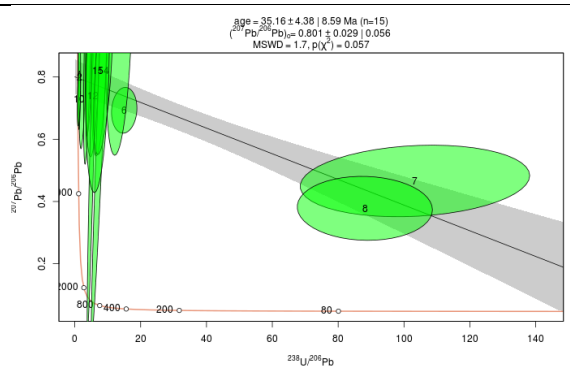

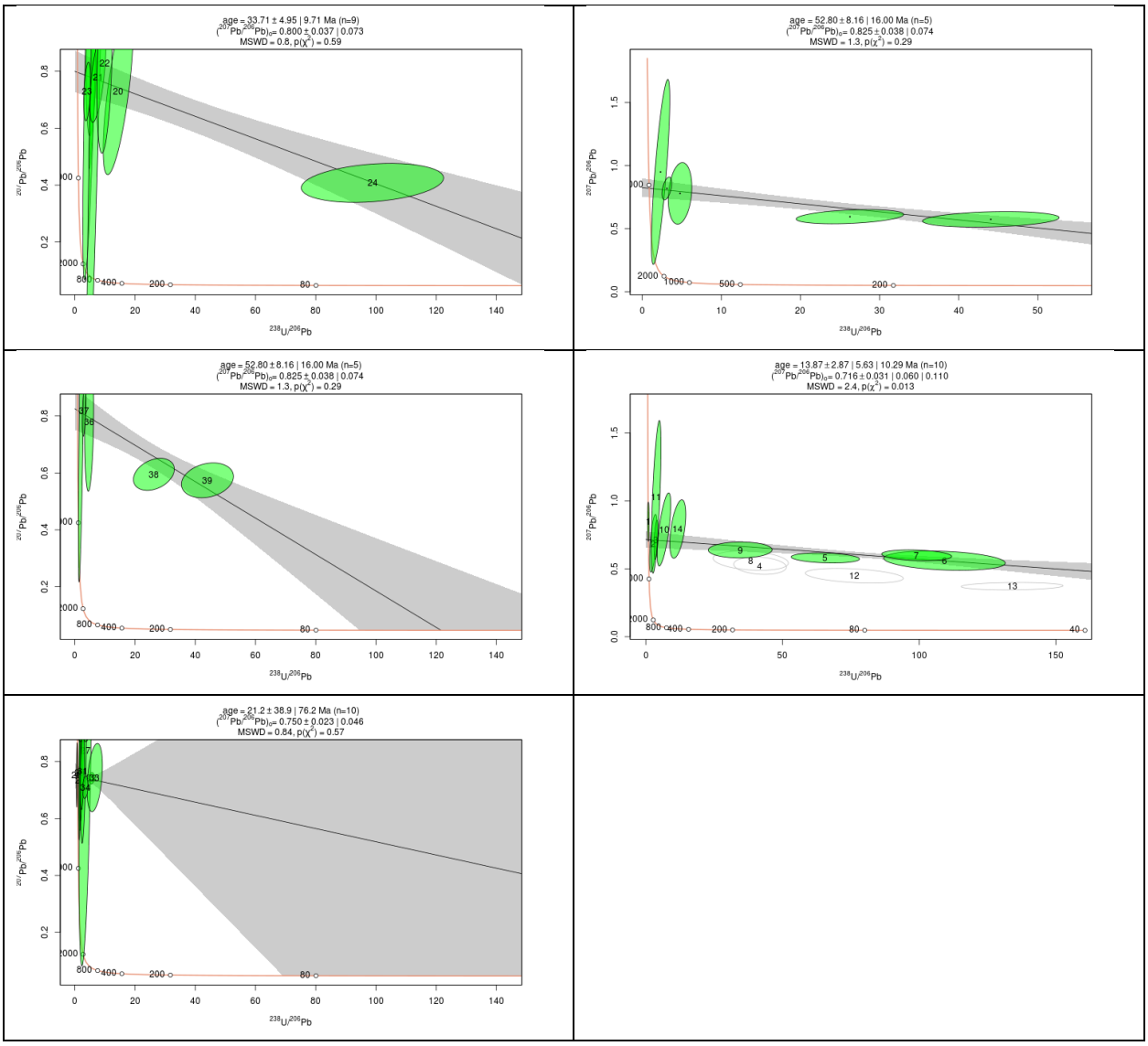
age = 33.71 ± 4.95 | 9.71 Ma (n=9)
MSWD = 0.8, p(χ²) = 0.59
age = 52.80 ± 8.16 | 16.00 Ma (n=5)
MSWD = 1.3, p(χ²) = 0.29
age = 52.80 ± 8.16 | 16.00 Ma (n=5)
MSWD = 1.3, p(χ²) = 0.29
age = 13.87 ± 2.87 | 5.63 | 10.29 Ma (n=10)
MSWD = 2.4, p(χ²) = 0.013
age = 21.2 ± 38.9 | 76.2 Ma (n=10)
MSWD = 0.84, p(χ²) = 0.57

Well 2 Sample 414 Limestone

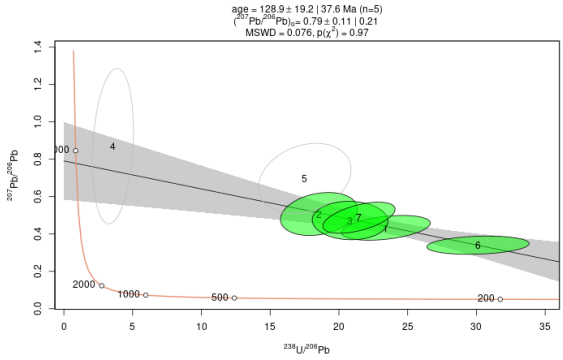

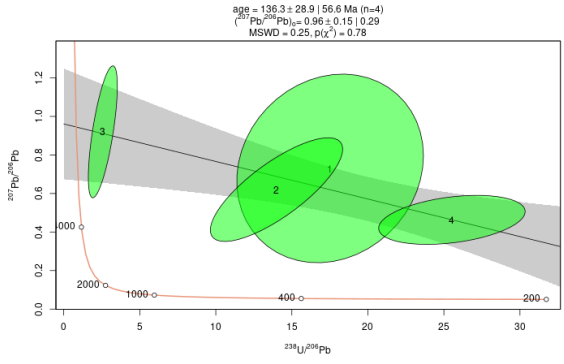

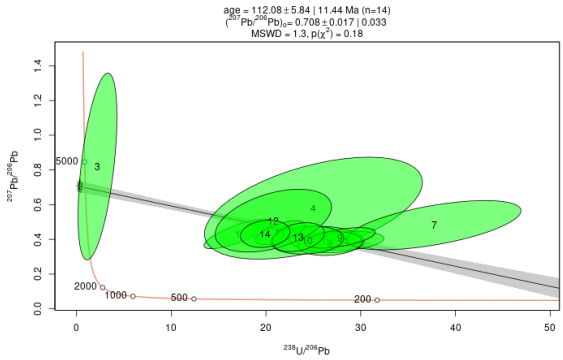

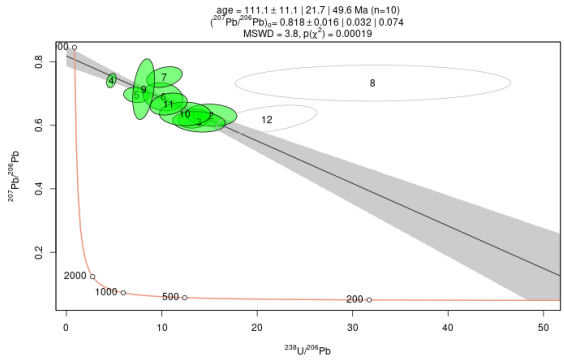

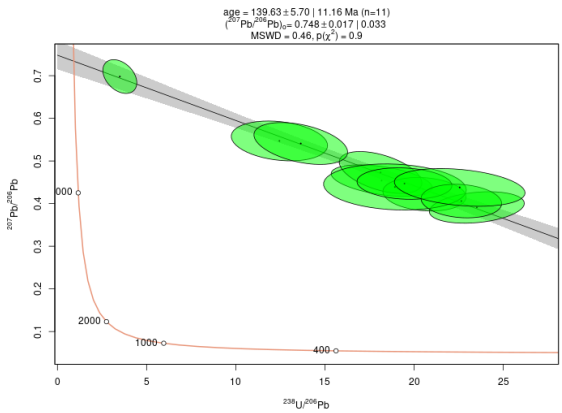

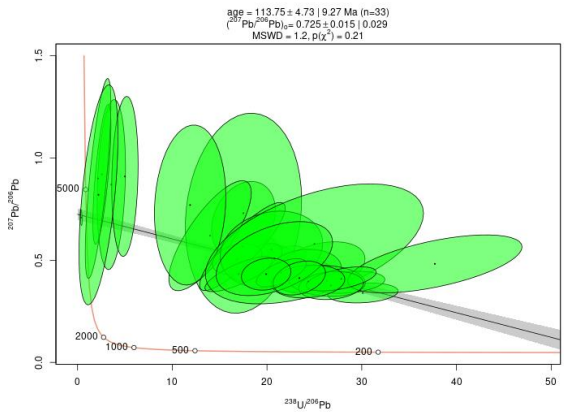

Well 2 Sample 439 Multiple Phases

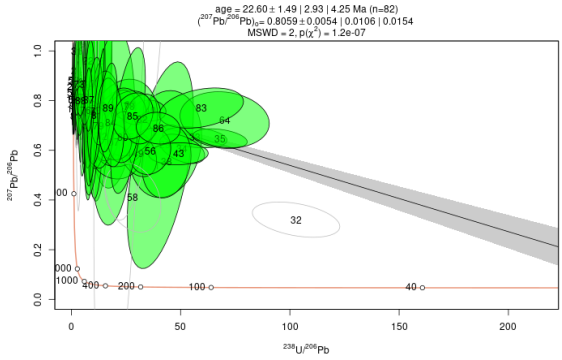

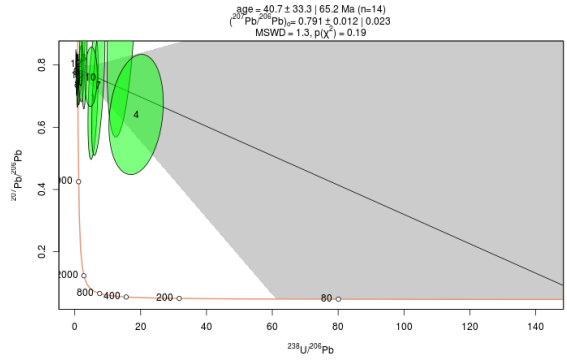

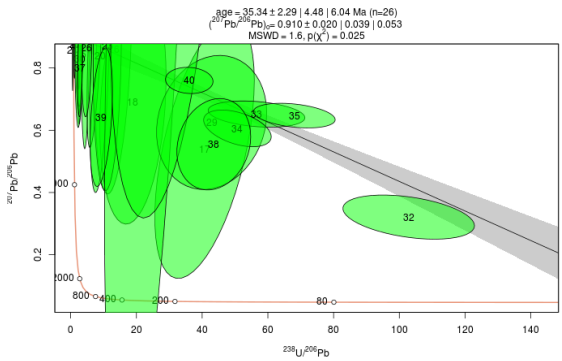

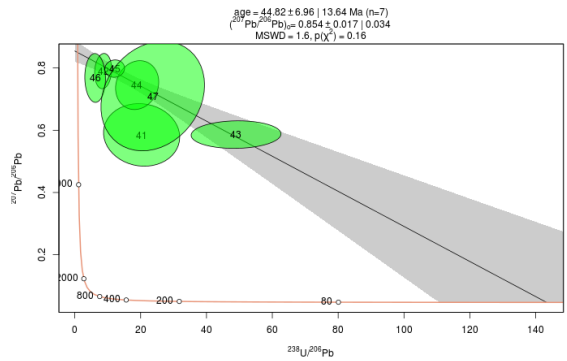

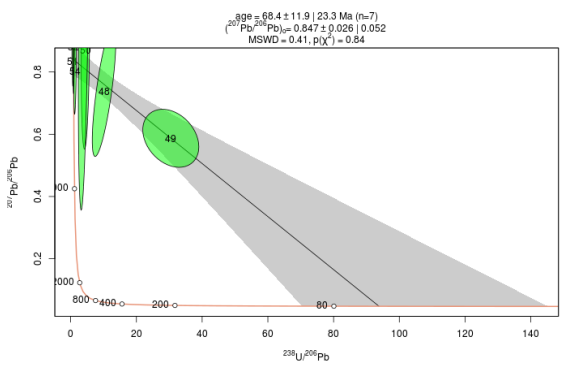

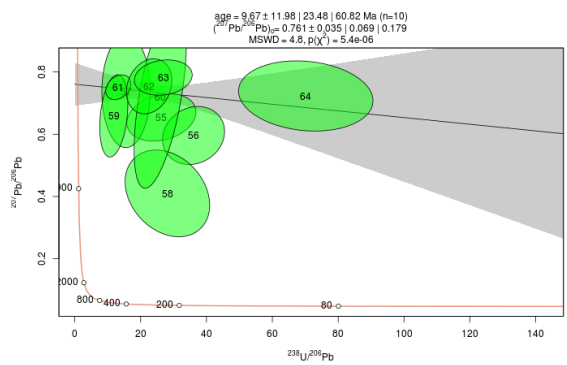

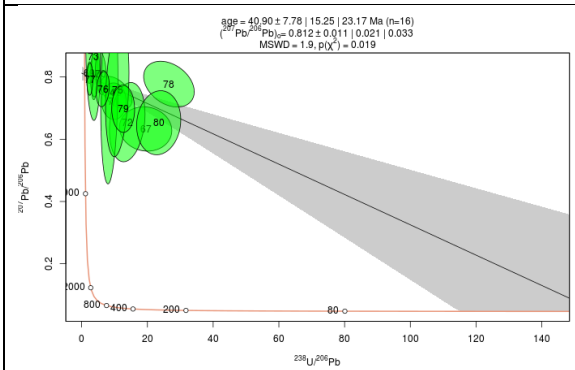

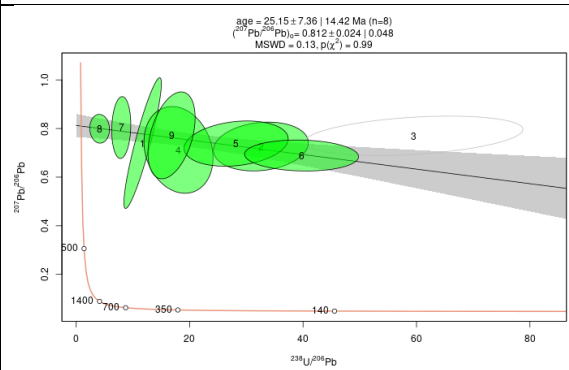

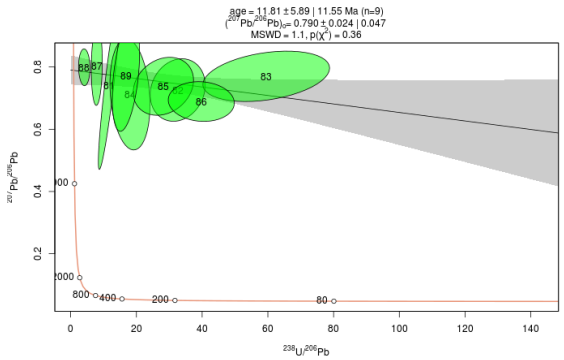
age = 11.81 ±5.89 | 11.55 Ma (n=9)
(207Pb/206Pb)i= 0.790 ± 0.024 | 0.047
MSWD = 1.1, p(χ2) = 0.36
88
87
89
85
86
83
1000
800
400
200
80
0.2
0.4
0.6
0.8
0
20
40
60
80
100
120
140
207Pb/206Pb
238U/206Pb

Well 2 Sample 480 Multiple Phases

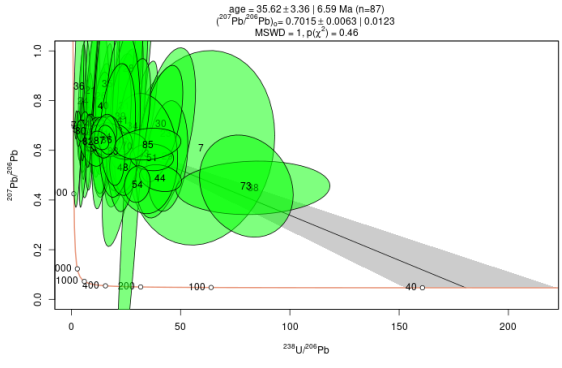

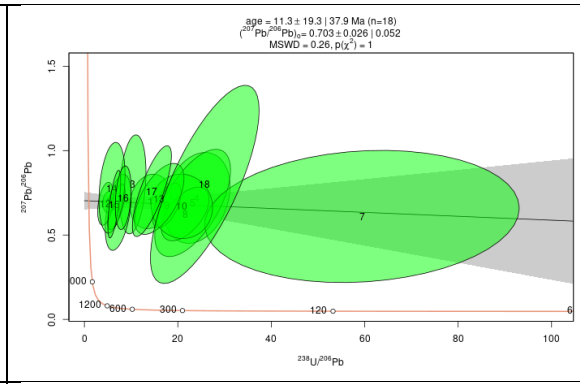

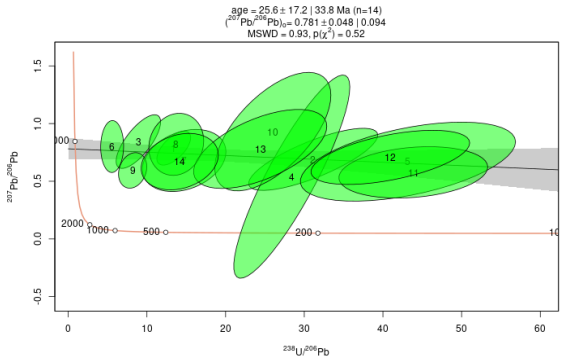

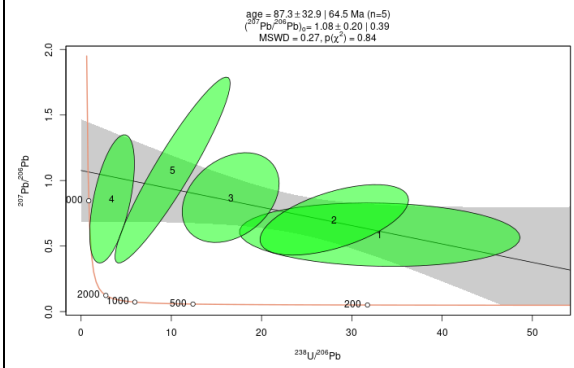

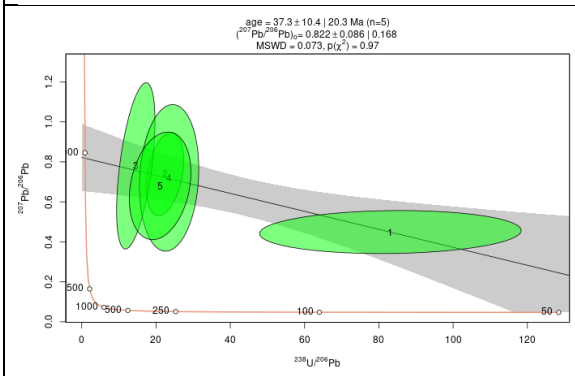

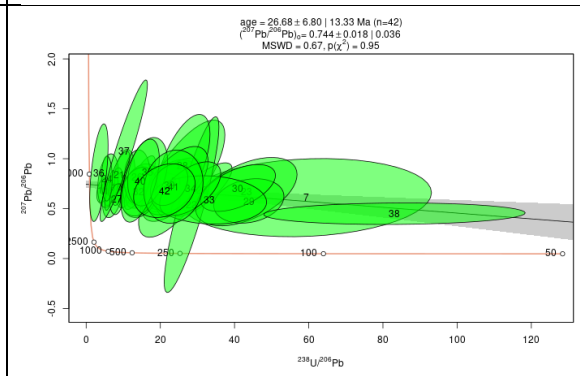

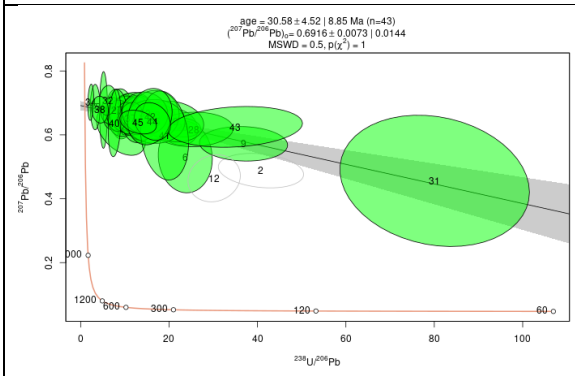

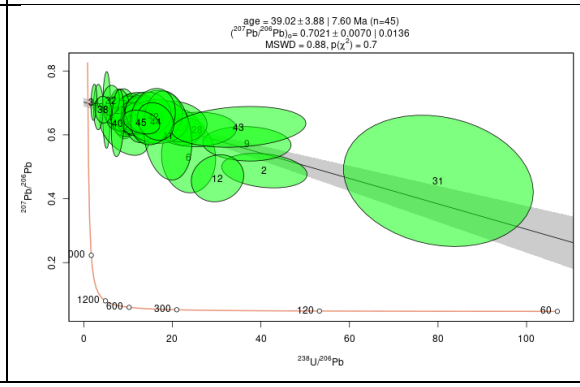

Well 2 Sample 520 Multiple Phases

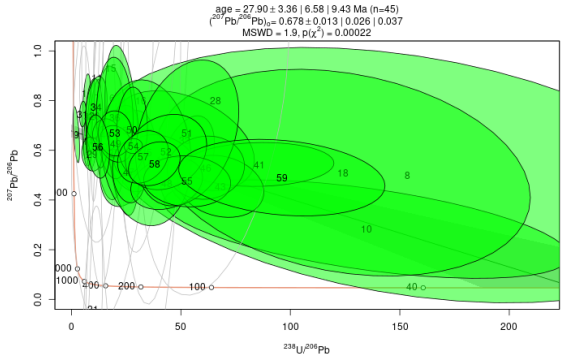

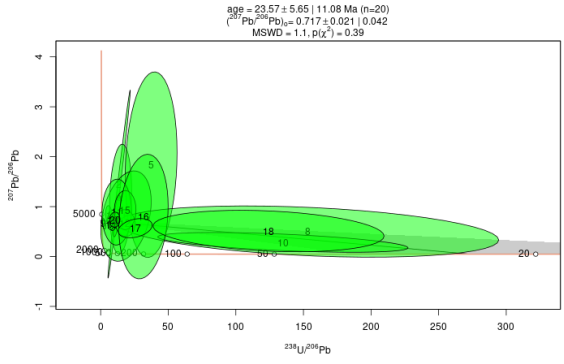

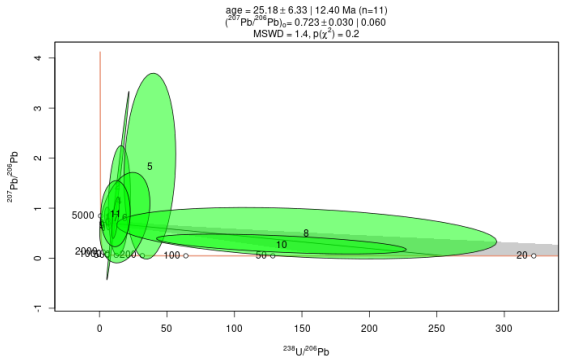

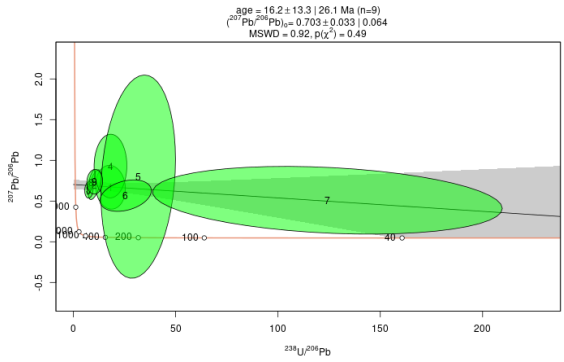

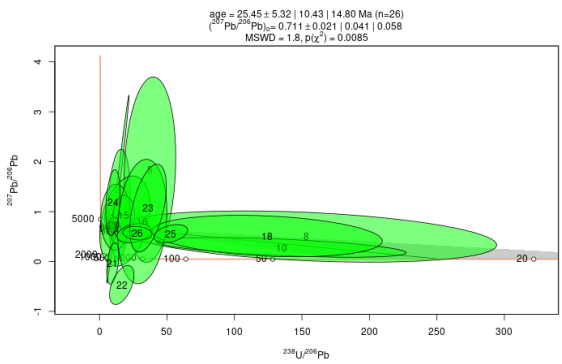

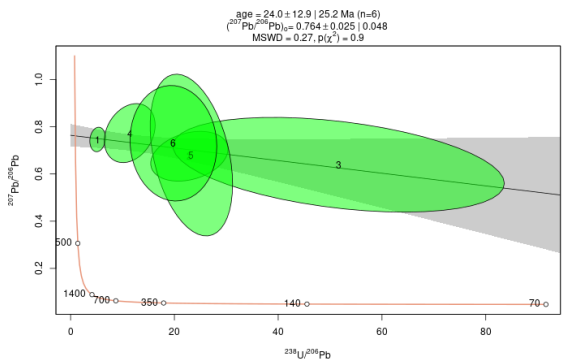

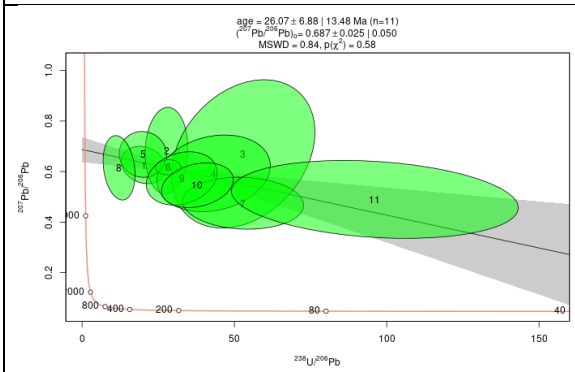

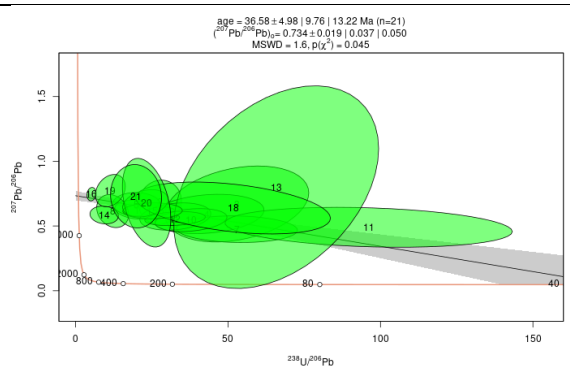

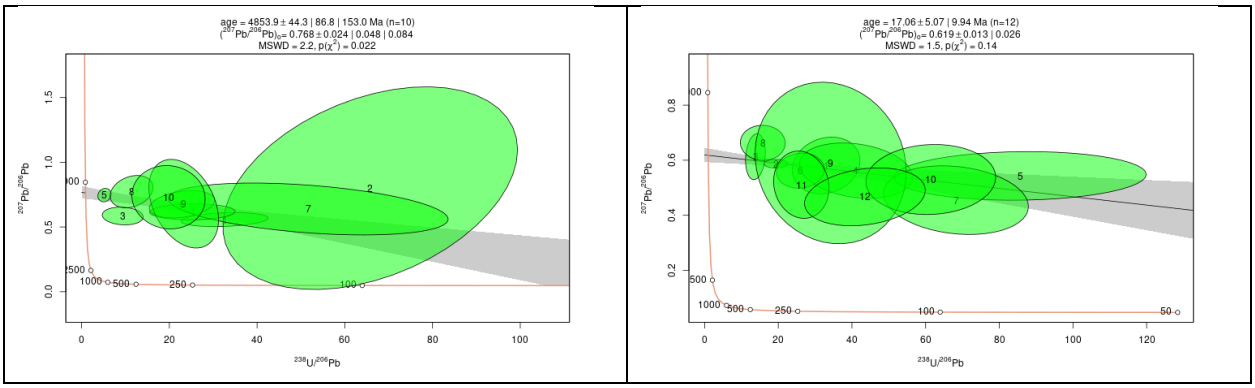
age = 4853.9 ± 44.3 | 86.8 | 153.0 Ma (n=10)
MSWD = 2.2, p(χ²) = 0.022
age = 17.06 ± 5.07 | 9.94 Ma (n=12)
MSWD = 1.5, p(χ²) = 0.14
²⁰⁷Pb/²⁰⁶Pb
²³⁸U/²⁰⁶Pb

Well 2 Sample 540 Multiple Phases

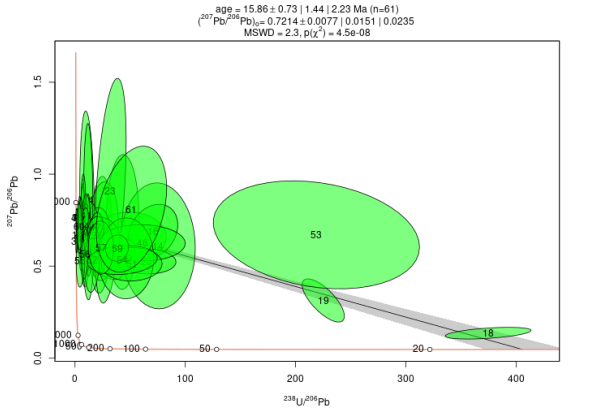

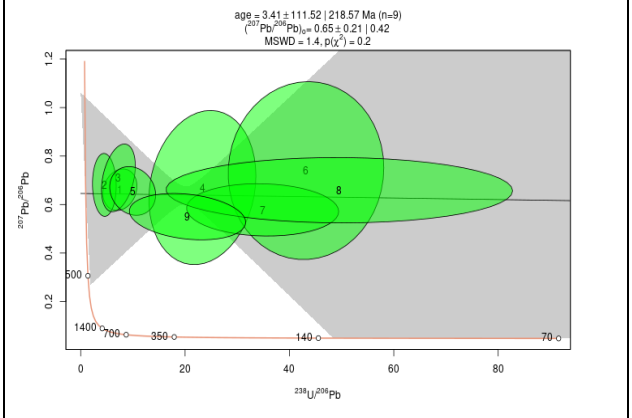

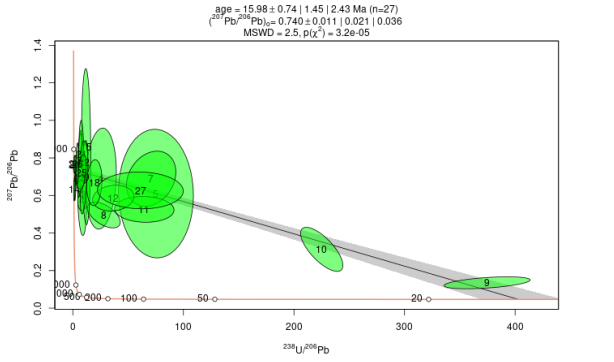

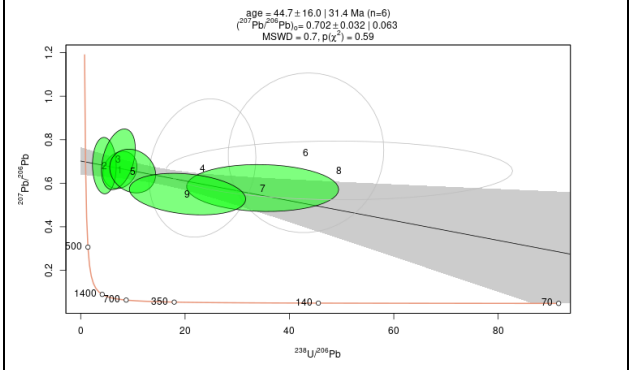

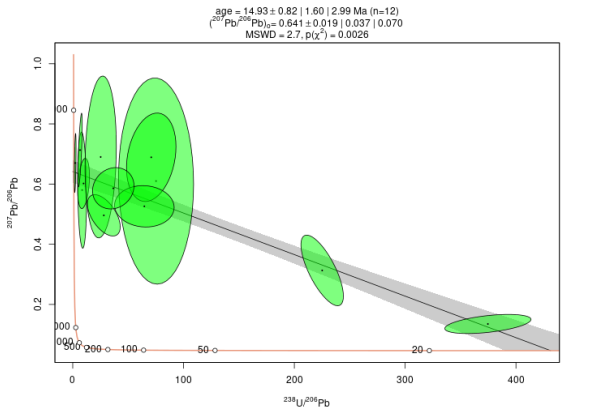

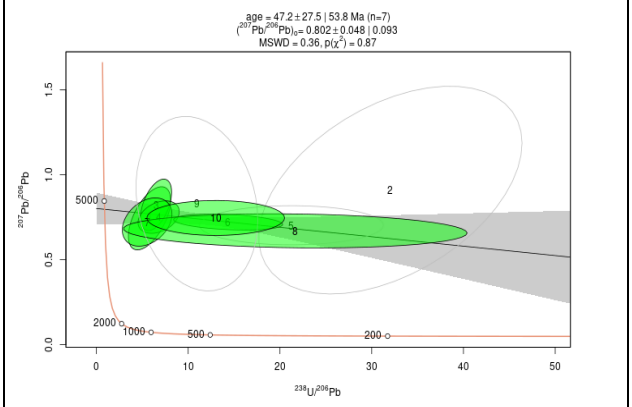

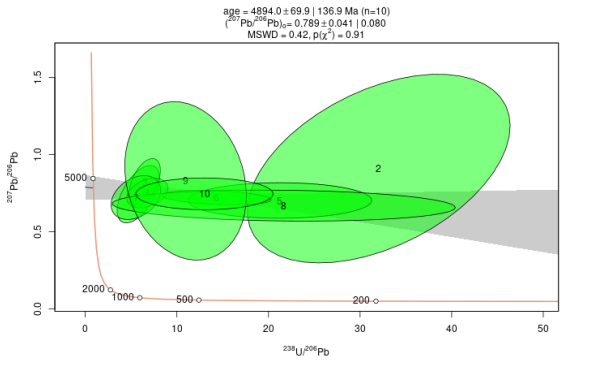

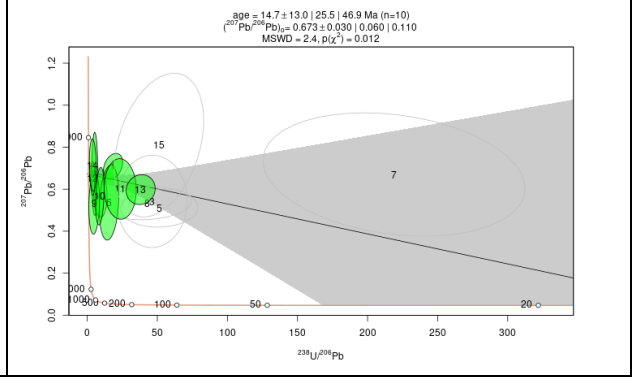

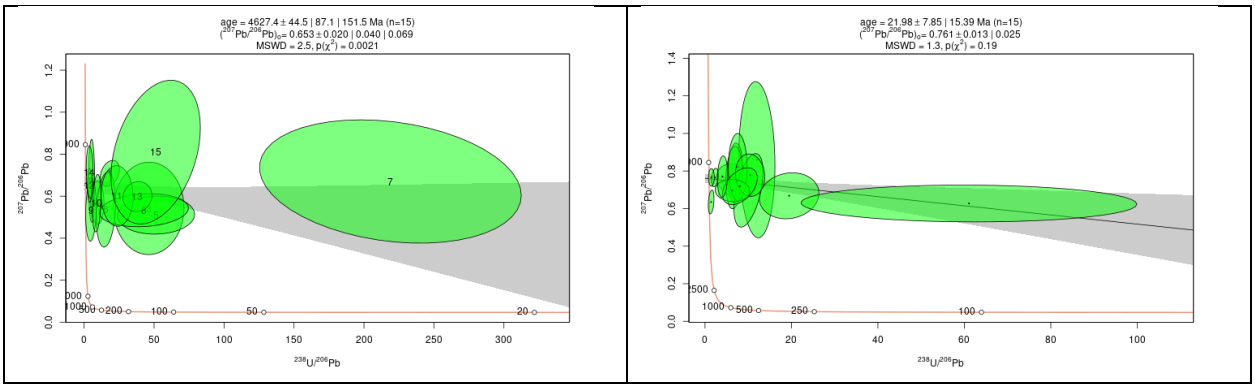
age = 4627.4 ± 44.5 | 87.1 | 151.5 Ma (n=15)
(207Pb/206Pb)i= 0.653 ± 0.020 | 0.040 | 0.069
MSWD = 2.5, p(χ2) = 0.0021
15
7
13
8
500
200
100
50
20
207Pb/206Pb
238U/206Pb
age = 21.98 ± 7.85 | 15.39 Ma (n=15)
(207Pb/206Pb)i= 0.761 ± 0.013 | 0.025
MSWD = 1.3, p(χ2) = 0.19
1000
500
250
100
207Pb/206Pb
238U/206Pb

Well 2 Sample 560 Multiple Phases

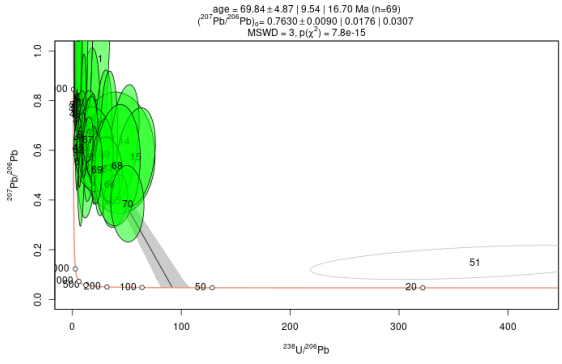

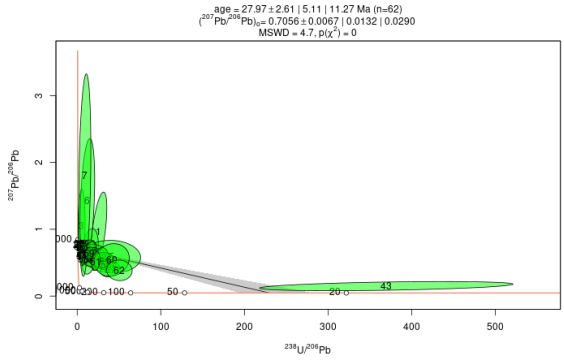

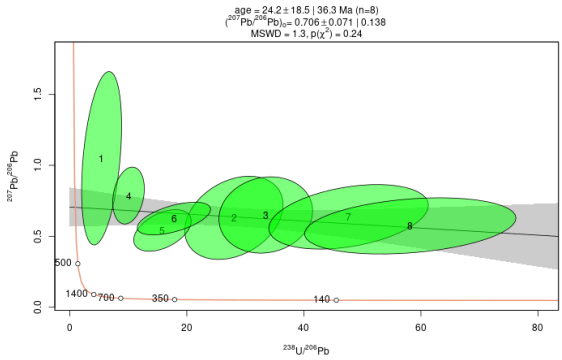

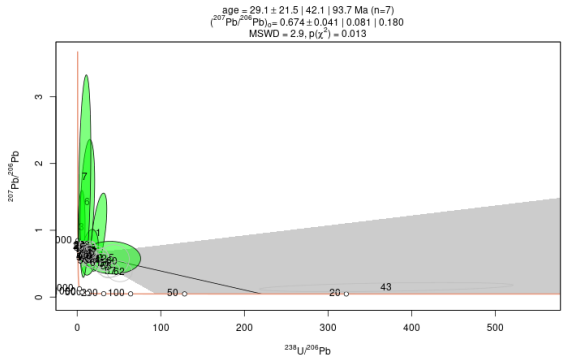

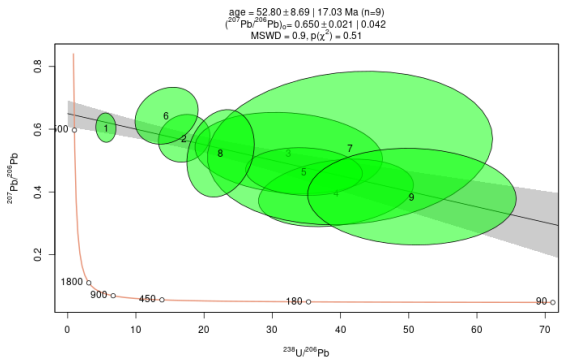

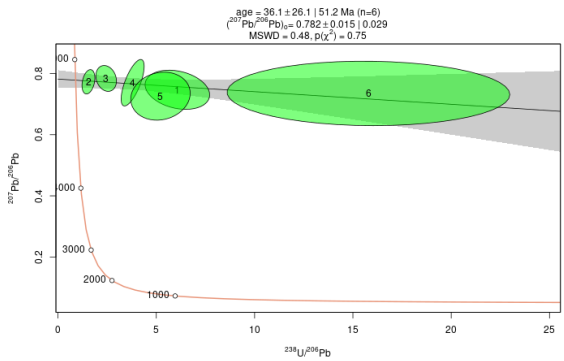

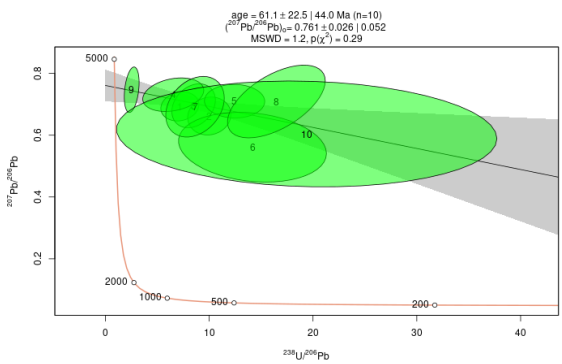

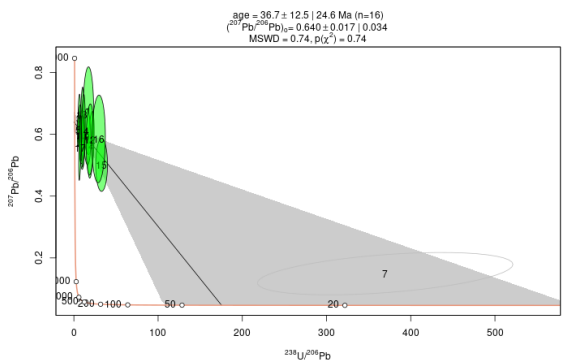

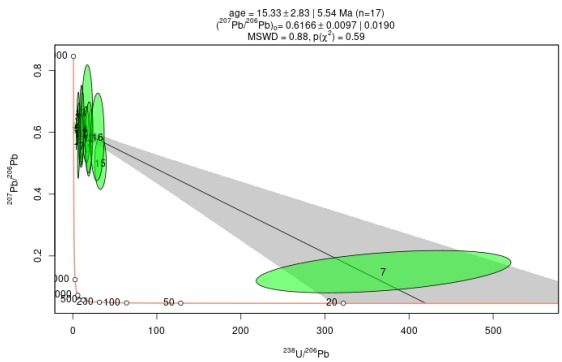
age = 15.33 ± 2.83 | 5.54 Ma (n=17)
(207Pb/206Pb)o= 0.6166 ± 0.0097 | 0.0190
MSWD = 0.88, p(χ2) = 0.59
207Pb/206Pb
238U/206Pb
0
100
200
300
400
500
0.2
0.4
0.6
0.8
7
20
50
100
230

Well 4 Sample 231 Multiple Phases

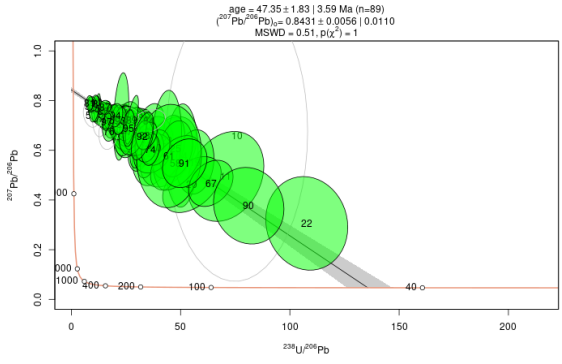

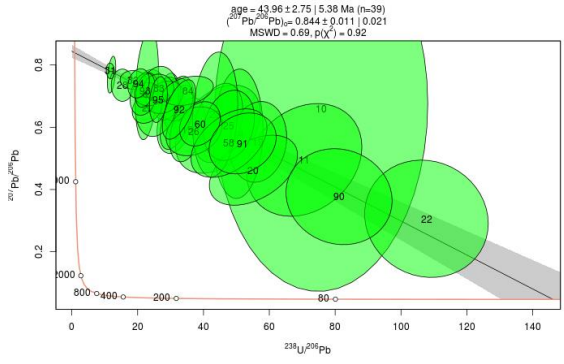

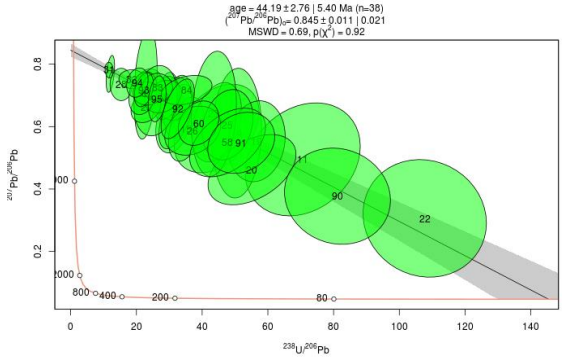

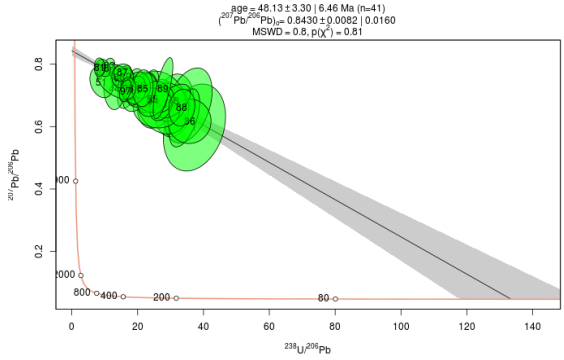

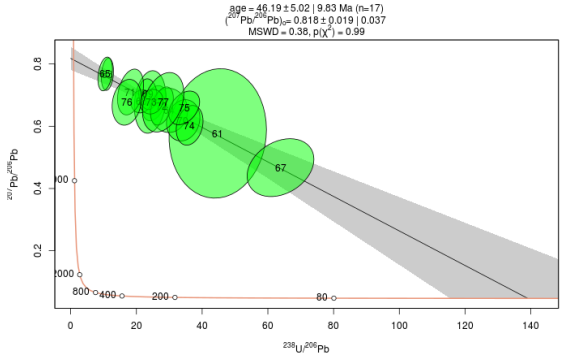

Well 4 Sample 338 Multiple Phases

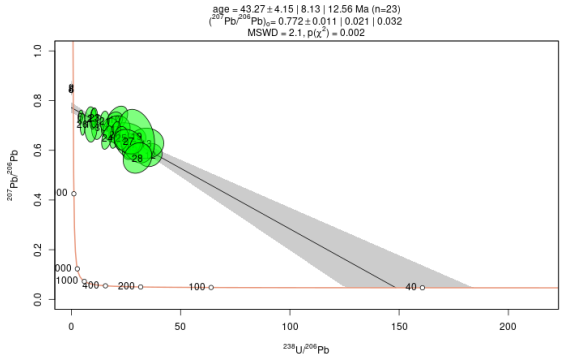

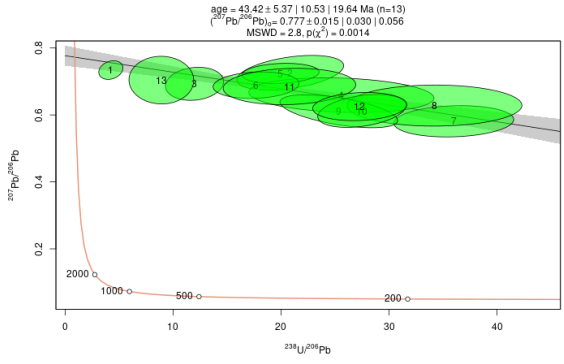

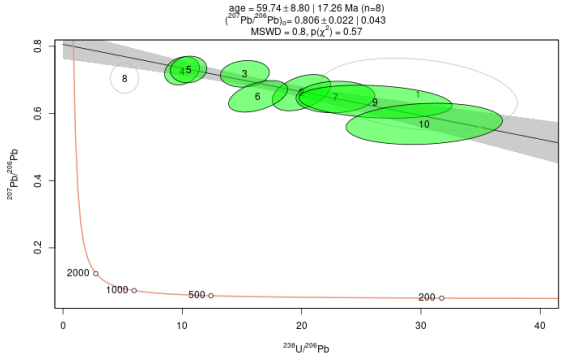

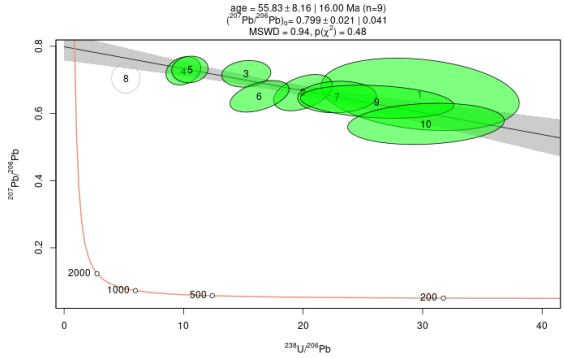

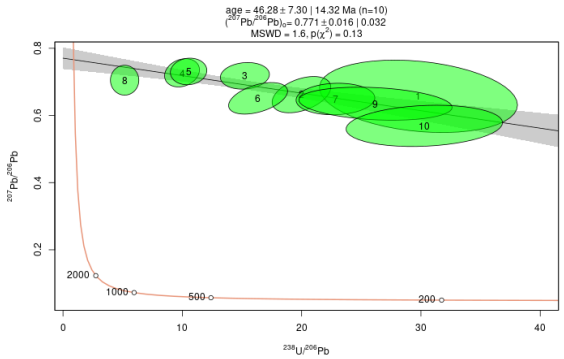

Well 6 Sample 92 Multiple Phases

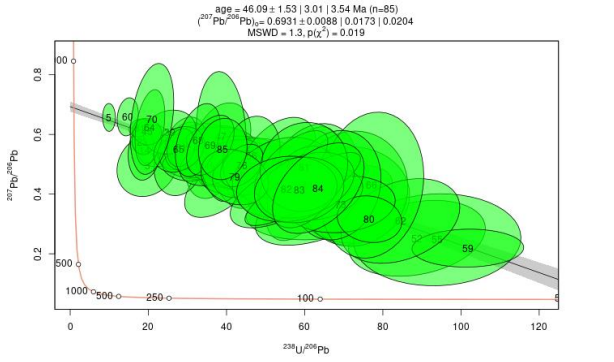

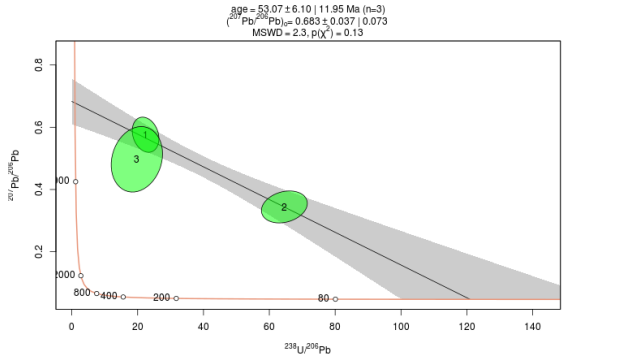

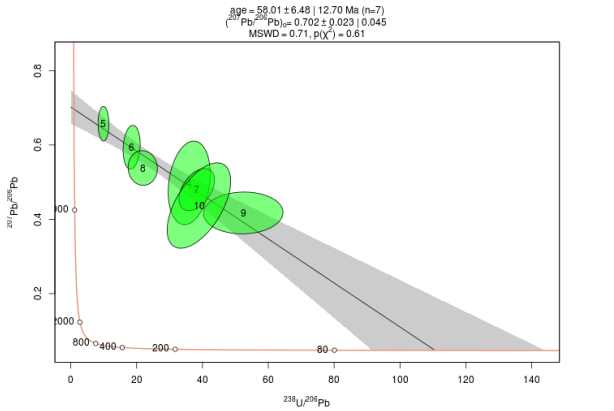

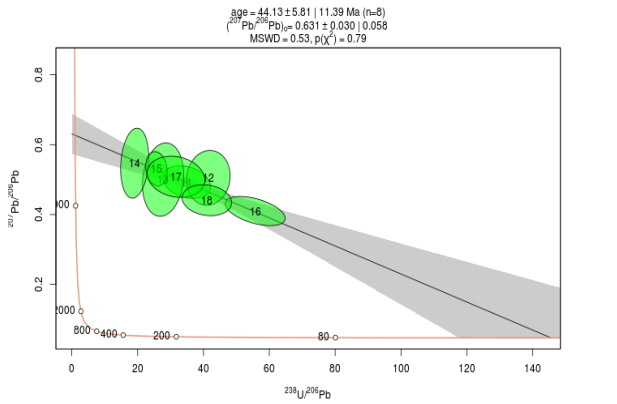

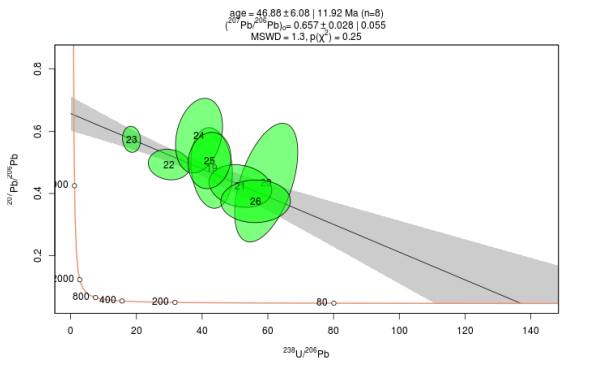

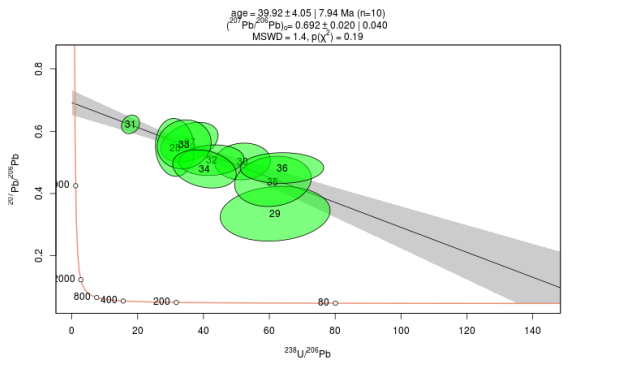

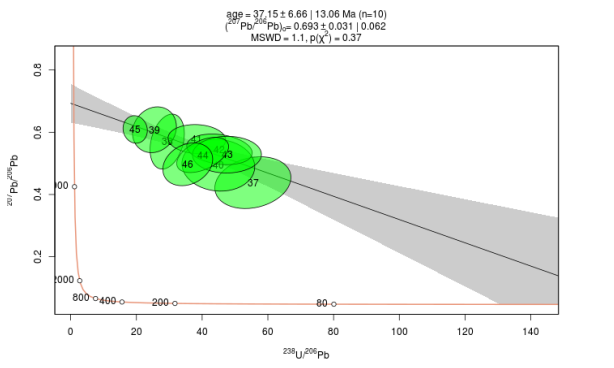

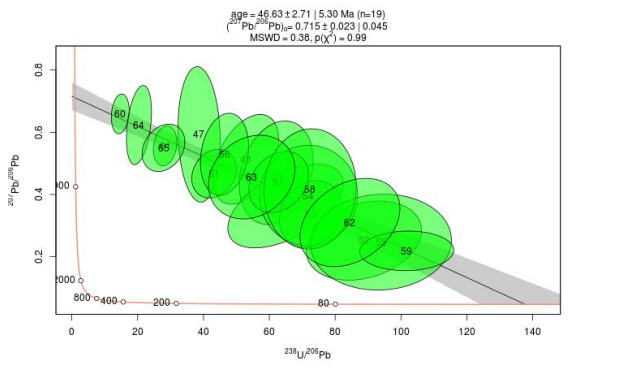

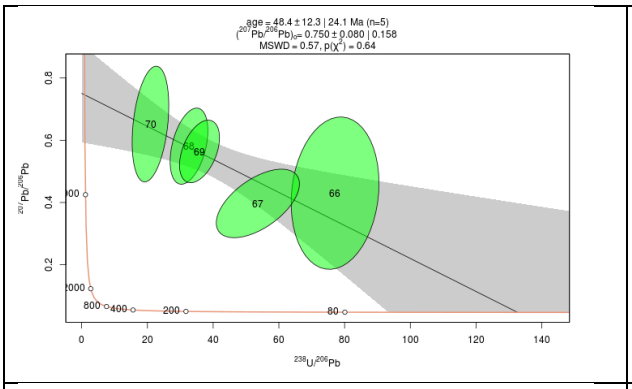
age = 48.4 ± 12.3 | 24.1 Ma (n=5)
MSWD = 0.57, p(χ²) = 0.64
70
69
67
66
80
200
400
800
0
20
40
60
80
100
120
140
0.2
0.4
0.6
0.8

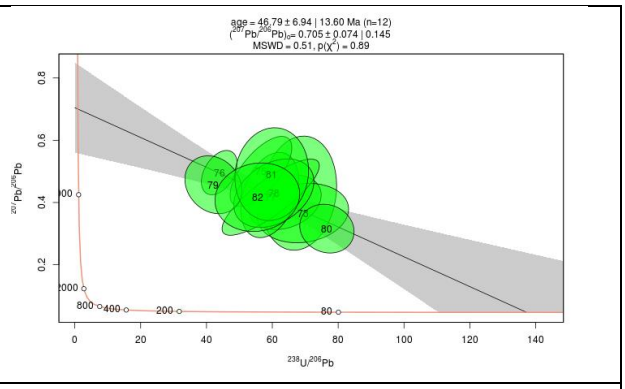
age = 46.79 ± 6.94 | 13.60 Ma (n=12)
MSWD = 0.51, p(χ²) = 0.89
79
82
80
80
200
400
800
0
20
40
60
80
100
120
140
0.2
0.4
0.6
0.8

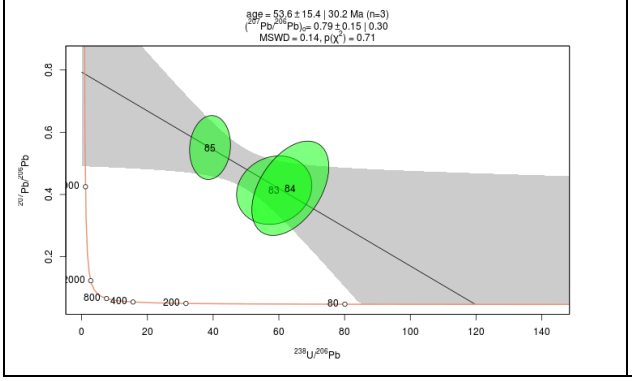
age = 53.6 ± 15.4 | 30.2 Ma (n=3)
MSWD = 0.14, p(χ²) = 0.71
85
83
84
80
200
400
800
0
20
40
60
80
100
120
140
0.2
0.4
0.6
0.8

APPENDIX D: Strontium Isotope Ratio ($^{87}Sr/^{86}Sr$) Data

Well	Sample	Plug	Facies	Lithology	$\delta^{18}O$ VPDB	$\delta^{13}C$ VPDB	$^{87}Sr/^{86}Sr$	Sr ppm
2	1	439	D4	Dolostone	-8.0	2.8	0.70764	23.9
2	2	471	D4	Dolostone	-9.9	3.2	0.70775	12.0
2	3	480	D3	Dolostone	-9.2	3.0	0.70779	24.2
2	4	490	D1	Dolostone	-9.6	2.9	0.70761	28.2
2	5	520	D2	Dolostone	-8.8	2.8	0.70747	6.8
2	6	540	D1	Dolostone	-9.0	2.8	0.70767	17.2
2	7	560	D3	Dolostone	-9.1	2.6	0.70778	17.6
4	1	231	D2	Dolostone	-6.6	1.4	0.70787	10.6
4	2	288	D1	Dolostone	-7.1	2.5	0.70784	11.3
4	3	351	D4	Dolostone	-5.7	2.7	0.70773	17.7
6	1	92	D4	Dolostone	-4.2	1.6	0.70784	90.3
6	2	94	D4	Dolostone	-4.9	1.6	0.70779	16.8
2	1	447		Limestone	-3.5	2.1	0.70701	143.9
2	2	457		Limestone	-5.0	2.6	0.70706	153.1
2	3	459		Limestone	-5.4	2.6	0.70714	6.5
2	1	443		Anhydrite	-8.4	2.7	0.70710	1653.1
2	2	449		Anhydrite	-5.8	0.1	0.70712	1362.5